INAUGURAL-DISSERTATION

zur

Erlangung der Doktorwürde

der

Naturwissenschaftlich-Mathematischen Gesamtfakultät

der

Ruprecht-Karls-Universität

Heidelberg

vorgelegt von Diplom-Chemiker

Helmut Kronemayer

aus Mannheim

Tag der mündlichen Prüfung: 16. November 2007

Laser-based temperature diagnostics in practical combustion systems

Laserbasierte Verfahren zur Temperaturmessung in technischen Verbrennungssystemen

Gutachter:

Prof. Dr. Jürgen Wolfrum

Prof. Dr. Christof Schulz

Abstract

Today's energy supply relies on the combustion of fossil fuels. This results in emissions of toxic pollutants and green-house gases that most likely influence the global climate. Hence, there is a large need for developing efficient combustion processes with low emissions. In order to achieve this, quantitative measurement techniques are required that allow accurate probing of important quantities, such as e.g. the gas temperature, in practical combustion devices.

Diagnostic techniques: Thermocouples or other techniques requiring thermal contact are widely used for temperature measurements. Unfortunately, the investigated system is influenced by probe measurements. In order to overcome these drawbacks, laser-based thermometry methods have been developed, that are introduced and compared in this work. A recently invented multi-line technique based on laser-induced fluorescence (LIF) excitation spectra of nitric oxide (NO) was thoroughly investigated within this thesis. Numerical and experimental studies were conducted to identify ideal spectral excitation and detection strategies. The laser system was improved such that twice the laser energy as before (3 mJ) at 225 nm is available. New detection filters were selected that enable efficient (85%) NO-LIF detection while blocking scattered laser light by a factor of 10^7, which is an improvement by two orders of magnitude. As a result, this calibration-free imaging method can be applied in harsh environments with an accuracy of ±1 K and without influencing the investigated system.

However, in highly turbulent regions, this time-averaged technique is not accurate. Therefore, the systematic error was quantified for all applications in this work. It contributes with ±3% to the measurement uncertainty in turbulent zones of spray flames. In contrast, the error is negligible for all other applications investigated here. When applying high laser fluences, the NO-LIF signal is saturated and interpretation is only possible based on the assumption that quenched molecules cannot return to the ground state within the time of the laser pulse. In cooperation with Dr. T. B. Settersten (CRF, Sandia, USA), experimental evidence was found for the first time that, in contrast to mechanisms proposed in the literature, up to 60% of the quenched molecules do return to the ground state. Hence, population cycling is important and must be taken into account in saturated LIF spectroscopy.

In comparison to LIF thermometry, tunable diode-laser absorption spectroscopy (TDLAS) allows an inexpensive and much more compact setup using fiber-coupled diode lasers. However, the accuracy of this line-of-sight technique is limited in inhomogeneous media. In collaboration with Prof. R. K. Hanson and Dr. J. B. Jeffries (Stanford University, USA) a two-line thermometry sensor based on TDLAS of water was built. Using transitions with high ground-state energies, flame temperature measurements were possible without interference from cold boundary layers.

Applications: Practical combustion devices are often based on spray combustion, involve soot formation, and are enclosed systems. However, sprays, soot, and regions close to solid walls are challenging for laser diagnostics due to intense elastic scattering. After efficient optimization, both techniques, multi-line NO-LIF thermometry and two-line H_2O TDLAS, could be applied within this thesis to quantitatively measure the gas temperature over a wide range of pressures (3 – 500 kPa) and temperatures (270 – 2200 K). This emphasizes the versatility of these techniques.

Data obtained with NO LIF in ethanol spray flames were used to validate new numerical models for ethanol spray combustion developed by Prof. E. Gutheil (Heidelberg University). In cooperation with the Robert Bosch GmbH, Germany, NO LIF was used to quantify the evaporative cooling in internal-combustion (IC) engine-relevant pulsed fuel-sprays with an excellent reproducibility of ±1 K. These results help to clarify misfires in promising direct-injection IC engines. The developed NO-LIF imaging technique has for the first time been successfully applied to sooting high-pressure flames up to 0.5 MPa. The results were required to calculate soot-particle sizes with laser-induced incandescence. It was also found that soot pyrometry can deviate several hundred Kelvin from NO-LIF results and, hence, should be used with care. In IC engines, many pollutants are formed close to the cylinder walls. Therefore, in collaboration with Toyota Central R&D Labs, Japan, new laser diagnostics were applied in boundary layers of solid-wall quenched flames. A high optical resolution of 29 µm was achieved in order to resolve the steep gradient close to the wall, but a step in the temperature profile is observed at the wall that is subject of ongoing discussions. The temperature data enables quantitative LIF species measurements and the optimization of the IC engine thermal management.

Nano-particle properties are strongly size dependent. Their size in turn is influenced by the temperature during production. In this thesis, NO LIF and H_2O TDLAS were applied to determine gas-temperature fields inside a flame-synthesis reactor. The data were taken to validate numerical models for nano-particle formation developed at the University of Duisburg-Essen that permit to control nano-particle sizes. Solid oxide fuel cells (SOFCs) permit an efficient energy conversion with low emissions. In cooperation with Shinko Electric Industries, Japan, and with Prof. J. Warnatz as well as Dr. W. G. Bessler (IWR, University of Heidelberg), H_2O TDLAS was applied to understand and optimize a direct-flame fuel cell (DFFC) system, whose power output is extremely temperature dependent. In the DFFC setup, a SOFC electrochemically converts unburnt fuel into electricity. This technology will be applied as combined heat and power system.

The versatile measurement techniques developed and improved within this thesis enable quantitative probing of the gas temperature in practical combustion devices. Accurate knowledge of this important quantity allows developing efficient power plants and engines with low emissions of green-house gases and toxic pollutants.

Zusammenfassung

Die heutige Energieversorgung basiert auf der Verbrennung fossiler Energieträger. Dies bringt Emissionen von toxischen Schadstoffen und Treibhausgasen mit sich, die potenziell das globale Klima beeinflussen. Folglich besteht großes Interesse an der Entwicklung effizienter Verbrennungsprozesse mit niedrigen Emissionen. Dafür werden Messtechniken benötigt, die eine quantitative Erfassung wichtiger Prozessparameter, wie z.B. der Gastemperatur, in praktischen Verbrennungsprozessen erlauben.

Diagnostik: Zur Temperaturmessung werden häufig Thermoelemente oder andere Techniken verwendet, die Kontakt mit dem Messobjekt voraussetzen. Unglücklicherweise wird das Zielsystem dabei beeinflusst. Daher wurden optische Methoden entwickelt, die in dieser Arbeit vorgestellt und verglichen werden. Eine kürzlich entwickelte Multilinientechnik, die auf Laserinduzierter Fluoreszenz (LIF) von Stickstoffmonoxid (NO) basiert, wurde in dieser Dissertation ausführlich untersucht. Mit Hilfe numerischer und experimenteller Untersuchungen wurden optimale spektrale Anregungs- und Detektionsstrategien entwickelt. Das Lasersystem wurde optimiert, sodass doppelt so viel Energie wie zuvor (3 mJ) bei 225 nm verfügbar ist. Neue Detektionsfilter ermöglichen eine effiziente Fluoreszenzdetektion (85%), während elastisches Streulicht 10^7-fach unterdrückt wird, was eine Verbesserung um zwei Größenordnungen darstellt. Diese kalibrationsfreie, abbildende Methode kann nun in schwierigen Umgebungen mit einer Genauigkeit von ±1 K eingesetzt werden, ohne das untersuchte System zu beeinflussen.

In hochturbulenten Systemen führt diese Technik aufgrund zeitlicher Mittelung zu unkorrekten Ergebnissen. Deshalb wurde der systematische Fehler für alle Anwendungen in dieser Arbeit quantifiziert. Nur in turbulenten Bereichen von Sprayflammen trägt dieser Effekt mit ±3% zur Messungenauigkeit bei, für die sonstigen Anwendungen erwies er sich als vernachlässigbar. Wenn hohe Laserflüsse verwendet werden, wird das NO-LIF Signal gesättigt und kann nur unter der Annahme quantifiziert werden, dass die Moleküle bei der Fluoreszenzlöschung nicht in den Grundzustand zurückkehren. In Kooperation mit Dr. T. B. Settersten (CRF, Sandia, USA) wurden, im Gegensatz zu theoretischen Vorhersagen der Literatur, erstmals experimentelle Hinweise gefunden, dass jedoch bis zu 60% der Moleküle innerhalb des Laserpulses in den Grundzustand zurückkehren. Der Populationstransfer beeinflusst folglich die Sättigungsspektroskopie und muss daher bei der Auswertung berücksichtigt werden.

Diodenlaserbasierte Absorptionstechniken (TDLAS) erlauben, im Vergleich zu LIF-Methoden, einen kostengünstigen und kompakten Aufbau. Jedoch ist die Genauigkeit von TDLAS in inhomogenen Medien aufgrund der Sichtlinienintegration beschränkt. In Zusammenarbeit mit Prof. R. K. Hanson und Dr. J. B. Jeffries (Stanford Universität, USA) wurde ein Sensor optimiert, der auf TDLAS von Wasser basiert. Durch die ausschließliche Verwendung von Übergängen mit hohen Grundzustandsenergien wurde die Empfindlichkeit für kalte Randzonen bei Flammenmessungen erheblich reduziert.

Anwendungen: Realitätsnahe Verbrennungssysteme sind umschlossen und basieren häufig auf Sprayverbrennung. Auch Rußbildung wird oft beobachtet. Wände, Sprays und Ruß stellen jedoch aufgrund des starken Streulichtes eine Herausforderung für Lasermesstechniken dar. Dank einer effizienten Optimierung konnten beide Methoden, die Multilinien NO-LIF Thermometrie und Zwei-Linien H_2O-TDLAS, in dieser Arbeit zur quantitativen Temperaturmessung in einem weiten Druck- (3 – 500 kPa) und Temperaturbereich (270 – 2200 K) eingesetzt werden und bewiesen dadurch ihre Vielseitigkeit.

Temperaturfelder wurden mit NO-LIF in Ethanol-Sprayflammen gemessen und dienten zur Validierung neuer numerischer Modelle, die von Prof. E. Gutheil (Universität Heidelberg) entwickelt werden. In Kooperation mit der Robert Bosch GmbH Deutschland wurde die Verdampfungskühlung in gepulsten Ethanolsprays mit einer exzellenten Reproduzierbarkeit von ±1 K quantifiziert. Diese Ergebnisse sind wichtig für die Aufklärung von Fehlzündungen in direkteinspritzenden Verbrennungsmotoren. Die NO-LIF Multilinientechnik wurde erstmals erfolgreich in rußenden Hochdruckflammen bis 0.5 MPa eingesetzt. Dies ermöglichte Rußpartikelgrößenmessungen mit Laserinduzierter Inkandeszenz. In dieser Arbeit wurde herausgefunden, dass Pyrometrie an Rußpartikeln um mehrere hundert Kelvin von NO-LIF Ergebnissen abweichen kann und daher kritisch bewertet werden muss. In Verbrennungsmotoren werden viele Schadstoffe nahe der Zylinderwand gebildet. Daher wurde diese Grenzschicht in einer Kooperation mit den Toyota Central R&D Labs, Japan, untersucht. Eine hohe räumliche Auflösung von 29 µm wurde erreicht, um den steilen Temperaturgradienten aufzulösen. Dennoch wurde and der Wand ein Sprung im Temperaturprofil beobachtet. Diese Daten ermöglichen quantitative LIF-Spezies-Messungen und die thermische Optimierung der Motoren.

Nanopartikeleigenschaften sind stark größenabhängig. Die Temperaturverteilung im Synthesereaktor wiederum beeinflusst die Partikelgröße. In dieser Arbeit wurden beide Methoden, NO-LIF und H_2O-TDLAS, eingesetzt, um die Temperaturverteilung im Reaktor zu messen. Die Ergebnisse dienten zur Validierung numerischer Modelle zur Nanopartikelbildung (Universität Duisburg-Essen), die nun eine kontrollierte, größenselektive Nanopartikelbildung ermöglichen. Festoxidbrennstoffzellensysteme (SOFC) erlauben eine effiziente Stromerzeugung mit sehr geringen Emissionen. In Zusammenarbeit mit Shinko Electric Industries, Japan, sowie Prof. J. Warnatz und Dr. W. G. Bessler (IWR, Universität Heidelberg) wurde H_2O-TDLAS genutzt, um ein Direktflammenbrennstoffzellensystem (DFFC) zu verstehen und zu optimieren. In der DFFC wandelt die SOFC unverbrauchten Brennstoff elektrochemisch in Strom um. Diese Technologie soll nun zur Kraft-Wärme-Kopplung eingesetzt werden.

Die Messtechniken, die in dieser Arbeit entwickelt wurden, erlauben eine quantitative Erfassung der Gastemperatur in praktischen Verbrennungsprozessen. Die genaue Kenntnis dieses wichtigen Parameters ermöglicht die Entwicklung effizienter Kraftwerke und Motoren mit niedrigen Emissionen von Schadstoffen und Treibhausgasen.

Contents

1 Introduction

There is strong scientific evidence that the rising energy consumption of our modern, globally acting societies causes a change in the world-wide climate [1]. Over the last decades, the average temperature on earth increased, which led to desert growing, glacier melting, and a rising sea level. It is known from paleo-climate research that drastic changes in the global climate occur naturally and even periodically. However, clarifying the reasons for these natural changes as well as for anthropogenic effects is subject of ongoing research and controversial discussions.

Physical models are being developed in order to explain historic changes as well as the recent temperature increase [1]. According to these models, the current temperature increase is primarily due to the enormous anthropogenic emissions of green-house gases like e.g. CO_2 and CH_4. The models also predict a rise of a few Kelvin in temperature within this century. However, since the world climate is very complex, strongly back coupled and poorly understood yet, projections from these models are associated with high uncertainties. In particular, the cooling effects of atmospheric aerosols are not quantified. Also, high concentrations of CO_2 in the atmosphere did not always result in a warmer climate in the past.

Green-house gas emissions arise from the development of industrialized societies [2]. Most of the required energy was and still is taken from the combustion of fossil fuels, e.g. coal, oil, and gas (cf. Fig. 1) since they are comparably inexpensive. In 2004, fossil fuels contributed 80% to the world-wide primary energy supply [3]. The pollutants produced by burning fossil fuels cause, next to the global green-house effect, also local environmental reactions. The emission of nitrogen oxides (NO_x) in the atmosphere leads to acid rain. Nano-sized particulate matter emitted by Diesel cars and unfiltered wood fires penetrates deeply into the lung and causes asthma, fibrosis and the development of tumors [4,5].

In general, mankind would be able to satisfy its energy needs by using solar energy only, since the solar irradiation at the earth surface (~10^{18} kWh/year) exceeds the current world-wide energy consumption (~10^{14} kWh/year) ten thousand times [3,6]. Wind, water and solar energy deliver most of this energy as electricity, that could supply a global power grid [7]. Unfortunately, the storage energy density for electricity (Li-ion

battery: ~10^2 Wh/kg) is still much lower than that of liquid fuels (gasoline: ~10^4 Wh/kg) [8,9]. Therefore, liquid fuels are necessary for mobile applications.

But these fuels do not necessarily have to be transformed in a combustion process. New technologies, like e.g. fuel cells are able to convert the chemically stored energy into electricity with NO_x and CO emissions that are two orders of magnitude lower than a combustion process reaches [10]. But fuel cell technology is still not long-term reliable and cost efficient. Due to the rising oil price and the increasing political instability in oil- and gas-producing countries, the development of renewable liquid fuels such as methanol in a biomass-to-liquid (BTL) process is of great interest [11-13].

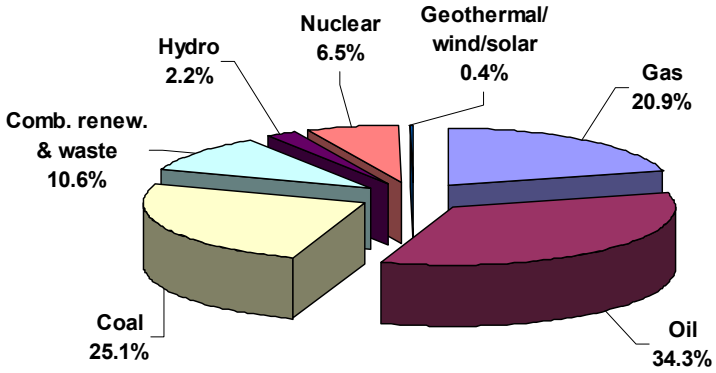

Fig. 1: Share of total primary energy supply in the world 2004 [3].

For these reasons, combustion technology will most probably stay the major energy transformation process within the next decades and there is a large need for improving the efficiency and cutting down the emissions of e.g. power plants and car engines, that together cover the largest part of today's consumption of fossil fuels. Exhaust-gas after treatment is a possible way to reduce pollutant emissions, but only at the cost of efficiency. Only an improvement and full control of the combustion process itself leads to higher efficiency. This, however, is only possible through detailed knowledge of the physical and chemical conditions of the combustion process and can hardly be achieved by trial-and-error methods any longer.

Since the first development of lasers in the 1960s, laser spectroscopy has become a most important tool in fundamental and applied combustion research [14]. The unique properties of laser light enable selective and quantitative probing of many physical (pressure, temperature), chemical (species composition), and gas dynamical (flow velocities, turbulence structures) parameters with high temporal and spatial resolution [15]. The optical nature of laser techniques allows access to enclosed systems with minimum perturbation [16] of the system under study in contrast to probe techniques [17].

The data gained by such measurements are then taken to develop numerical models that describe the individual combustion process physically and mathematically [18]. This way, parameter studies can be conducted numerically without the need of expensive experiments. But so far, the complete, realistic description of a macroscopic combustion process like an internal combustion (IC) engine based on precise physics with e.g. direct numerical simulation (DNS) is not possible, even with parallel computing [19]. Therefore, simplifications must be made in the numerical models. These cause unknown errors, and the models must validated with well-defined laboratory experiments to prove their physical reliability before they can be used for the development of practical combustion systems.

This thesis focuses on the development of laser-diagnostic techniques for the measurement of the gas-phase temperature in practical, particle-laden combustion processes. Temperature distributions are of major interest in the description of reactive and non-reactive flow systems, where they play a crucial role in chemistry (reaction rates, equilibrium state) and physics (heat transfer, fluid dynamics, and droplet evaporation).

A number of fundamentally different laser-based techniques were developed and have been applied for temperature measurements in gas-phase flows [20]. Detailed discussions can be found in the book of Dreizler and Schulz [21] and in the review articles of Stricker [22] and Laurendeau [23]. However, spray combustion, sooting flames, and regions close to solid walls are present in most practical combustion devices, but provide a harsh environment for gas-phase laser diagnostics because the stray light at particles or surfaces has to be greatly reduced in order to obtain reliable data.

The most frequently used laser-based thermometry methods principally rely either on the temperature dependence of the total number density (e.g. Rayleigh scattering, spontaneous Raman scattering) given by the ideal gas law or on the temperature dependent quantum state population distribution of atomic or molecular probes given by the Boltzmann law (e.g. spontaneous Raman scattering, Coherent Anti-Stokes Raman Scattering (CARS), laser-induced fluorescence (LIF), absorption spectroscopy). However, there is to date no versatile, accurate and robust technique that can be applied to all experimental conditions.

CARS thermometry has a high accuracy but allows point-wise measurements only. Rayleigh scattering provides relatively strong signals but usually requires calibration. Spontaneous Raman scattering is frequently used for temperature evaluation in one-dimensionally resolved multi-species measurements, but the signal intensity is low. LIF thermometry provides strong signals and has been frequently used for imaging thermometry. Absorption techniques necessarily accumulate information along the line of the laser path through the measurement volume.

In this work, the theoretical background is provided to understand the physics and spectroscopy of the most successful laser-based temperature diagnostics. Two techniques were further developed and are thus described in detail:

- Multi-line thermometry based on laser-induced fluorescence excitation spectra of nitric oxide [24] is a powerful technology since it is calibration free, accurate, and can be applied in practical combustion environments with strong scattering.
- Two-line thermometry with tunable diode laser absorption spectroscopy [25] based on absorption of water vapor is a promising, calibration-free method with a compact setup and a high time resolution.

In the last part of this thesis, applications of these two techniques to a broad range of practical combustion systems are presented reaching from spray combustion, spray evaporation, soot diagnostics, wall-quenched flames, and nano-particle synthesis to fuel cell technology.

2 Theoretical background

The temperature range observed in our universe spans several orders of magnitude. Temperatures close to absolute zero have been reached in laboratories in order to investigate the behavior of matter under these extreme conditions [26]. Matter changes its behavior only because of its temperature. Superconductivity is observed with e.g. mercury. The electrical resistance suddenly disappears when the metal is cooled below 4.3 K. Below 10^{-10} K molecular motion is almost frozen and new states of matter were found such as Bose-Einstein condensates [27]. On the other hand, temperatures in stars can reach 10^7 Kelvin. Here, molecules and atoms are ionized and form a plasma.

The temperature range that is important for human life lies somewhere in between these extremes. Here, we find the traditional states of matter: gas, liquid and solid phases. Measuring ambient temperature at home is a simple and cheap task for today's technology standards. However, measurements in other temperature ranges as well as in difficult environments with high spatial and temporal resolution are subject of ongoing research. In this chapter, the theoretical background for laser-based temperature diagnostics will be given. Fundamental knowledge about temperature itself, lasers, as well as molecular spectroscopy is necessary.

2.1 What is temperature?

Temperature is a physical property of a system and one of the principal variables of thermodynamics. Something with a high temperature is called hot and low temperature is defined as cold. It is a macroscopic, intensive property of matter and only valid for an ensemble of particles. On a molecular scale, the absolute temperature T of an ensemble of particles is defined as the average energy $<E>$ of motion of a single particle per degree of freedom of motion:

$$T = \frac{2 < E >}{k_B} \tag{1}$$

The proportionality constant k_B between units of temperature in Kelvin and energy in Joules is called Boltzmann constant; its numerical value is $k_B = 1.38 \times 10^{-23}$ J/K. All properties of temperature mathematically follow from this definition. For a solid, these microscopic motions are principally the vibrations of the constituent atoms about their sites in the solid. For an ideal monatomic gas, the microscopic motions are the translational motions of the constituent gas particles. For multi-atomic gas rotational and vibrational motion should be included as well. Thus a diatomic gas, with extra degrees of freedom like rotation and vibration, will require a higher energy input to change the temperature by a certain amount, i.e. it will have a higher heat capacity than a monatomic gas. Internal energy of a particle is also due to excitation of an electronic energy level, electron spin or atomic nucleus spin.

In thermodynamics, temperature is defined within the laws of thermodynamics, independent of molecular quantum states of molecular species. The zeroth law of thermodynamics describes the behavior of systems in thermal equilibrium. A system in thermal equilibrium is a system whose macroscopic properties (like pressure, temperature, volume, etc.) are not changing in time. Two systems are said to be in thermal equilibrium when both of the systems are in a state of equilibrium, and they remain so when they are brought in contact.

The first law describes the energy conservation in an enclosed system and the second law states the ever rising entropy in a thermodynamically favoured process. Finally, the third law of thermodynamics states that as a system asymptotically approaches absolute zero of temperature all processes virtually cease and the entropy of the system asymptotically approaches a minimum value.

The temperature of a system at thermodynamic equilibrium can be defined by a relation between the amount of reversible heat transfer in a Carnot process dQ_{rev} incident on the system during an infinitesimal quasi-static transformation, and the variation dS of its entropy during this transformation. Contrary to entropy and heat, whose microscopic

definitions are valid even far away from thermodynamic equilibrium, temperature can only be defined at thermodynamic equilibrium [28].

$$T = \frac{dQ_{rev}}{dS} \tag{2}$$

2.1.1 Temperature scales

Temperature is measured with thermometers that may be calibrated to a variety of temperature scales. The entire scientific world measures temperature using the Kelvin scale, which is the basic unit in the international systems of units (SI). Throughout the non-scientific world (except for in the U.S.), the Celsius scale is used for most temperature measuring purposes. The U.S., however, uses the Fahrenheit scale.

The Kelvin scale is an absolute temperature scale and reaches from zero to infinity. The process of cooling involves removing energy from a system. When there is no more energy able to be removed, the system is said to be at absolute zero, which is the point on the absolute temperature scale where all kinetic motion in the particles comprising matter ceases and they are at complete rest in the "classic" (non-quantum mechanical) sense. By definition, absolute zero is a temperature of precisely 0 K and −273.15°C. At absolute zero, matter contains no thermal energy. Also, the triple point of water is defined as being precisely 273.16 K and 0.01°C. This definition fixes the magnitude of the Kelvin unit as being precisely one part in 273.16 parts the difference between absolute zero and the triple point of water. Also, it establishes that one Kelvin has precisely the same magnitude as a one degree increment on the Celsius scale. Further, it establishes the difference between the two scales' null points as being precisely 273.15 K.

On the Celsius scale, 0°C corresponds to the temperature at which water freezes and 100°C corresponds to the boiling point of water at sea level. On this scale, a temperature difference of 1 degree is the same as a 1 K temperature difference, so the scale is essentially the same as the Kelvin scale, but offset by the temperature at which water freezes (273.15 K). Thus the following equation can be used to convert from Kelvin to degree Celsius:

$$°\mathrm{C} = \mathrm{K} - 273.15 \tag{3}$$

In the United States, the Fahrenheit scale is widely used. On this scale, the freezing point of water corresponds to 32°F and the boiling point to 212°F. The following formula can be used to convert from Fahrenheit to Celsius and Kelvin:

$$°\mathrm{F} = °\mathrm{C}\frac{9}{5} + 32 = \mathrm{K}\frac{9}{5} - 459.67 \tag{4}$$

Physicists sometimes describe a temperature of one single particle in order to express its energy. In the field of plasma physics, because of the high temperatures encountered

and the electromagnetic nature of the phenomena involved, it is customary to express temperature in electron volts (eV) where 1 eV = 11606 K. Other temperature scales such as Rankine, Delisle, Newton, Réaumur, and Romer have been introduced in the past and are not discussed in detail here since they are no longer used.

2.1.2 Temperature measurement techniques

Many methods have been developed for measuring temperature. All of them rely on measuring some physical property of matter that varies with temperature. A summary of the most common temperature measurement techniques is given in Table 1 together with their physical background. First, methods are presented that require thermal contact with the observed medium. After that, methods based on radiation are described.

Measurement technique	Thermal contact required	Physical base
Glass thermometer	Yes	Thermal expansion of liquids
Gas thermometer	Yes	Thermal expansion of gases
Thermocouples	Yes	Thermoelectric effect upon contact of two metals
Resistance thermometer	Yes	Temperature-dependent resistance of metals
Pyrometer, IR detector	No	Planck's law of black body radiation
Laser-based diagnostics	No	Boltzmann distribution or ideal gas law

Table 1: Temperature measurement techniques.

Methods based on thermal contact

The glass thermometer consists of a glass tube filled with mercury or some other liquid, which acts as the working fluid. A temperature increase causes the fluid to expand; the temperature can be determined by measuring the volume of the fluid. Such thermometers are usually calibrated, so that one can read the temperature simply by observing the level of the fluid in the thermometer.

Another type of thermometer is the gas thermometer. Keeping the volume V of the enclosed apparatus constant, the temperature T can be determined from the change in pressure p upon thermal contact using the ideal gas law:

$$pV = nRT \tag{5}$$

Here, n represents the number of gas molecules in moles (1 mol = 6.022×10^{23} molecules) and R is the universal gas constant with the numerical value R = 8.314 J/(molK). To be more accurate, gases should be treated by a non-ideal gas law such as the Van-der-Waals equation. Here, inter-molecular forces and the space the molecules themselves have are taken into account. However, for all applications presented in this thesis, the ideal gas law is a good approximation.

Frequently, temperature is measured with thermocouples. If two metals are in contact, a voltage can be measured between them that rises with increasing temperature. This is called the thermoelectric effect or Seebeck effect. Type K (Chromel (Ni-Cr alloy) / Alumel (Ni-Al alloy)) thermocouples are cheap and can be applied in the 100 – 1500 K range. The sensitivity is approximately 41 μV/K. Type B (Pt-Rh-Pt) thermocouples can measure temperatures up to 2100 K and are thus frequently used in combustion research.

Resistance thermometers use the temperature-dependent resistance of materials. Commercially available platinum sensors in Europe (PT-100) are produced to have a resistance of 100 Ω at 273.15 K and a sensitivity of 0.385 Ω/K. Because resistance can be measured very precisely, they are suitable for high-precision temperature measurements [29].

All thermometers presented so far require contact to the target object until thermal equilibrium is reached. The major drawback of this strategy is that, upon contact, the system to be measured is necessarily influenced and the "real" temperature can never be measured. Additionally, the probe surface often exhibits catalytic behavior in reactive media and severely affects the system. Even worse, the thermometer itself can be influenced by the system. Further, the time resolution is limited since one has to wait until thermal equilibrium is reached. Also, the thermometer radiates at high temperatures and the measured values have to be corrected for radiation losses.

Methods based on photon radiation

Optical techniques were developed that overcome these disadvantages in order to remotely measure the accurate temperature by the use of light. Infrared cameras and pyrometers detect the black-body radiation emitted from the target material described by Planck's law.

$$I(\lambda,T)=\frac{2hc^2}{\lambda^5}\frac{1}{\exp\left(\frac{hc}{\lambda k_B T}\right)-1}\varepsilon(\lambda) \tag{6}$$

Here, the spectral radiance $I(\lambda,T)$ at a certain wavelength λ is only dependent on the temperature T. Planck's constant h and the speed of light c are natural constants. For an ideal black body, the emissivity $\varepsilon(\lambda)$ is 1 and does not depend on the wavelength. However, real surfaces do not emit like an ideal black body and are thus called "grey body" with emissivities between 0 and 1 in case of continuous emission spectra. For accurate practical measurements in a wide temperature range (200 – 4000 K), the wavelength dependence of the emissivity of the material must be known as well, e.g. for soot temperature measurements (cf. section 5.3.2). If the target object mainly emits at specific

wavelengths, it is called a line emitter. This is the case especially for gases, where this method cannot be used.

In order to obtain gas temperature in combustion research, pyrometry can be applied to measure the surface temperature of e.g. a platinum bead that is placed into the flame. After correction for radiation losses to the walls, the platinum bead temperature is assumed to be identical to the gas temperature. However, the flame itself is disturbed by this intrusive strategy by introducing catalytically active surfaces [30].

In sooting flames, the emission of soot particles can be detected without disturbing the flame and the soot particle temperature can be assumed to be similar to the gas temperature (cf. chapter 5.3.2). The major drawback of pyrometry in a gas-phase system is the unknown origin of the detected radiation. The detection system usually integrates the light along a line-of-sight through the flame, as far as the radiation can penetrate the dense soot cloud. Additionally, the overall radiation power P of a black body rises extremely with increasing temperature which is described by the Stefan-Boltzmann law: $P \sim T^4$. Therefore, only the maximum temperatures within the observed volume are accessible with pyrometry since the hotter regions emit much more light than colder areas.

The spectral distribution of the black body radiation is described by eq. 6 and is plotted in Fig. 2 in a range from 2000 – 3000 K. Note that even for 3000 K, most of the radiation is emitted in the infra red (IR). With increasing temperature, the maximum intensity of the emitted light shifts towards lower wavelengths.

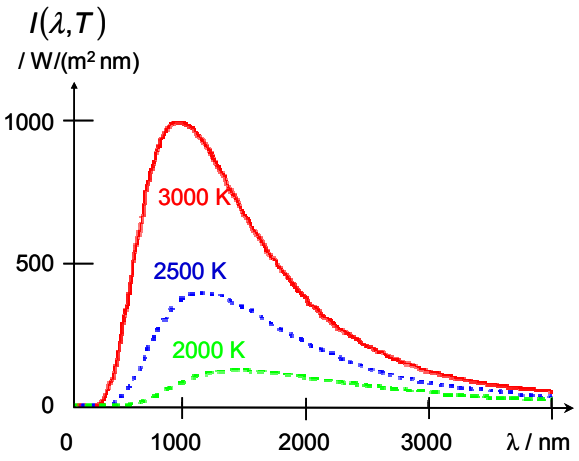

Fig. 2: Thermal radiation of a black body according to Planck's law (eq. 6).

In order to overcome the drawbacks of the above mentioned methods, multiple laser-based diagnostic techniques were developed to access accurate local gas-temperature information without perturbing the system under study. Some of them rely on the ideal gas-law (eq. 5) and measure number densities of molecular species (Section 3.3 and 3.4).

Others are based on measuring the quantum state population distribution of rotational, vibrational, or electronic modes of molecular species (Sections 3.1, 3.2, 3.4, and 3.5). Here, temperature is calculated using the Boltzmann distribution

$$\frac{N_i}{N} = \frac{g_i \exp\left(-\frac{E_i}{k_B T}\right)}{Z(T)} = f_{B(i)} \tag{7}$$

that predicts the distribution function for the fractional number of particles N_i / N occupying a set of states i which each has energy E_i. T is temperature, k_B is the Boltzmann constant, g_i is the degeneracy, or number of states having energy E_i, N is the total number of particles:

$$N = \sum_i N_i \quad . \tag{8}$$

$Z(T)$ is the partition function, which is derived from statistical thermodynamics. It is a measure for the number of energetic states the molecule is able to populate at a certain temperature. Its numerical value is small at low temperatures and rises with increasing temperature.

$$Z(T) = \sum_i g_i \exp\left(-\frac{E_i}{k_B T}\right) \tag{9}$$

It is equal to the degeneracy g_i times the Boltzmann factor $exp(-E_i/k_B T)$ summed over all states i. The Boltzmann fraction $f_{B(i)}$ (eq. 7) is the fraction of an ensemble of molecules that populate one single molecular energy state at a given temperature. Measuring the Boltzmann fractions of one or more states is the physical base of the laser-based temperature diagnostics developed and applied in this thesis. Single energy states of specific molecules are accessible by the use of laser light. Therefore, laser systems applied in this thesis are described in the following section.

2.2 Laser systems

There are a number of experimental and spectroscopic requirements in order to produce laser light (*"light amplification by stimulated emission of radiation"*). Due to the theory of stimulated emission, the photons in a laser beam are coherent: they have identical energy (wavelength) and travel in the same direction with the same phase and polarization. A large number of different laser systems were developed. The recently developed free electron lasers use a relativistic electron beam, which passes through a periodic magnetic field, as lasing medium. This results in a wider spectral tuning range than any of the common laser systems based on molecular or atomic states, which include the following features to generate laser radiation:

- Laser medium: This is the material capable of emission of radiation. Depending on the medium, gas lasers, liquid lasers, and solid-state lasers are distinguished.
- Cavity: During the laser process, light is amplified through the process of stimulated emission (cf. section 2.3.2): An incoming photon may induce emission of a second, coherent photon upon interaction with the excited laser medium. In order to enable coherent amplification of a large number of photons, the lasing medium is arranged inside a so-called cavity, e.g. two mirrors, which form a resonator with the length L. Hence, all longitudinal modes whose wavelengths λ are equal the resonance condition $L = n \times \lambda/2$ are amplified and yield a multi-mode laser beam. If single mode radiation with a precise wavelength is desired, the cavity must be modified in order to discriminate the side modes, e.g. by the use of an optical grating.
- Generation of population inversion: Stimulated emission from excited molecules competes with stimulated absorption by molecules in their ground state. Therefore, in order to enable continuous photon amplification, the population of the involved transition needs to be inverted, i.e. the population of the excited state must be larger than that of the ground state. Experimentally, this is achieved by so-called pumping of the population from the ground state into the excited state. Depending on the laser system, pumping may be performed by light, electric discharge, electric current or other means.

All laser-induced fluorescence (LIF) measurements presented in this thesis were done with ultra violet (UV) laser radiation originating from a Raman-shifted krypton fluoride (KrF) excimer-laser system. In general, there are multiple laser systems that yield similar radiation, like e.g. a neodymium-doped yttrium-aluminum-garnet (Nd:YAG) laser in combination with a dye laser and frequency doubling, where the Nd:YAG laser is used to pump the dye laser. This setup allows spectral tuning over a wider range. However, the Raman-shifted KrF excimer laser system performance is sufficient for all measurements presented here.

All absorption measurements presented use laser light in the near IR generated by a distributed-feedback (DFB) diode laser. Theory to excimer lasers, the stimulated Raman effect, and diode lasers are described in the following sections. Detailed treatment can be found, for example, in the textbooks by Kneubühl [31] and Demtröder [32].

2.2.1 Excimer lasers

Excimer (= *exci*ted hetero*mer*) molecules are molecules that are stable only in their excited electronic state. The ground state (life time ~10^{-12} s) is repulsive or only weakly bond so that the molecule dissociates thermally at room temperature. Once created, excimers therefore yield by definition ideal population inversion and are therefore well-suited for laser processes. Thus, excimers were proposed as laser media as early as 1960, with first lasers constructed in 1970 [31]. As an example of an excimer molecule, a schematic potential energy diagram of KrF is shown in Fig. 3. The $B\ ^2\Sigma_{1/2} \rightarrow X\ ^2\Sigma_{1/2}$ is used as laser transition. A detailed description of excimer lasers can be found in the textbook by Rhodes [33].

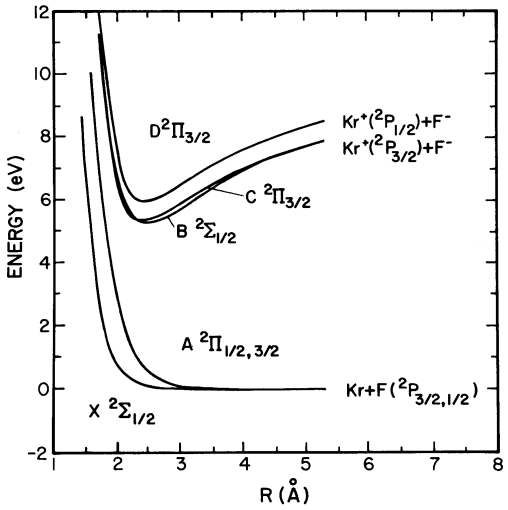

Fig. 3: Potential energy diagram of the KrF noble gas halogen excimer [33].

Typical excimer lasers applied in combustion research use noble gas halogens, most commonly ArF (193 nm), KrF (248 nm), XeCl (308 nm), and XeF (351 nm). They are created from a noble gas/halogene mixture by high-voltage (20 – 25 kV) electrical discharge. Because of the high powers required for the discharge, excimer lasers are pulsed; typical pulse durations are 20 ns.

Fig. 4 shows the emission spectrum of KrF. The excimer emission has a spectral bandwidth of several nanometers. Narrow-band operation is possible by inserting a dispersive element (e.g. a grating) into the laser resonator. In commercially available tunable excimer lasers (Lambda Physik) the laser beam is broadened by three prisms

and reflected at a grating in a high-order Littrow arrangement. Thus the grating is one of the end mirrors of the laser cavity, and wavelength selection is possible by adjusting the grating angle. The energy of the resulting laser beam, however, is strongly reduced. Therefore, a two-cavity oscillator/amplifier system is often used. This arrangement yields narrow-band ($\Delta\nu$~0.5 cm^{-1}), tunable (within 1 nm), high-energy (up to 250 mJ/pulse) pulsed UV laser operation.

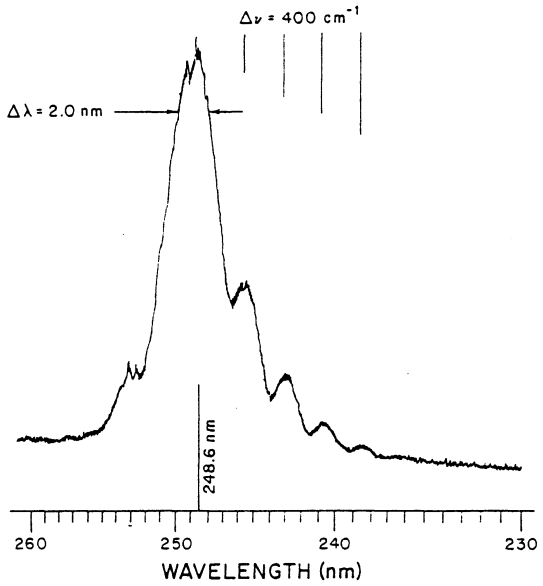

Fig. 4: KrF spontaneous fluorescence spectrum (no lasing) from a mixture of 1% Kr and 0.1% F_2 in Ar at a total pressure of 2.7 bar after electron beam excitation. From Brau and Ewing [34].

Stimulated Raman scattering for wavelength conversion

For Stimulated Raman Scattering (SRS) [35], the laser beam is focused into a pressure cell filled with 5 – 10 bar of a Raman-active medium (e.g. H_2, N_2, CH_4). Vibrational and rotational Raman scattering is induced in the medium. Unlike spontaneous Raman scattering (explained in detail in section 3.4), the resulting Stokes and Anti-Stokes photons are coherent, i.e. laser radiation is emitted from the focal point of the pump beam. Multiple scattering processes take place, resulting in a spectrum of emissions with shorter and longer wavelengths than the fundamental laser beam, with regular frequency shifts corresponding to the vibrational or rotational excitation energy of the Raman medium.

SRS emission takes place, both in forward and backward direction relative to the incoming laser beam. The conversion efficiency is a nonlinear function of pump laser energy; it furthermore depends on the cell pressure and the geometrical arrangement (lens focal length) [36-38], and the addition of foreign gases (typically noble gases) [39,40]. In the work presented in this thesis, a hydrogen-filled cell (5 – 10 bar) was used

to convert the fundamental of a KrF excimer laser (~248 nm) to its first Anti-Stokes frequency (~225 nm) for accessing the NO *A*–*X*(0,0) electronic transition (cf. section 4.1).

2.2.2 Laser diodes

In a laser diode, the active medium is a semiconductor similar to that found in a light-emitting diode (LED). It is formed from a p-n junction and powered by injected electrical current. As in other diodes, when this structure is forward biased, holes from the p-region are injected into the n-region, where electrons are the majority carrier. Similarly, electrons from the n-region are injected into the p-region, where holes are the majority carrier. When an electron and a hole are present in the same region, they may recombine by spontaneous emission; the electron may re-occupy the energy state of the hole, emitting a photon with energy equal to the difference between the electron and hole states involved. These injected electrons and holes represent the injection current of the diode, and spontaneous emission gives the laser diode below lasing threshold similar properties to a LED.

Under suitable conditions, the electron and the hole may coexist in the same area for some microseconds before they recombine. Then a nearby photon with the energy equal to the recombination energy can cause recombination by stimulated emission, that causes gain in an optical wave in the injection region, and the gain increases as the number of electrons and holes injected across the junction increases. The emitted wavelength is a function of the band-gap of the semiconductor and the modes of the optical cavity. The maximum gain will occur for photons with energy slightly above the band-gap energy, and the modes nearest the gain peak will lase most strongly.

The first laser diode was developed as early as 1962 [41]. Since then, multiple laser diodes have been developed with different properties such as power, wavelength tuning range, tuning velocity and mode selection [25]. Room-temperature diode lasers are available over a range of wavelengths extending from the visible spectrum to above 2.2 μm in the mid-IR. An overview is given in Fig. 5.

The shortest wavelength InGaAlP lasers produce a visible beam and are used for HeNe replacements in laser pointers and barcode scanners. AlGaAs lasers in the 780 – 900 nm wavelength region are the largest volume/lowest cost lasers used for CD data storage and laser printers. With InGaAsP devices used for telecommunication transmission and InP substrates, devices can be grown with lasing wavelengths between about 1100 and 1650 nm.

Also, different types of laser diodes have been developed: Fabry-Perot (FP) lasers have a simple structure. The laser medium end walls act as partially transmitting mirrors and form an optical cavity. However, these lasers show some drawbacks concerning the reproducibility of the emitted wavelength. If high power and a large tuning range

are necessary, External Cavity Diode Lasers (ECDL) or Distributed Bragg Reflector (DBR) lasers are applied. Vertical-Cavity Surface-Emitting Lasers (VCSEL) emit the laser light along the direction of current flow rather than perpendicular to the current flow as in conventional edge-emitting laser diodes. The VCSEL production process is advantageous since the lasers can be tested during synthesis and mass production is easy [42].

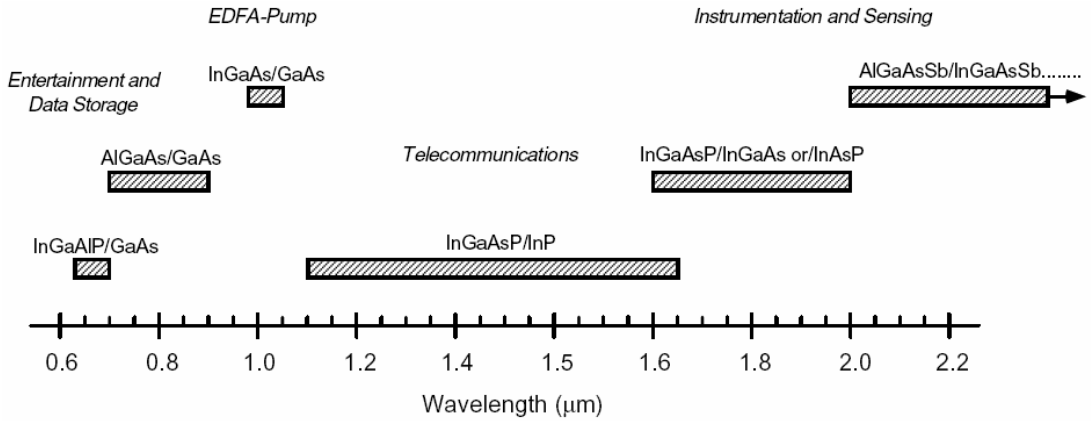

Fig. 5: Approximate spectral windows of commercially available room-temperature diode laser sources [25].

Prices of DFB laser diodes, that were used in this thesis, became cheaper recently because they are frequently used in telecommunication applications all over the world [25] since they can be easily modulated. To stabilize the lasing wavelength, a diffraction grating is etched close to the p-n junction of the diode. This grating acts like an optical filter, causing a single wavelength to be fed back to the gain region and lase. Therefore, these lasers yield single-mode, spectrally narrow-band ($\Delta\nu$ ~0.001 cm^{-1}), tunable (within ~4 nm), continuous-wave (cw) laser light in the IR. Due to diffraction, the beam diverges rapidly after leaving the chip by up to 30 degrees. Therefore, the beam must be collimated by a lens or coupled to an optical fiber.

All diode lasers can be wavelength tuned in two ways: (1) By adjusting the temperature of the diode, the effective optical index of the waveguide is changed, thereby adjusting the resonant condition of the laser cavity. Using this approach, DFB lasers can typically be tuned by 3 – 5 nm between 275 and 325 K. Because of the thermal mass of the diode and heater/cooler element, this type of tuning is usually restricted to a few Hz maximum bandwidth. (2) At any given temperature, the injection current can be varied to modulate the optical index. Of course the output power is also modulated, but the laser wavelength may be tuned extremely rapidly with several kHz. The injection current tuning range is only 1 – 2 cm^{-1} and is limited by the lasing threshold at the low end and output facet damage at the high end.

2.3 Spectroscopy

The quantitative interpretation of signals obtained by laser-based diagnostics requires a detailed understanding of the spectroscopy of the probed species. Fundamentals of molecular spectroscopy are introduced in this chapter. Details on nitric oxide and water spectroscopy are given later in sections 4.1.1 and 4.2.1, respectively. The following introduction is based on the textbooks of Herzberg [43], Eckbreth [44] and Hirst [45] as well as the introductory textbooks of Haken and Wolf [46] and Wedler [47].

The two energy units wavenumber (in [cm^{-1}]) and frequency (in [Hz]) are both used in literature, and are usually denoted by the same symbol ν. Throughout this thesis, the symbol ν always means wavenumber and has the unit [cm^{-1}].

2.3.1 Molecular spectroscopy

The Schrödinger equation

For any atom or molecule (in fact, for any quantum mechanical system), the energy levels may be determined by solving the time independent Schrödinger wave equation,

$$\mathbf{H}\,\Psi = E\,\Psi . \tag{10}$$

H is the Hamiltonian operator (Operators are typed in boldface here), E the total system energy, and Ψ the wave function. The total energy in a system consisting of multiple particles (e.g. electrons and nuclei) is the sum of kinetic and potential energy, and the Hamiltonian may be written as

$$\mathbf{H} = \mathbf{T} + \mathbf{V} , \tag{11}$$

where **T** is the kinetic energy operator that includes the momentum operators for each particle, and **V** is the operator of the potential energy of the system. The stationary Schrödinger equation is a partial differential equation.

The fundamental finding of quantum mechanics is that valid solutions of this equation exist only for certain discrete values of energy, given by the eigenvalues of the differential equation. Each eigenvalue E_n (n = 0, 1, 2, …) is associated with an eigenfunction Ψ_n. The set of E_n make up the allowed energy states of the molecule that are described by quantum numbers. If more than one eigenfunction is associated with the same energy, the energy levels are called degenerate. The absolute value of the square of the eigenfunction, $|\,\Psi_n\,|^2$, is the probability density of the particles of the system in the quantum state n.

A full analytical solution of the Schrödinger equation is only possible for the simplest systems (e.g. a hydrogen atom). In general, simplifications or approximations are necessary for the solution (analytically or numerically). A fundamental approach is the

so-called separation approach where different contributions to the total energy (and thus the Hamiltonian) are assumed to be independent. This approach yields model Hamiltonians that are used to solve the Schrödinger equation. In general, the solutions to model Hamiltonians are not able to quantitatively predict the energy levels of an atom or molecule, but they yield expressions as a function of quantum numbers and numerical parameters that can be adjusted to match experimentally determined energy levels.

For molecules, an important separation approach was proposed in 1927 by Born and Oppenheimer. They showed that, because electrons are much lighter than nuclei, the wave equation can be separated into a part describing the electronic motion and a part describing the slower motion of the nuclei. In essence, the nuclei move within an effective potential field created by the motion of the electrons. The motion of the nuclei may further be separated into a vibrational and a rotational part. The states are thus determined by three major motions: The orbiting and spin of the electrons, vibration of the nuclei with respect to each other, and rotation of the molecule normal to the internuclear axis. The Hamiltonian may then be separated into an electronic ($\mathbf{H}_{\mathrm{el}}$), a vibrational ($\mathbf{H}_{\mathrm{vib}}$) and a rotational ($\mathbf{H}_{\mathrm{rot}}$) part and written as

$$\mathbf{H} = \mathbf{H}_{\mathrm{el}} + \mathbf{H}_{\mathrm{vib}} + \mathbf{H}_{\mathrm{rot}} \,, \tag{12}$$

yielding solutions (eigenvalues) of the Schrödinger equation with the total energy

$$E = E_{el} + E_{vib} + E_{rot} \,, \tag{13}$$

where E_{el} is the electronic energy, E_{vib} the vibrational energy, and E_{rot} the rotational energy, each depending on one or more quantum numbers.

The picture resulting from the Born-Oppenheimer approximation in which electronic motion is strictly separated from vibrational and rotational motion is not exactly correct. In a diatomic molecule, the magnetic coupling of electron orbital, electron spin, and molecular rotation plays an important role and leads to a fine structure, i.e. splitting of the energy levels that would otherwise be degenerate.

Electronic states

The electronic quantum state of a diatomic molecule is described by the total electron orbital angular momentum and the total electron spin angular momentum, both of which are quantized. The orbital angular momentum is described with the quantum number L, where $L = 0, 1, 2, \ldots$ is an integral number. The spin angular momentum is described with the quantum number S being integral or half integral depending on whether the total number of unpaired electrons is even or odd. The electronic state is further characterized by the components of L and S along the internuclear axis, M_L and Σ, where

$$M_L = L, L–1, L–2, \ldots, –L \tag{14}$$

$$\Sigma = S, S–1, S–2, \ldots, –S \,. \tag{15}$$

In diatomic molecules, states differing only in the sign of M_L are degenerate. It is therefore appropriate to classify the electronic states according to the absolute value of M_L and to define the quantum number Λ where

$$\Lambda = | M_L | . \tag{16}$$

Λ may have values of 0, 1, 2, 3, …, and the corresponding molecular state is described by the Greek letters Σ, Π, Δ, Φ, …, where Π, Δ, Φ,… states are doubly degenerate with quantum numbers ± M_L. For a given value of Λ there are $2S + 1$ different values of $\Lambda + \Sigma$ due to the different projections of the spin angular momentum on the internuclear axis.

For given values of Λ and S, the total number of possible states is called the electronic degeneracy g_e, and we find from eqs. 14-16 that

$$g_e = (2S + 1) \text{ for } \Lambda = 0 \tag{17}$$

$$g_e = 2(2S+1) \text{ for } \Lambda > 0 . \tag{18}$$

Electronic states are thus identified by the values of S and Λ. This information is contained in the term classification symbol

$$^{2S+1}\Lambda_{\Lambda+\Sigma} . \tag{19}$$

The value $2S + 1$ is called the multiplicity of the electronic term. Electronic states are also distinguished by letters. The ground state is labelled X, excited states of the same multiplicity are labelled A, B, C etc. in order of increasing energy. States of different multiplicity than the ground state are labelled with lower case letters a, b, c, etc. Electronic states are further characterized by their symmetry properties (+/– notation for symmetry of the wavefunction upon reflection at a plane that runs through the internuclear axis, g/u notation in homonuclear molecules for the parity, i.e. symmetry of the wavefunction upon inversion at the center of symmetry).

Vibrational states

The allowed vibrational energies are determined by solving the stationary wave equation for the vibrational part of the total wave function. For this, the potential energy function $V(r)$ of the molecule in dependence on the internuclear distance r is needed. For many diatomic molecules, the potential energy function for small values of vibrational energy may be approximated as that for a harmonic oscillator. In this case the allowed term values G [cm^{-1}] for vibrational energy (eigenvalues) become

$$E_{vib} = \omega(v + ½) , \tag{20}$$

where $v = 0, 1, 2, 3, \ldots$ is the vibrational quantum number and ω [cm^{-1}] is the vibrational frequency measured in wavenumbers (the actual number of vibrations per second is 2.998×10^{10} m/s times as large). These states are not degenerate.

For real molecules the potential energy function is not exactly harmonic, even for small vibrational energies. As a result, the spacing of vibrational levels is not constant as predicted for a harmonic oscillator, but decreases with v, until the vibrational energy approaches an asymptotic limit at the dissociation energy. Spectroscopists early developed polynomial expansions to fit experimental term data. Vibrational values were often fitted using an expression of the form

$$G(v) = \omega_e(v + ½) - \omega_e x_e(v + ½)^2 + \omega_e y_e(v + ½)^3 + \ldots \ , \tag{21}$$

where $\omega_e x_e$ [cm^{-1}], for example, is called the anharmonic vibrational constant. Values of these parameters are given in Herzberg [43].

Rotational states

Let us first ignore any effect of vibrational or electronic motion on the rotation of the nuclei. The solution of the wave equation for a rigid rotator reveals that both the total rotational energy and the projection of that energy on the inter-nuclear axis are quantized, and that the rotational energy terms E_{rot} [cm^{-1}] are given by

$$E_{rot}(J) = B\ J(J+1) \ \ , \tag{22}$$

where J = 0, 1, 2, 3, … is the rotational quantum number and B [cm^{-1}] is called the rotational constant. It is also found that rotational states are degenerate with a degeneracy of

$$g_J = 2J + 1 \ . \tag{23}$$

As the rotational energy increases, centrifugal forces cause an increase in the moment of inertia. Therefore, the energy is not exactly linear in $J(J+1)$. Again, spectroscopists developed polynomial expansions to fit experimental data. Rotational term values were often fitted using an expression of the form

$$F_v(J) = B_v J(J+1) - D_v[J(J+1)]^2 + H_v[J(J+1)]^3 + \ldots \ , \tag{24}$$

where the subscript v indicates that the constants may be different for different vibrational levels v. To account for the interaction of vibrational and rotational motion, the rotational constant B needs to be expanded by

$$B_v \cong B\ - \alpha\ (v + ½) \ . \tag{25}$$

Values of the parameters B, D and α that appear in these expressions are tabulated for a large number of molecules in Herzberg [43]. For e.g. NO X, B = 1.70 cm^{-1} and α = 0.018 cm^{-1}. For NO A, B = 2.00 cm^{-1} and α = 0.016 cm^{-1}.

Ground-state population distribution

The laser-based thermometry techniques applied in this thesis derive temperature information from the Boltzmann distribution (eq. 7) by measuring the ground-state population distribution of molecules. In principal, electronic, vibrational, and rotational distributions can be used. If the system is in thermal equilibrium, they all yield the same temperature results. However, if molecular collisions are too slow to reach thermal equilibrium after a sudden change in temperature (e.g. at low pressure), the so-called electronic, vibrational and rotational temperatures differ because their thermalization times are unequal.

For the temperature range investigated here (250 – 2500 K), only the rotational distribution can be used. Excited electronic and vibrational states in two-atomic molecules are hardly populated at room temperature; hence, no distribution can be measured. Knowing the basics of molecular spectroscopy we are now able to predict the rotational ground state population distribution of diatomic molecules. Combining eqs. 7, 9, 22, and 23, we obtain the Boltzmann fractions for the rotational levels $f_{B(J)}$.

$$f_{B(J)} = \frac{(2J+1)\exp\left(-\dfrac{BJ(J+1)}{k_B T}\right)}{\sum_J (2J+1)\exp\left(-\dfrac{BJ(J+1)}{k_B T}\right)} \tag{26}$$

For a simplified calculation for the NO rotational ground state population distribution of the electronic and the vibrational ground state, $B = 1.70\ \mathrm{cm^{-1}}$ and the rigid rotator is assumed. Boltzmann fractions are plotted for the first 40 rotational levels in Fig. 6 for 300, 600, and 1000 K.

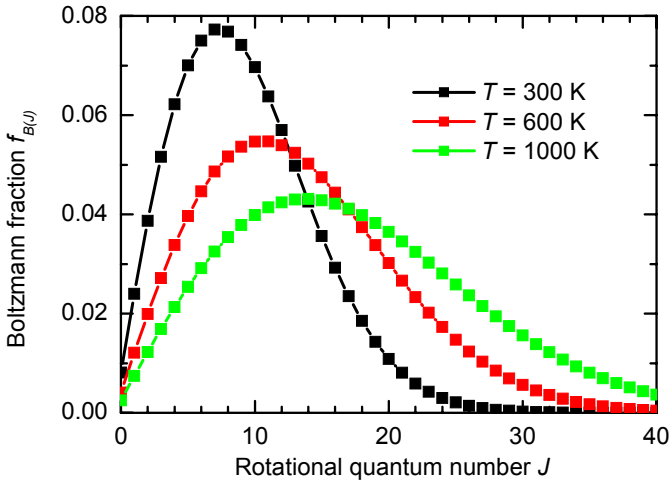

Fig. 6: Rotational ground state population distribution for the NO molecule (eq.26).

Generally, the first levels are hardly populated except for very low temperatures. The rising part at low J is due to the increasing degeneracy of rotational states. This is over compensated for higher J by the exponential term in eq. 26. With increasing temperature, the maximum of the distribution shifts to higher J. Simultaneously, the absolute values of the Boltzmann fractions decrease because more states are populated at higher temperature. Note that at room temperature, already 25 levels are populated sufficiently to be used for temperature measurements.

2.3.2 Electronic transitions, selections rules

So far, we discussed the state energies (terms) of diatomic molecules. For absorption and laser-induced fluorescence spectroscopy, not only the absolute term values, but dipole-radiation-induced transitions between the states are relevant. The transition energies are determined by term energy differences and the transition strengths by selection rules and transition probabilities. These may be calculated from quantum mechanics.

In spectroscopy nomenclature, transitions between two states are symbolized by an arrow, where the upper state (with higher energy) is at the left side and the lower state (at lower energy) on the right side, and the arrow indicates the transition from initial to final state, for absorption or emission. The quantum numbers of the upper state get a single prime (v', J') and those of the lower state a double prime (v'', J''), and the vibrational quantum numbers are often given in brackets to the electronic term symbols, e.g. A (v' = 0)←X (v'' = 2) or simply A–X(0,2). The lower-state state energy E'' (or ground-state energy) is defined in contrast to the upper-state energy E'.

Interaction of quantum mechanical systems with electromagnetic radiation

If the interaction with an electromagnetic field is introduced into the time-dependent Schrödinger equation of a molecular system, it is found that a non-zero probability of transition 2 ← 1 from a state 1 with energy E_1 to a state 2 with energy $E_2 > E_1$, the so-called stimulated absorption, arises only if radiation of the energy $\Delta E = E_2 - E_1$ is present (Bohr frequency condition). The probability of the transition under the influence of radiation is determined by the properties of the wavefunctions (eigenfunctions) Ψ_1 and Ψ_2 of the two states. The interaction of an electromagnetic wave having an electric field vector $\vec{E}$ with a molecule is in a first approximation the interaction with its electric dipole moment $\vec{\mu}$. The interaction energy $\vec{E}\vec{\mu}$ can be introduced into the time-dependent wave equation, and it is found that the transition probability is proportional to the square of the magnitude of the vector quantity $\vec{R}^{21}$ [Cm], the transition moment or matrix element of the electric dipole moment, where

$$\vec{R}^{21} = \int \Psi_1^* \boldsymbol{\mu} \Psi_2 \, d\tau \ , \tag{27}$$

$\boldsymbol{\mu}$ is the operator of the transition dipole moment, and τ refers to integration over the whole configuration space. If a molecular system is irradiated with light, the photon absorption rate b_{12} [1/s] is given by an expression derived by Einstein,

$$b_{12} = \frac{B_{12} I_\nu}{c^2} \ , \tag{28}$$

where the light intensity is defined as the spectral irradiance I_ν [W/(cm^{2}cm^{-1})], the total photon energy per time per area per wavenumber interval. B_{12} [m^3/Js^2] is the Einstein coefficient for stimulated absorption, and c is the speed of light. It can be shown that the Einstein coefficient is related to the transition moment through

$$B_{12} = \frac{8\pi^3}{3h^2 \varepsilon_0 g_1} \left| \vec{R}^{21} \right|^2 \ , \tag{29}$$

where h is the Planck constant, ε_0 the permittivity of free space [8.854×10^{-12} C^2/Jm], and g_1 the degeneracy of state 1.

Similarly, one finds that a quantum mechanical system, if irradiated with an electromagnetic wave, may undergo a transition 2 → 1 from a state with higher energy to a state with lower energy by emitting a photon coherent to the incident photon, the so-called stimulated emission. The probability of such a process may be given by the Einstein coefficient for stimulated emission B_{21} [m^3/Js^2], which is related to the B_{12} coefficient through

$$g_1 B_{12} = g_2 B_{21} \ , \tag{30}$$

where g_1 and g_2 are the degeneracies of states 1 and 2, respectively. The stimulated photon emission rate b_{21} [1/s] is given by

$$b_{21} = \frac{B_{21} I_\nu}{c^2} \ . \tag{31}$$

Furthermore, there is a certain probability that a system in an excited state 2 spontaneously undergoes a transition 2 → 1 into a lower-energy state 1 by emitting a photon, the so called spontaneous emission. The probability is given by the Einstein coefficient for spontaneous emission A_{21} [1/s], which is related to the Einstein coefficient for stimulated absorption through

$$\frac{A_{21}}{B_{21}} = 8\pi h \nu^3 \ . \tag{32}$$

If the eigenfunctions Ψ_1 and Ψ_2 of two states are known, we can calculate the probabilities for stimulated absorption, stimulated emission, and spontaneous emission between these states, and thus the intensity of the emitted or absorbed light (eqs. 27-32).

Selection rules

We find that $\vec{R}^{21}$ and thus B_{12}, B_{21} and A_{12} differ from zero only if certain symmetry relations between the two wavefunctions are fulfilled, and a transition is considered allowed only for finite values of $\vec{R}^{21}$; otherwise, it is called forbidden. Since the states are represented by their quantum numbers, this leads to the concept of selection rules for specific quantum numbers.

For electronic transitions in diatomic molecules, the multiplicity (eq. 19) must not change, the quantum number of total electronic spin S has to remain constant. Further, the quantum number of the electron orbit angular momentum Λ (eq. 16) is allowed to remain or to change by ±1. The symmetry of the molecular system has to change from + to – or vice versa.

When exciting electronic transitions, vibrational and rotational levels are often altered simultaneously. No restrictions are given to changes in the vibrational quantum number v (eq. 20). The quantum number of the total angular momentum J (eq. 22) is allowed to remain or to change by only ±1. Altogether, molecular transitions are only allowed for:

$$\Delta\Lambda = 0, \pm 1; \tag{33}$$

$$\Delta S = 0; \tag{34}$$

$$\Delta v = 0, \pm 1, \pm 2, \pm 3 \ldots ; \tag{35}$$

$$\Delta J = -1 \text{ (P-branch)}, 0 \text{ (Q-branch)}, +1 \text{ (R-branch)} \tag{36}$$

$$+ \leftrightarrow - \quad (e \leftrightarrow f \text{ for Q branches}, e \leftrightarrow e \text{ and } f \leftrightarrow f \text{ for P and R branches}). \tag{37}$$

2.3.3 Line shapes of molecular transitions

The energy of a dipole transition is given by the difference in term energies of the two involved states. In practice, the transitions that are observed in absorption or emission are not monochromatic but have a certain spectral width and spectral shape. Since line shape and line width depend on pressure, temperature, and concentration of collision partners in the system, they play an important role in the interpretation of optical spectra. Furthermore, the laser light itself has a certain spectral width and shape that interacts with the spectral shape of the molecular transition. In the following, we will discuss the broadening mechanisms and their influence on spectral width and shape.

In a simple model there are three broadening mechanisms that contribute to the observed line width: the natural line width, the Doppler width, and the collisional width. The spectral shape depends on the broadening mechanism and is of Lorentzian or Gaussian type as summarized in Table 2. In practice, all three mechanisms contribute to

the spectral broadening and, hence, the line shape is a convolution of both line shapes called a Voigt function [31]. Unfortunately, the Voigt-shape function cannot be expressed in an analytical form. It can be gained via approximation [48-50].

Broadening mechanism	Spectral shape	Physical origin	Type
Natural broadening	Lorentzian	Heisenberg uncertainty principle	Homogeneous
Doppler broadening	Gaussian	Brownian motion of molecules	Inhomogeneous
Collisional broadening	Lorentzian	Heisenberg u. p.; molecular collisions	Homogeneous
	Voigt	Combination of all	Inhomogeneous

Table 2: *Broadening mechanism, resulting spectral shape, physical origin, and type of the observed line shape.*

The width of a transition is defined in terms of its full width of half maximum (fwhm) $\Delta\nu$ [cm^{-1}], that is the spectral width in wavenumbers when the line strength has dropped to the half of its maximum as indicated in Fig. 7. This figure also shows a comparison of Lorentzian- and Gaussian-shape functions. The spectral shape of the transition is given by the line-shape function $\Phi(\nu)$ [1/cm^{-1}] which is normalized such that

$$\int_{-\infty}^{\infty} \Phi(\nu) d\nu = 1 \ . \tag{38}$$

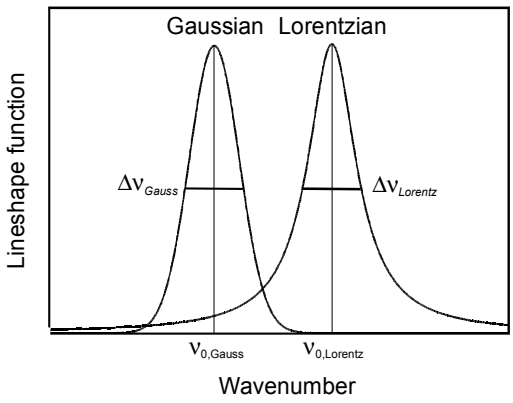

Fig. 7: Comparison of Gaussian and Lorentzian line shapes with the respective center frequencies $\nu_{0,Gauss}$ *and* $\nu_{0,Lorentz}$*, and the line widths* $\Delta\nu_{Gauss}$ *and* $\Delta\nu_{Lorentz}$.

Natural line broadening

According to the Heisenberg uncertainty principle, energy and time cannot be precisely measured simultaneously. Due to the limited lifetime of either involved quantum state, an energy and thus frequency or wavenumber spread in absorption or emission is observed. This is termed the natural line width. The uncertainty principle yields $\Delta E \cdot \tau \geq h/2\pi$, where τ is the transition lifetime. With the Einstein relation $E = hc\nu$ we get a spectral uncertainty of

$$\Delta\nu_N = \frac{1}{2\pi c\,\tau} \quad . \tag{39}$$

For allowed dipole transitions ($\tau = 1/A$ ~10 – 100 ns) one finds natural line widths $\Delta\nu_N$ in the order of ~10^{-4} – 10^{-3} cm^{-1} which is much smaller than the line width resulting from either Doppler or pressure broadening at typical ambient conditions. The natural line broadening can be neglected for all experiments presented in this thesis. However, if a molecule is excited into a non-bonding or weakly bonding state, it may rapidly dissociate (so-called predissociation, cf. section 3.1), thereby reducing excited state lifetime and increasing the line width. This effect is termed predissociation broadening and can be observed, for example, for many UV transitions of O_2, leading to predissociation line widths of up to ~4 cm^{-1} [51].

Doppler broadening

The thermal motion of atoms or molecules causes line broadening due to the Doppler effect. It depends on the velocities of the molecules relative to the detector and therefore on temperature T. The distribution of velocities is given by the Maxwell-Boltzmann relation. By calculating the Doppler shift for each velocity component and averaging over the distribution of velocities, we can calculate the fwhm $\Delta\nu_D$ of a Doppler-broadened line,

$$\Delta\nu_D = \frac{2\nu_0}{c}\sqrt{\frac{2\ln 2 \cdot k_B T}{m}} \tag{40}$$

where ν_0 [cm^{-1}] is the center wavenumber of the line, and m the molecular mass. The Doppler line-shape function is given by

$$g_D(\nu) = \frac{1}{\nu_0}\sqrt{\frac{m}{2\pi kT}}\,\exp\left(-4\ln 2 \cdot \frac{(\nu-\nu_0)^2}{\Delta\nu_D^2}\right) \tag{41}$$

Mathematically, this is a Gaussian function, and the Doppler line shape is also termed a Gaussian line shape (Fig. 7). Since the Doppler effect is different for each individual molecule (depending on their individual velocities), Doppler broadening is also termed inhomogeneous broadening, and the resulting line width is termed inhomogeneous line width. For NO, we can easily calculate the Doppler line width from eq. 40, and we find $\Delta\nu_D$ = 0.10 cm^{-1} at 300 K and 0.26 cm^{-1} at 2000 K for a center wavelength of 225 nm.

Collisional broadening (pressure broadening)

A molecule interacting with radiation either in absorption or emission will be interrupted by collisions. This results in a reduced lifetime of the interaction, which, according to the Heisenberg uncertainty principle, leads to an increased line width. While the

physical origin of the broadening is similar as for the natural line width, the collisional width depends on pressure, temperature, as well as on the properties and concentrations of the colliding species.

Due to the complex interaction mechanism during collisions, it is not possible to derive a closed analytical expression for the collisional width. Instead, models were set up that yield empirical expressions with adjustable parameters that are derived from measurements [52]. Under the assumption that collisional broadening is independent for different colliders i with partial pressure p_i, we can write

$$\Delta\nu_C = \sum_i 2\,\gamma_i(T)\,p_i \tag{42}$$

that is, the collisional width $\Delta\nu_C$ [cm^{-1}] is proportional to the partial pressure for each individual collider. The broadening coefficient 2γ [cm^{-1}/bar] depends on temperature through the empirical expression

$$2\gamma = c \cdot T^{-n} \tag{43}$$

The parameters 2γ, c and n were determined for NO A–X(0,0) transitions by Chang, DiRosa and Hanson in shock tube experiments [52-54] and by Vyrodov in LIF measurements [55] for collision partners Ar, He, N_2, H_2O, O_2, and NO. Unfortunately, data for other important major species in flame gases (CO_2, CO, methane, ethylene, hydrogen) are missing. The broadening coefficients 2γ for NO are in the range of 0.5 – 0.8 cm^{-1}/bar at room temperature. Collisional width decreases with increasing temperature and reaches values around 0.2 cm^{-1}/bar at 2000 K.

Pressure broadening leads to a line shape that was first calculated by H. A. Lorentz and is therefore termed a “Lorentzian” line shape. The line-shape function is given by

$$g_C(\nu) = \frac{\Delta\nu_C}{2\pi}\,\frac{1}{(\nu-\nu_0)^2 + (\Delta\nu_C/2)^2} \tag{44}$$

An example was shown in Fig. 7. Since the pressure broadening is the same for individual molecules, it is also called homogeneous broadening, and the line width is termed homogeneous line width.

Collisional line shifting

Not only is the line width influenced by pressure and temperature, but also the center wavenumber ν_0. This is a consequence of collisions of the molecular system with other particles and is therefore termed collisional shifting or pressure shifting.

The nature of collisional shifting can be explained in terms of the schematic potential energy diagram in Fig. 8, which plots the potential energy of a ground and an excited molecular state versus the average intermolecular distance R. The potential energy of a

molecular system depends on R which is a function of pressure and temperature. Since this dependence may be different for different molecular states, the transition energy $\Delta\nu_0$ between two states also depends on R. The transition is shifted in relation to that of a single molecule in an ideal vacuum ($p = 0$, $R = \infty$), $\Delta\nu_{0,ideal}$.

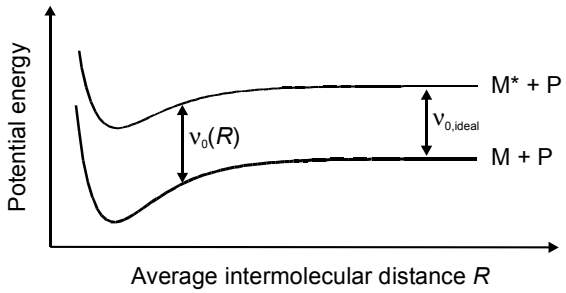

Fig. 8: Collisional line shifting.

The empirical treatment of collisional shifting is analogous to that of collisional broadening. Independent shift for different collision partners i is assumed, proportional to their respective partial pressure p_i, according to

$$\Delta\nu_S = \sum_i \delta_i(T)\ p_i \tag{45}$$

where

$$\delta = c \cdot T^{-n} \tag{46}$$

is the shifting coefficient [cm^{-1}/bar]. The empirical parameters δ, c and n were measured for NO with different colliders [52-55]. For NO A–X(0,0) transitions, δ is in the range of –0.15 to –0.20 cm^{-1}/bar.

3 Laser-based temperature diagnostics

Temperature distributions are of major interest in the description of reactive and non-reactive gaseous flow systems, where they play a crucial role in chemistry (reaction rates, equilibrium state) and physics (heat transfer, fluid dynamics, and droplet evaporation). Laser spectroscopy has become a most important tool in fundamental and applied research in natural sciences such as physics, chemistry, biology, and medicine. The unique properties of laser light enable quantitative temperature measurements with high temporal and spatial resolution, and the optical nature of laser techniques allows access to systems with minimum perturbation of the system under study. A number of fundamentally different laser-based techniques were developed and applied for temperature measurements in gas-phase flows. An excellent review is available in the book of Dreizler, Ebert, and Schulz [21].

Many thermometry methods principally rely either on the temperature dependence of the total number density (e.g. Rayleigh scattering, spontaneous Raman scattering) given by the ideal gas law (eq. 5) or the temperature dependence of the population of different rotational, vibrational, or electronic states of atomic or molecular probes (e.g. spontaneous Raman scattering, Coherent Anti-Stokes Raman Scattering (CARS), Laser-Induced Fluorescence (LIF), Absorption Spectroscopy (AS)) given by the Boltzmann distribution in eq. 7. In addition, there are multiple techniques that use other temperature-dependent properties of matter, such as the decay time of excited states (Thermographic phosphors [56]). However, there is to date no versatile, accurate and robust technique that can be applied to all experimental conditions. The selection of a specific method depends on the actual problem. An overview is given in Table 3.

Thermometry technique	Section	Physical base
Laser-induced fluorescence	3.1	Boltzmann distribution
Absorption spectroscopy	3.2	Boltzmann distribution
Rayleigh scattering	3.3	Ideal gas law
Raman scattering	3.4	Boltzmann distribution or ideal gas law
CARS	3.5	Boltzmann distribution
Others	5.4	e.g. life time of excited states

Table 3: Laser-based thermometry techniques.

CARS thermometry typically provides the highest accuracy, but it allows point-wise measurements only. The other techniques can in principle be used for imaging. Rayleigh scattering and filtered Rayleigh scattering provide relatively strong signals that can be used to determine temperature. Spontaneous Raman scattering is frequently used for temperature evaluation in one-dimensionally resolved multi-species measurements, but the signal intensity is low.

LIF thermometry provides strong signals and has been frequently used for imaging thermometry. Due to their high intensities, Rayleigh scattering and LIF can provide instantaneous imaging information at high repetition rates to investigate turbulent systems.

While all these techniques mentioned above access local temperatures, absorption techniques necessarily accumulate information along the line of the laser path through the measurement volume. However, spatially-resolved measurements are possible via multi-path absorption tomography.

3.1 Laser-induced fluorescence

Laser-induced fluorescence (LIF) is the process of spontaneous emission from an excited electronic state populated upon absorption of a laser photon. Large cross-sections mainly in the visible and UV spectral range enable species detection down to the parts-per-billion (ppb) range. Many combustion-relevant species like OH, O_2, NO, CH, CN, NH, and C_2 can be accessed selectively. Also, organic molecules like ketones or atomic species (e.g. indium) are frequently used. Detailed treatments are given in the textbooks of Eckbreth [44], Kohse-Höinghaus and Jeffries [57], and in the review articles of Kohse-Höinghaus [58] and Daily [59]. An experimental setup is shown in section 4.1.2 (Fig. 23).

The processes involved in LIF are summarized in the simplified, non-transient, three-level model in Fig. 9. LIF can be understood as two subsequent steps, starting in the energetic ground state 1. Absorption of (typically) one photon with the rate of stimulated absorption b_{12} (eqs. 27-29) leads to the population of a (typically electronically) excited state 2 in the respective atom or molecule.

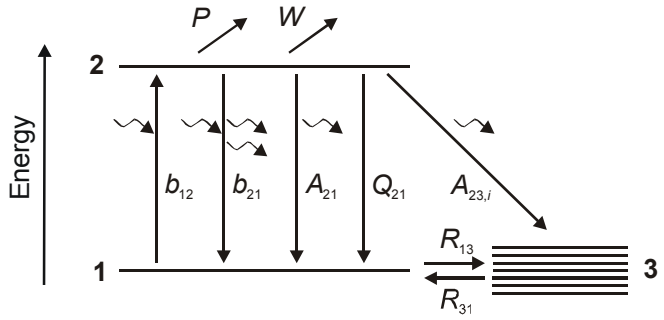

Fig. 9: Three-level LIF model with rates [s^{-1}] of stimulated absorption b_{12}, stimulated emission b_{21}, spontaneous emission A, collisional quenching Q, rotational energy transfer R, predissociation P, and ionization W.

After a certain lifetime τ this excited species can relax into lower-lying states by emitting a fluorescence photon. Relaxation is possible directly back to the laser-coupled ground state 1 by emission of a photon of the excitation wavelength with the rate A_{21} (eq. 32). Also, with the rate A_{23}, the molecule can relax via an allowed transition into any other energy level of the molecule, summarized in level 3, emitting a photon with a wavelength of the energy difference between level 2 and 3.

Fluorescence typically competes with alternative processes that lead to a depopulation of the excited level 2. Stimulated emission takes place to the laser-coupled level 1 with the rate b_{21} (eq. 30 and 31). Also, out of state 2, ionization W of the molecule is possible by absorption of another photon that excites an electron into continuum. Further, the molecule can dissociate, which is called predissociation P.

Additionally, non-radiative, collision-induced processes depopulate level 2. This effect is termed electronic energy transfer (EET) or quenching Q. The overall quenching rate Q [s^{-1}] for all species j in the system is given by

$$Q = \frac{p}{kT} \sum_j x_j v_j \sigma_{Q,j} \quad , \tag{47}$$

where $\sigma_{Q,j}$ are the quenching cross sections upon collision with the species j, x_j is the mole fraction of the species j, $v_j = (8kT/\pi\mu)^{1/2}$ [m/s] is the average relative velocity between colliding particles with the reduced mass $\mu = m_1 m_2/(m_1+m_2)$.

Quenching can occur directly to the laser-coupled ground state 1, but also to other states summarized in level 3. Rotational (RET) and vibrational energy transfer (VET) then lead to thermalization of the population distribution. However, the detailed energy transfer cascade of non-radiative processes is complex and subject of investigation in section 4.1.7 for the NO molecule. For NO, VET in the electronic ground state is much slower than RET and can be neglected during the laser pulse duration. RET, on the other hand, is fast and continuously exchanges population between levels 1 and 3, indicated by R in Fig. 9. This leads to continuous thermal equilibrium within these levels. In practice, this assumption holds for low laser intensities and high collisional frequencies. The population of level 1 is then given by its Boltzmann population (eq. 7).

Note that RET and VET can also occur in the excited state 2. This especially gains importance if levels with significantly different effective fluorescence lifetimes are involved. Furthermore, fluorescence signal may be shifted to different spectral regions compared to the direct transitions from the laser-populated level. The implications of these effects are discussed in further detail in [44,60]. However, RET in the upper state has only a minor influence on total NO fluorescence intensity since levels populated by RET can also fluoresce with similar rates (note that this may be different for molecules other than NO).

For NO, the quenching rate does not depend on the excited state rotational level [61-63], in contrast to OH. Thus, a constant fluorescence yield can be assumed for RET-populated levels. Furthermore, the LIF experiments that are performed in this work use spectrally integrated LIF-signal detection over the complete rotational manifold, making the recorded signal independent on a small change in emission wavelength due to RET. We can thus neglect RET in the upper state.

3.1.1 Quantitative laser-induced fluorescence

The goal of a LIF experiment is to obtain quantitative state population distributions or total population prior to laser excitation, measuring temperature or species concentrations. We would therefore like to derive expressions that relate observed LIF signals to

undisturbed state populations. This can be achieved using a rate equation approach: For each quantum state of the molecule, the population dynamics can be described in terms of infill and loss rates due to the various processes described above. The set of rate equations for each state can then be solved simultaneously.

When setting up the rate equations for simple systems for constant laser intensity, the state populations reach a steady state after some characteristic time τ. If the temporal laser pulse width Δt_{laser} is much larger than τ, the steady-state solution may be used to describe the overall LIF process. This yields relatively simple non-transient LIF models that adequately describe the LIF process. This is true in particular for nanosecond-laser excitation and high-pressure environments.

In a non-transient approach we assume a constant laser intensity I_ν^0 and therefore constant b_{12} and b_{21} (eqs. 28 and 31). The population dynamics of the two states 1 and 2 can be described in the rate equation approach,

$$\frac{dN_1}{dt} = -N_1 b_{12} + N_2 (b_{21} + A_{21} + Q_{21}) \tag{48}$$

and

$$\frac{dN_2}{dt} = N_1 b_{12} - N_2 (b_{21} + A_{21} + Q_{21}) \quad , \tag{49}$$

where N_i [cm^{-3}] is the population number density of state i and t the time. These rate equations form a system of differential equations that can be solved analytically with the assumption of boundary conditions. We assume that for $t = 0$, the onset of the laser pulse, the population of the excited state is negligibly small, that is

$$N_2^0 = 0 \ . \tag{50}$$

For electronic levels with excitation wavelengths in the UV, this condition is given even at elevated temperatures. The Boltzmann fraction f_B (cf. eq. 7) for the upper state of the NO A–X(0,0) band ($\Delta\varepsilon = hc/\lambda = hc/(225\text{ nm})$) is only ~$2\times10^{-14}$ at typical flame temperatures of 2000 K. We furthermore assume constant total population, that is

$$N_1 + N_2 = N_1^0 \tag{51}$$

The integration of the differential equations 48 and 49 under consideration of the boundary conditions (eqs. 50 and 51) yields

$$N_2(t) = N_1^0 \frac{b_{12}}{b_{12} + b_{21} + A_{21} + Q_{21}} \left(1 - \exp\left(-t/\tau\right)\right) \tag{52}$$

with

$$\tau = (b_{12} + b_{21} + A_{21} + Q_{21})^{-1} \ . \tag{53}$$

Here, τ [s] is a characteristic timescale of the LIF process. After the onset of the laser pulse, N_2 increases until it reaches a steady state for $t >> \tau$. For typical laser pulse

durations (Δt ~20 ns), the condition $t >> \tau$ is fulfilled, the exponential term in eq. 52 can be neglected, and we can assume steady population of state 2 of

$$N_2 = N_1^0 \frac{b_{12}}{b_{12} + b_{21} + A_{21} + Q_{21}} \quad . \tag{54}$$

Using eqs. 28 and 31 we can also write

$$N_2 = N_1^0 \frac{B_{12}}{B_{12} + B_{21}} \frac{1}{1 + I_\nu^{sat} / I_\nu^0} \quad , \tag{55}$$

where

$$I_\nu^{sat} = \frac{A_{21} + Q_{21}}{\Gamma(B_{12} + B_{21})} c^2 \tag{56}$$

is the saturation intensity. We now search for an expression for the actual measured signal, the fluorescence power S_{LIF} [W]. S_{LIF} is proportional to the population N_2 of the excited state and to the fluorescence rate A_{21}. It furthermore depends on the detection solid angle Ω, the detection volume V, and the energy $hc\nu$ of the emitted photons. The exact relationship is given by

$$S_{\mathrm{LIF}} = hc\nu \frac{\Omega}{4\pi} V \, A_{21} N_2 \quad . \tag{57}$$

Using eq. 55 we get

$$S_{\mathrm{LIF}} = hc\nu \frac{\Omega}{4\pi} V \, A_{21} \, N_1^0 \frac{B_{12}}{B_{12} + B_{21}} \frac{1}{1 + I_\nu^{sat} / I_\nu^0} \quad . \tag{58}$$

This equation is the main result of the simple two-level LIF model (Fig. 9 without state 3). It describes the relation between the measured fluorescence signal and the initial ground state population. It therefore enables the interpretation of LIF signals for measuring ground state populations that can be related to species concentrations or temperatures.

In literature, different units for the fluorescence signal are used. Next to the fluorescence power S_{LIF} [W], the fluorescence intensity I_{LIF} [W/m²] is often used. From eq. 58 we can derive two limiting cases:

(1) High laser intensities $I_\nu^0 >> I_\nu^{sat}$: this is the so-called saturated regime. The equation simplifies to

$$I_{\mathrm{LIF}} \propto N_1^0 \frac{B_{12}}{B_{12} + B_{21}} A_{21} \quad . \tag{59}$$

The fluorescence signal becomes independent of the laser intensity. In practical application, this technique is called saturation spectroscopy or laser-induced saturated fluorescence. Signals are independent of laser intensity and quenching and are therefore relatively easy to interpret. However, the high saturation laser intensities require

careful experimental procedures, and complete saturation is difficult to achieve, especially at elevated pressures.

(2) Low laser intensities $I_\nu^0 << I_\nu^{sat}$: this is the so-called linear regime. Eq. 60 describes the LIF intensity I_{LIF} for one species in the regime of weak excitation as

$$I_{\mathrm{LIF}} \propto I_{\mathrm{laser}} \cdot N(p,T) \cdot f_{\mathrm{B}}(T) \cdot B_{ik} \cdot \Gamma_\nu(p,T) \cdot \left[\sum_{k,j} \frac{A_{kj}}{A_{kj} + Q_k + P_k + W_k} \right] \cdot \frac{\Omega}{4\pi} \cdot \eta \cdot f \cdot \varepsilon \qquad (60)$$

Absorption	Emission	Detection
	Fluorescence quantum yield ϕ	Experimental

I_{laser}	Laser intensity in the probe volume.
$N(p,T)$	Number density of molecules in the probe volume.
$f_{\mathrm{B}}(T)$	Boltzmann fraction of the laser-coupled ground state.
B_{ik}	Einstein B coefficient for stimulated absorption describing the absorption probability for transition $i \rightarrow k$.
$\Gamma_\nu(p,T)$	Overlap integral of molecular absorption and laser excitation line width.
A_{kj}	Einstein A coefficient for spontaneous emission from the excited level k via any allowed transition into any level j.
Q_k	Quenching rate coefficient of the excited state k.
P_k	Predissociation rate coefficient of the excited state k.
W_k	Ionisation rate coefficient of the excited state k.
Ω	Solid angle of the detection optics.
η	Transmission function of the target object.
f	Transmission function of the detection filters.
ε	Wavelength-dependent efficiency of the detector.

I_{LIF} is proportional to the number density of the excitable molecules in the probed volume V which is determined by $N(p,T)$ times the temperature-dependent Boltzmann fraction $f_{\mathrm{B}}(T)$ giving the population of the initial level i. Within the linear regime, the fluorescence intensity depends linearly on the laser intensity I_{laser} and the spectral overlap $\Gamma(p,T)$ of the laser profile and the absorption line. All these factors determine the number density of excited molecules and, therefore, the absorption part of the LIF process.

The fluorescence quantum yield ϕ in eq. 61 gives the ratio of the spontaneous emission rate (from level k) versus the total rate of (radiative and non-radiative) relaxation processes:

$$\phi = \sum_{kj} \frac{A_{kj}}{A_{kj} + Q_k + P_k + W_k} \tag{61}$$

ϕ therefore depends on the rate of spontaneous emission (given by the Einstein A_{kj} coefficient) divided by the sum of the rates of all depopulation processes of the excited state (spontaneous emission from state k to all possible ground state levels: ΣA_{kj}, quenching $Q_k(p,)$ predissociation P_k, and ionization W_k). The detection efficiency of fluorescence photons further depend on the observed solid angle $\Omega/4\pi$, the transmission of the investigated system η and the detection filters f as well as the response of the detector ε. Effects of polarization are discussed in [60].

3.1.2 LIF thermometry

When quantifying signal intensities obtained from LIF one must usually account for numerous temperature-dependent effects. The resulting over-all temperature dependence in turn is the basis for LIF thermometry. The spectral overlap factor $\Gamma(p,T)$ can be calculated from spectra simulations which are available for the most important combustion relevant species [64,65]. This is mainly important in high-pressure applications where collisional broadening causes the individual rotational lines to blend yielding absorption features which are spectrally broader than the laser line.

At atmospheric pressure and above the denominator in the fluorescence quantum yield ϕ is dominated by fluorescence quenching ($Q >> A$). For a large number of colliders, quenching rates for, e.g., OH and NO have been determined as a function of temperature and pressure enabling the development of simulation models [66,67]. Therefore, quenching can be quantified as long as the local gas composition and temperature are known.

The choice of the target molecule for LIF thermometry influences the accessible temperature range, versatility of the technique, experimental approach, and spectroscopic evaluation procedure. Temperature measurements have been performed using atomic fluorescence tracers like indium [68-70], diatomic species like OH [71-78], NO [24,40,75,77-95], O_2 [72,96-99], iodine [100,101], CH [88] and C_2 [88], and organic molecules like ketones [102-105] or toluene [106-108]. The availability of these molecules differs in reactive systems. The presence of OH and hot O_2 is limited to regions of reactive or hot gases like behind the flame front in combustion processes; the indium technique requires the activation of a precursor within a flame front; CH and C_2 are short-lived combustion intermediates; organic molecules that can be added to the fuel are only available in unburned gases and are therefore limited to temperature measurement in unburned mixtures.

For LIF excitation thermometry, various methods have been established that involve generally different experimental and data evaluation procedures: Single-line techniques

(where only a single ground state is probed), two-line techniques (where two ground states are probed and the temperature is inferred from the ratio of two intensities), and multi-line techniques (where three or more ground states are probed and temperature is inferred from a Boltzmann plot or by fitting spectral simulations). Theoretical analysis of line shape, quenching, energy transfer, and noise effects for the different techniques have been performed by several authors [71,74,80,85,109].

Particularly relevant in this context are of course the temperature-dependent terms. The dominant temperature influence in eq. 60 is given by the Boltzmann fraction (eq. 7) of the total species population in the laser-coupled ground state. The temperature dependence is due to both the exponential factor for the particular transition and the partition function Z. The spectral overlap fraction Γ depends on temperature via collisional broadening and shifting effects. Finally, the number density N of the target LIF species depends on concentration and temperature via the ideal gas law (eq. 5). In LIF measurements, the quenching rate Q depends on temperature due to both, the varying collisional frequency and cross-sections.

Single-line LIF thermometry

In single-line thermometry, an overall temperature dependence of the LIF signal can be calculated from eq. 60, if the spectroscopic data (term energies for Boltzmann fraction, collisional broadening, quenching) are known. The laser intensity I_{laser} is readily measured and corrected for. It is, however, evident from eq. 60 that the concentration of the target species N must be known. This is the case in non-reactive flows where concentrations are constant (e.g., O_2 in the inlet stroke of internal combustion engines [99], or NO seeded in constant amounts to a flow [85]) or when concentrations can be derived from chemical kinetic simulations (as shown, e.g., for NO in a low-pressure flame [89]). Finally, the calculated relative temperatures need to be calibrated at a known temperature.

Two-line LIF thermometry

Two-line thermometry is much more frequently used. In this approach, two LIF measurements are performed from different ground states. The fluorescence ratio R from the two measurements is then given by:

$$R_{12} = \frac{I_{\text{LIF},1}}{I_{\text{LIF},2}} = \frac{c_1 I_{\text{laser},1} g_1 \exp(-\varepsilon_1 / kT) B_1 \Gamma_1(p,T) A_1 / \left(A_1 + Q_1(p,T)\right)}{c_2 I_{\text{laser},2} g_2 \exp(-\varepsilon_2 / kT) B_2 \Gamma_2(p,T) A_2 / \left(A_2 + Q_2(p,T)\right)} \tag{62}$$

By taking the ratio, the species concentration, which is the major unknown factor in most applications, cancels out. This makes the two-line techniques applicable to reacting systems. It should be noted that also the partition function Z cancels out in the ratio.

Commonly, there are more assumptions being made as to the remaining temperature dependent factors: Q is assumed to dominate over A (which is usually the case in atmospheric or high-pressure systems); if Q is the same for the excited states in both measurements (by choosing either a molecule where Q does not depend on rotational quantum number like NO, or by choosing transitions that excite into the same upper state), then Q also cancels out: the ratio R_{12} gets independent of quenching processes. If, finally, the temperature dependence of the overlap coefficients and the influence of laser-energy fluctuations are neglected, then the fluorescence ratio is given by a Boltzmann relation (eq. 7) only,

$$R_{12} \propto \exp\left(-\frac{\Delta\varepsilon_{12}}{kT}\right), \tag{63}$$

depending on the temperature T, the ground state energy difference $\Delta\varepsilon_{12}$, and the Boltzmann constant k. Eq. 63 reduces the temperature dependence of the LIF ratio to the temperature dependence of the relative ground state populations, which represents the most relevant temperature influence in the two-line technique. Nevertheless, additional influence of the overlap fraction $\Gamma(T)$ and quenching $Q(T)$ may become important depending on the specific target species.

The constants c_1 and c_2 in eq. 62 summarize the efficiency of the detection system. If they are the same for both excitation wavelengths, quantitative temperature measurements are in principle possible without calibration. In many cases, however, using known temperature data is necessary to calibrate for the c_1/c_2 ratio.

Multi-line thermometry

Multi-line LIF thermometry offers high temperature sensitivity in a wide temperature range by probing a number of ground states with different term energies. In a basic approach we can assume, similar to the two-line technique, that the main temperature influence of the LIF signal arises from the ground state population only. Furthermore, it is assumed that the temperature influence on the overlap fraction and quenching is equal for all transitions, c is equal for all transitions, and $A << Q$ is valid. Then, for any transition i, eq. 60 can be rewritten as

$$\ln\left(\frac{I_{\mathrm{LIF},i}}{I_{\mathrm{laser},i}}\frac{g_i}{A_i B_i}\right) = -\frac{1}{T}\frac{\varepsilon_i}{k} - \ln\left(\frac{Z(T)}{c\ N(T)\,\Gamma(p,T)\,Q(p,T)}\right) \tag{64}$$

where the last term is constant for all transitions. The signals $I_{\mathrm{LIF},i}$ and the laser intensity $I_{\mathrm{laser},i}$ are measured, and g_i, A_i and B_i are spectroscopic constants. By plotting the left term of eq. 64 versus ε_i for different transitions, the temperature can be derived from the slope of the plot which is $-1/kT$. This is called a Boltzmann plot (Fig. 10).

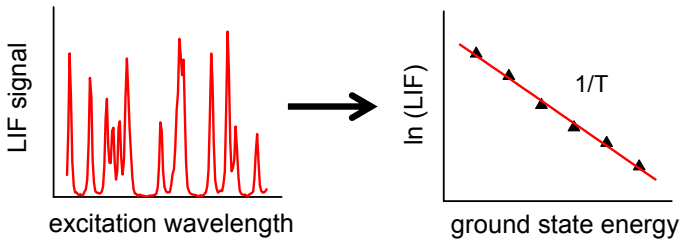

Fig. 10: Section of a typical LIF excitation scan (here NO at ~225.3 nm) and the resulting Boltzmann plot. The slope of the Boltzmann plot gives the negative inverse temperature.

In many practical applications there are a number of effects that complicate the simple analysis as given above:

- The assumption that Q is constant for all transitions does not always hold. In OH, for example, Q is known to depend on the rotational quantum number J [71].
- Transitions may overlap, so that the LIF signal does not arise from a single ground state. This is the case e.g. for NO, especially at elevated pressures. The overlap fractions Γ of many transitions must then be considered simultaneously.
- In many practical applications, background signals are present, such that $I_{\text{total}} = I_{\text{LIF}} + I_{\text{background}}$. The simple eqs. 60-64 then cannot be applied; instead, corrections for the background contribution are necessary.
- The assumption of weak laser excitation that was used for deriving eq. 60 may not be adequate. LIF saturation and rotational energy transfer may have significant effects on thermometry techniques [109,110].

Accurate LIF thermometry techniques need to include a full description of these effects. This can either be done by multi-temperature calibration measurements (yielding an empirical description of the temperature-dependence of the signals) or by using detailed spectral simulations.

For NO-LIF thermometry, a multi-line scanning approach was developed [111] that simultaneously considers the effects of line shape and background contribution based on numerical simulations of excitation spectra [65]. Therefore, the technique can be applied even in systems with strong scattering and fluorescence background and is independent on local variations in laser intensity [112]. Because the complete shape of the spectra (including several absorption features and line-broadening) is included in the data evaluation, the technique is robust and more precise than two-color thermometry or a Boltzmann plot. This recently developed technique is described in detail in section 4.1 and used in several applications presented in sections 5.1 – 5.5.

3.2 Absorption spectroscopy

Absorption spectroscopy is one of the oldest techniques for the non-intrusive investigation of gaseous media. The subject of interest in laser absorption spectroscopy (LAS) is mostly the absolute concentration of one or more atomic or molecular species which are present in a mixture [113,114]. Apart from that, LAS is able to determine simultaneously the physical boundary conditions (such as temperature, velocity, pressure or mass flux etc.) to which the absorbers are exposed [25].

Fig. 11: Experimental setup for absorption spectroscopy.

The basic setup of an absorption spectrometer is sketched in Fig. 11 and can be described as a light source, which emits radiation with an initial intensity I_0 through the sample towards a radiation detector. Part of the radiation is absorbed by atomic or molecular constituents along each path increment of the free beam in a simple one step process. The transmitted light intensity I_t behind the sample is monitored to determine the total loss and is used as a quantitative measure for the number of absorbers along the beam path. The transition frequency ν at which the absorption occurs is characteristic for the absorbing substance, therefore simultaneous species identification is possible (spectral fingerprint). Integration of the light losses over the total absorption path with a length L leads, under the assumption of a homogenous absorber distribution and a monochromatic light source, to the Lambert-Beer equation

$$\frac{I_t}{I_0} = \exp(-k_\nu L) \tag{65}$$

with the spectral absorption coefficient k_ν. For an isolated transition i,

$$k_\nu = P x_{abs} S_i(T) \Phi_\upsilon \tag{66}$$

where P is the total pressure of the gas, x_{abs} is the mole fraction of the absorbing species of interest, and $S_i(T)$ is the line strength of the transition i. The latter contains the temperature dependence of the spectral absorption coefficient due to the Boltzmann distribution (eq. 7) and can be calculated by

$$S(T) = S(T_0)\frac{Z(T_0)}{Z(T)}\left(\frac{T_0}{T}\right)\exp\left[-\frac{hcE''}{k}\left(\frac{1}{T}-\frac{1}{T_0}\right)\right]\frac{1-\exp\left(\frac{-hc\nu_0}{kT}\right)}{1-\exp\left(\frac{-hc\nu_0}{kT_0}\right)} \tag{67}$$

where $S(T_0)$ is the line strength at a reference temperature T_0 and ν_0 is the center frequency of the transition. Z is the partition function (eq. 9). For measurements within a small temperature and frequency range (e.g. the measurements presented in this work), the last term of eq. 67 can be neglected.

The exponent in eq. 65 is called the spectral absorbance α_ν and is given by

$$\alpha_\nu \equiv -\ln\left(\frac{I_t}{I_0}\right)_\nu = k_\nu L = P x_{\text{abs}} S_i(T) \Phi_\nu L \ . \tag{68}$$

The line-shape function Φ_ν describes the spectral broadening effects and is usually approximated using a Voigt profile characterized by the collisional width and the Doppler width (cf. section 2.3.3). The integrated absorbance can be expressed as the area A of the peak i on the frequency axis:

$$A_i = \int_{-\infty}^{\infty} \alpha_\nu d\nu = k_\nu L = P x_{\text{abs}} S_i(T) L \ . \tag{69}$$

3.2.1 Direct absorption thermometry

In any combustion-related sensor for molecular species it is very important to recognize that $S(T)$ is a strong function of temperature due to the Boltzmann factor (eq. 7). If the pressure remains constant during the temperature change the absorber density will be modified with $1/T$. A change in temperature of several hundred degrees can cause variations in the integrated absorbance over two orders of magnitude. This strong temperature dependence can be used to measure the temperature by ratioing the integrated absorbances A_i of at least two suitable transitions [115]. The scientist typically measures A_i simultaneously with the same pressure, same mole fraction and identical path length. Their ratio R simply reduces to the ratio of their line strengths which is a function of the absorber temperature T only:

$$R = \frac{A_1}{A_2} = \frac{S_1(T)}{S_2(T)} = \frac{S_1(T_0)}{S_2(T_0)} \exp\left[-\frac{hc}{k}(E_1" - E_2")\left(\frac{1}{T} - \frac{1}{T_0}\right)\right] \tag{70}$$

Finally, the gas temperature is determined from the ratio of the experimentally determined integrated absorptions of two isolated transitions with different temperature dependence:

$$T = \frac{\left(\frac{hc}{k}\right)(E_2" - E_1")}{\ln\left(\frac{A_1}{A_2}\right) + \ln\left(\frac{S_2(T_0)}{S_1(T_0)}\right) + \left(\frac{hc}{k}\right)\left(\frac{E_2" - E_1"}{T_0}\right)} \tag{71}$$

In principle, there are different ways to measure the integrated absorbance. A common approach is to use tunable, spectrally narrowband light sources and tune the wavelength over the absorption features to derive entire line shapes. If diode lasers are used, this technique is referred to as tunable diode laser absorption spectroscopy (TDLAS). This method is described in detail in section 4.2 of this thesis and applications are shown in section 5.5 and 5.6.

The tuning approach has some advantages in contrast to simple peak absorption measurements since one can use the integrated areas of the peaks to derive temperature more accurately, species concentration can be measured and one is able to calculate other physical parameters like pressure (due to pressure broadening) from the line shape. Alternatively, spectrally broadband light can be transmitted over the region of interest and the signal can be detected wavelength dispersed. This way several absorption peaks appear on the wavelength axis whose center frequencies correspond to molecular transitions.

Two-line thermometry has good temperature sensitivity within a limited temperature range (several hundred Kelvin) that depends on the corresponding ground state energies of the two transitions used. In principle, the two peaks should have a large difference in ground state energies to make sure the ratio of the lines changes strongly with temperature. But the absorbance of the two lines should be in the same order of magnitude ($0.25 < \text{ratio} < 4$) to prevent one line from dominating the ratio [116]. For low temperatures, lines with low ground state energies should be used and for flame temperatures, transitions originating from higher ground state energies are necessary.

If higher accuracy over a wider temperature range is desired, several absorption features of transitions with different ground state energies must be measured. A sensor has demonstrated excellent temperature sensitivity from 300 – 2500 K by using three ratios [117] of four transitions with different ground-state energies. Each ratio has good temperature sensitivity (a steep slope) in a different range as shown in Fig. 12.

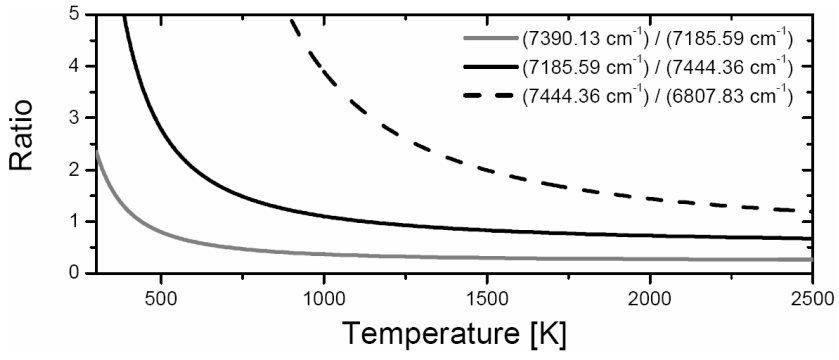

Fig. 12: Three absorbance ratios are used to enable measurements over a wide temperature range [117].

The multiplexing approach also enables to monitor temperature and several species concentrations simultaneously, e.g. fuel and water in an engine [118]. The drawback of the multiplexed sensor is that the system becomes more complex since the different wavelengths of the transmitted light must be separated and detected by multiple detectors. In a 600 MW power plant, CO, H_2O and gas temperature were measured simultaneously [119].

It is important to mention that absorption techniques necessarily accumulate information along the laser path through the measurement volume. In homogeneous media signal interpretation from two or multiple lines or the evaluation of line shapes is straight forward. In systems with strong concentration and temperature inhomogeneities within the interaction path, results must be critically interpreted. Multi-line strategies are being developed to interpret an inhomogeneous temperature distribution.

3.2.2 Wavelength modulation spectroscopy

In the simple direct absorption approach, the sensitivity is limited to absorbances of typically >1%. This is due to the limited signal-to-noise (S/N) ratio since the small absorption signal has to be separated from the huge 100% transmission signal and a baseline must be taken from a reference channel or from a fit to the wings of the wavelength scan (Fig. 13 a).

If one uses peaks with lower absorbance, the laser tuning (at e.g. 1 kHz) can be overlaid with a fast modulation frequency (of e.g. 500 kHz). This approach is called wavelength-modulation spectroscopy (WMS). The signal is detected with a lock-in amplifier to separate the phase-coupled signal from noise. When the second harmonic (2f) of the modulated signal is detected as shown in Fig. 13 b), the signal sits on a zero background making a zero absorption baseline unnecessary.

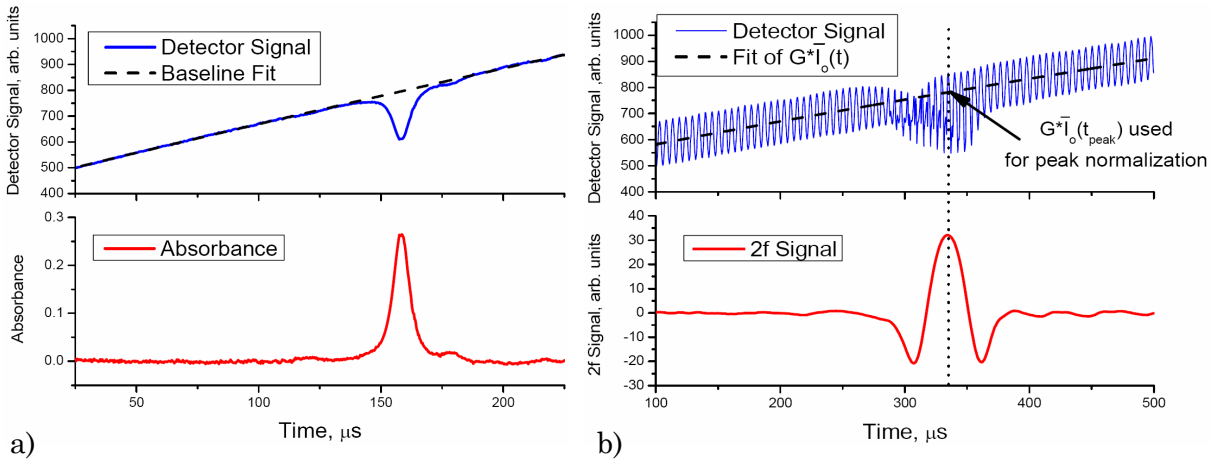

Fig. 13: Comparison of the TDLAS direct absorption method (a) and the WMS technique with 2f detection (b) [120].

The gain in S/N ratio is especially good for weak lines (Fig. 14). This gain in sensitivity comes at the expense of a more complex sensor and a more difficult interpretation of the signal. For thermometry, it is sufficient to take the ratio of the peak intensities, and not integrated areas. This makes the evaluation of the WMS technique with 2f detection straight forward [121].

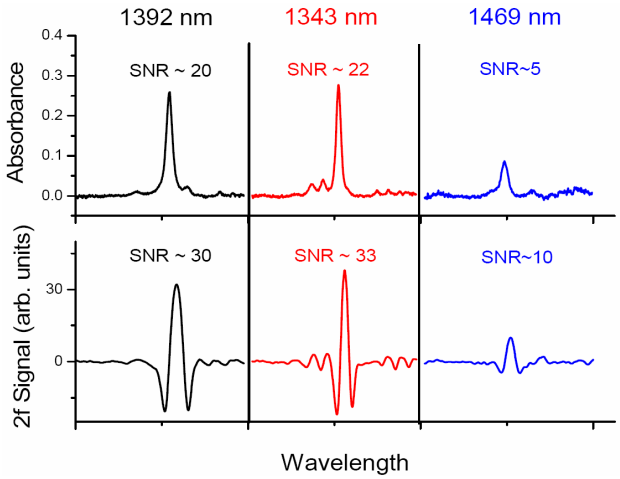

Fig. 14: Comparison of signal-to-noise ratios in direct absorption (upper row) and wavelength modulation with second harmonic detection (lower row) [120].

3.3 Rayleigh scattering

If a photon of energy $\hbar\omega_0$, that is non-resonant with any allowed single- or multi-photon transition, interacts with a molecule, with a certain probability elastic or in-elastic light scattering occurs. This process is sketched in Fig. 15. The more probable elastic scattering process is termed Rayleigh scattering, whereas the much weaker in-elastic process is called spontaneous Raman scattering. After a Rayleigh-scattering process, the molecule returns into its original quantum state. In contrast, Raman scattering is associated with a net energy exchange between photon and molecule. The energy transfer might have in- or decreased the rotational (denoted by *J*) and/or vibrational quantum state (denoted by *v*) of the molecule. Due to energy conservation scattered Raman photons contain correspondingly de- or increased energy $\hbar(\omega_0 \mp \omega_k)$ with $\hbar\omega_k$ being the energy difference between initial $|i\rangle$ and final $|f\rangle$ quantum states involved to the process. $|i\rangle$ and $|f\rangle$ denote wave functions and are solutions of the corresponding Schrödinger equation (eq. 10). In analogy to the postulate of Stokes [122], that fluorescence is shifted towards longer wavelength relative to the exciting wavelength, red-shifted Raman scattered photons $\hbar(\omega_0 - \omega_k)$ are termed Stokes-lines and blue-shifted photons $\hbar(\omega_0 + \omega_k)$ anti-Stokes-lines.

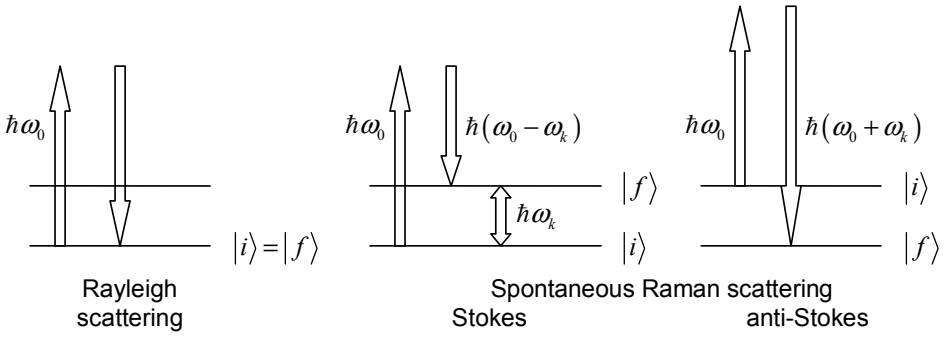

Fig. 15: Energy level diagram for Rayleigh scattering and spontaneous Raman scattering [21].

In Rayleigh thermometry, the number density is measured and temperature is calculated from the ideal gas law (eq. 5). It is a technique relying in many practical applications on single laser shots [57]. Thereby a high temporal resolution much shorter than typical Kolmogorov time-scales in turbulent (reactive) flows can be accessed. With comparatively low experimental effort, Rayleigh scattering can be applied in an imaging setup. A typical experimental setup is identical to the LIF setup described in section 4.1.2 (Fig. 23). Only the detection filters must be changed.

Rayleigh thermometry has therefore been widely applied to turbulent systems, e.g. in turbulent flames [123,124] or internal combustion engines [125]. In Rayleigh scattering, all chemical species contained in a finite sized probe volume give rise to a measured

signal. Therefore, inferring number densities from scattering data requires information about local effective Rayleigh cross-sections and, hence, the local gas composition, which is usually unavailable in inhomogeneously mixed or reactive systems [126]. In combustion, special fuel blends have been proposed that provide similar total cross-sections for unburned and burned gases [124,127], enabling Rayleigh thermometry even in turbulent combustion systems. Alternatively, Raman scattering can be applied simultaneously with Rayleigh scattering to measure the gas composition [128]. This is, however, limited to measurements in one spatial dimension [129].

Rayleigh thermometry suffers from problems with background scattering (e.g. off walls or windows); in the presence of particles, like in sooting flames, this technique is therefore not feasible. Here, a filtered Rayleigh scattering technique has been developed [130-132]. This approach makes use of the fact that scattering off gas-phase molecules has a wider Doppler width due to their thermal motion (~0.1 – 0.3 cm^{-1}) than scattering from surfaces (walls, particles, droplets). If a single longitudinal mode laser is used, the signal of surface-scattered light can be rejected by narrow-band (< 0.05 cm^{-1}) filters (usually molecular filters like iodine or atomic vapor filters like mercury contained in quartz cells).

Increasing temperature is causing a larger Doppler width of the Rayleigh-scattered light originating from the gas phase. This line broadening causes an increasing signal via by-passing the narrow-band filter. The principle of filtered Rayleigh scattering thermometry is shown in Fig. 16. Exact control of laser wavelength, spectral profile, absorption profile of the molecular or atomic line filter, and knowledge of line broadening is required.

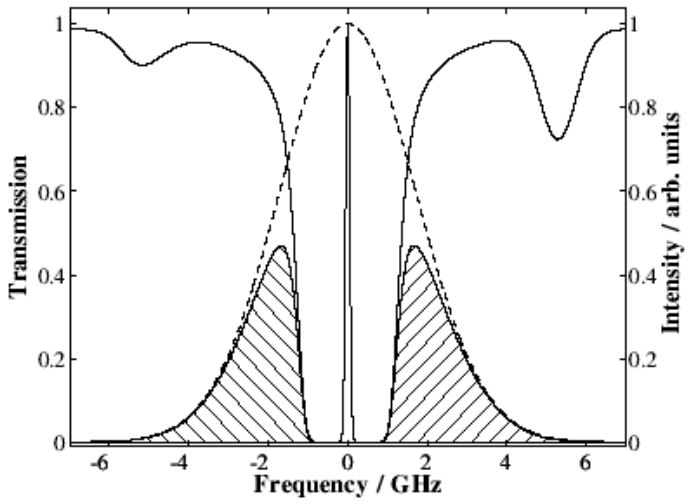

Fig. 16: Molecular line shape of Rayleigh-scattered light at elevated temperature (dashed line), transmission profile of atomic vapor such as mercury (solid line) and spectral laser emission (peak at 0 GHz). The spectral overlap of the atomic notch filter and the Doppler-broadened Rayleigh profiles result into the spectral wings transmitted to the detector (hatched area). Reproduction from [133].

3.4 Raman scattering

Spontaneous Raman scattering is frequently used for temperature evaluation in one-dimensionally resolved multi-species measurements [134]. It is typically too weak for two-dimensional imaging. It has, however, been demonstrated for instantaneous concentration imaging with long-pulse flash-lamp-pumped dye lasers as high-energy light sources [135]. A typical Raman setup is shown in Fig. 17. The laser beam is formed as desired and transmitted through the region of interest. The scattering light is detected rectangular, wavelength dispersed in an imaging spectrograph, and recorded with an intensified CCD camera. The photo diode is used for laser-energy referencing.

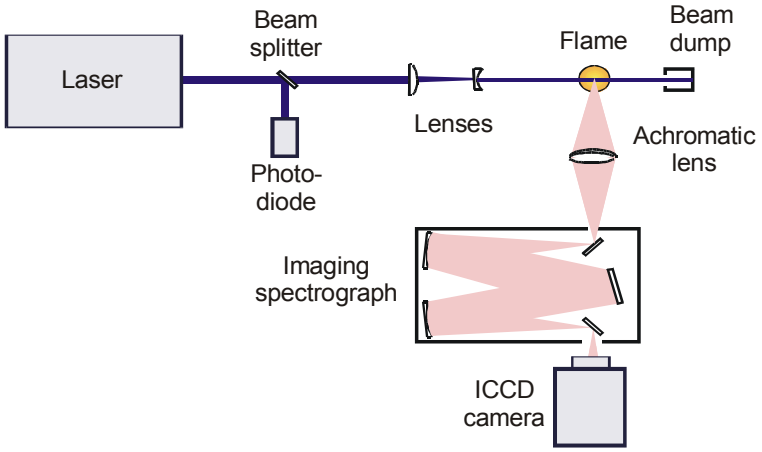

Fig. 17: Experimental setup of a Raman-scattering experiment.

Each chemical species exhibits a red- or blue-shift (Stokes and anti-Stokes lines) according to the energy difference $\hbar\omega_k$ between initial and final states involved to the process as shown in Fig. 15. Table 4 summarizes averaged relative normalized differential Raman cross-sections for Q-branches $(\partial\sigma/\partial\Omega)_Q(T=300K)$ and Raman frequency-shifts of combustion-related molecules. Averaged differential Raman cross-sections scale non-linearly with temperature.

In contrast to pure Rayleigh scattering, signals from different chemical species show species-specific Raman frequency-shifts and therefore must be spectrally dispersed before detection. The advantage of Raman thermometry is that dispersed Raman spectra contain all necessary information to deduce gas temperature. This is in contrast to Rayleigh thermometry or LIF schemes, where additional information on gas composition and collisional energy transfer pathways in case of LIF is required for a thorough analysis. Therefore, despite of the rather low scattering cross-sections that need to be overcome by high excitation laser photon fluxes and low-noise detection components, Raman thermometry can be an important alternative if this additional information is not provided. Notice, that in addition to temperature, the gas composition can be evalu-

ated as well (→ simultaneous Raman/Rayleigh scattering [136]). By this, Raman scattering is a multi-scalar diagnostic based on a single excitation frequency.

Molecule	Raman shift $\omega_k/2\pi c$ [cm^{-1}]	$(\partial\sigma/\partial\Omega)_Q\,(T=300\mathrm{K})$
CO_2 (ν_2)	1285.0	0.75
CO_2 (ν_1)	1388.0	1.13
O_2	1555.0	1.04
CO	2143.0	0.93
N_2	2331.0	1.0
CH_4 (ν_1)	2914.0	8.55
CH_4 (ν_2)	3017.0	5.7
H_2O	3652.0	3.51
H_2	4155.2	3.86

Table 4: Raman shifts and averaged normalized differential Raman cross-sections for the Q-branch of some combustion-related molecules at room temperature. The absolute Raman cross-section of the Q-branch of nitrogen is $(5.05\pm0.1)\times10^{-48}\times(\omega_0/2\pi c-2331\mathrm{cm}^{-1})$ $\mathrm{cm}^6/\mathrm{sr}$ *[137].*

Local temperatures can be extracted from Raman spectra in different ways. For the case of high spectral dispersion, single rotational or ro-vibronic lines might be resolved. Raman spectra can be simulated and fitted to the measured spectra [138]. However, line widths must be considered as well. Raman lines might be pressure- and Doppler-broadened. In addition, limited spectral resolution of the spectrometer broadens the measured lines as well. Therefore, each allowed transition needs to be convoluted with an effective line shape and a spectrum is received from superposition of all relevant allowed transitions. Fig. 18 shows schematically ro-vibronic N_2-Raman bands at various temperatures. In this example the effective line width is broad compared to the spectral separation of adjacent transitions. This leads to an overlap of ro-vibronic Raman lines resulting in a single Raman band up to approximately 400 K and additional hot-bands at higher temperatures than 500 K. It is obvious, that Raman bands and spectral intensities are strongly temperature dependent, due to the Boltzmann distribution (eq. 7).

A second way to extract temperatures from Raman scattering is to determine number densities of each major chemical component present in the probe volume. For this purpose it is assumed that the gas composition is comprised of only Raman-active species at sufficiently high concentrations to allow accurate detection and Stokes-shifts into spectral regions that are actually monitored. Then the number density of all chemical components can be added up to result in the overall number density in the probe volume under consideration. With the validity of the ideal gas law (eq. 5) assumed, as in Rayleigh thermometry, the total number density in connection with the (measured) pressure can be used to determine a local temperature.

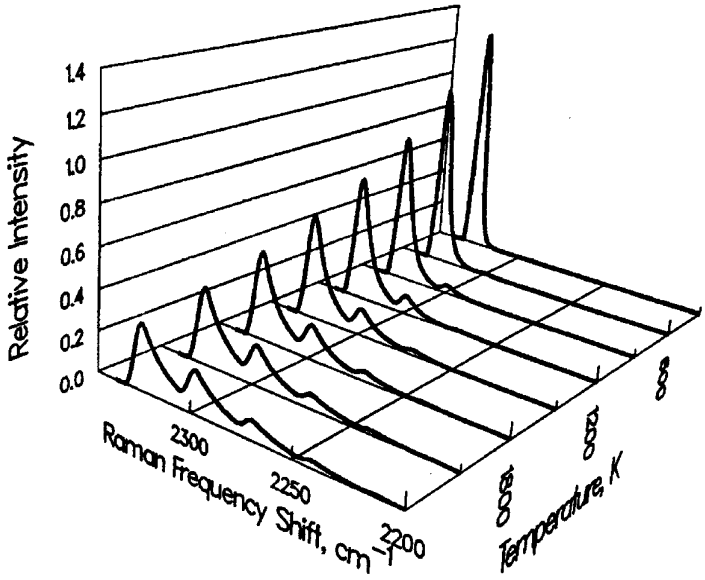

Fig. 18: Relative Raman scattering intensities of molecular nitrogen for different temperatures. Reproduction from [20].

The third way to determine temperatures from Raman scattering is to perform measurements of both Stokes and anti-Stokes shifted Raman lines (or bands). In the limit of the harmonic approximation and identical degeneracy factors for both quantum states, the measured ratio of Stokes and anti-Stokes lines is given by:

$$\frac{S_{Stokes}}{S_{anti-Stokes}} = \left(\frac{\omega_0 - \omega_k}{\omega_0 + \omega_k} \right)^3 \exp\left(\frac{\hbar c \omega_k}{kT} \right) \tag{72}$$

The intensity ratio must be a value which can be measured with sufficient signal-to-noise ratio. This requires sufficiently high population in the excited state from which anti-Stokes Raman scattering takes place. Near room temperature Raman lines shifted in the range from 0 to 500 cm^{-1} are useful, whereas for around 1000 K spectral shifts up to 2000 cm^{-1} should be used. Raman signals are very weak, therefore high energy lasers and high quantum efficiency detectors are necessary. However, the laser power density is limited by air breakdown, therefore pulse stretching is often used.

3.5 Coherent anti-Stokes Raman scattering

Coherent anti-Stokes Raman scattering (CARS) belongs to the class of nonlinear, coherent processes. Nonlinear wave mixing phenomena usually are not observed at the low light intensities of incoherent thermal radiators. However, the development of high power tunable laser systems has triggered the study of numerous new nonlinear optical phenomena [44]. The CARS energy level scheme is sketched in Fig. 19 together with the experimental setup.

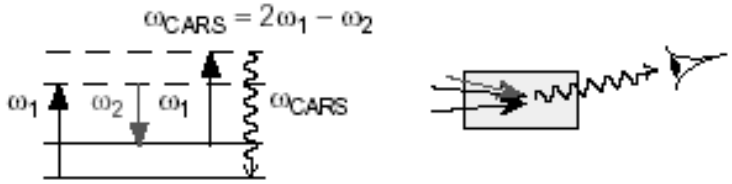

Fig. 19: Left: Energy level diagram of Coherent anti-Stokes Raman scattering (CARS). Right: Schematic experimental arrangements of laser beams and direction of signal detection [21].

The nonlinear susceptibilities are enhanced whenever one or more of the frequencies of the interacting laser beams coincide with allowed single- or multi-photon transitions. This produces a coherent signal beam in a direction determined by the phase-matching condition

$$\vec{k}_{sig} = \sum \vec{k}_j \quad , \tag{73}$$

where $|\vec{k}_j| = n_j \omega_j / c$ is the magnitude of the respective beam wave vector. Through focusing of the beams good spatial resolution transverse to the beam propagation direction can be obtained with sample volumes of several tens of μm^3.

In particular, CARS is advantageous for temperature measurements under difficult combustion conditions such as gas turbine combustors [139]. The signals of coherent processes are generally strong and emitted in a laser-like beam, but the signal generation depends nonlinearly on the concentration of the probe molecules and is also intrinsically a nonlinear function of the exciting laser intensities. CARS therefore imposes stronger demands on the laser source such as to stability, beam quality, and mode structure, and, since two laser beams are involved, on alignment.

For thermometry in air-breathing flames, N_2 is used preferentially as probe molecule because of its high concentration and the availability of a complete spectroscopic database. The CARS technique allows only point measurements; simultaneous thermometry of an extended line or plane (as in LIF or Raman) is not possible. However, due to its high accuracy, CARS is often used to define a temperature standard for the investigation

and validation of other thermometry methods such as multi-line NO-LIF thermometry (section 4.1.3). A typical experimental sketch is presented in Fig. 20.

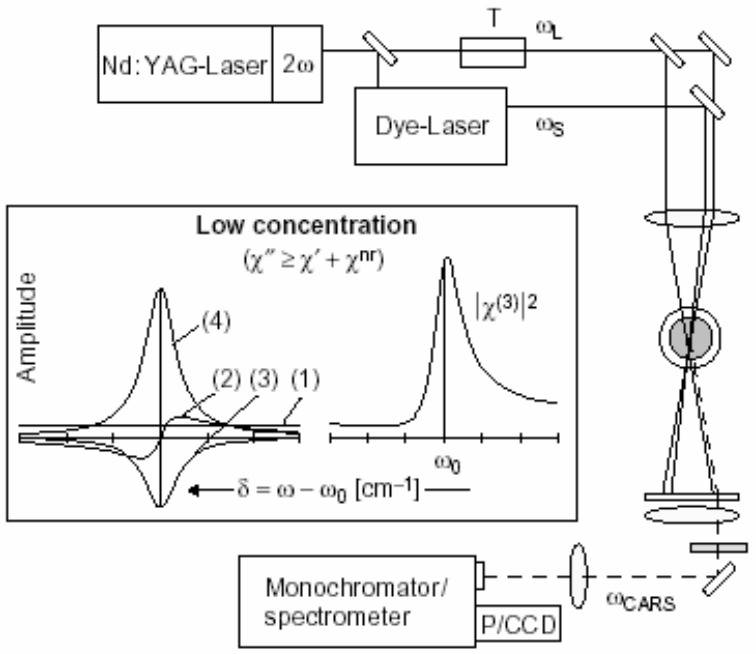

Fig. 20: Experimental arrangement of a CARS spectrometer. The dye laser can be either a narrow band laser for scanning CARS or a broadband laser for single-shot CARS thermometry. In case of scanning CARS a photomultiplier tube is used at the exit plane of the monochromator, in case of the broadband dye laser a CCD camera is used in connection with a spectrometer. The insets show a typical CARS line-shape function for an isolated transition at low concentration of the species under consideration. It is composed of the constant non-resonant background (1), the interference contributions with χ^{nr} (2,3) and the Lorentzian-shaped resonant part (4) of the third order susceptibility $\chi^{(3)}$. Taken from [21].

In single-shot CARS experiments one fixed frequency (pump, ω_1) and one broadband (Stokes, ω_2) laser beam in the visible with their frequency difference equal to a Raman-allowed transition are aligned and focused into the sample to create, in a four wave mixing process, a coherent beam at the anti-Stokes frequency ($2\omega_1 - \omega_2$), well separated spatially and spectrally from all incoming beams. The CARS radiation then is dispersed in a spectrometer and detected with a CCD camera. In the non-saturated regime the CARS intensity at frequency $\omega_{CARS} = \omega_3 = 2\omega_1 - \omega_2$ for an isolated transition [44] can be written as

$$I_{CARS} = I_3 = \frac{\omega_3^2}{n_1^2 n_2 n_3 c^4 \varepsilon_0^2} (lN\Delta_j)^2 I_1^2 I_2 \left|\chi_{CARS}^{(3)}\right|^2 \tag{74}$$

where I_1 and I_2 are the intensities of the pump and Stokes beams, respectively, and n_i are the refractive indices at frequency ω_i. I_{CARS} is also dependent on the square of the interaction path length l and number density difference $N\Delta_j$ between lower and upper

Raman level of the *j*-th transition. Eq. 74 is written for perfect phase matching of the beams, i.e. when eq. 73 holds and the corresponding signal intensity is maximized.

The third-order susceptibility $\chi^{(3)}$ in general consists of a non-resonant part χ^{nr}, which is independent of the frequency of the exciting beams, and a more complex Raman-resonant contribution. For low concentrations the (real) non-resonant contribution χ^{nr} in the susceptibility is significant and limits the detection sensitivity due to interference with the resonant contribution. To illustrate this behavior, the real and imaginary susceptibility components determining the CARS line shape are depicted in the inset of Fig. 20 for an assumed low concentration of the resonant species in a non-resonant buffer gas.

The overall CARS signal is an accurate measure of the gas temperature. This is exploited for thermometry applications through least squares fitting of computer generated to experimental CARS spectral shapes, if proper account is taken for the various physical effects contributing to the CARS spectral signature, such as coherences in the CARS pump beams [140,141], saturation and collisional effects [142,143] or the noise characteristics when broadband Stokes lasers are employed [144].

4 Optimization of the applied techniques

In section 4.1, a recently developed, scanning multi-line thermometry technique based on laser-induced fluorescence of nitric oxide is presented. The experimental setup is explained in detail and improvements are shown in the detection strategy of NO fluorescence. Temperature sensitive spectral excitation ranges are identified for every application. Also, the accuracy of the time-averaged multi-line LIF technique in turbulent systems is investigated and saturated LIF spectroscopy is discussed.

In section 4.2, a two-line thermometry technique based on tunable diode-laser absorption spectroscopy is introduced. This method is based on linear absorption spectroscopy of water. The experimental setup, sensor optimization, as well as the data evaluation procedure is presented.

Both thermometry techniques were applied to different combustion systems in a wide range of pressures (3 – 500 kPa) and temperatures (250 – 2500 K). Applications and results are described in section 5.

4.1 Multi-line NO-LIF thermometry

Nitric oxide (NO), seeded to reactive flow systems, has the advantage for combustion-related thermometry to be present in both, the unburned and the post-flame gases. It is stable at room temperature and elevated temperatures and therefore has the potential of making a wide temperature range (250 – 2500 K) accessible for LIF thermometry (cf. section 3.1.2). NO seeding is easy to perform and does not require difficult procedures like for indium, where the fluorescing species must be activated from a precursor [70]. In contrast to OH, which is only present in the flame front and hot exhaust gases, the fresh gases and cold boundary layers are accessible with NO. Furthermore, NO provides strong red-shifted fluorescence signals. Therefore, only low seeding concentrations that do not influence the system under study are necessary for thermometry (~100 – 1000 ppm). Since NO is produced in many combustion systems, seeding may not be necessary at all.

In contrast to single- and two-color LIF thermometry [40,89] the scanned multi-line technique yields absolute temperatures without calibration [145]. Multi-line techniques were applied in stable low-pressure [78,146], atmospheric-pressure [77,87] and high-pressure flames [30,86,147-149], sooting flames [24,148-150], spray systems [95,151,152], and in an arcjet reactor [88]. Comparisons were performed among NO single-, two- and multi-line techniques [85,87,89]. NO thermometry has also been compared to LIF methods using other target molecules [75,77,78,88]. In contrast to OH, fluorescence quenching in the NO $A\ ^2\Sigma^+$, $v' = 0$ state is insensitive to rotational quantum number [61-63]. Therefore, it is not required that both laser-excited transitions populate the same excited rotational level.

4.1.1 Nitric-oxide spectroscopy and LIF-spectra simulations with LIFSim

NO is a major pollutant that is emitted from combustion systems. For diagnostics purposes, extensive research has been conducted to characterize the NO molecule spectroscopically. However, the electronic structure of the NO molecule is complex. Laser-induced fluorescence experiments involve a number of different electronic states with extensive fine structure: NO optical spectra show thousands of transitions in the UV. The fundamentals of molecular spectroscopy have been described in section 2.3. A thorough description of NO spectroscopy is available in the literature [153]. This section gives a brief overview in order to understand the shape of NO spectra. All NO spectroscopic experiments that are described in this thesis were carried out within the $A\ ^2\Sigma^+$ and $X\ ^2\Pi$ electronic states. Therefore, these states and the transitions between them are shortly described.

A potential energy diagram of the NO molecule with the five lowest doublet electronic states is given in Fig. 21. The ground state is termed X and the excited states are sorted alphabetically. In the electronic ground state *X*, NO has one single unpaired electron. Therefore, the spin angular momentum quantum number $S = 1/2$ and the multiplicity $(2S + 1) = 2$, yielding molecular doublet states. The single electron is in a π^* molecular orbital, therefore $\Lambda = 1$. The term symbols for the NO ground state are thus $^2\Pi_{1/2}$ and $^2\Pi_{3/2}$. The electronic degeneracy $g_e = 4$: the two terms are further split by lambda doubling to *e* and *f* states. However, lambda doubling is quite small compared to spin-orbit splitting and is often not resolved in NO spectra except for high *J* [154].

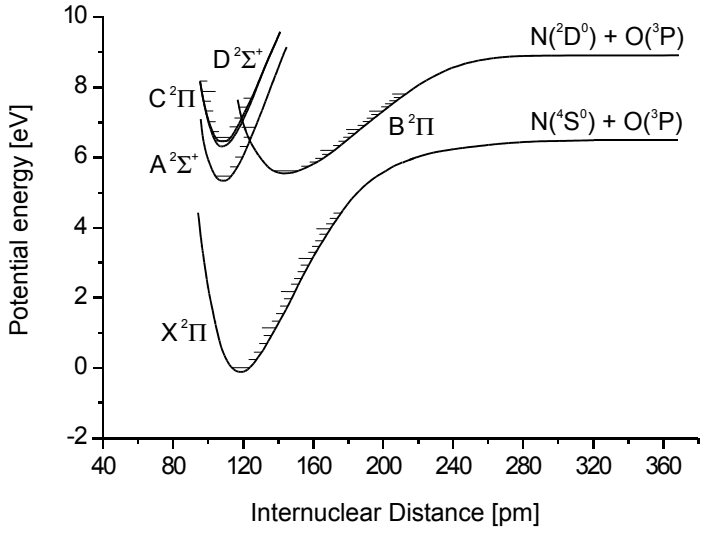

Fig. 21: Potential energy diagram of NO. After Gilmore [155].

In the first excited NO doublet state *A*, the single electron is excited from the π^* to a σ^* molecular orbital, leading to $\Lambda = 0$. The term symbols for this states are thus $^2\Sigma^+_{1/2}$ and $^2\Sigma^+_{-1/2}$. The electronic degeneracy $g_e = 2$. These two states have slightly different energies through spin-rotation splitting. For the ground vibrational level, $\gamma \sim -0.00268$ cm^{-1} [156]. Note that since $\Lambda = 0$, no lambda doubling occurs in the *A* state. The electronic energy T_e is ~43966 cm^{-1} [43].

NO is one of the few examples for diatomic molecules that show a decrease in bond length upon excitation, in this case from 116 pm in the *X* state to 106 pm in the *A* state [43] (cf. Fig. 21). For NO *X*, $\omega_e = 1904$ cm^{-1} and $\omega_e x_e = 13.97$ cm^{-1}. For NO *A*, $\omega_e = 2371$ cm^{-1} and $\omega_e x_e = 14.48$ cm^{-1}. The larger vibrational energy in the excited state reflects the stronger bonding.

Once excited into the A($v' = 0$) band, NO molecules can relax to all vibrational bands in the ground state according to the transition probabilities given by the Franck-Condon factors. These probabilities originate from the overlap integrals of the respective vibrational bands in the A and X states and are shown in Fig. 22. Note that ~50% of the total

fluorescence can be detected using the two NO *A*–*X*(0,1) and (0,2) bands only, that emit in a small wavelength range from 230 – 250 nm (cf. section 4.1.4).

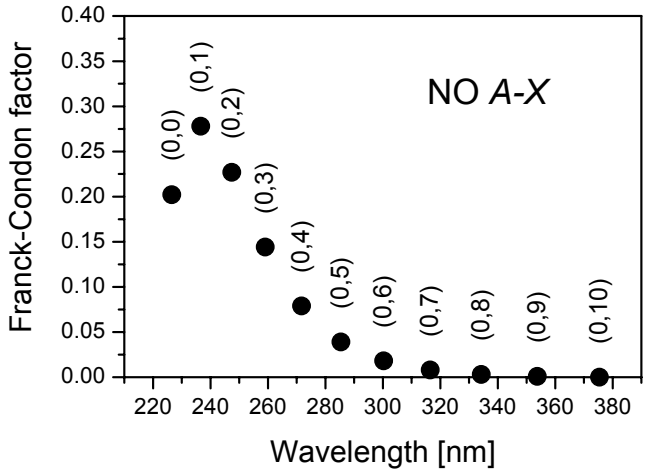

Fig. 22: Franck-Condon factors of the NO A–X *(0,v") system. From Piper and Cowles [157].*

LIFSim: numerical simulation of NO LIF

In order to simulate NO-LIF spectra, a large number of detailed spectroscopic parameters of the NO molecule were implemented in a recently developed software tool called LIFSim [65]. Term energies are needed for the calculation of ground state populations and the partition function. Transition energies enable the calculation of line positions [156,158]. Transition strengths (Einstein *A* and *B* coefficients) are necessary as well as collisional line broadening and shifting parameters [159,160]. Quenching cross sections for different molecules were included [161,162].

The simple non-transient three-level LIF model shown in Fig. 9 (cf. section 3.1) is used for the calculation of LIF signals. Although some assumptions are made, experimental LIF measurements are well described with this model, and the simplicity enables rapid calculation of LIF signals. This is important for multi-parameter non-linear fitting procedures where a large number of calculations must be performed. In particular, the features of the model are:

- Equilibrium population of laser-coupled ground state (i.e. rapid ground state RET) is assumed.
- Single laser-coupled upper state, no excited-state energy transfer processes.
- Fluorescence emission takes place from the single upper state within the allowed branches to all possible rotational and vibrational levels of the electronic ground state.
- Quenching is the only non-radiative depopulation mechanism of the excited upper state.

The steady-state rate equation approach in the linear regime yields the following expression for the LIF signal, where A << Q has been assumed (cf. section 3.1) [163]:

$$I_{\mathrm{LIF}}(p,T,\nu_{\mathrm{laser}},x_{\mathrm{gas}}) \sim N_{\mathrm{NO}}\ I_{\nu}^{0} \sum_{i}\left(f_{\mathrm{B},i}(T)\ \Gamma_{i}(p,T,\nu_{\mathrm{laser}},x_{\mathrm{gas}})\ B_{i}\ \sum_{j}\left(A_{ij}/(Q(p,T,x_{\mathrm{gas}}))\right)\right) \quad (75)$$

The summation i is over all simultaneously excited absorption lines, the summation j over all allowed emission transitions. The LIF signal is a function of pressure p [bar], temperature T [K], laser wavenumber ν_{laser} [cm^{-1}], and gas phase composition x_{gas}. The dimensionless overlap fraction Γ and the normalized irradiance I_{ν}^{0} are calculated following the definition of Partrige and Laurendeau [164]. Both absorption line and laser spectral distribution are represented as Voigt profiles. The laser line width is adjustable, while the absorption line width is calculated from the contributions of Doppler, collisional, and predissociative broadening.

LIFSim allows the calculation of LIF intensities, LIF excitation spectra, LIF emission spectra, and tables of temperature and pressure dependences of LIF signals. It also allows the fit of simulated LIF excitation spectra to experimental data in order to evaluate experimental temperatures and laser line widths.

4.1.2 Experimental setup and temperature evaluation procedure

In order to achieve a selective excitation of specific molecules in an inhomogeneous medium, a narrowband, tunable light source is desirable. Further more, the detected LIF signal has to be discriminated against room light and flame luminosity. These requirements are satisfied by pulsed, tunable, narrowband laser systems in combination with spectrally filtered, gated, and intensified CCD cameras. These systems allow imaging measurements with high spatial (~ 10^{-3} mm^3), spectral (< 0.5 cm^{-1}), and temporal (< 20 ns) resolution.

The general setup of the multi-line NO-LIF thermometry is shown in Fig. 23. A tunable, narrowband KrF excimer laser (Lambda Physik EMG 150 TMSC) emits laser radiation with a pulse energy of 200 mJ/pulse, a spectral fwhm of $\Delta\nu$ ~ 0.5 cm^{-1}, and a pulse length of 20 ns at 248 nm (cf. section 2.2.1). This laser light is frequency-shifted in a Raman cell (Lambda Physik) of 1 m length and 30 mm inner diameter equipped with two spherical lenses f = 700 and 300 mm filled with 5 – 10 bar hydrogen [38]. The frequency shift of 4155.2 cm^{-1} (cf. Table 4) is due to stimulated Raman scattering (cf. section 2.2.1). The different wavelengths are dispersed by a Pellin-Broca prism and the 1st anti-Stokes beam at 225 nm is selected by an aperture. Typically, pulse energies of 3 mJ at 225 nm are reached. Complete separation from the fundamental wavelength is realized by implementing a short pass filter (235 nm).

Then, the laser beam is focused with a cylindrical $f = 1000$ mm lens to a light sheet of typically 50×0.5 mm² to illuminate a plane in the region of interest. Here, NO molecules are excited in the NO A–X(0,0) band. Finally, the LIF signal is recorded with a spectrally-filtered intensified CCD camera. Different scan-ranges were used that have been optimized with regard to every application. An overview is given in section 4.1.3. Further, different ICCD cameras were used and various detection filter strategies were applied (cf. section 4.1.4).

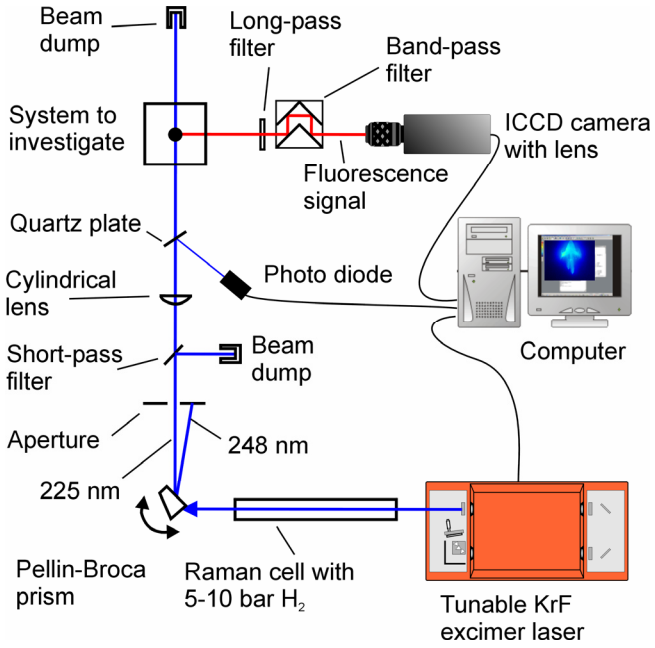

Fig. 23: Experimental setup of the multi-line NO-LIF thermometry.

In contrast to previous research, it was found that there is no need to implement a beam polarizer between the excimer laser and the Raman shifter [24]. It was previously used to reach a better polarization of the excimer laser light (~99:1 instead of ~60:40, laser manual). Now, without the beam polarizer, twice the laser energy (3 mJ) is available at 225 nm, without any measurable contribution of 248 nm laser light.

All LIF measurements presented in this thesis use the strategy of laser excitation at 225 nm in the NO A–X(0,0) band with red-shifted detection. In the presence of scattering particles such as droplets, soot, and nano particles, it is very important to completely eliminate any 248 nm laser light traveling within the 225 nm beam, since the applied detection filters were optimized to detect the most intense NO fluorescence of the NO A–X(0,1) and (0,2) bands at 235 and 246 nm, respectively (cf. Fig. 22 and Fig. 31). Scattering at 248 nm therefore significantly decreases the signal-to-noise ratio of the fluorescence signal.

Data acquisition and temperature evaluation

The laser is tuned over a part of the absorption spectrum of the NO molecule while individual fluorescence images are taken with an intensified CCD camera for each excitation wavelength. From the resulting stack of images (each with the laser tuned to the next wavelength) LIF excitation spectra are extracted for every single pixel. Numerical calculations of NO excitation spectra are fitted to experimental data via a non-linear least-square fitting routine (Levenberg-Marquardt algorithm [165]). The fitting procedure includes two steps in order to reduce the number of free fitting parameters. A schematic of the entire procedure is shown in Fig. 24. Sequence 1 (upper row) shows the initial fit to extract laser line shape and line positions. Sequence 2 (lower row) then shows the pixel-by-pixel fit with a reduced number of fitting parameters. NO-LIF excitation spectra are simulated and fitted using the software LIFSim [65].

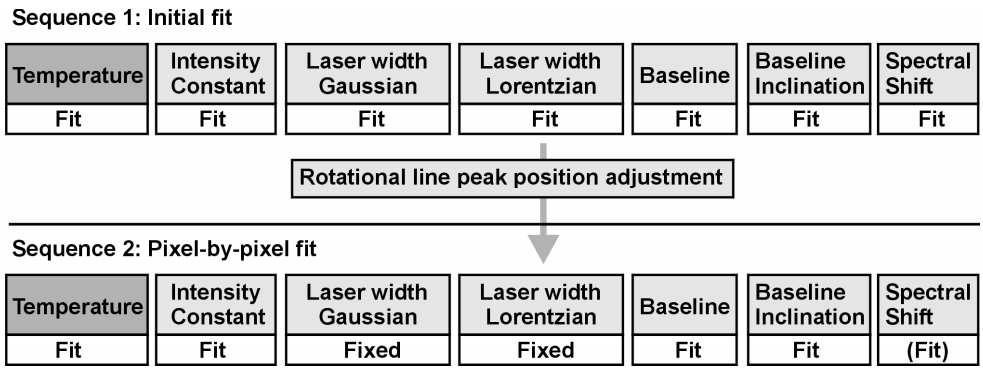

Fig. 24: Schematic of the multi-line fit procedure. Sequence 1 (upper row) fits all parameters to determine laser line shape and line positions. Sequence 2 (lower row) extracts temperature with a reduced number of fitting parameters.

In the first step, the laser line shape (combination of Gaussian and Lorentzian terms) and the exact position of the excitation lines are determined by evaluating a homogeneous area in the LIF images with good signal-to-noise ratio. The final pixel-by-pixel fit includes temperature (our target parameter), NO-LIF signal strength (intensity constant) and baseline signal (defined here as all signal in addition to NO-LIF).

For a precise evaluation, the gas composition must be known in order to calculate the collision-induced shift of excitation spectra. If the gas composition is constant in the entire image, the spectral shift can be calculated. If the gas composition varies within the image, the spectral shift parameter must be fitted, which is the case in most practical applications. This procedure may double the time effort for the fit. However, if the spectral shift is not fitted but calculated incorrectly, the spectra cannot be fitted correctly and the fit ends in a local minimum. Hence, the fitted temperatures are not reliable.

4.1.3 Optimizing temperature sensitivity: Selection of excitation strategies

The precision of any thermometry technique depends on the sensitivity of the involved LIF signal strength(s) on temperature. In a two-line technique, high sensitivity of the fluorescence ratio R_{12} on temperature is desired, i.e. a large change in R_{12} with temperature. Mathematically, this can be expressed as the second derivative being zero:

$$\frac{d^2 R_{12}}{dT^2} = 0 \quad \Leftrightarrow \quad T = \frac{\Delta\varepsilon_{12}}{2k} \tag{76}$$

Depending on the temperature range that should be investigated in the two-line technique, this equation gives the condition for ground state energy differences that yield highest temperature sensitivity. For much higher or lower temperatures, the sensitivity may decrease severely. A two-line technique is therefore most sensitive within a certain temperature range only. Table 5 compares the sensitivities of different NO two-line thermometry methods used in flames.

Reference	Excited NO lines	Maximum temperature sensitivity $\Delta\varepsilon_{12}/2k$
Tamura *et al.* [89]	A–X(0,0) O_{12}(1.5) and A–X(0,0) O_{12}(19.5)	498 K
Tsujishita *et al.* [77]	A–X(0,0) Q_2(17.5) and A–X(0,0) Q_2(27.5)	566 K
Bessler *et al.* [40]	A–X(0,0) Q_1+P_{21}(33.5) and A–X(0,2) O_{12}(5.5)	1420 K
Bell *et al.* [93]	A–X(0,0) R_1+Q_{21}(21.5) and A–X(0,2) O_{12}(8.5–10.5) bandhead	2300 K

Table 5: Comparison of the temperature sensitivities of different NO two-line LIF thermometry methods in flames [21].

Sensitivity of the multi-line NO-LIF thermometry

In the multi-line approach, the choice of optimal scan ranges is an important issue since the applicable temperature range and temperature precision is influenced by these factors. For a high temperature precision the shape of the observed spectra should exhibit a strong temperature-dependence. This is achieved by selecting a part of the excitation spectrum where the present peaks assess transitions with a large variation in ground state energies in reference to eq. 76. However, in NO excitation spectra, peaks usually overlap and cannot be treated as individual transitions.

Therefore, in order to optimize temperature sensitivity for the scanned multi-line approach, a statistical analysis based on multi-line fitting of simulated spectra with synthetic noise based on LIFSim [65] was adapted as described in [24]. Excitation spectra are simulated at a given temperature, noise is added to the spectra, and finally the fit routine determines the fitted temperature. The synthetic noise characteristics are chosen to reflect the noise of the detection system. The procedure is repeated 200 times

and the standard deviation of the 200 fitted temperatures becomes a measure for the precision of the fitting technique.

For a variety of start wavelengths (spectral resolution: 1 cm^{-1}) and scan ranges (5, 10, 20, and 40 cm^{-1}), the condition which provides minimal standard deviation is then identified as being the optimal scan range. Simulations were performed at atmospheric pressure for 300 K in order to optimize e.g. spray evaporation measurements at room temperature and at 2000 K to achieve optimum flame temperature measurements. Excitation spectra were simulated with a spectral resolution of 0.1 cm^{-1} in order to clearly resolve the spectral features.

The results of the sensitivity analysis (Fig. 25) indicate that a minimum in standard deviation of temperature within the tuning range of the Raman-shifted excimer-laser system exists in spectral ranges from 44412 – 44422 cm^{-1} at 300 K and 44407 – 44417 cm^{-1} at 2000 K. They are indicated (*) in row c) and d) of Fig. 25. The temperature sensitivity of these ranges is actually almost the global optimum within the entire NO *A*-*X*(0,0) band for the investigated conditions. This can be seen from row b) of Fig. 25.

This analysis is helpful to determine the spectral region with highest temperature sensitivity. However, practical considerations must be taken into account. The scan ranges described above are very short and begin and end on top of peaks. In theory, the peaks are symmetric and no information is lost by measuring only half of them. However, for a precise temperature evaluation, the baseline as well as the baseline inclination of the spectra must be known precisely. For this reason, the scan ranges must be extended above the wings of all peaks.

The optimized range for flame imaging is the combination of both intervals found in the sensitivity analysis and reaches from 44406 – 44425 cm^{-1} (225.19 – 225.10 nm). It yields excellent temperature sensitivity from 250 K to 2500 K. For room temperature measurements the scan range was further extended to 44405 – 44435 cm^{-1} (225.20 – 225.05 nm) in order to extract reliable baseline information. With this strategy, temperature measurements are possible with an accuracy of ±1 K at room temperature. For high-pressure measurements, the scan range should be further extended to 44398 – 44433 cm^{-1} (225.24 – 225.06 nm) since collisional broadening blurs the shape of the spectra and thus more information is needed. An overview of the applied scan ranges as well as their applicable temperature and pressure range is given in Table 6. Excitation spectra of the corresponding scan ranges are shown in Fig. 26.

In scan range C (44406 – 44425 cm^{-1}) transitions originating from ground state rotational quantum numbers J''= 17.5 to J''= 46.5 in the NO *A*–*X*(0,0) band are found. This large variation in ground state energy in a small spectral range is the reason for the high temperature sensitivity over a wide temperature range from 250 – 2500 K. The 12 transitions are blend into five distinct features numbered 1 – 5 in Fig. 26. Details about the transitions are summarized in Table 7.

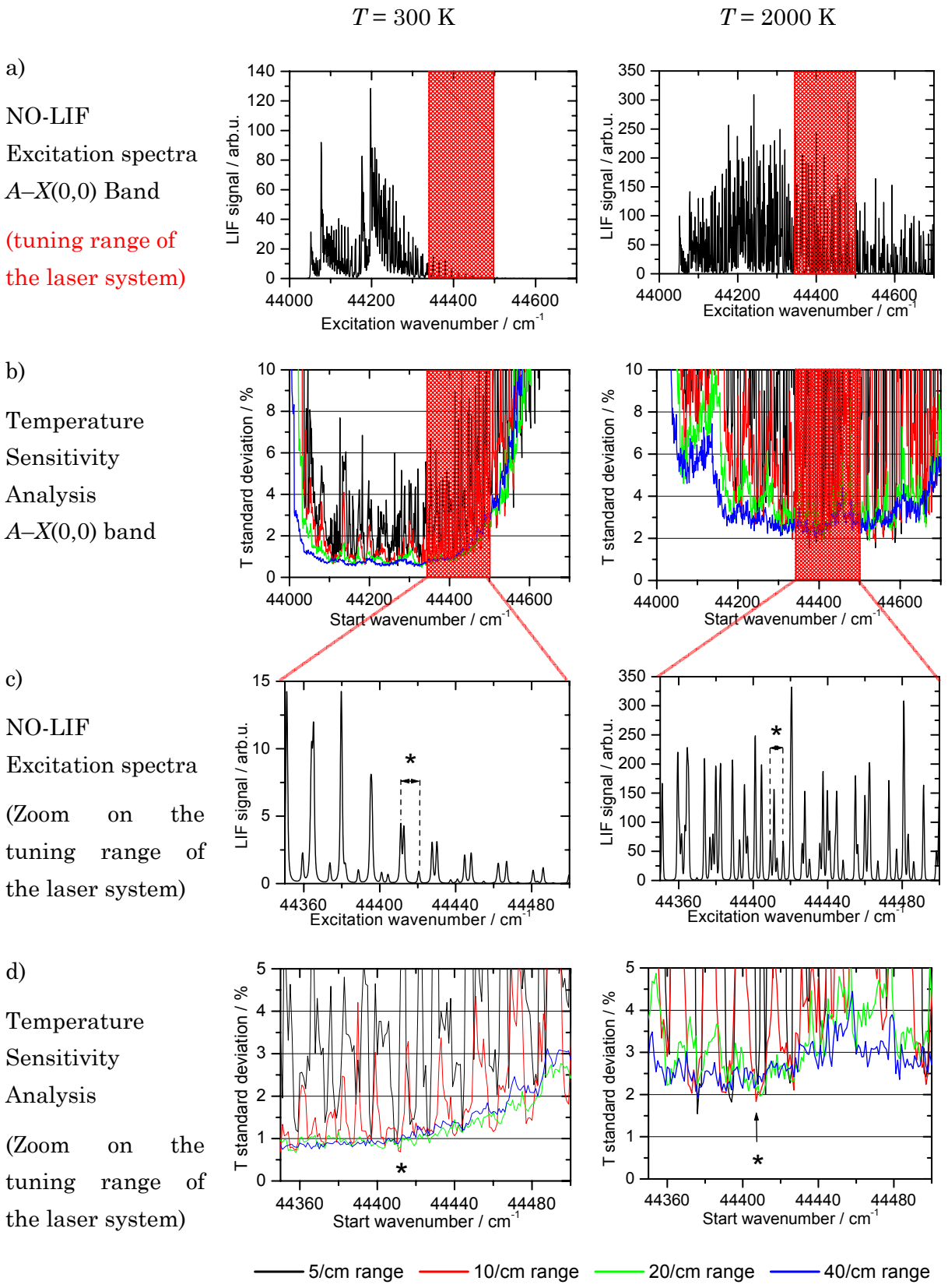

Fig. 25: Results of the sensitivity analysis of the multi-line thermometry at atmospheric pressure. The entire A–X(0,0) band was investigated at 300 K (left) and 2000 K (right) for spectral scan ranges of 5, 10, 20, and 40 cm⁻¹. NO-LIF excitation spectra are presented in row a) and c) and the corresponding sensitivity analysis is shown in row b) and d). Optimum ranges are marked (*) in row c) and d).

Nr	Scan range / cm^{-1}	Scan range / nm	Optimized temperature range / K	Tested pressure range / kPa	Used in section
A	44405 – 44435	225.19 – 225.04	250 – 350	100	5.2
B	44398 – 44433	225.24 – 225.06	250 – 2500	100 – 500	5.3.1
C	44406 – 44425	225.19 – 225.10	250 – 2500	3 – 100	5.4; 5.5
D	44407 – 44417	225.19 – 225.13	1000 – 2500	100	5.1; 5.3.2
E	44350 – 44500	225.48 – 224.72	100 – 3000	3 – 500	

Table 6: Overview of excitation-spectra scan ranges used in this thesis.

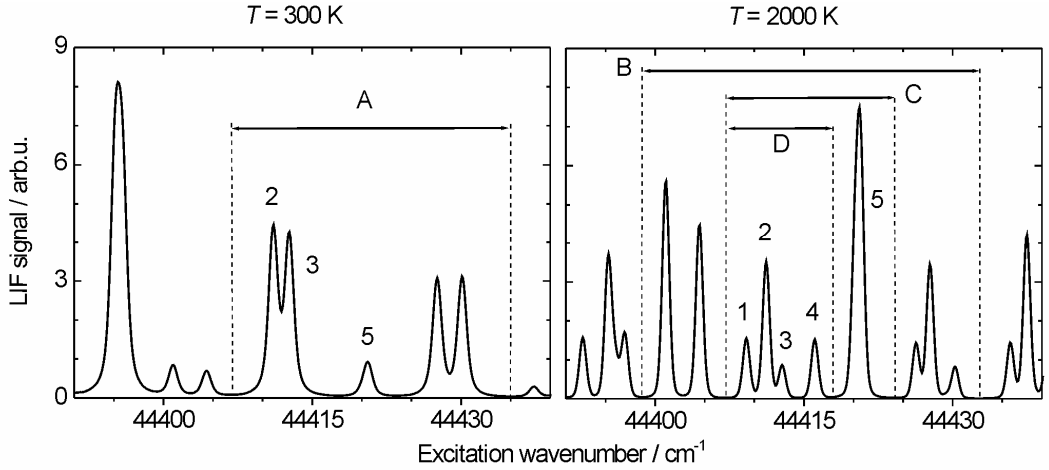

Fig. 26: Simulated NO-LIF excitation spectra at 300 K (left) and 2000 K (right) showing the scan ranges used in this thesis, named A,B,C, and D after Table 6. The transitions corresponding to the peaks named 1-5 (contained in scan range C) are explained in detail in Table 7.

Fig. 26	NO *A*–*X*(0,0) transition	Center wavenumb. / cm^{-1}	Ground state energy ε/k / K
1	$O_{12}(46.5)$	44409.0	5579
	$P_1(36.5)$	44409.3	3285
2	$R_1+Q_{21}(22.5)$	44411.2	1269
3	$S_{21}(17.5)$	44412.9	777
4	$P_2+Q_{12}(38.5)$	44416.1	3905
5	$R_{12}+Q_2(31.5)$	44420.1	2690
	$Q_1+P_{21}(29.5)$	44420.8	2160
	$R_2(25.5)$	44420.9	1836

Table 7: Relevant transitions within scan range C (44406 – 44425 cm^{-1}) are given with their rotational branch, rotational quantum number, ground state energy, and are sorted by their center wavenumber.

The temperature dependence of the LIF signals for the five peaks present in scan range C is shown in Fig. 27 for constant NO mole fraction and atmospheric pressure in air, conditions that are often found for flames seeded with NO. The LIF signal temperature dependencies reflect the Boltzmann populations of the respective rotational ground states of the transitions. High J'' peaks show their maximum LIF signal at a higher temperature, whereas low J'' peaks are already strong below 1000 K. The absolute intensities depend on the Einstein A and B coefficients of the transitions.

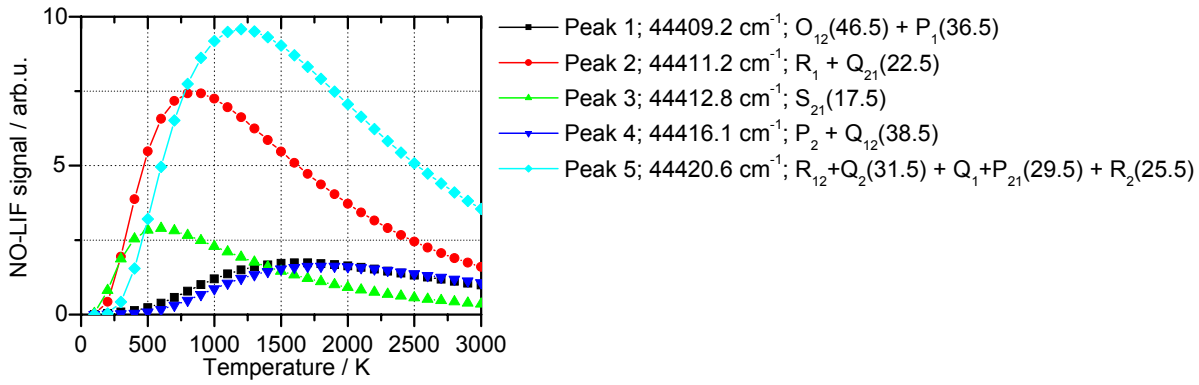

Fig. 27: Temperature dependence of the NO-LIF intensity for the peaks within scan range C (44406 – 44425 cm⁻¹) for atmospheric pressure and constant NO mole fraction in air. Relevant transitions are given with their rotational branch, rotational quantum number, ground state energy, and are sorted by their center wavenumber.

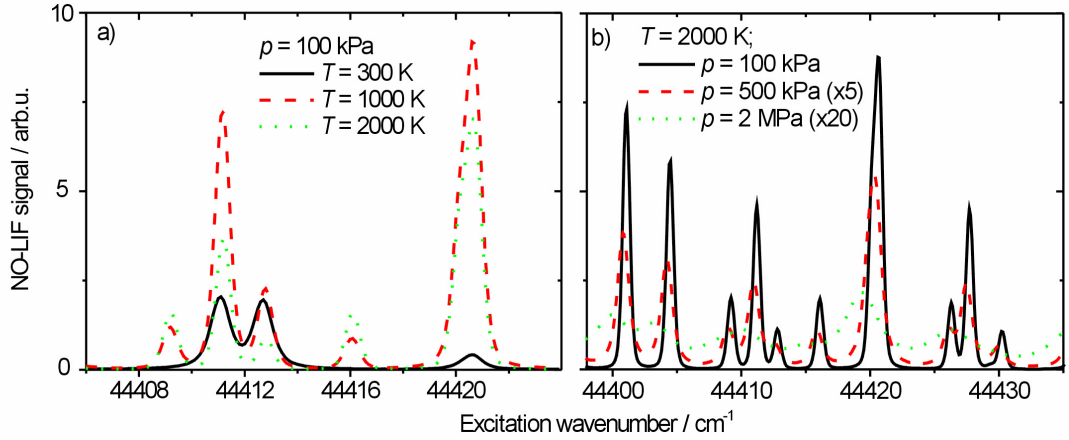

Fig. 28: a) Simulated NO-LIF excitation spectra showing the temperature dependence of scan range C; b) Effect of pressure on scan range B. Note the different scaling for elevated pressures.

At room temperature, sufficient LIF signal can only be detected for transitions coupled to rotational ground states with $J''< 25.5$, which is emphasized by Fig. 28 a). The shape of the excitation spectra of scan range C changes strongly with temperature, which is necessary for good temperature sensitivity. All calculations are based on LIFSim [65]. The pressure dependence of LIF excitation spectra is shown exemplary in Fig. 28 b) for the scan range B used for high pressure flame measurements. The LIF signal intensity decreases by two orders of magnitude when increasing the pressure from atmospheric to 2 MPa. This effect is due to both, stronger quenching and line broadening at higher pressure. Also, the line positions are displaced by line shifting (cf. section 2.3.3).

In previous research [24] and for some measurements presented in this thesis (sections 5.1 and 5.3.2), the smaller scan range D (44407 – 44417 cm⁻¹) was used. This range yields excellent temperature sensitivity and reliable results above 1000 K, which was the

primary goal of these measurements. However, range D shows poor sensitivity at room temperature since it is reduced to a two-line thermometry. Additionally, in the temperature range from 400 – 1000 K, the fit of this spectral range expresses some instabilities because the two peaks (Numbers 1 and 4 in Fig. 26 and Table 7) coupled to high rotational ground states begin to appear in the spectra but are rather recognized as noise than as peaks. Therefore, the spectra are misinterpreted and the fitted temperature can be several hundred Kelvin too low (Fig. 29 b). In order to precisely measure temperatures in the entire range from 250 K to 2500 K scan range C (44406 – 44425 cm^{-1}; 225.19 – 225.10 nm) should be used (Fig. 29 a).

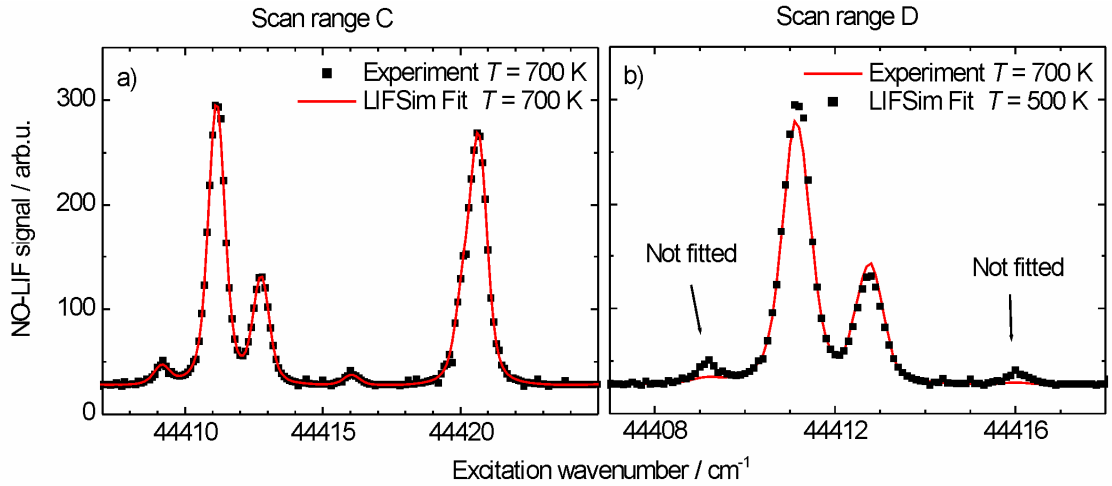

Fig. 29: a) Scan range C can be fitted well at 700 K; b) Scan range D for the same experimental conditions. Range D cannot be fitted correctly.

The signal-to-noise ratio of the experimental excitation spectra is usually increased by averaging the LIF signal. In spray flame imaging presented in section 5.1, a total of 500 laser shots (50 LIF images between 44407 and 44417 cm^{-1} with a spectral resolution of 0.2 cm^{-1}, each averaged over 10 single shots) were used to get a temperature precision of ±4 %. With a total of 5000 laser shots (50 images each averaged over 100 laser shots) the temperature precision is ±2 % in the flame under same conditions. At a repetition rate of 25 Hz, it takes about one and five minutes for 500 and 5000 laser shots, respectively, to acquire the data [95].

Accuracy of the multi-line NO-LIF thermometry

The accuracy of the multi-line NO-LIF technique was proven by comparisons with thermocouple readings in a heated nitrogen flow (Fig. 30). The accuracy was better than ±1% (±1 K on the averaged values) for measurements in a 2 × 2 × 2 mm^3 volume. For flame temperatures at ~2000 K, CARS was used to validate the temperature results in stabilized Bunsen flames [24]. Good agreement was found within ±2 %. Note that no

calibration is necessary with this technique. However, in order to prove the accuracy in the temperature range between 500 and 1500 K, a systematic investigation in a heated flow cell is necessary in order to validate the spectroscopic database and all assumptions made in the LIF model.

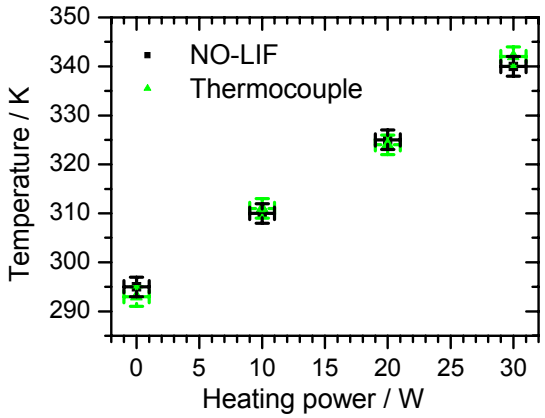

Fig. 30: Validation of the accuracy of the multi-line NO-LIF thermometry technique by comparison to conventional thermocouple measurements at different heating powers for a heated nitrogen flow seeded with NO [95].

4.1.4 Optimizing fluorescence detection in harsh environments

Because LIF signals are often weak, a sensitive detector is required like an intensified camera, yielding sensitivities down to single photons. The detector must also be capable of short detection gating (~100 ns) to discriminate the pulsed laser-induced signal against continuous background light. For all LIF measurements described in this work, we used intensified charge-coupled device (CCD) cameras by LaVision. Technical details on the camera systems are given in Table 8.

Model	**Resolution** [pixel]	**Image intensifier gate**	**Phosphor decay time**	**Frame rate as used**	**Used in section**
Flowmaster with intensifier	1280 × 1024	10 ns – 1 ms	~100 µs	~25 Hz	5.1, 5.2, 5.3
Image Intense with intensifier	1374 × 1038	5 ns – 1 ms	~1 ms	~8 Hz	5.4, 5.5

Table 8: LaVision ICCD camera systems used in this work.

The newer Image Intense model has about an order of magnitude higher intensification due to a more efficient phosphor in the intensifier and a more sensitive CCD chip. The Flowmaster model could be operated at a higher frame rate. The image intensifier gate was adjusted for each measurement. At atmospheric pressure and in air, NO fluorescence can only be detected up to 10 ns after the laser pulse has finished. In

contrast, at low pressure or in pure nitrogen, fluorescence quenching is low and the gate was extended to 200 ns to collect the entire LIF signal.

An important part of the setup is the filter system used for selection of the desired detection wavelengths. All LIF measurements presented in this thesis use the strategy of laser excitation at 225 nm in the NO *A*–*X*(0,0) band with red-shifted detection. On the one hand, filters are necessary to reject the elastic scattering of the laser light at 225 nm. This is important in particle laden systems like in e.g. sprays, sooting flames, or close to walls, where the stray light is several orders of magnitude more intense than the LIF signal, which is the case in all applications presented in this thesis.

On the other hand, fluorescence from other species that are simultaneously excited has to be suppressed, such as e.g. acetone [95], oxygen [30], polycyclic aromatic hydrocarbons (PAH, section 5.3), or metal atoms and particles (section 5.5). Fortunately, most of these species fluoresce at other wavelengths than NO does. This enables selective detection of NO LIF.

In this work, long-pass and band-pass detection filters were used. They are usually characterized by a specific wavelength. Long-pass filters transmit wavelengths longer than the given one; band-pass filters transmit only within a certain wavelength range, characterized by the band-pass width around the center wavelength. There are two general types of filters: Absorption filters (the wavelengths not transmitted are absorbed in the filter material, e.g. Schott color glass filters) and reflection filters (typically dielectrically coated substrates, the wavelengths not transmitted are reflected).

In the latter type, the reflected instead of the transmitted light may also be used. If the optimum reflection angle is 45°, then a combination of 4 such filters yields an overall filter combination where the single reflection curve is multiplied four times by itself. Such an arrangement is shown in Fig. 23. This is an efficient way to achieve a steep gradient in a band-pass like transmission curve in the UV. Transmission characteristics for all filters used in this work are summarized in Table 9 and illustrated in Fig. 31.

Nr.	Filter specifications	Filter type	Company	T @ 225 nm / %	T @ 235-246 nm / %	Used in section
I	Band-pass 245 nm	Reflection	Laser Optik	0.5	50	5.1; 5.2; 5.3; 5.4
II	Long-pass 230 nm	Reflection	LayerTec	0.5	95	5.5
III	Color glass, 3 mm	Absorption	Schott UG 5	1.5	33	5.1; 5.3.2; 5.4
IV	Color glass, 5 mm	Absorption	Schott UG 5	0.1	18	5.2; 5.3.1

Table 9: Detection filters used in this work with transmission T (cf. Fig. 31).

In Fig. 31, NO LIF in the A–X(0,*v*") band is shown spectrally resolved as expected from the Franck-Condon factors (cf. Fig. 22). The band-pass filter (I, Laser Optik, 50% transmission at 235 – 250 nm) consists of four mirrors coated to reflect around 245 nm in

45° angle (Fig. 23). This setup enables selective NO-LIF detection of the most intense NO *A*–*X*(0,1) and (0,2) bands at 235 and 246 nm, respectively, while suppressing fluorescence from other species above 260 nm. Also, the laser light at 225 nm is suppressed by 2.5 orders of magnitude.

In order to reject the laser wavelength, a dielectrically coated long-pass filter (II, LayerTec) is used that transmits only 0.5% at 225 nm while featuring 95% transmission above 235 nm. The transmission curve for this filter shown in Fig. 31 is valid for an angle of ~15°. When the angle is increased, the transmission at 225 nm increases. With smaller tilt, the transmission curve moves to the right by roughly 0.3 nm per degree. At 0°, the NO fluorescence at 235 nm is blocked.

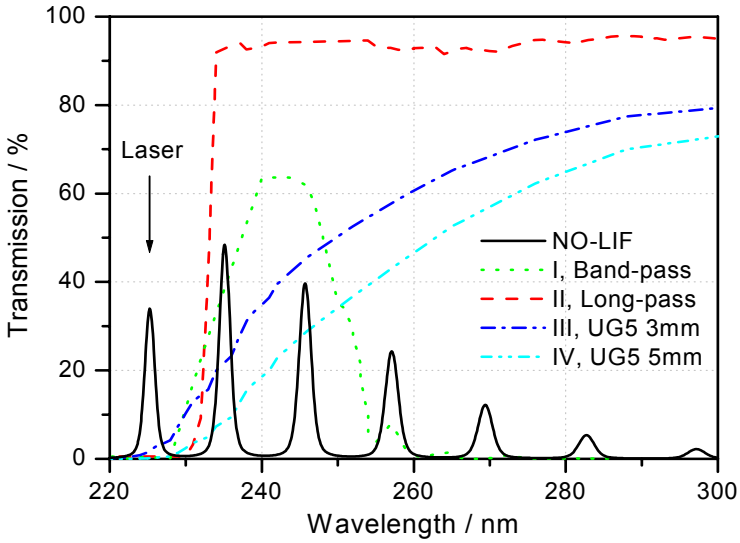

Fig. 31: Transmission curves of the available detection filters and a typical NO-LIF emission spectrum. The laser wavelength is indicated.

UG 5 filters (III and IV, Schott) act as long-pass filters in this wavelength region and can be applied to reject elastic scattering at 225 nm with detection of the red-shifted NO fluorescence. However, their gradient in the transmission curves (Fig. 31) is very flat. The discrimination of 225 nm versus fluorescence at 235 – 246 nm is acceptable with about 1:180 for the 5 mm filter, but the total LIF transmission is only 18 %. This must be compensated by a higher intensification of the camera which induces noise. Note that UG 5 filters also absorb the visible electromagnetic spectrum (400 – 700 nm).

It should be noted that the camera system itself acts as a broad band-pass filter; sensitivities of the ICCD cameras used in this work are highest in the 250 – 400 nm range. Similarly, other optical elements like the camera lens or burner housing windows have specific transmission properties. Regular (window, BK7) glass does not transmit in the UV. Fused silica (quartz) transmits ≥ 90% down to 200 nm and is used in all experiments presented here.

Often, a combination of several filters is used. Filter I and IV are used in series in section 5.2 and 5.3.1. to suppress the laser scattering by 5.5 orders of magnitude while maintaining 10% of the total NO fluorescence at 235 – 246 nm. A combination of three long-pass filters (II, LayerTec) is used in section 5.5. Here, the 225 nm laser light is suppressed by 7 orders of magnitude while still transmitting 85% of the NO-LIF signal above 235 nm. An overview of all applied excitation strategies and filter combinations is given at the beginning of section 5.

4.1.5 Accuracy in turbulent systems

In this section, an investigation of the systematic deviations of the measured NO-LIF temperature from the arithmetically averaged (Favre-averaged) temperature in turbulent systems is presented. The scanned multi-line approach yields accurate temperature results in steady systems but has some drawbacks in turbulent systems due to the necessity of LIF signal averaging over time before evaluating the temperature. In turbulent systems, the real temperature fluctuates at one point in space, and the LIF signal is averaged over time for different temperature values. This results in a systematic error to the measured temperature because the LIF signal does not change linearly with temperature. Spatially averaging the LIF signal over temperature-inhomogeneous regions, e.g. steep gradients or a flame front, leads to the same issue.

Simulations based on LIFSim were performed to quantify the systematic error on the temperature evaluation of averaged excitation spectra. Therefore, excitation spectra were computed around an assumed mean temperature of e.g. 1100 K. In a worst case scenario at a turbulent flame edge, the temperature can vary from e.g. ~300 K up to ~1900 K. This corresponds to fluctuations of 1100 K ±770 K (±70%), from room air to flame temperatures. Excitation spectra of the optimum scan range C described in section 4.1.3 were calculated for 15 equidistant temperatures at 330 K, 440 K, 550 K, ….1870 K for constant NO volume fraction. The large non-linear variation in the shape of these spectra with temperature is obvious in Fig. 32 a). For clarity, only 7 of the 15 spectra used for averaging are shown.

The 15 spectra were averaged with even weight and the averaged spectrum was fitted to obtain the resulting “experimental” mean temperature. Fig. 32 b) shows the deviation between the real excitation spectrum for 1100 K and the spectrum obtained by averaging the 15 spectra for 1100 K ±770 K. The averaged spectrum can not be fitted precisely and the best fit yields 1017 K, which is a deviation of –83 K from the calculated average temperature. This means that the multi-line NO-LIF thermometry systematically under-predicts the real Favre-averaged temperature by 7.5% in this case.

This procedure is repeated for different mean temperatures from 300 to 2500 K in steps of 200 K for different fluctuations of ±5%, ±20%, ±50%, and ±70% around every

mean temperature (e.g. 1000 K ±50K, ±200K, ±500K, ±700K). The results are presented in Fig. 33. The graph shows the arithmetic mean temperature on the *x*-axis and the deviation of the "measured" fluctuating temperature on the *y*-axis on a relative [%] deviation scale.

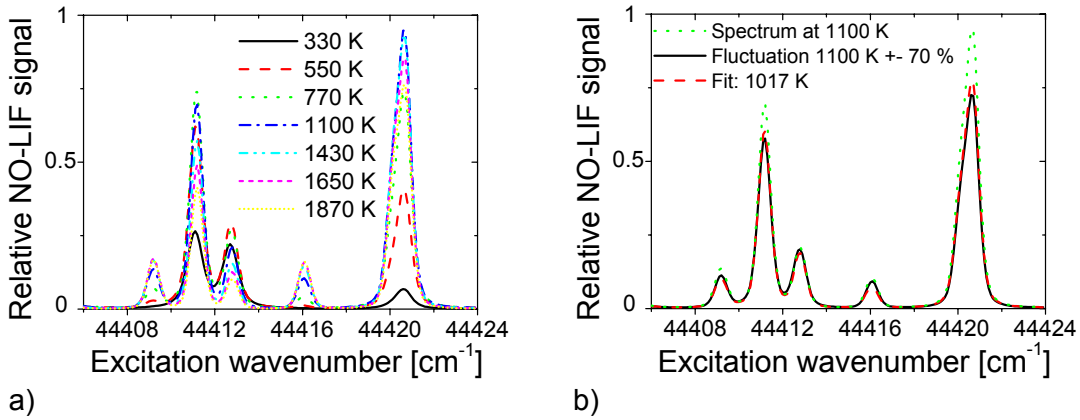

Fig. 32: a) Simulated fluctuations of NO-LIF excitation spectra around 1100 K ±70%; b) Real spectrum at 1100 K (dotted line) and the comparison with the averaged spectrum (solid line). The dashed line shows the fit.

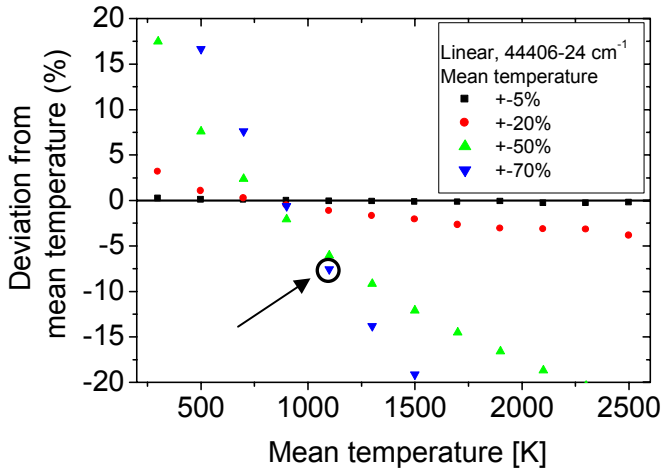

Fig. 33: Deviations of the accuracy of the multi-line NO-LIF thermometry in turbulent systems. The case investigated in Fig. 32 is indicated.

It is found that deviations are positive at temperatures below 900 K and negative at higher temperatures. Hence, measurements systematically over-predict mean temperatures below 900 K and under-predict them above this value. The systematic error of symmetric fluctuations around 900 K is negligible even for strong fluctuations of 900 ±630 K (±70%). Generally, larger deviations are observed for stronger fluctuations. Temperature fluctuations of less then ±5% result in a negligible error in temperature deviation of less then ±0.5%. However, for larger fluctuations, systematic deviations up to 20% can occur for e.g. systems varying ±1000 K around 1500 K.

Different spectral excitation ranges were investigated in order to find a spectral region that is insensitive to fluctuations. Besides scan range C (Table 6, 44406 – 24 cm^{-1}), range D (44406 – 18 cm^{-1}) was investigated since it was used to measure temperature in turbulent spray flames presented in section 5.1 [24,95]. Also, a larger scan range covering almost the entire tuning range of the Raman-shifted excimer laser system (44356 – 453 cm^{-1}), was tested and the results are presented in Fig. 34.

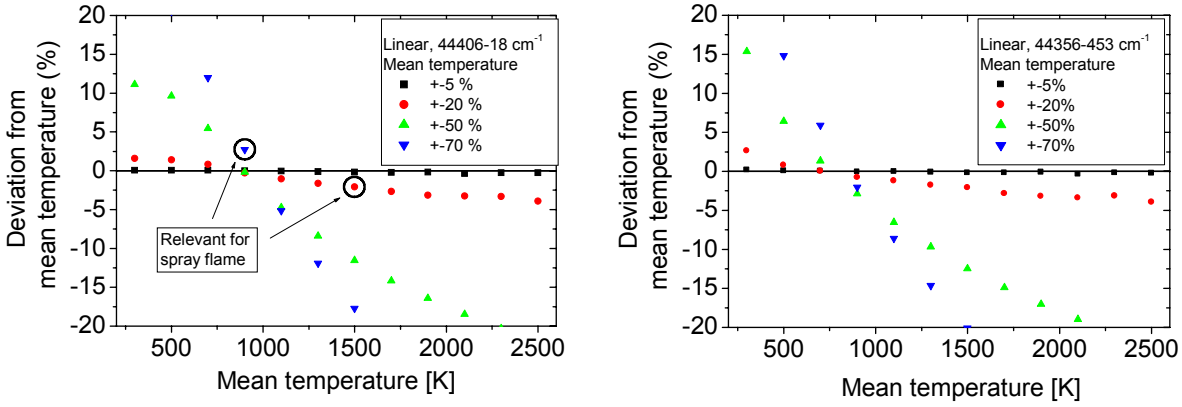

Fig. 34: Results for scan range D (left) and a much larger range (right). The results relevant for spray flame temperature imaging are marked in the left panel.

Surprisingly, all spectral ranges behave in a very similar way. For fluctuations around a mean temperature of 300 K, positive deviations can be seen. The smallest spectral range (Fig. 34, left panel) shows the smallest error at fluctuations around 300 K. No significant difference can be seen in the behavior of the largest scan range, although it covers up to 34 peaks. For fluctuations of ±20%, ±50%, and ±70%, the maximum deviation in the measured temperature is smaller than ±3%, ±15%, ±25%, respectively.

This investigation is important for practical temperature measurements in turbulent flames that are presented in section 5.1. In regions with moderate temperature fluctuations (e.g. in the inner flame zone: 1200 – 1800 K), the measured temperature deviates by –31 K (–2%) from the arithmetic average of 1500 K. For strongly fluctuating regions (e.g. near the flame edge, 300 – 1500 K), the simulation predicts a measured value of 925 K instead of the arithmetic average of 900 K, which is a deviation of +3%. These respective results are marked in Fig. 34.

This investigation is also relevant for section 5.2, where gas-temperature is measured in a turbulent, evaporating ethanol spray. However, within the temperature range (278 – 298 K), the systematic deviation of the measurements is negligible and significantly less than one Kelvin.

In contrast to the linearly distributed temperature fluctuations presented so far, fluctuations in practical combustion systems can also be bimodally distributed. In turbulent

non-premixed gas turbines, fresh air or a reacting gas can be found intermittently at one point in space. This will result in even larger errors in the NO-LIF thermometry measurements, although the definition of a mean temperature does not make much sense here. Also, Gaussian distributed fluctuations can be found, which results in smaller errors compared to the linear distribution.

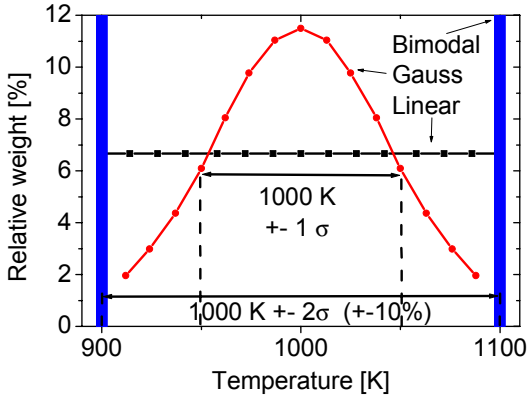

Fig. 35: Simulation of a temperature distribution with 15 equidistant temperature steps. Shown is the relative statistic weight of a Gaussian (circles), a linear (squares) and a bimodal (columns) temperature distribution.

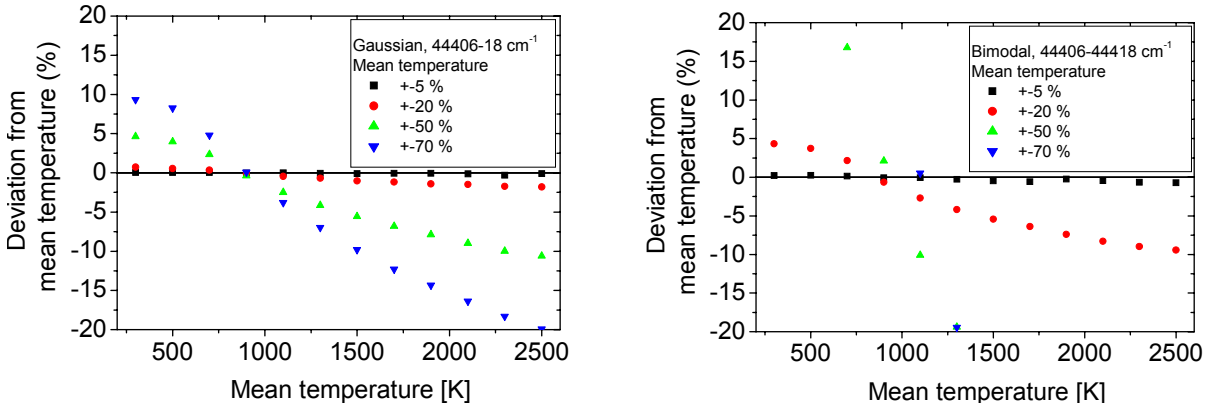

Fig. 36: Results for the Gaussian (left) and bimodal (right) distribution.

Bimodal, Gaussian, and linear distributions are investigated by weighting the excitation spectra as shown in Fig. 35. For bimodal distributions of 1000 K ±10% (±100 K), simply one spectrum at 900 and one at 1100 K are averaged. Gaussian distributions are simulated with 15 equidistant temperature steps that are weighted accordingly. As expected, Gaussian distributed temperature fluctuations result in a lower deviation than linear fluctuations. The bimodal distribution has the worst effect on LIF thermometry. This is shown in Fig. 36.

4.1.6 Effect of saturated LIF on thermometry

With increasing laser intensity a transition from the linear LIF response (as given in eq. 60) towards a saturation regime (eq. 59, with I_{LIF} independent on I_{laser}) is observed. In general, LIF thermometry is also possible in the saturated regime. However, the quantitative evaluation of saturated spectra is significantly more complex than for linear LIF. For NO-LIF thermometry evaluated with the non-transient model LIFSim [65] used in this thesis, special care must be taken to ensure that the excitation energy of the laser is low enough that saturation of the LIF signal does not influence the temperature measurements.

Transient LIF models were developed in order to enable quantitative saturated LIF signal interpretation. These models involve solving the fully time-dependent rate equations [60,166] and take into account the influence of RET, VET, and EET on the LIF process. However, some parameters concerning these processes are just not known yet.

At low pressure, collisional quenching of the excited NO molecules is much reduced compared to atmospheric pressure. Hence, the excited state lifetime is much higher with an increasing probability for stimulated emission and population cycling. Additionally, ground-state RET is slow at lower collision rates. This limits the thermalization of the population of the rotational states [167]. Accordingly, the ground state rotational level can be easily partially depleted by strong pumping. Both processes cause a deviation from linear signal response on laser intensity and therefore distort the relative intensities measured on the different transitions which in turn influences the temperature evaluation.

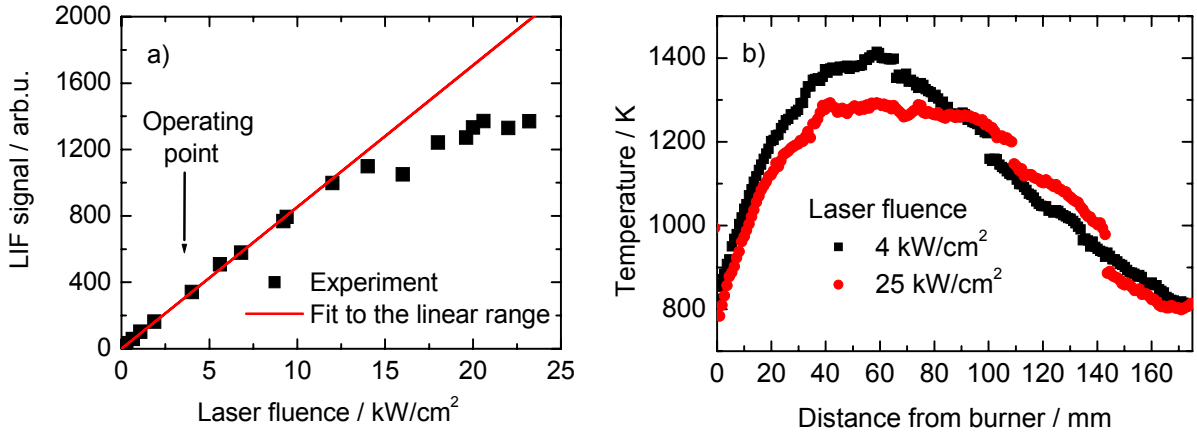

Fig. 37: a) NO-LIF intensity as a function of laser fluence at 44420 cm⁻¹. The arrow marks the laser fluence used for the actual temperature measurements; b) Effect of saturation of the LIF signal on the resulting temperature profile.

The linearity of the LIF signal of all transitions in scan range C (44406 – 24 cm⁻¹, cf. Table 6,) was investigated at a pressure of 3 kPa. From Fig. 37 a) it can be seen that a

50×5 mm² light sheet can easily saturate the NO transition at ~44420 cm^{-1} above a power density of 12 kW/cm². This feature has the largest transition moment within the spectral range investigated. In the temperature measurements presented in section 5.5, the light sheet thickness was therefore extended to 10 mm and spectra were taken at a fluence of 4 kW/cm², which corresponds to a laser power of 0.4 mJ. The LIF signal was evaluated for different NO concentrations to ensure that the camera was working in the linear range.

Fig. 37 b) shows the effect of saturation on the temperature measurements. Without corrections for the saturation effect, the saturated measurements can differ by up to 100 K from the real temperature. These results have been published in [168].

4.1.7 Branching ratios for quenching of NO

When linear NO-LIF signals are too weak for effective detection, increased signal may be produced using higher laser pulse energies, which saturate the excitation transition(s). Interpretation of saturated LIF signals, however, is significantly more complicated than for linear LIF (cf. eq. 60), which is adequately described by the three-level model (Fig. 9) that is the base for simplified models (cf. section 4.1.1) used for NO-LIF thermometry in this thesis [64,65]. At saturating intensities, a substantial fraction of the ground-state population is excited during the laser pulse, and the resulting depletion of the ground-state population has been identified as a potentially serious shortcoming for quantitative measurements [44].

The degree of ground-state population depletion depends on the relative rates of laser pumping and repopulation, which results from RET (cf. section 3.1) within the ground electronic state and (potentially) from quenching of the excited electronic state. VET for the lowest vibrational levels in NO $X\ ^2\Pi$ typically occurs on a time scale that is much longer than the duration of a pulsed nanosecond laser. Therefore, we assume that direct quenching from the laser-excited states to $X\ ^2\Pi(v'' = 0)$ is the only effective quenching pathway that can lead to significant refilling of the pumped levels during the excitation process.

Recently, Daily et al. [167] developed a transient state-resolved model that addresses both ground- and excited-state population kinetics taking the relevant laser–molecule interactions and energy transfer processes into account. Although there have been numerous studies of total quenching rates for many molecules, there is no data available in the literature describing the resulting product distributions for NO after quenching. However, this information is necessary for an accurate interpretation of saturated LIF signals, since the rapid quenching of laser-excited molecules to the ground state and subsequent rapid RET can refill the laser-pumped level during a saturating laser pulse.

In order to obtain insight into the quenching product distributions, pump-probe experiments were setup at the Combustion Research Facility (CRF) at the Sandia National Laboratories, Livermore, USA (T. B. Settersten), designed to measure the fraction of nitric oxide molecules that undergo quenching from $A\ ^2\Sigma^+(v' = 0)$ directly to $X\ ^2\Pi(v'' = 0)$. The detailed experimental setup and data evaluation was published in [169]. An energy level diagram for NO is shown in Fig. 38 (cf. Fig. 21) with the pump, probe, and fluorescence transitions used in these experiments indicated by arrows.

An intense nanosecond laser pulse ("pump"), tuned to the NO $A\ ^2\Sigma^+$–$X\ ^2\Pi(0,0)$ Q_{11} + $^pQ_{21}$ band head at 226.3 nm, depopulated more than 20% of the equilibrium population in the $X\ ^2\Pi(v'' = 0)$ manifold. Pump-induced fluorescence from $A\ ^2\Sigma^+(v' = 0)$ was monitored by detecting the A–$X(0,1)$ band at 236 nm. A weak, time-delayed, pico-second laser pulse ("probe"), tuned to the $A\ ^2\Sigma^+$–$X\ ^2\Pi$ (1,0) Q_{11} + $^pQ_{21}$ band head at 214.9 nm, probed recovery of population in $X(v'' = 0)$ via subsequent LIF in the A–$X(1,0)$ band, which is blue-shifted with respect to the pump-induced fluorescence.

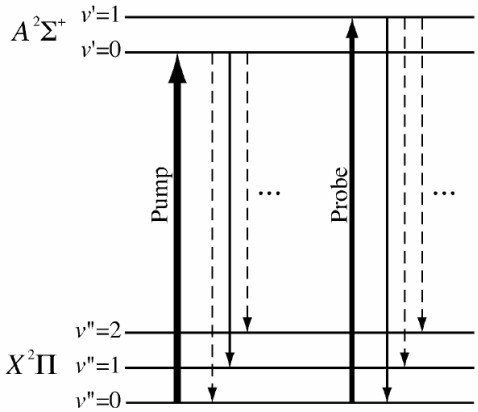

Fig. 38: NO energy level diagram. Pump and probe excitation transitions are depicted as upward arrows and vibrational progressions of fluorescence are shown as downward arrows. The detected fluorescence bands are shown as solid downward arrows.

A "probe-only" fluorescence signal is proportional to the equilibrium population in the ground state. When a pump pulse precedes the probe pulse, it depletes some fraction of the equilibrium ground-state density, defined here as $\Delta\rho_1$, causing the probe signal to decrease proportionally. The fractional depletion of the ground-state population can be expressed in terms of the measurements of the probe-only (S_{pr}) and pump-probe ($S_{pu–pr}$) fluorescence intensities as follows:

$$\Delta\rho_1 = 1 - S_{pu–pr} / S_{pr} \tag{77}$$

As the delay between the pump and probe pulses is increased, collisions and radiative relaxation drive the system towards equilibrium, and $\Delta\rho_1$ decreases. The measurement of $\Delta\rho_1$ as a function of the pump-probe delay characterizes the recovery of the ground-state population in time.

Fig. 39 illustrates the significance of ionization in the current experiments. Here, the intense pump pulse was detuned from NO absorption lines and delayed by 20 ns with respect to the probe pulse. The pump pulse ionized ~24% of the probe-excited population in $A\ ^2\Sigma^+(v' = 0)$, producing a significant decrease in the time-resolved probe-induced fluorescence. In order to obtain accurate data for the ground-state depletion and refill, ionization was implemented in the model and taken into account in the data evaluation.

Quenching from $A\ ^2\Sigma^+(v' = 0)$ directly to $X\ ^2\Pi(v'' = 0)$ was investigated for room temperature collisions with O_2, CO, CO_2, and H_2O by measuring recovery of the ground-state population following intense laser excitation. Experiments were conducted in a room temperature flow cell containing dilute mixtures of NO, N_2, and the quenching gases.

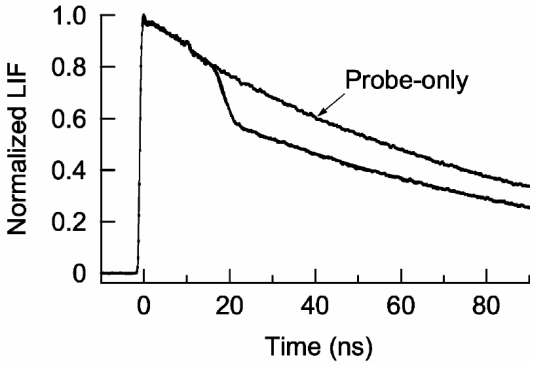

Fig. 39: Time-resolved probe-induced fluorescence from NO $A\ ^2\Sigma^+(v' = 0)$. Ionization by the time-delayed pump pulse produces the fluorescence dip at 20 ns. The unperturbed probe-induced signal is shown for reference. A simulation result, shown as the solid curve, is indistinguishable from the experimental data, shown as dots.

The depletion of the ground state $\Delta\rho_1$ (eq. 77) is plotted in Fig. 40 a) for different time delays after the pump pulse. The solid line represents a fit of the measured data. A depletion of ~25% is observed for a pump-probe delay of 0 ns. Within the first 200 ns after the pump pulse, some percentage of the population recovers due to the direct quenching channel. The dotted curves correspond to the minimum and maximum possible recovery for the experimental conditions. The minimum recovery (upper) curves result from the case where the ground state population recovery is primarily due to radiative relaxation. The maximum recovery (lower) curves result from quenching contributing maximally to ground-state population recovery.

The branching ratio β is plotted in Fig. 40 b) for all quenchers investigated. It is defined as the ratio of the direct quenching from the $A\ ^2\Sigma^+(v' = 0)$ to the $X\ ^2\Pi(v'' = 0)$ vibrational manifold and the total quenching to all vibrational levels. Remarkably large branching ratios were observed for direct quenching to $X\ ^2\Pi(v'' = 0)$. H_2O, CO, and O_2 quench NO $A\ ^2\Sigma^+(v' = 0)$ to $X\ ^2\Pi(v'' = 0)$ with branching ratios that are approximately 0.3. The significantly higher branching ratio for quenching by carbon dioxide is 0.6. These results

indicate that the direct quenching channel to the laser-coupled ground state accounts for 30 – 60% of total quenching and therefore can affect population kinetics, and this process should be considered in kinetic modeling of saturated laser-induced fluorescence.

These results do, however, stand in contrast to the predictions of Paul et al. [67,170] in their description of NO $A\ ^2\Sigma^+$ quenching via the combination of collision complex formation and a charge-exchange (harpoon) interaction. The harpoon model predicts that, as the NO and quencher molecule approach one another in a collision, the NO Rydberg electron jumps to the quenching molecule. This electron transfer occurs at an outer crossing from the neutral intermolecular potential surface to an ion-pair potential surface. The Rydberg character of the NO $A\ ^2\Sigma^+$ state leads to vertical transitions to the ion ground state $NO^+\ X\ ^1\Sigma$ ($v = 0$) from NO $A\ ^2\Sigma^+$ ($v = 0$) [171]. As the ion pair separation decreases on the repulsive wall of the ion-pair potential, there is a second crossing to the neutral ground-state surface.

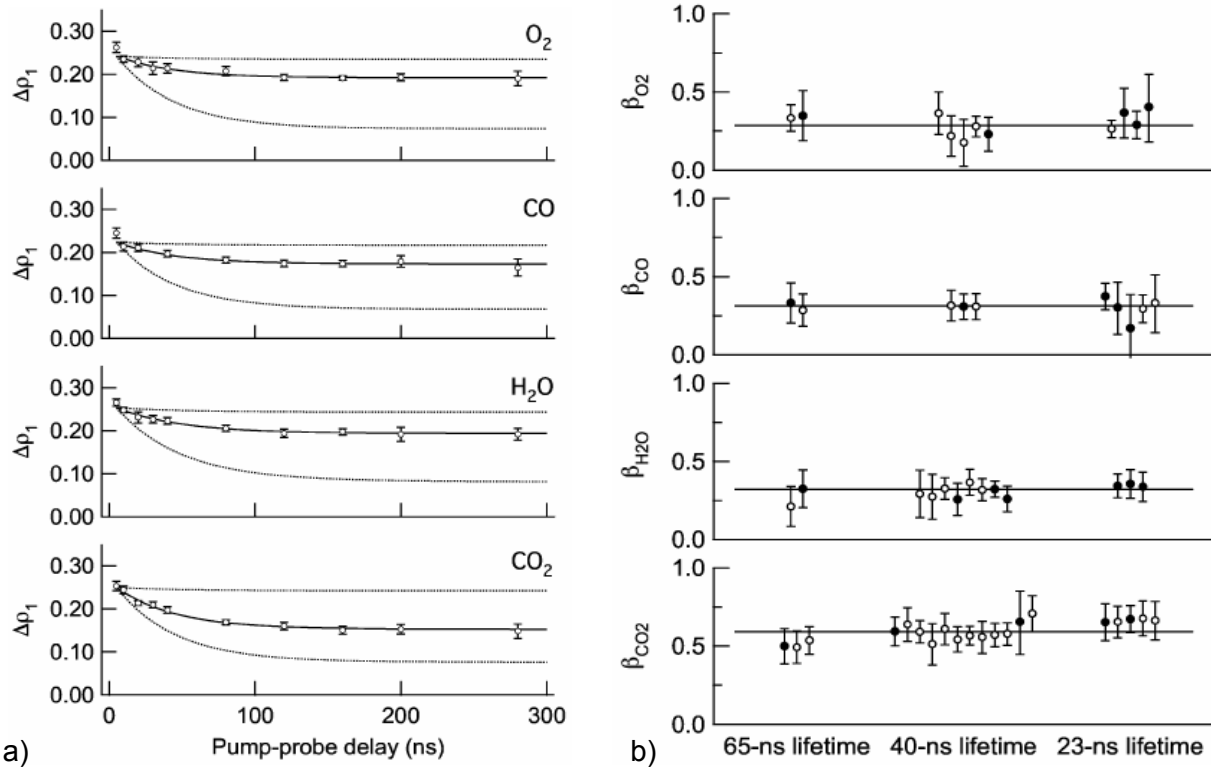

Fig. 40: a) Pump–probe delay scans indicating recovery of ground-state population following pump-induced depletion. The dominant quenching species for each case is indicated in the figure. The solid curves are the result of least-squares fitting to the data. The dashed curves correspond to the minimum and maximum possible recovery for the experimental conditions in each case shown. b) Branching ratios for three quenching conditions as indicated on the horizontal axis. Open and filled symbols represent data acquired with pump laser fluence of ~2500 J/m² and ~1100 J/m², respectively. Solid lines are weighted means of the data.

Although Paul et al. [67,170] did not address specifically the mechanics of the transfer through the exit channel for the harpoon mechanism, they asserted that there should

be a strong tendency for quenching of NO to produce vibrationally excited NO $X\ ^2\Pi$. Because $X\ ^2\Pi$ VET is slow, they concluded that there should be little or no cycling of population during LIF, even under saturating conditions. The current results indicate, however, that quenching branching ratios to the ground vibrational state are significant and that population cycling can affect saturation.

The observation of significant direct quenching to $X\ ^2\Pi$ (v" = 0) with similar branching ratios for O_2, CO, and H_2O may be the result of a quenching collision that is sudden, such that the vibrational motion is frozen on the time scale of the collision. This assumption implies that a long-lived complex is not formed during the collision. In this limit, the crossing to the neutral potential surface and the resulting distribution of vibrational levels in the ground state depends on the Franck-Condon factors between the ground states of the NO cation and neutral. The Franck-Condon factors for $NO^+\ X\ ^1\Sigma$ (v = 0) – NO $X\ ^2\Pi$ (v") are 0.16, 0.26, 0.24, 0.16, and 0.09 for v" = 0, 1, 2, 3, and 4, respectively.

If a Franck-Condon approximation is appropriate, branching ratios for harpoon quenching to v" = 0 should be on the order of 16%, which is approximately one-half of the observed branching ratios for O_2, CO, and H_2O, and one-quarter of that observed for CO_2. If, however, the harpoon entrance channel crosses to the $NO^+\ X\ ^1\Sigma$ (v = 1) surface instead of $NO^+\ X\ ^1\Sigma$ (v = 0), the Franck-Condon factors describing exit channel crossing back to the neutral ground state predict ~33% branching to NO $X\ ^2\Pi$ (v = 0), in accord with the branching ratios observed for O_2, CO, and H_2O.

The role of Franck-Condon factors in vibrational partitioning of product states, however, remains a topic of debate [172] and experimental evidence indicates that Franck-Condon product state distributions are the exception rather than the rule. These data alone, however, are not sufficient to determine whether Franck-Condon factors successfully describe the product distribution of quenched molecules.

The significantly larger branching ratio observed for CO_2 is explained in terms of a reactive quenching process that leads to the dissociation of CO_2. This reaction is only energetically favourable if the NO product is formed in its vibrational ground state.

It is important to emphasize that the current measurements apply to room-temperature quenching. At higher temperature, we expect that other quenching mechanisms become important [162], and quenching product distributions are likely to change. Further experiments at elevated temperature will be necessary to determine the temperature dependence of the branching ratios.

More comprehensive measurements of the product vibrational distributions are necessary to provide insight into the physical mechanisms of quenching NO $A\ ^2\Sigma^+(v' = 0)$. In addition to the experimental investigations, there is a clear need for complementary theoretical development of the potential energy surfaces for the interaction between NO $A\ ^2\Sigma^+(v' = 0)$ and small molecules.

4.2 Two-line H_2O-TDLAS thermometry

Water (H_2O) is present in the exhaust of almost every combustion process. It has a rich absorption spectrum in the mid-IR. Therefore it is practical to use it as target species for thermometry techniques, since no seeding is necessary (as with NO LIF, section 4.1) that might influence the system under study. However, temperature information is only accessible in the exhaust gases and not in the fresh gases, except they are humidified or the air humidity is sufficient. Also, the technique is generally restricted to line-of-sight measurements.

Laser diodes (cf. section 2.2.2) are small, easy to handle and provide laser light at almost any desired wavelength in the mid-IR [25]. This enables selective detection of water absorption signals without interference from other species. Two-line thermometry based on tunable diode laser spectroscopy (TDLAS) has been introduced in section 3.2. Sensors using this technique were developed [173-175] and have been applied to measure the exhaust temperature in harsh environments like internal combustion engines [176], scramjet combustors [120,177], pulse detonation engines [117,178,179], and gas turbines [175]. TDLAS sensors can be optimized to yield real-time temperature information with a kHz bandwidth which enables for example active control of engines [180].

4.2.1 Water molecular spectroscopy

Water is one of the most important molecules for life on earth. More important for this research: water is formed in every combustion process using fuels that contain hydrogen in their molecular structure and oxygen as oxidizer as shown in the reaction for methane combustion:

$$CH_4 + 2\ O_2 \rightarrow CO_2 + 2\ \mathbf{H_2O}$$

The molecular structure of water is more complex than for the two-atomic NO molecule because water contains three atoms. The vibrational as well as rotational structure of water is much more detailed. The three fundamental vibration modes are shown in Fig. 41 and characterized in Table 10. Also, rotation around all three spatial axes is possible.

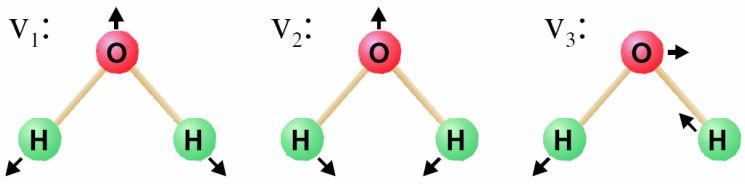

Fig. 41: The structure of the water molecule and its three fundamental vibrations ν_1, ν_2, and ν_3.

Vibrational mode	Frequency [cm^{-1}]	Description
ν_1	3651	Symmetric stretch
ν_2	1595	Symmetric bend
ν_3	3756	Antisymmetric stretch

Table 10: Fundamental vibrations, frequencies, and description for H_2O [181].

Due to this complexity, water has a rich absorption spectrum in between 1 to 2 µm (Fig. 42). Spectral positions, ground state energies and further information about more than 100,000 water absorption lines can be found in the HITRAN/HITEMP database that contains over 1.7 million absorption lines of 37 molecules [182].

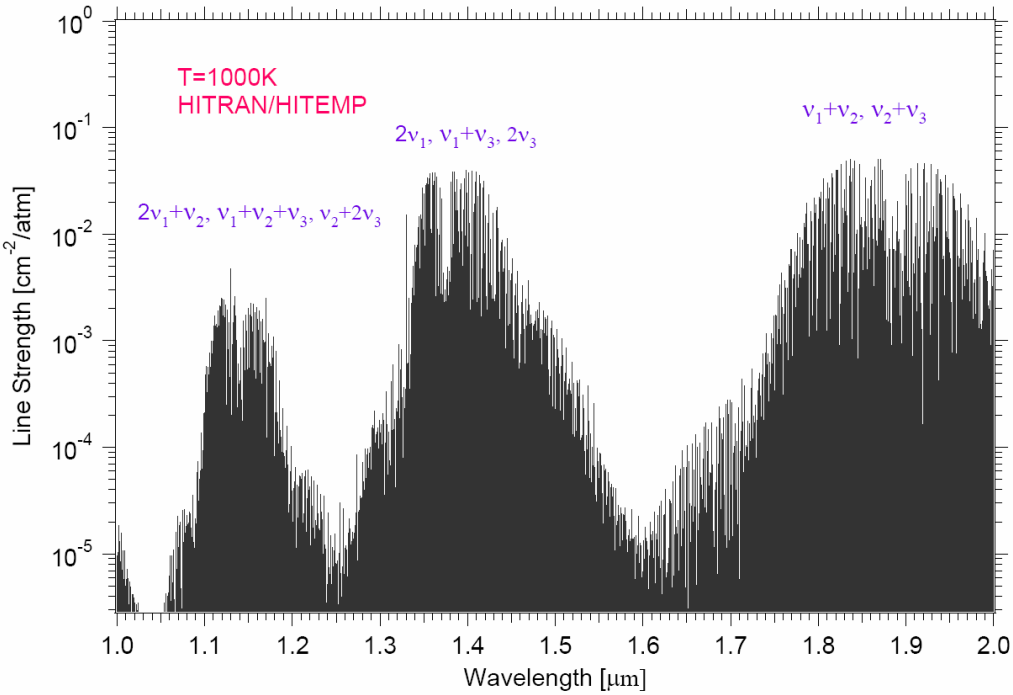

Fig. 42: Survey spectra of H_2O at 1000 K in the near-infrared region based on the HITRAN/HITEMP database.

4.2.2 Optimizing temperature sensitivity: Selection of line pairs

In order to find suitable transitions for a two-line thermometry sensor, the H_2O absorption spectrum between 1 and 2 µm has been systematically analyzed in the group of Prof. R. K. Hanson at Stanford University, USA, using the HITRAN 2004 database [174]. The following criteria were investigated to optimize the sensor:

- Both lines need sufficient but not too strong absorption regarding the target application with a path length of about 5 cm and a water mole fraction of ~0.1 at atmospheric pressure in the temperature range from 1000 – 2000 K.

- Interference from ambient H_2O as well as cold boundary layers is minimized by using transitions with high ground-state energies (E'' > 1700 cm^{-1}). This ensures that the absorbance at low temperature is negligible.
- The wavelength of both absorption lines must lie within one single laser scan (2 cm^{-1}) and should not overlap significantly at atmospheric pressure (spacing of 0.3 – 1 cm^{-1}).
- The line pair must have sufficiently different lower state energy to be sensitive to temperature in the range from 1000 – 2000 K ($\Delta E''$ > 700 cm^{-1}, eq. 76).
- The two lines must be isolated from nearby transitions.
- The wavelength should be in the 1.25 – 1.65 µm range. Here, fiber-coupled telecommunication lasers and equipment are available.

Out of four line pairs meeting the above mentioned criteria, a line pair at 7154 cm^{-1} was chosen. Since the uncertainty in the HITRAN 2004 database is relatively large for high E'' lines, the transitions were characterized experimentally in previous work and the database was updated accordingly [174]. The experimentally obtained line strength data is used for temperature evaluation and is given in Table 11. At a closer look, the high E'' feature consists of two transitions with the same lower-state energy. However, their transition frequencies are spaced by only 0.03 cm^{-1}. Therefore, they can be evaluated as a single transition because spectral broadening is much larger.

Line	**Transition frequency**		**Line strength at 296 K**	**Ground state energy**
	λ [nm]	ν [cm^{-1}]	[cm^{-2}/bar]	E'' [cm^{-1}]
High E''	1397.87	7153.748	8.05E-6	2552.9
Low E''	1397.75	7154.354	3.67E-4	1789.0

Table 11: Details of the transitions used for two-line thermometry.

The line strengths of both transitions are calculated following eq. 67 and are shown in Fig. 43 a). Its temperature dependence mainly reflects the respective ground-state populations as described by the Boltzmann distribution (eqs. 7-9) The partition function is calculated by a polynomial given in [173]. The line strengths show the typical behavior for relatively high E'' states: they are weak below room temperature, reach a maximum at ~1000 K and are still significant at temperatures up to 3000 K.

At room temperature, the low E'' line is significantly stronger than the high E'' line. This becomes obvious from the ratio of the two lines, plotted in Fig. 43 b). This ratio is a unique function of temperature (eqs. 70 and 71). The ratio is ~10 at 500 K and approaches 1.8 at 3000 K. The temperature sensitivity depends on the slope of the curve. The precision of the temperature measurement is higher in regions with a steep slope. However, taking into account that the absorption of both lines should be on the same

order of magnitude to prevent one line from dominating the ratio [116], the applicable temperature range for a sensor using these two lines is between about 700 and 2000 K.

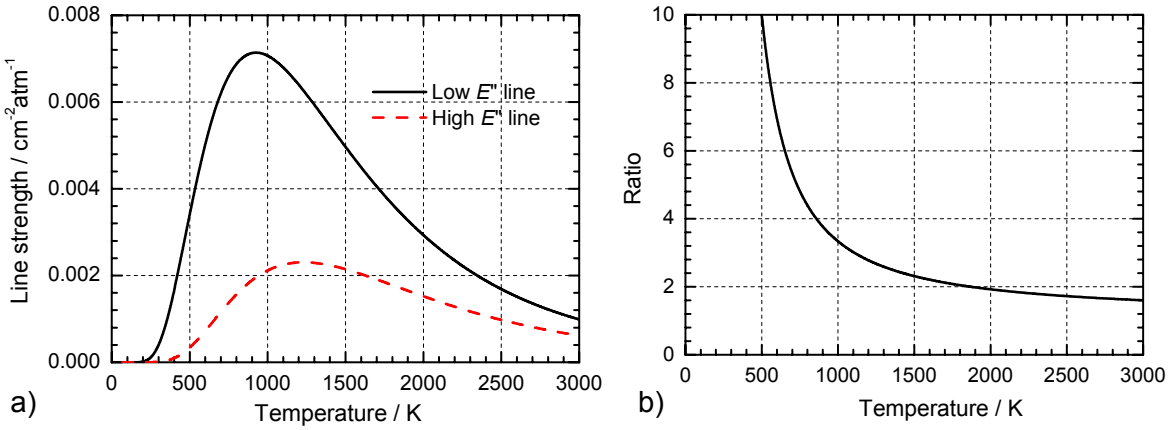

Fig. 43: Line strength (a) and ratio (b) dependence on temperature for the transitions described in Table 11.

Absorption spectra of the region around both lines are simulated using the HITRAN 2004 database. The temperature is varied between 300 K and 2000 K for a path length of 0.1 m. Simulation results are shown in Fig. 44 a) for a low pressure H_2/O_2 flame with a H_2O mole fraction of 0.4 (cf. section 5.5) and in Fig. 44 b) for an atmospheric pressure CH_4/air flame with a H_2O mole fraction of 0.19 (cf. section 5.6). For these cases, the maximum observed absorbance is on the order of 0.01 and 0.1, respectively. Hence, direct absorption spectroscopy can be applied. There is no need for WMS with 2f detection (cf. section 3.2.2).

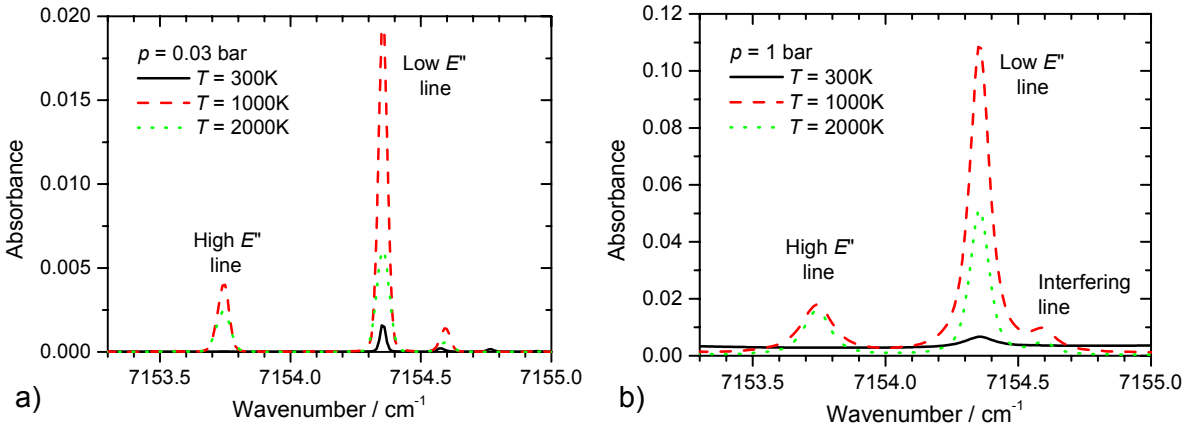

Fig. 44: Simulated absorption spectra for the target lines at low pressure (a) and atmospheric pressure (b) for 0.1 m path length.

At low-pressure (Fig. 44 a), both target lines are isolated from nearby transitions. As expected from Fig. 43, the absorption for the high *E"* line is negligible at 300 K and maximum absorption for both lines are observed at ~1000 K. At atmospheric pressure (Fig. 44 b), a weak offset of the 300 K spectrum is noticeable, which is absorption in the wings of stronger lines at a large spectral distance. However, the linear background can be subtracted as baseline and does not influence the temperature measurements. At atmospheric pressure, the line at 7154.6 cm^{-1} overlaps significantly with the low *E"* line. This interference can be compensated by fitting all three peaks simultaneously.

The low *E"* line exhibits some absorption at room temperature. Hence, the temperature results will be influenced if the beam is transmitted through room air. However, the mole fraction of water in room air is at least 20 times lower compared to the cases shown in Fig. 44. Therefore, the ambient air interference is negligible if the absorption length in ambient air is shorter than the path length within the target region.

4.2.3 Experimental setup

A simplified setup for absorption spectroscopy was shown in Fig. 11. The detailed experimental arrangement of the TDLAS sensor applied in this thesis is presented in Fig. 45. The DFB laser diode (NEL) is temperature and injection current controlled by a laser diode controller (ILX LDC-3908). The laser diode is current-tuned by applying a saw-tooth signal generated by a function generator. A trigger signal synchronizes the data acquisition board (NI PCI 6115) controlled with LabVIEW.

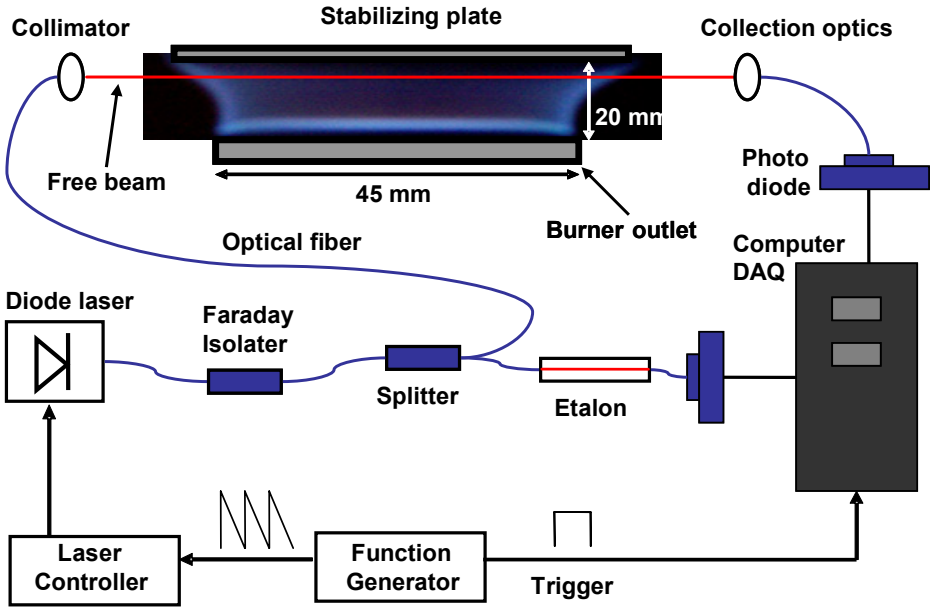

Fig. 45: Experimental setup of a TDLAS temperature sensor.

The laser light is transmitted through optical single-mode fibers, collimated (Thorlabs F230FC-C) and pitched across the region of interest, e.g. a McKenna type flat flame. Finally the laser beam is collected into a multi-mode fiber (Thorlabs BFL37-400) and detected by a photo diode (Thorlabs PDA10CS-EC). A part of the laser light is extracted by a splitter (Laser 2000) and transmitted through an etalon device (Micron Optics) to monitor the wavelength tuning by counting fringes. A Faraday isolater (Laser 2000) reduces back-scattering into the laser diode by ~50 dB that would otherwise cause severe interference.

4.2.4 Data acquisition and temperature evaluation

Due to current tuning of the laser diode, the detected signal exhibits a non-linear saw-tooth shape. The ramp for current tuning is chosen such that the injection current falls below the lasing threshold of the laser diode at the end of the scan (Fig. 46 a). This procedure is necessary to do quantitative absorption measurements since one has to correct for an offset in the photo diode signal.

After that, a third order polynomial is fitted to the non-absorbing wings of the spectrum indicated in Fig. 46 a). After subtraction of this baseline, an absorption spectrum is obtained on a time scale. In this case, the laser was current tuned with 100 Hz. The time scale is transformed to frequency by monitoring the laser tuning with an etalon. Then, the features in the obtained absorption spectrum are fitted as Voigt peaks (Fig. 46 b). The integrated areas A_i of the peaks are used to calculate the temperature with eq. 71.

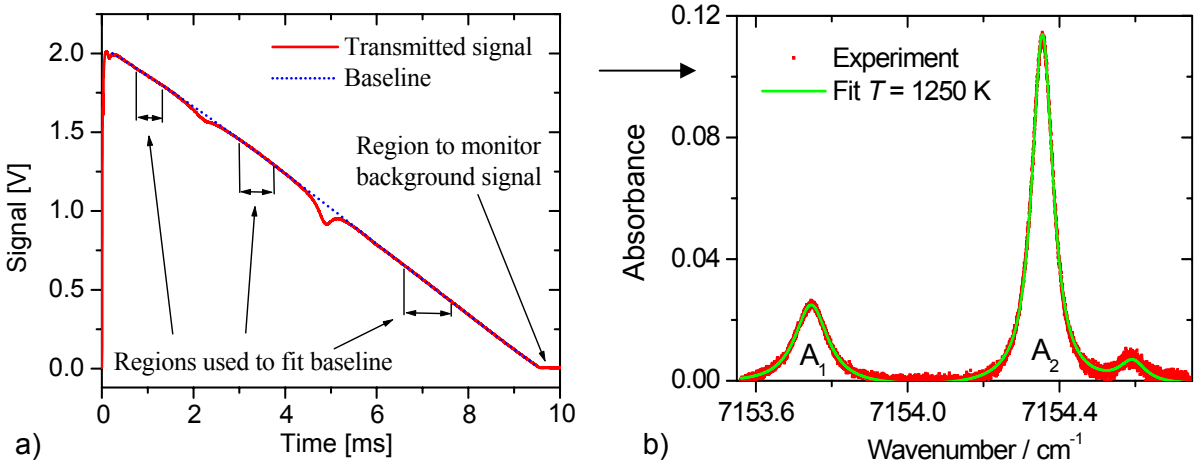

Fig. 46: The raw signal on a time scale (a) is evaluated to obtain the integrated areas of the peaks on a frequency scale (b).

Fig. 47 shows the transmission through the fiber-coupled etalon with a free spectral range (FSR) of 0.267 cm^{-1} and a finesse of 25. It is noticeable that, after the current is set

to maximum at $t = 0$, the laser needs almost 1 ms to reach the desired wavelength. After that, the wavelength follows the current ramp almost linearly. For evaluation of Fig. 47, the peak positions on the time scale are plotted against the wavelength axis given by the FSR and a fourth order polynomial is fitted to the resulting graph.

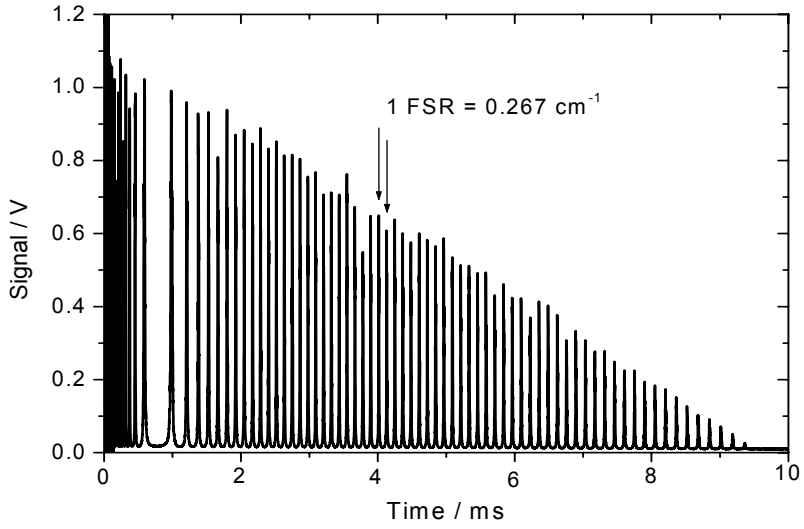

Fig. 47: Transmission through the etalon during current tuning at 100 Hz. The free spectral range (FSR) is indicated as the distance between two peaks.

5 Applications

Both thermometry techniques discussed in section 4, multi-line NO-LIF temperature imaging and two-line H_2O-TDLAS thermometry, were applied to a number of different combustion systems. An overview is given in Table 12 with the thermometry method used and the respective excitation scan ranges as well as the detection filters used for NO-LIF measurements. First, experimental and simulated gas-phase temperature fields in ethanol spray flames [95] are presented and discussed [152] in section 5.1 followed by IC-engine relevant spray diagnostics in section 5.2. Measurements in sooting atmospheric-pressure [150] and high-pressure flames [148] relevant for laser-induced incandescence (LII) are shown in section 5.3. In section 5.4, a wall-quenched flame is investigated [183]. In section 5.5, the temperature influence on nano-particle synthesis is presented [146,184]. Also, a comparison of results of both methods, NO LIF and H_2O TDLAS (sections 4.1 and 4.2, respectively), is shown. At last, temperature measurements in a direct-flame solid-oxide fuel-cell system [185] are presented.

Application	Section	Thermometry method	Spectral range	Filters
Spray flame	5.1	NO LIF	D	I + III
Evaporative cooling in sprays	5.2	NO LIF	A	I + IV
Sooting flat flame	5.3.2	NO LIF	D	I + III
Sooting high-pressure flame	5.3.1	NO LIF	B	I + IV
Wall-quenched flame	5.4	NO LIF	C	IV
Nano-particle synthesis reactor	5.5	NO LIF + H_2O TDLAS	C	II + II + II
Direct-flame fuel cell	5.6	H_2O TDLAS		

Table 12: Mapping of thermometry methods and applications with the respective NO-LIF excitation ranges (Table 6 and Fig. 26) and detection filters (Table 9 and Fig. 31) used.

5.1 Spray flame temperature imaging

Several modern combustion devices are based on fuel spray combustion. Usually the fuel is injected into a combustion chamber, where a spray develops, evaporates and mixes with air to form an ignitable mixture. The gas- and liquid-phase temperature distribution, the droplet-size distribution and the mixing process of fuel and air are crucial for combustion efficiency, stability, and pollutant emission. In order to evaluate and optimize the spray combustion process, reliable experimental and numerical tools are required. These tools need to be tested on model spray flames.

Numerous experimental [186] as well as computational [187] studies of spray flames are available in the literature. In this section, experiments are presented with a burner that was developed at the UC Berkeley and has been set up in Heidelberg. Its specific benefit lies in the fact that a stable spray flame with no bluff-body or pilot flame stabilization is generated; thus, no special mathematical treatment is required. This facilitates numerical model developments. While the Berkeley studies focused on gas flames in vitiated coflows [188], the Heidelberg burner has been used to study spray flames in an air coflow.

Multi-line NO-LIF thermometry has been used to quantitatively image the gas temperature in the ethanol/air spray flame. The experimental setup, the results, and parameter variations are described and discussed in section 5.1.1 and have been published in [95]. The gas-phase temperature measurements are combined with liquid-phase temperature distributions (in collaboration with I. Düwel; published in [189-191]) and other experimental data in order to provide a database for the development and validation of numerical models for spray combustion.

In cooperation with H.-W. Ge from the group of Prof. E. Gutheil at the University of Heidelberg, the measurements close to the nozzle exit are used as initial conditions for numerical simulations, that were published in [152,192-194] and are presented in section 5.1.2. The experimental data set and the numerical results were published on a website to allow other groups to evaluate their experimental and/or numerical data (http://www.uni-due.de/ivg/vg/forschung/fo_sp_brenner.shtml).

5.1.1 Experimental setup, results and discussion

The spray burner setup is shown in Fig. 48. The nozzle (Delavan #67700-5) produces a hollow cone spray with a spray angle of 45°. It is surrounded by a homogeneous air coflow seeded with 1000 ppm NO. A stable flame was obtained by pre-heating the fuel to 45°C at the nozzle exit. The resulting flame has two flame zones [195]. The inner flame is located directly above the nozzle exit while the outer flame position depends on the fuel pressure and coflow velocity. It is located 15 – 20 mm above the nozzle, further away

for higher injection pressures. The thermal power of the spray flame is about 11 kW. For multi-line NO-LIF thermometry, the spectral scan range D was chosen (Table 6, 44407 – 44417 cm^{-1}). A combination of a UG 5 filter and the band-pass filter described in section 4.1.4 was used to reject scattered light (cf. Table 12). The intensified CCD camera (Flowmaster, LaVision) was equipped with a Halle, f = 100 mm, achromatic UV lens.

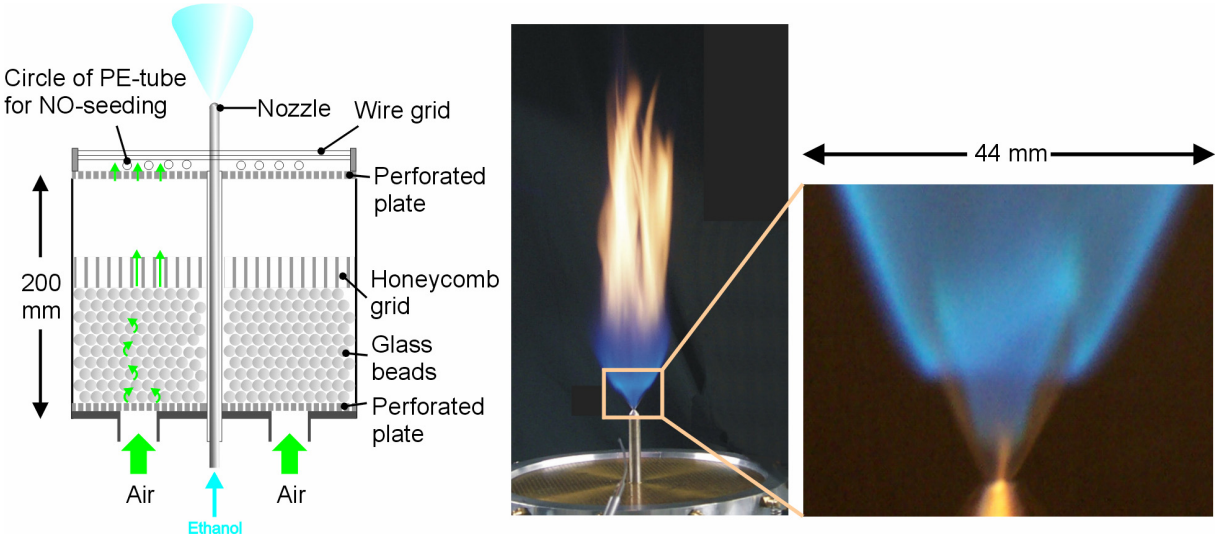

Fig. 48: Schematic of the spray burner with nozzle and coflow generation (left) together with a flame photograph and the magnified imaged region (right).

Fig. 49 a) shows a flame photograph as well as the temperature distribution in a 44 × 36 mm^2 area of the flame above the nozzle (Fig. 49 b). The nozzle exit is visible in the middle of the lower part of the frame. The post-processing routine simultaneously yields images of the scattering background (which is the baseline intensity of each spectrum, Fig. 49 c) and the relative NO-LIF signal strength (which is the intensity of the spectra for each pixel, Fig. 49 d). Note that an inhomogeneous NO-LIF signal distribution due to unequal NO seeding does not influence the temperature evaluation since temperature is gained from relative peak heights and not from absolute values. The spatial resolution of Fig. 49 b), c), and d) is 0.45 × 0.45 mm^2.

Measurements for fuel pressures of 1.4, 2.0, and 2.4 bar injection pressure with liquid flow rates of 30, 35, and 40 ml/min and air coflow velocities of 0.32 and 0.64 m/s were performed. The resulting temperature fields and horizontal temperature profiles at 10, 20, and 30 mm height above the nozzle exit are presented in Fig. 50. Temperatures in the coflow are 300 ±4 K (±1%).

In the following discussion, temperature values at 20 mm above the nozzle exit in a homogeneous 2 × 2 mm^2 rectangle in the center of the inner flame are compared for the different conditions. For the 1.4 bar, 0.32 m/s case, 1900 ±40 K (±2%) are found in the inner flame. Excitation spectra were acquired using a total of 5000 laser shots. The

maximum temperature does not change when doubling the coflow velocity to 0.64 m/s. However, the outer flame zone is compressed and ignites further downstream. When increasing the ethanol injection pressure to 2.0 bar, the droplet velocity increases and the ignition of the outer flame zone takes place a few millimeters further downstream. Temperature at 20 mm height above the nozzle in the inner flame is now decreased to 1775 ±75 K (±4%). Here, 500 laser shots were used for spectra acquisition only, resulting in reduced precision.

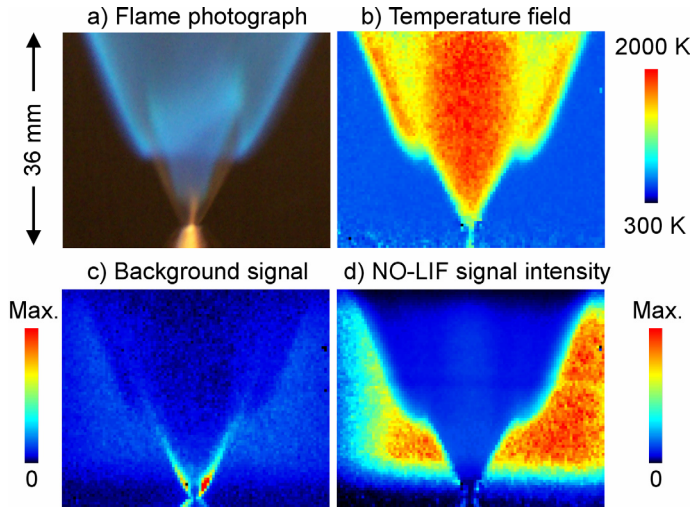

Fig. 49: a) Flame photograph. The post-processing routine calculates b) temperature distribution, c) scattering background in the ethanol spray flame that indicates the position of the spray close to the nozzle exit and d) NO-LIF signal strength. Taken from [95].

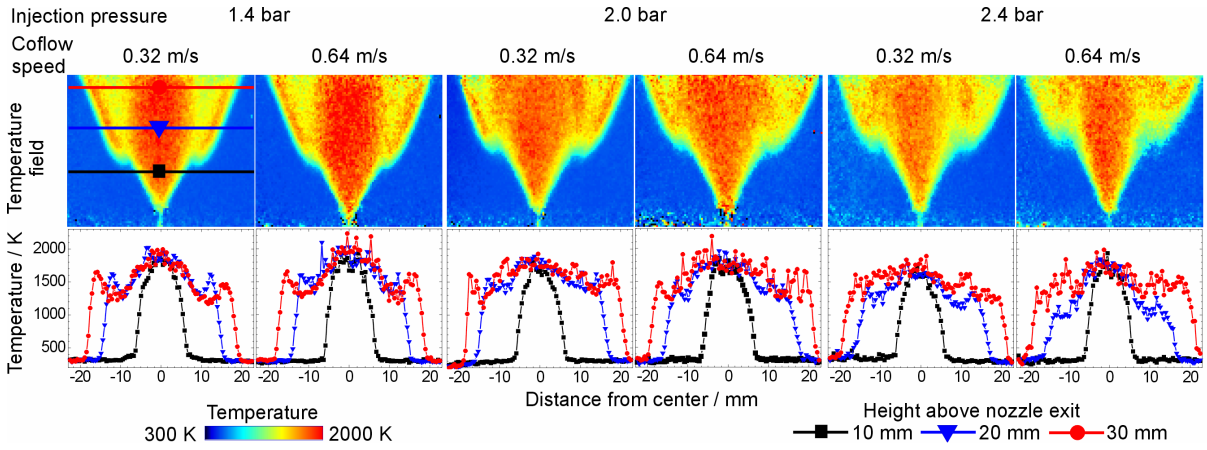

Fig. 50: Images show the temperature distribution (44 × 36 mm²) of the ethanol spray flame at different fuel injection pressures and air coflow speeds. The graphs show horizontal temperature profiles in 10, 20, and 30 mm height above the nozzle exit indicated in the first temperature field.

At 2.4 bar injection pressure the outer flame is shifted even further downstream. The temperature at 20 mm height for the 2.4 bar 0.32 m/s case is 1645 ±65 K (±4%). When doubling the coflow velocity, we find an increase in temperature to 1740 ±85 K (±5%). In

summary, we find that temperatures at 20 mm height above the nozzle in the inner flame decrease by about 125 K for every increase in the injection pressure investigated. The inner flame is only slightly affected by a variation in coflow velocity. The outer flame ignites further downstream when increasing both, injection pressure or coflow velocity.

The scanning measurement requires approximately one minute. In areas with fluctuating temperature a systematic error occurs that has been quantified by modeling the fluctuating NO spectra with subsequent evaluation of the resulting time-averaged spectra as described in section 4.1.5. For regions with moderate temperature fluctuations (e.g. in the flame zone: 1200 – 1800 K, equally distributed), the measured temperature deviates only by –31 K (–2%) from the arithmetic average of 1500 K (Fig. 34). For strongly fluctuating regions (e.g. near the flame edge, 300 – 1500 K, equally distributed), the simulation predicts a measured value of 925 K instead of the arithmetic average of 900 K, which is a deviation of 3%.

5.1.2 Comparison to numerical simulations of spray flames

The spray-flame was investigated thoroughly before by different experiments in order to provide a data set for the initial conditions of numerical simulations that were validated with this data. Various experimental techniques were applied to study the spray and the flame. Well-established techniques like Phase Doppler Anemometry (PDA) have been used and new techniques such as LIF/Mie drop-sizing [196-198] and two-color LIF liquid-phase thermometry [199,200] have been adapted to the system by different researchers.

The experimental liquid-phase temperature field is shown in Fig. 51 a). The hot zones on the inside of the spray cone correspond with the location of the flame as indicated by the photograph in Fig. 51 b) as well as in the measured gas-phase temperature field (Fig. 51 c). Note that the droplet temperature decreases when the outer flame zone ignites. This can be explained by the fact that the smaller droplets evaporate quickly in the flame and the colder large droplets remain.

The gas-phase temperature field was simulated by H.-W. Ge from the group of Prof. E. Gutheil at the University of Heidelberg for the case with 2.0 bar injection pressure and 0.32 m/s coflow velocity [194]. We use the nozzle position as origin. The section at $z = 2$ mm, after spray breakup, is taken as inlet profile. The gas velocity at the inlet is set to 0.32 m/s. The initial gas temperature is taken from the 2D NO-LIF measurement in the same case. The droplet size and droplet velocity distributions at the inlet are taken from PDA measurements.

Two numerical models are applied to calculate the development of the spray. An Eulerian-Lagrangian model including Reynolds-averaged Navier-Stokes (RANS) calculations is applied. Detailed chemistry is implemented through the spray flamelet model [201]. A k-ε turbulence model extended by terms accounting for interaction of the gas

and the spray is employed [201]. The simulated gas-phase temperature field is presented in Fig. 51 d). The numerical results and the experimental data show agreement in the center of the flame, and some discrepancies appear at the flame edge. The simulation cannot reproduce the hot wings of the spray flame that were found in the experiment (Fig. 51 c). A complete description of the numerical model is available in [152].

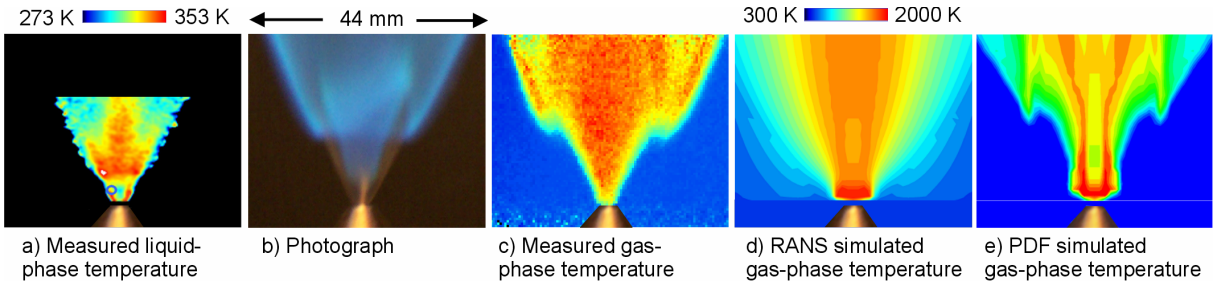

Fig. 51: Photograph of the spray flame together with measured liquid- and gas-temperature fields as well as simulation results of the flame at $p_{(inj)} = 2.0$ bar and $v_{(coflow)} = 0.32$ m/s.

Also, a novel joint probability density-function (PDF) method is applied by H.-W. Ge to calculate the development of the spray flame [202,203]. In the PDF transport equation, the terms of convection, body force, mean-pressure gradient, and chemical reactions are treated without any assumptions. Thus, the PDF method is a powerful tool to study the turbulence-chemistry interaction. For turbulent spray flows, the source terms are represented exactly in the PDF transport equation. Research has been done to extend the PDF method to turbulent spray-flame modeling [204,205]. A detailed ethanol/air combustion mechanism consisting of 38 species and 337 elementary reactions is implemented through a spray flamelet model [201]. The results are shown in Fig. 51 e). Good agreement with the experiment is found.

A more detailed comparison of the experimental data and the two numerical simulation methods is presented in Fig. 52. Profiles of the gas-phase temperature fields shown in Fig. 51 c), d), and e) at different height above the nozzle: x = 6, 10, 20, and 25 mm are plotted. Symbols are the measured data. The solid lines indicate the numerical results of the present PDF method. The dashed lines indicate the numerical results of the RANS modeling [152]. The PDF method gives considerably better agreement than the RANS modeling. The hot wings of the spray flame are well predicted by the PDF method (cf. the section x = 20 mm). RANS modeling over-predicts the flame width, and it fails to predict the two reaction zones. Discrepancies in the PDF modeling mainly result from the unknown liquid flux distribution and turbulence quantities at the inlet profile. The predicted temperature profile at the section x = 6 mm is broader than the experimental data. It may be due to the k-ε turbulence model, which usually over-predicts the spreading speed of the jet flow [202].

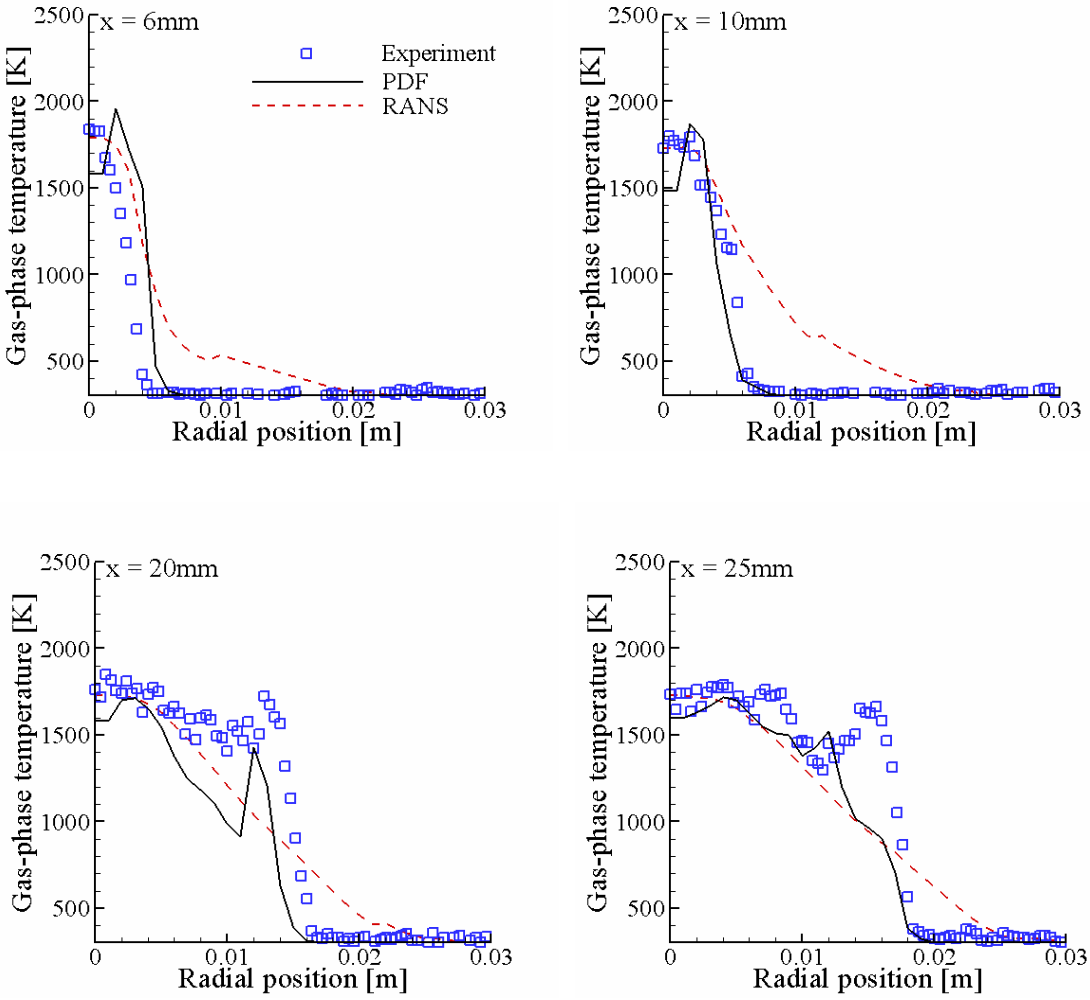

Fig. 52: Gas-phase temperature profiles at various heights, x, above the nozzle exit (indicated in the figures). Measured (symbols) as well as PDF- (solid lines) and RANS-simulated (dashed lines) temperature profiles are presented (cf. Fig. 51 c), d) and e).

In contrast to other spray flames, the two reaction zones in this spray flame are not formed by recirculation, because there is no recirculation zone observed in the experiments. This was proven by particle image velocimetry measurements previously [191,206]. Instead, the two reaction zones are formed due to the different development stages of the spray. The ethanol vapor from the first stage of the spray mixes and reacts with the entrained air, which forms the inner flame. The remaining part of the spray is heated and ignited by the heat production of the inner flame, and then develops into the outer flame. A joint PDF of higher degree may improve the results of the numerical computations relaxing assumptions of statistical independence of further characterizing variables in future work.

5.2 Evaporative cooling of IC engine-relevant sprays

Stratified-charge spark-ignited direct-injection (SC-SIDI) internal-combustion (IC) engines show high fuel efficiency at part load because throttling losses are reduced [207]. For a reliable operation of spray-guided engines, the complex process of spray injection and ignition must be precisely controlled. In order to reduce pollutant emissions, accurate experimental data of physical parameters such as e.g. liquid-phase distribution [207] and fuel/air ratio [208] inside the cylinder are needed to develop numerical models for engine optimization [209]. Gas-phase temperature is of great interest, since after injection of the fuel, the spray evaporation process cools down the gas phase. Consequently, the fuel-air mixture might leave ignition limits while passing the spark plug, which leads to misfires that cannot be explained by investigating the fuel/air ratio only.

Temperature information can in principle be gained from various techniques such as e.g. 3-pentanone LIF [210] or atomic-fluorescence techniques [70], that have already been applied to in-cylinder temperature imaging before and after ignition, respectively. Coherent anti-Stokes Raman scattering (CARS) was applied to measure the gas-phase temperature variation due to evaporative cooling inside a similar spray cloud [211], but only point measurements are possible with this technique (cf. section 3.5).

In cooperation with the Robert Bosch GmbH, Germany, multi-line NO-LIF thermometry was applied to measure two-dimensional gas-phase temperature fields in the evaporating spray cloud. The results were published in [212]. The method simultaneously visualizes the liquid phase by detecting a fraction of the elastically scattered light. The spectral range A (Table 6, 225.19 – 225.04 nm) was used to acquire excitation spectra. An example is shown in Fig. 53 a). Simulated NO-LIF excitation spectra of this range at 278, 288 and 298 K are shown in Fig. 53 b) to visualize the temperature sensitivity of this spectral range. The peak heights change by over 20% for a variation in temperature of 10 K only.

The scanned multi-line thermometry approach is not instantaneous. The acquisition of signal over many laser shots therefore leads to signal averaging over time. In case the process under investigation is repetitive in time (like a pulsed spray in the beginning of its evolution) time resolution can be achieved by phase sampling. This strategy is employed here.

For each scan, images at 301 wavelength positions, each averaged over 20 laser shots, were taken at equal spectral steps of 0.1 cm^{-1}. Signal averaging was limited to spectral ranges, where LIF signal is actually present, which is the case in only half of the spectral positions. In between the peaks of the excitation spectrum, the images were averaged over two laser shots only and the baseline of the spectra was smoothed in the post processing. This procedure shortens the data acquisition time to 50 minutes without loosing any information. For each scan, about 3000 injection event were necessary.

In cases where full reproducibility of the flow field is not guaranteed (i.e. in a turbulent flow or also in the outer areas of the developing spray), an averaged temperature is obtained. Time-averaging the LIF signal in a fluctuating situation, however, does not lead to a mathematically correct average temperature after analysis of the excitation spectra, as explained in detail in section 4.1.5. The procedure causes a systematic deviation in the accuracy of the resulting mean temperature in the fluctuating regions because the LIF signal does not linearly depend on temperature. This non-linear behaviour becomes obvious from Fig. 53 c) for the transitions relevant for this work.

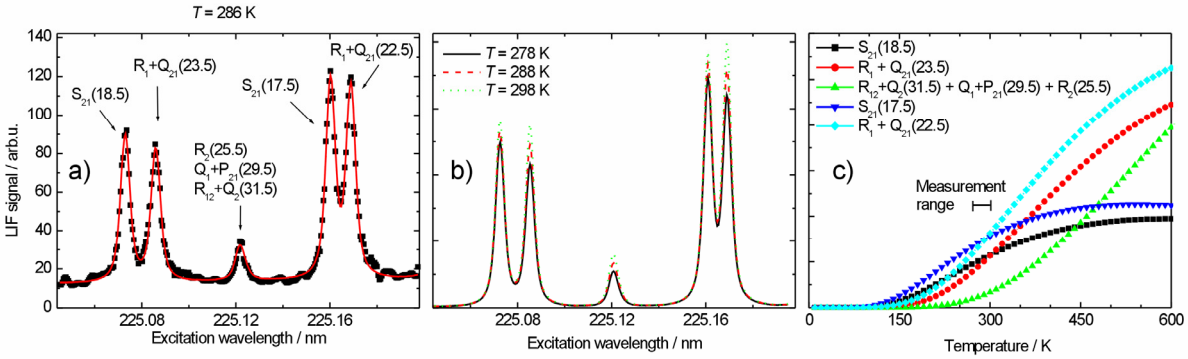

Fig. 53: a) Experimental (symbols) and fitted (line) NO-LIF excitation spectra from inside the spray cloud. The LIF signal is averaged over a 2 × 2 × 2 mm³ region and 20 shots per wavelength position. The labels show the respective rotational transition in the NO A-X(0,0) band. b) LIFSim numerical simulations of NO-LIF excitation spectra for the investigated temperature range. c) LIFSim numerical simulations of the LIF signal intensity evolution with temperature for the five spectral features for air and constant NO mole fraction. The investigated temperature range is indicated.

Numerical simulations were done with LIFSim to quantify this error. In the observed spray process, an average minimum temperature of about 288 K was measured. It is hardly possible that this temperature was homogeneously distributed in the gas-phase between the droplets. It is more realistic to assume colder regions close to the droplets and warmer areas further away. To simulate this case, excitation spectra were calculated for the temperature ranging from 278 – 298 K for every degree.

These 21 spectra were averaged with even weight and the fitting procedure was applied to obtain the temperature from the averaged spectrum. The resulting fitted temperature is 288.2 K instead of the mathematically correct average of 288.0 K. Accordingly, with the spectral range used here, the multi-line NO-LIF thermometry systematically over-predicts the temperature in the fluctuating regions by significantly less then 1 K. Fortunately, the error is small and negligible for the measurements presented here.

5.2.1 Experimental setup

The experimental setup is shown in Fig. 54. It is similar to the general setup shown for multi-line NO-LIF thermometry in section 4.1.2. NO is seeded (1000 ppm) to the flow of air inside the chamber to provide a homogeneous NO atmosphere. The laser beam is focused with a vertical lens of a focal length f = 2 m to a vertical light sheet of approximately 75 × 2 mm² at the spray position.

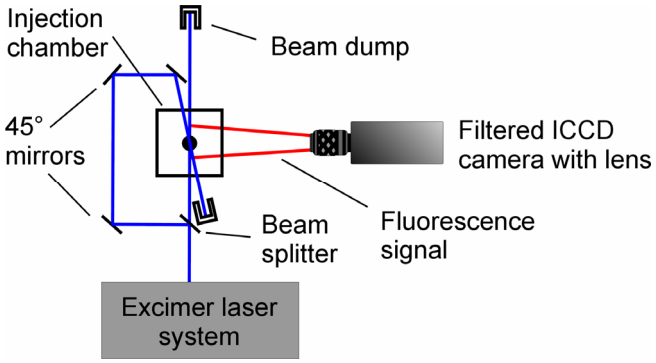

Fig. 54: Experimental setup of the multi-line NO-LIF thermometry applied to an evaporating spray.

The spray cloud early in the evaporation process scatters as much as 90% of the laser light. In general, this does not affect the temperature results as long as there is any LIF signal left, since temperature information is gained from relative peak heights of the spectra and not from absolute intensities. However, the precision of the measurement decreases in regions with very low LIF signal since the signal-to-noise ratio of the excitation spectra is low. Therefore, the beam is divided by a beam splitter into two equal parts that are pitched through the cell from opposite sides. This should not be mistaken with the strategy of bi-directional LIF that aims at quantitative concentration measurements [213]. Here, the approach simply ensures a more homogeneous illumination over the cross-section of the spray cloud. The laser beams cross in the center of the chamber with an angle of two degrees.

The LIF signal is recorded with an ICCD camera (Flowmaster, LaVision) equipped with a Halle UV lens with a focal length f = 100 mm and an f-number $f_\#$ = 2. The laser energy is recorded on a shot-by-shot basis, and the LIF image is linearly corrected for variations in laser pulse energy. Care was taken to not saturate the LIF signal but to stay in the linear range. Elastically-scattered light is suppressed by a Schott UG5 filter by three orders of magnitude and an additional reflection band pass filter by another 2.5 orders of magnitude (section 4.1.4).

The injection nozzle was centered on top of a cubic flow cell with 20 × 20 × 20 cm³ size. Details are shown in Fig. 55. The cell is equipped with large fused-silica windows on four sides to enable full optical access to the spray. A plate with 1600 holes generates a

homogeneous air flow from top to bottom to exchange the cell volume after injection. The spray is generated by a gasoline direct-injection swirl nozzle (Bosch). Ethanol is used as fuel, which is pressurized to 15 MPa by an air-driven fluid pump (Haskel). The injection is controlled by a 12 V automobile injection system (Bosch).

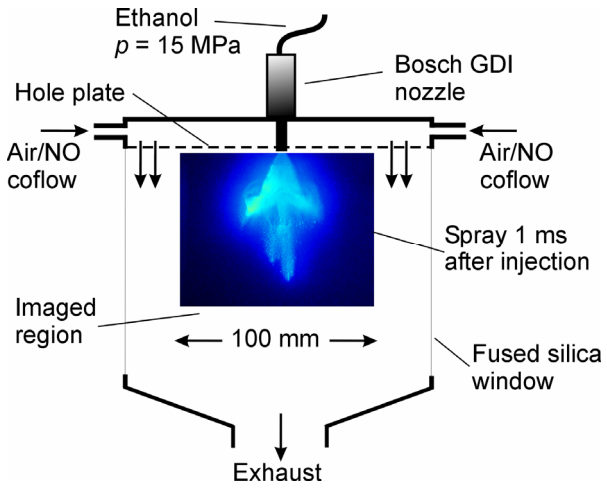

Fig. 55: Setup of the optically-accessible spray chamber with the spray visualized by Mie scattering.

5.2.2 Results and Discussion

The gas-phase temperature and the liquid-phase distribution of the evaporating ethanol spray were measured at various time delays of 0, 1, 2, 3, 5, 10, 20, and 50 ms after the visible start of injection (SOI) and are presented in Fig. 56. With an injection duration of 1 ms and an injection pressure of 15 MPa, 15 µl ethanol were injected. For spectra acquisition, the repetition rate was limited to 1 Hz to ensure a complete gas exchange in the optical chamber before the next injection. The air-flow velocity of 20 cm/s is slow enough to avoid an influence on the spray atomization.

The first row of Fig. 56 shows single-shot Mie-scattering images at 225 nm in a $93 \times 75 \times 1$ mm^3 area directly below the nozzle exit with a projected pixel size of 0.1×0.1 mm^2 in the plane. The second and third rows show the results of the multi-line NO-LIF thermometry in an $80 \times 60 \times 2$ mm^3 region beginning 15 mm below the nozzle exit in the center of the spray. The second row shows the baseline intensity of the excitation spectra fitted for each pixel, which is caused by Mie scattering. The third row shows the gas-phase temperature distribution of the evaporating spray. In the second and third row of Fig. 56, the optical resolution in the plane is 2×2 mm^2 to enhance the NO-LIF signal-to-noise ratio by binning the CCD chip of the camera. This is necessary since the LIF signal is about four orders of magnitude lower than the Mie-scattering intensity in the present experiment. In the third row of Fig. 56, the intensity values cover the range from 280 – 320 K only. Small pixel-to-pixel fluctuations in temperature

therefore appear as significant variations in the intensity scale. Despite the "noisy" appearance of the images, the standard deviation in a region with homogeneous temperature is in the ±1 %, i.e. ±3 K range only.

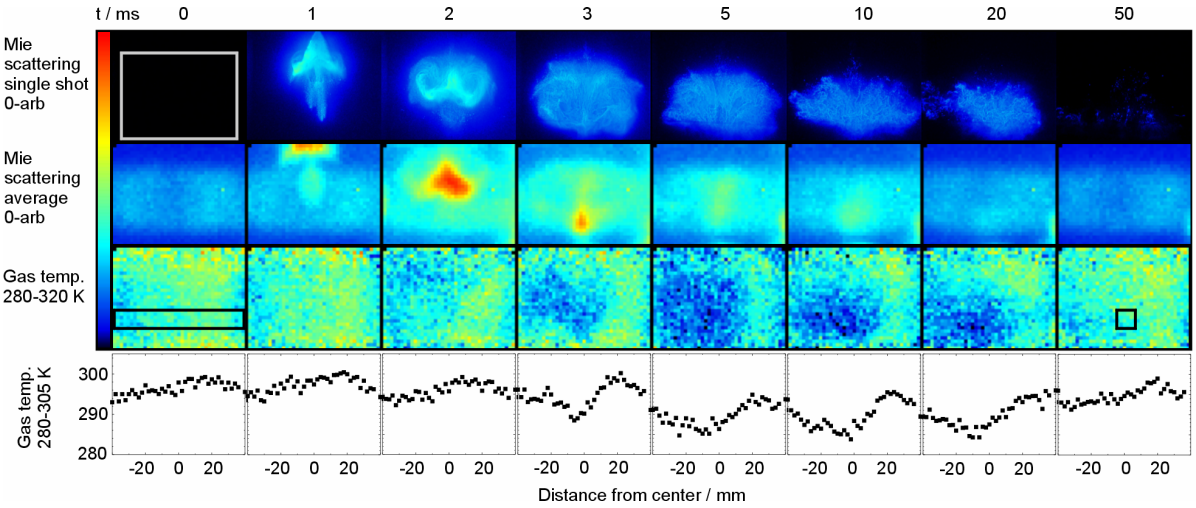

Fig. 56: Simultaneous spray and gas-temperature imaging in an evaporating ethanol spray: The first line shows 93 × 75 × 2 mm³ single-shot Mie-scattering images at different time delays after the injection start. The rectangle in the upper left image shows the 80 × 60 × 2 mm³ area used for the multi-line NO-LIF thermometry presented in the next two lines. The pixel-by-pixel fitting method yields time-averaged Mie-scattering images as baseline of the spectra (second row) and the gas-temperature fields (third row). The lowest row shows temperature profiles extracted at a distance of 60 mm below the nozzle exit specified in the first image of the third row. The rectangle in the last image of the third row shows the area averaged for Fig. 57.

In the Mie-scattering images at 1 and 2 ms after SOI, some large droplets are visible in the center of the leading portion of the main spray cloud, but they do hardly evaporate, hence no cooling of the gas phase is detected. At 2 and 3 ms, the swirl effect becomes visible and the spray begins to evaporate causing an almost stationary spray distribution in the center of the detected area. From 3 to 5 ms, the Mie-scattering intensity diminishes and the gas-phase temperature decreases strongly. Later, the spray cloud further evaporates and moves downwards out of the observed range. The temperature at the detected position recovers to ambient temperature after ~100 ms because of the fast exchange of the bath gas.

In the last row of Fig. 56, horizontal temperature profiles are presented that were extracted from the corresponding temperature images at 60 mm below the nozzle exit. The exact region is specified in the first temperature image. When the spray cloud arrives, the temperature in the center of the image drops from room temperature to ~287 K and recovers later. The measured temperature distribution is not symmetric because the spray is not perfectly symmetric. However, a negligible systematic gradient can also be seen, when no spray is present.

Fig. 57 shows the gas-phase temperature evolution versus time after SOI in a $10 \times 10 \times 2$ mm^3 region 60 mm below the nozzle exit specified in the last temperature image in Fig. 56. Before injection, the temperature inside the cell measured by a thermocouple was 298 K. When the spray cloud arrives at this position, the temperature drops by about 10 K at 5 ms after SOI and recovers slowly to ambient temperature, when the spray moves further downwards.

At a lower injection pressure of 10 MPa, the spray cloud has less impulse and takes a longer time to travel through the imaged area. The temperature at 60 mm drops down later, reaches its minimum at 10 ms after SOI, and the temperature recovers later. The standard deviation of the temperature measurements is ±3 K and is plotted as error bars in Fig. 57. It is derived from the root mean square (RMS) deviation of temperature values in a homogeneous area of the temperature images including all minor systematic errors discussed above. Multiple measurements were made to ensure reproducibility, which is better than ±1 K.

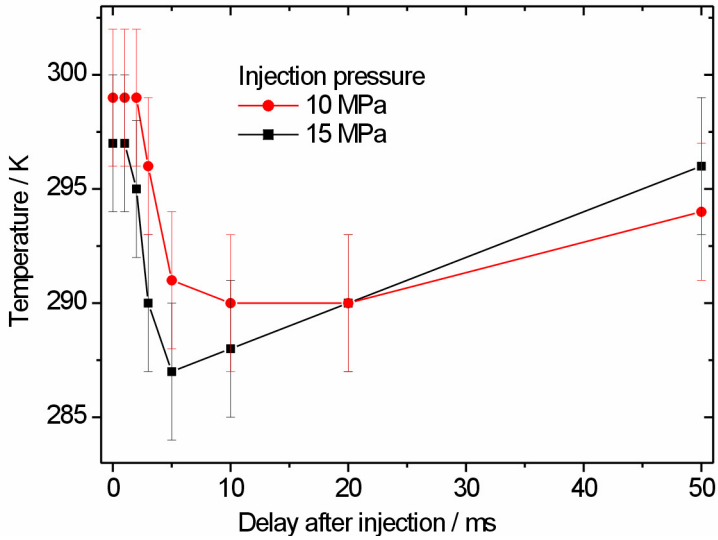

Fig. 57: Gas-phase temperature 60 mm below the nozzle exit plotted versus the time delay after the injection start for two different injection pressures. The error bars show the standard deviation of the measurements.

From thermodynamic calculations using the enthalpy of evaporation of ethanol (~40 kJ/mol) and the heat capacity of air (~29 J/(K mol)) one would expect a much larger cooling effect of about 70 K in a $50 \times 50 \times 50$ mm^3 volume if complete evaporation of the liquid is assumed. It is obvious that only a small part of the ethanol evaporates at the present conditions within the observed area. In order to achieve complete evaporation, a heated and pressurized environment is necessary.

Temperature measurements with multi-line NO-LIF thermometry have been carried out at engine-relevant pressures of up to 6 MPa and flame temperatures [30]. The

measurement precision decreases with higher pressure because of collisional broadening effects of the spectral features. On the other hand, the higher temperature inside the cylinder leads to faster evaporation and the temperature gradients are much larger and accordingly easier to detect. Therefore, in-cylinder temperature measurements of the entire combustion cycle should be possible to quantify the cooling effect by spray evaporation and afterwards image the flame temperature after ignition. This will be investigated in future work.

Electrospray

Enhancing the evaporation rate of the spray is of great interest for IC engine development. Especially under transient fuelling conditions such as the cold starting of the engine, active control of the liquid atomization process is desired. In general, an electrospray can be used to achieve this, since highly charged droplets release their coulombic strain by droplet fission and, hence, evaporate faster [214,215]. The electrospray effect is nowadays frequently applied in mass spectrometry, where it is used to smoothly ionize large bio-molecules by charging droplets (containing the target molecule), which transfer their charge to the bio-molecule after evaporation [216]. Electrospray injection in automotive engines was successfully tested with intake-manifold fuel injection by Ford ten years ago [217,218], but was never commercially introduced.

Within this work, the electrospray effect on the gasoline direct-injection system described in the previous section was investigated. A counter electrode was installed inside the spray chamber that was described in Fig. 55. An electric field (up to 3 kV/cm) was setup between the nozzle exit and the counter electrode in order to investigate the electrospray effect on the pulsed spray. Water was used as liquid since it has a higher dielectric constant than ethanol, and it cannot ignite inside the optical chamber. Mie-scattering at 532 nm was applied to measure the liquid phase distribution with and without electric field. However, no significant influence on the spray evaporation behavior could be observed, even with water containing 1 mol/l NaCl [219].

5.3 Sooting combustion

Soot formation has been a major issue in combustion research over the last decades as soot is emitted by many technical combustion processes, e.g. power plants and IC engines. Soot is the result of incomplete combustion of hydrocarbons if not enough oxygen is available for the reaction to carbon dioxide and water. Soot consists mainly of carbon but may have rather different properties and composition [220]. Transmission electron microscopy (TEM) shows that soot consists of primary particles which have a typical size between 5 and 100 nm. Primary particles form larger aggregates that contain up to several hundred primary particles and have a fractal structure. A typical TEM image of soot obtained from the exhaust gas of a Diesel engine is shown in Fig. 58.

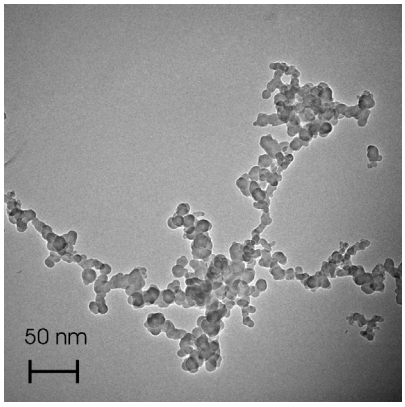

Fig. 58: TEM image of soot collected from the exhaust gas of a Diesel engine [149].

Tools for soot diagnostics are important since nano-sized soot particles as emitted by IC engines are suspected to cause asthma, heart attacks and cancer, as they can penetrate deeply into the lungs [4,5]. The emission standards for particulate matter (PM) for diesel cars in the European Union (EU) decreased by a factor of ~6 from 0.14 g/km in 1992 to 0.025 g/km in the EURO IV norm in 2005 [221]. However, in the case of PM not only the emitted mass is important but also the emitted particle sizes, as smaller particles have enhanced health effects. Therefore, tools for soot diagnostics are required that are able to probe both soot volume fractions and primary particle sizes. Laser-induced incandescence (LII) is often used to measure these quantities in a non-intrusive way [222,223].

The laser-induced incandescence (LII) signal is due to thermal radiation (Planck's law, eq. 6) from soot particles that are heated by an intense laser pulse. Subsequent cooling occurs until the particle temperature reaches ambient gas temperature again. Smaller particles cool down faster due to their higher surface/volume ratio. After calibration, a numerical model is fitted to the LII signal decay curve to derive the particle size and the width of the size distribution. Numerous models have been developed [224-229]

to predict the temporal behavior of the LII signal. One model called “LIISim” is available via the web (www.liisim.com) [230].

Although LII seems to be quite well understood in atmospheric-pressure systems, research is still necessary at elevated pressures as this is the common case in practical combustion devices such as IC engines. With increasing pressure the LII signal decay is faster due to increased heat conduction [231]. The gas-phase temperature is required in order to determine particle sizes from LII decay curves. In the following section 5.3.1, gas-phase temperature imaging in sooting high pressure flames is shown [148]. This data was then used as input for the LIISim model. In collaboration with M. Hofmann, soot particle sizes and size distributions were obtained in the high-pressure flame. The results were published in [148,149,232].

Commonly, pyrometry of soot (cf. section 2.1.2) is used to determine the flame temperature [233]. However, this method is a line-of-sight technique and does not give the temperature at the exact LII measurement location. Additionally, the obtained temperature is the soot-particle temperature and not the gas-phase temperature. Commonly, it is assumed that these temperatures are similar, when particle and gas phase are in thermal equilibrium. But this is questionable in the region of soot formation and oxidation and is subject of investigation in section 5.3.2. In cooperation with K. Omerbegovic, comparisons between soot pyrometry and multi-line NO-LIF thermometry in atmospheric pressure flames are presented that were published in [150].

5.3.1 Temperature measurements in sooting high-pressure flames

The burner used in this study was installed inside a high-pressure chamber equipped with four quartz windows for optical access. It is described in detail in [232]. Premixed laminar sooting ethylene/air flat flames were stabilized on the central burner matrix that has a diameter of 20 mm and consists of sintered metal foam of stainless steel (Siperm® R10, 10 mm thick). In order to obtain a homogeneous sooting flame the central burner is surrounded by a second burner with a diameter of 56 mm that is made of a sintered bronze disc, in which a cooling coil of copper is embedded. A rich methane/air flame is used here. The two burners are surrounded by a ring of sintered bronze through which a co-flow of air is led to further stabilize the flame and to keep the windows clean of soot and water deposition. The burner assembly is shown in Fig. 59 a). The equivalence ratio of the sooting flame used in this study was $\phi = 2.1$, corresponding to a C/O ratio of 0.7, with a gas velocity of 8 cm/s for all flames.

Gas-phase temperature distributions in the sooting high-pressure flame were measured with multi-line NO-LIF thermometry. The experimental setup is identical to the one shown in Fig. 23. A close-up of the burner region is shown in Fig. 59 b). Gas temperatures were measured in the ethylene/air flames at pressures of 1, 2, and 5 bar.

Respective flame photographs, gas-temperature fields and excitation spectra are shown in Fig. 60.

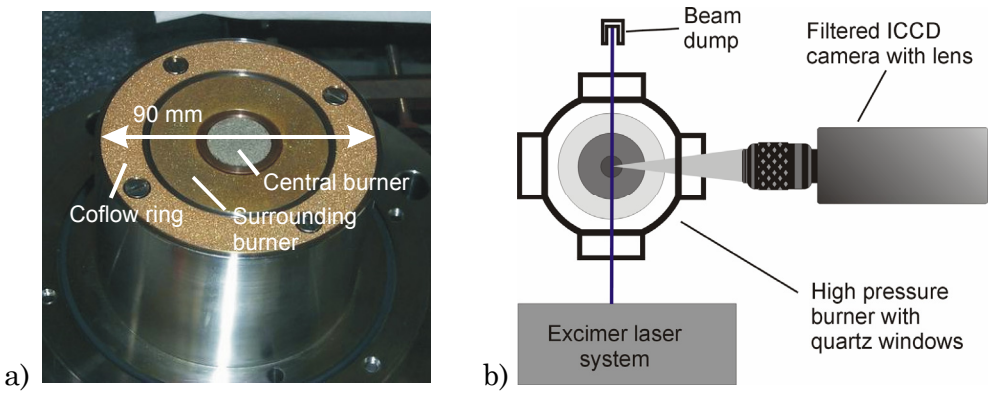

Fig. 59: a) Setup of the burner head; b) Setup of the LIF experiment.

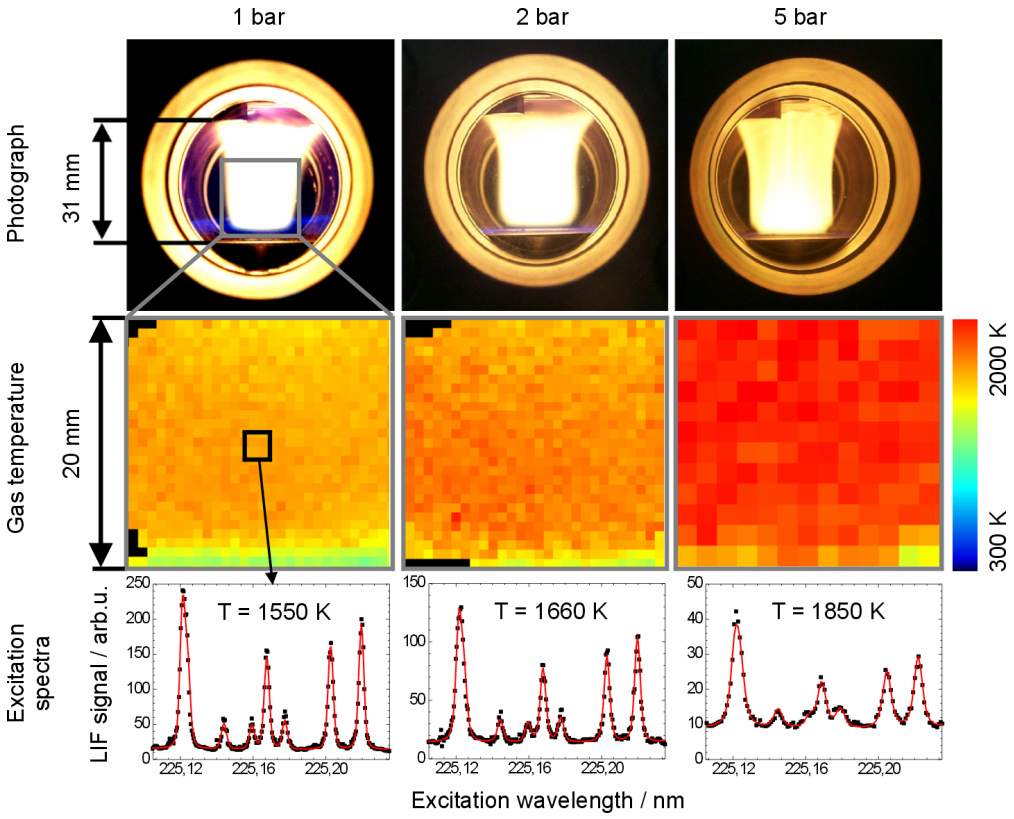

Fig. 60: The first row shows photographs of the sooting flame at pressures of 1, 2, and 5 bar. The second row shows the respective gas-temperature field of the inner burner. The last row shows excitation spectra at the position indicated in the temperature field. Symbols are experimental data and the lines show the fitted spectra.

5000 ppm NO were added to the fresh gas of the inner burner to generate sufficient LIF signal despite strong reburn reactions of added NO in rich flames [89,234]. The scan range B (Table 6, 225.24 – 225.09 nm) was used to acquire excitation spectra. The spectra were acquired with equal spectral steps of 0.1 cm^{-1}. The 271 images were each

averaged over 50 single shots. A combination of a UG5 filter and the band-pass filter described in section 4.1.4 was used to reject scattered light and to suppress fluorescence from PAH. The ICCD camera (Flowmaster, LaVision) was equipped with a Halle, f = 200 mm, achromatic UV lens.

The flame photographs in Fig. 60 were taken through one of the four windows for optical access and show the central strongly sooting flame as well as the surrounding flat flame close to the burner outlet for the different pressures. The cold fresh gas is visible in the lower part of the temperature fields. Temperatures peak at around 5 mm height above the burner surface (HAB) and slowly decrease later in the flow. Due to the surrounding flame, the horizontal temperature distribution is very homogeneous. The flame temperature increases with pressure due to the fact that the fresh gas velocity was kept constant and the flow rates and hence the thermal power was increased accordingly with rising pressure. The spatial resolution in the temperature fields for 1 and 2 bar is 0.8 × 0.8 mm² and 1.6 × 1.6 mm² for 5 bar in order to enhance the LIF excitation spectra signal-to-noise ratio.

The temperature in the center region of 2 × 2 mm² (indicated in Fig. 60) of the flame at 1 bar was measured to 1560, 1550, 1500, and 1400 ±20 K at 5, 10, 15, and 20 mm HAB respectively. Temperatures at 2 bar were 1660, 1660, 1600, and 1500 ±30 K for 5, 10, 15, and 20 mm HAB, respectively. At 5 bar we find gas temperatures of 1850, 1850, 1830, and 1750 ±40 K at 5, 10, 15, and 20 mm HAB. Excitation spectra of the respective experiments are presented in the last row of Fig. 60. The observed LIF intensities strongly decrease with rising pressure due to increased quenching and spectral broadening effects, which are considered in the fit.

5.3.2 Comparison of soot-particle temperature and gas temperature

In combustion research, the temperature of sooting flames is often determined by pyrometry [233]. The radiation emitted by soot particles is measured spectrally resolved and temperature is evaluated using Planck's law (cf. section 2.1.2). Hereby, the soot-particle temperature is assumed to be identical to the gas-phase temperature in the flame. However, due to chemical reactions at the soot-particle surface such as oxidation and radiative energy losses, the temperatures might differ.

Pyrometry and multi-line NO-LIF thermometry were applied to measure the soot-particle temperature and the gas-phase temperature, respectively, under identical conditions [150] as shown in Fig. 61. A laminar, sooting ethylene/air flat flame was stabilized on a water-cooled sinter matrix (60 mm diameter) of a McKenna burner [235]. The flow rate of the fresh gas was 10 l/min with a fuel/air ratio ϕ = 2. A steel plate situated 21 mm above the burner surface as well as air or nitrogen coflows stabilize the flame.

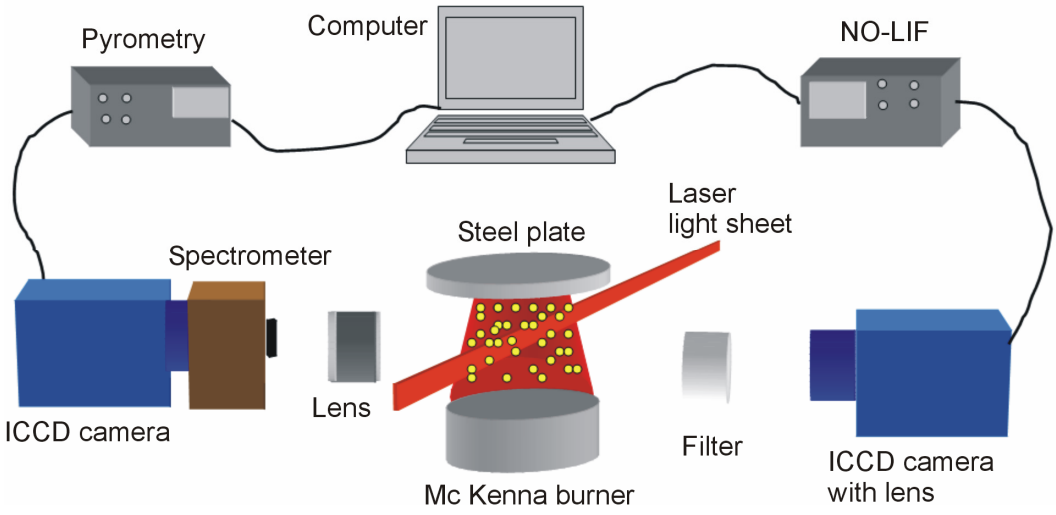

Fig. 61: Experimental setup of pyrometry (left) and NO-LIF thermometry (right).

Two-color pyrometry was applied to the flame by K. Omerbegovic, evaluating the wavelengths at 550 and 650 nm, which yields optimum temperature sensitivity [233]. For multi-line NO-LIF thermometry, 5000 ppm NO was added to the fresh gases in order to obtain enough NO-LIF signal despite of reburn reactions in rich flames that severely diminish the NO concentration [89,234]. The spectral scan range D (Table 6, 44407 – 44417cm^{-1}) was chosen for laser excitation. A combination of a UG5 filter and the band-pass filter described in section 4.1.4 was used to reject scattered light and to suppress fluorescence from poly-cyclic aromatic hydro-carbons (PAH). The ICCD camera (Flow-master, LaVision) was equipped with a Halle, $f = 100$ mm, achromatic UV lens. The resulting gas-temperature fields as well as photographs of the flame with both air and nitrogen coflow are shown in Fig. 62.

For a quantitative comparison, the temperature results of pyrometry and NO-LIF thermometry are plotted versus the height above the burner (HAB) in Fig. 63. The temperature distribution is typical for a flame in a stagnation point flow configuration. The fresh gases are heated up by the enthalpy release and the temperature peaks at about 6 mm HAB. Then, the combustion gases cool down by radiation and convective heat transfer to the steel plate, and the temperature decays.

The gas-temperature field in Fig. 62 is divided in two sections α and β. The first zone α represents the center of the burner. Here, the gas-temperature is identical for both coflow gases, reaching a maximum of 1600 K and dropping down to 1300 K close to the steel plate. The second zone β is averaged over a wider horizontal area that partly includes the edges of the flame. With air surrounding the flame, the oxygen can mix with the partially burnt gases of the rich flame by diffusion and a second hot flame zone can be seen to the left and to the right of the left temperature field in Fig. 62. This cannot happen with nitrogen as coflow. As a result, the zone β is hotter with an air coflow.

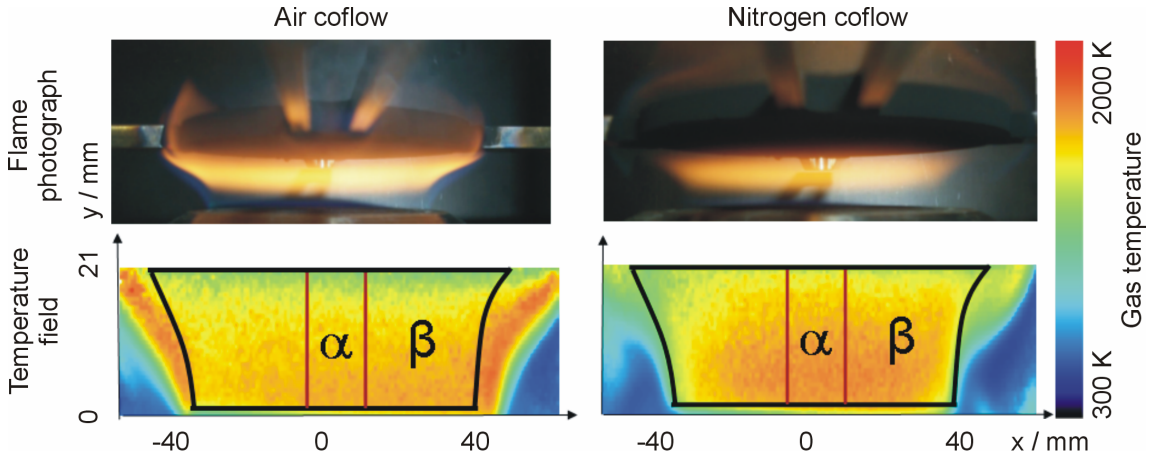

Fig. 62: Flame photographs (upper row) and gas-phase temperature fields (lower row) for the sooting flame with air (left) and nitrogen (right) coflow. The regions α and β are evaluated for a quantitative comparison in Fig. 63.

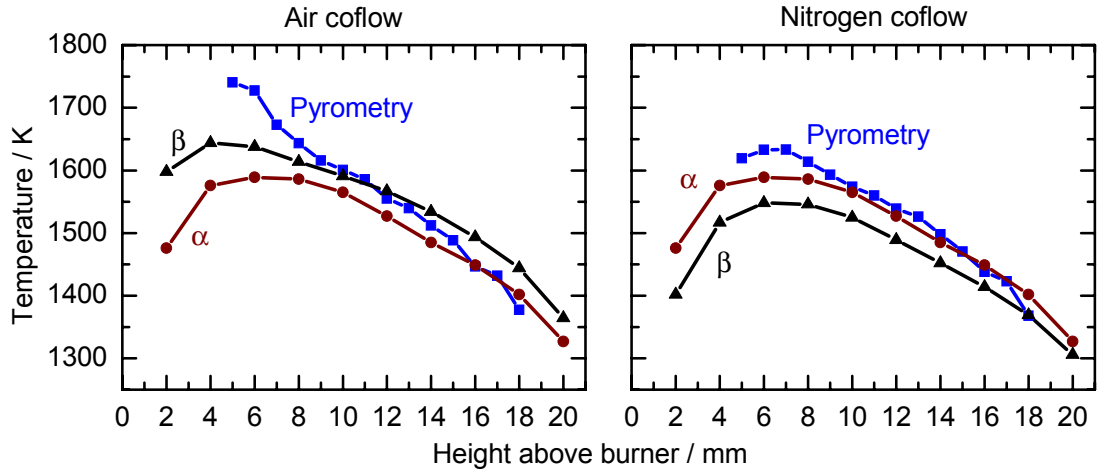

Fig. 63: Quantitative comparison of soot-particle temperature (Pyrometry) and gas temperature (NO-LIF) in the regions α and β (Fig. 62) at different heights above the burner for air (left) and nitrogen coflow (right).

The comparison to the soot-particle temperature measured by pyrometry shows significant differences in the first 8 mm above the burner. This region can be assumed as the main reaction zone of the flame. Here, pyrometry over-predicts the gas temperature by up to several hundred Kelvin. Higher in the flame, the temperatures of both methods fit better. A drawback in pyrometry measurements is that the actual measurements location is unknown due to the line-of-sight nature. Also, for a correct evaluation of pyrometry, the wavelength-dependent soot particle emissivity has to be known [236]. Several models are available for the refractive index of soot but, unfortunately, they yield very different temperature results [237].

5.4 Quenched flames and surface boundary layers

A detailed understanding of transport phenomena in boundary layers is essential for the quantitative description of reactive flows, as they appear in internal combustion engines, power plants, etc. Within the recent years, laser diagnostics have been frequently applied to combustion analysis, e.g. in internal combustion engines [23,238]. However, most of these techniques have been used to measure pure gas-phase combustion. The zone of interaction between solid walls and the free flame has not been studied in very much detail so far. Therefore, in a project with T. Fuyoto and K. Akihama from Toyota Central R&D Labs, Japan, the latest laser-based imaging techniques are applied to measure the boundary layer in vicinity of solid surfaces, in order to investigate the diagnostics potentials and limitations. The results have been published in [183].

Temperature measurements in boundary layers are more important than velocity and species concentrations for the following reasons. First, the temperature distribution close to surfaces in a cylinder of reciprocating engines directly affects flame propagation, knocking, and quenching. These phenomena dominate engine performance and exhaust emissions. Second, temperature information is very useful for LIF measurement of species, such as OH and fuel compounds. The temperature dependences of their LIF signals hamper the application of LIF techniques to conditions with spatial temperature gradients. If the temperature distribution is known, however, the LIF signal can be corrected for its temperature dependence.

5.4.1 Experimental setup and temperature measurements

Inside a burner housing, premixed methane/air flat flames, shown in Fig. 64 a), were stabilized on a flat-flame burner [239,240]. The flame holder is a 40 mm diameter disk with 805 holes, each 1 mm in diameter. It was made of brass, which has high thermal conductivity, to uniform the temperature distribution. The surface was nickel plated to prevent corrosion due to the seeded nitric oxide. The burner has a co-flow nozzle to stabilize the flat flame. The flow rate of the co-flow was adjusted to the velocity of the unburned mixture flow. 0.5 mm above the flame holder, an edged metal wall with polished surface was located. It was made of stainless steel, with a cooling-water channel inside. The cooling-water temperature was kept at 60°C. Four thermocouples were embedded close to the surface.

Multi-line NO-LIF thermometry was applied to measure the gas-phase temperature as close as possible at the wall surface. The horizontal laser sheet passed over the flame-holder. The cross-section of the light sheet was ~3×0.2 mm² at the burner center. It was arranged at a small angle $\theta < 1°$, relative to the metal wall surface (cf. Fig. 64 b) to prevent blind spots close to the surface. For the same reason, a 45° mirror was shifted

slightly towards the CCD camera to observe the illuminated plane at an angle that slightly deviates from 90°. Therefore, the field of view included not only fluorescence images on the horizontal cross-section, but also the mirror images from the wall surface.

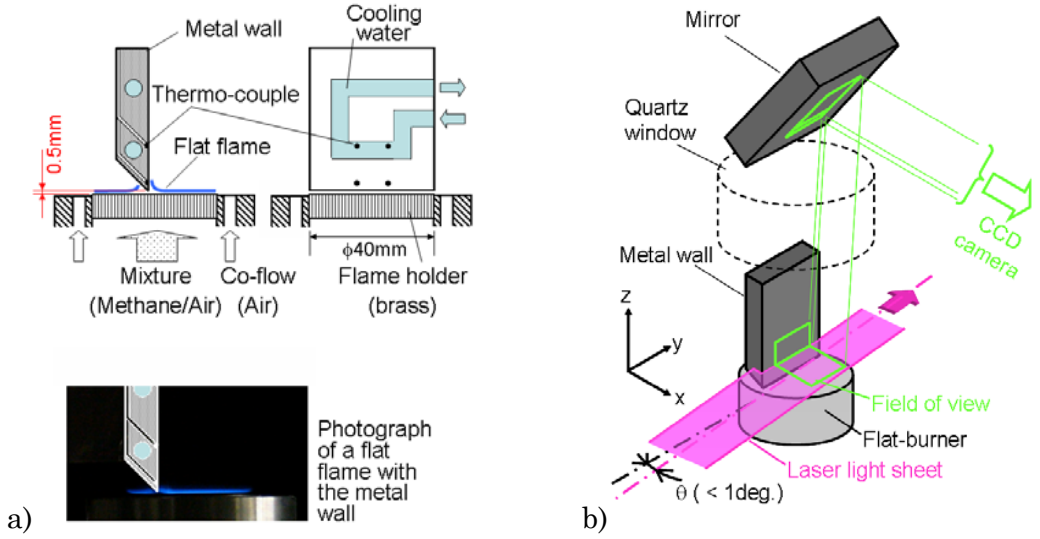

Fig. 64: a) Structure of the flat flame burner and the metal wall. b) Details for the application of laser diagnostics.

Excitation spectra were obtained with 0.2 cm^{-1} spectral resolution using scan range C (Table 6, 44406 – 44425 cm^{-1}). At each wavelength position, LIF signals of 50 images were averaged. A UG 5 filter separated the signal light from elastically scattered light and other interference. LIF signals were focused (Halle, f = 300 mm achromatic UV lens) onto an ICCD camera (Image Intense, LaVision) with 100 ns exposure time. Eight rows of pixels were binned on the y-axis to enhance the signal level.

Temperature images were obtained in the xy-plane (Fig. 64 b) for different heights z (0.5 – 14 mm, 0.5 mm resolution), above the burner nozzle and compressed on the y-axis to obtain one x-profile. These one-dimensional temperature distributions on the x-axis at different heights z were combined and interpolated to generate a 2D-image in the xz-plane as shown in Fig. 65.

The detection of the wall position is important to achieve high spatial accuracy. The raw LIF images and the evaluated temperature fields were obtained with the wall position within the visible area. Accordingly, a mirror image was obtained at the other side of the wall due to the polished metal surface of the quenching wall. The position of the lowest temperature in the image was considered as the wall position, because the temperature must be the lowest on the cooled wall. The dispersion of the lowest temperature position was ± 3 pixels (± 0.01 mm).

Temperature distributions close to the wall surface were measured with the flame operated at two different flow-rates: 7.5 l/min (case 1) and 15 l/min (case 2), yielding mean flow velocities of 6 cm/s and 12 cm/s respectively. The equivalence ratio of the lean flames was $\phi = 0.9$ in both cases. The concentrations of seeded NO were 1000 ppm. Fig. 65 shows the resulting temperature distributions. The pairs of narrow black lines indicate the position and thickness of the laser light sheets. The temperature distributions between the lines were interpolated. In each case, the flat flame was bent upward by the metal wall, and the left edge of the flame was lifted to approximately 2 mm above the flame holder. From this height, the quenching layer thickness increased in downstream direction. The layer thickness at $z = 6$ mm in case 1 is around 1 mm, which reduces by ~50% in case 2.

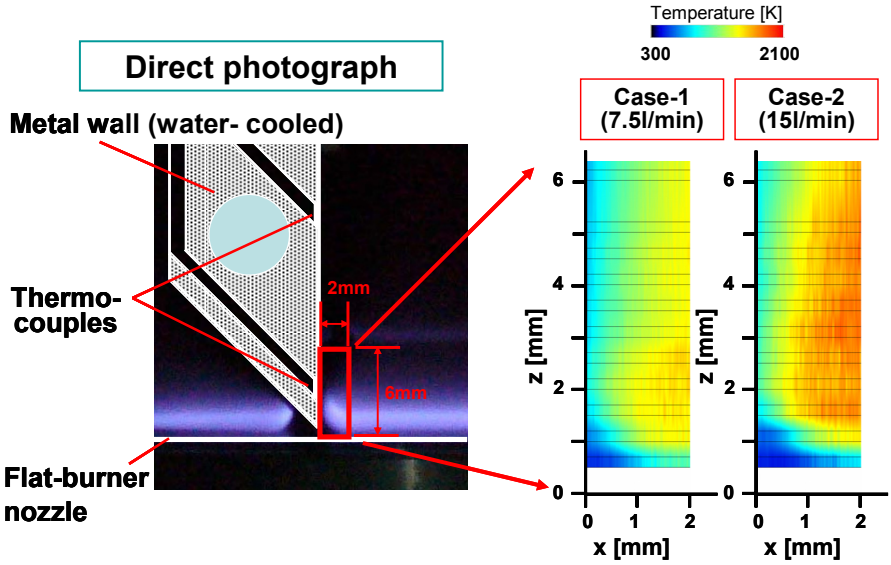

Fig. 65: Close up of the quenched-flame photograph and resulting temperature fields for two cases differing in the total gas-flow rate.

For a quantitative comparison of gas- and solid-phase temperatures close to the wall, 3D graphs were plotted, shown in Fig. 66. The solid lines show the temperature distributions on the wall ($x = 0$). Each small circle shows the average temperature measured by a pair of thermocouples at the same height. Wall temperatures measured by the upper thermocouples were close to the cooling water temperature (333 K) in both cases, because of the short distance between the thermocouples and the water channel.

Note, that the thermocouple measurements do not show the true wall temperature, because the contact points of the thermocouples were located inside the wall, ~0.2 mm away from the wall surface, resulting in a temperature drop within the solid-phase. Therefore, the correct wall surface temperature was measured using thermographic phosphors [56]. Here, the phosphorescence decay time is temperature dependent. Both wall surface temperatures were found to be almost identical (Fig. 66).

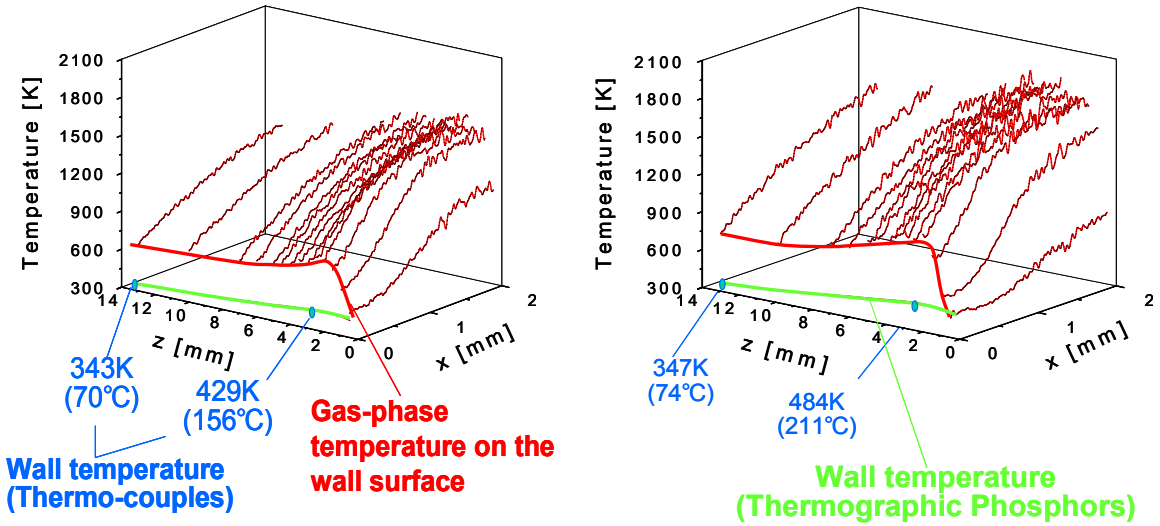

Fig. 66: Quantitative comparison of measured gas- and wall temperatures for case 1 (left, 7.5 l/min) and case 2 (right, 15 l/min).

Maximum flame temperatures further away from the wall exceed 2000 K. A temperature drop is observed close to the wall, where flame reactions are quenched. The distance between the red and the green line in Fig. 66 shows a temperature drop from gas-phase to solid-phase on the wall surface of up to 400 K depending on the height above the burner and the flow rate. A maximum difference is found at the flame front position at about 2 mm height.

From a thermodynamic point of view, the temperature in the gas phase directly at the wall should be identical to the wall temperature. No temperature drop should be observed. The difference is partially caused by the insufficient spatial resolution of the measurements that cannot resolve the steep temperature gradient close to the wall. The spatial resolution was ~29 µm as determined with a 1951 USAF resolution target. This resolution is based on the following contrast function CTF = $(I_{max}–I_{min})/(I_{max}+I_{min})$ = 0.05. This means that two neighboring bright lines on a dark target with a distance of 29 µm can be resolved in an image such that the intensity between these lines drops by ~10%.

In order to quantify this blurring effect on the temperature results, NO-LIF images were simulated assuming a temperature of 600 K at the wall (Fig. 67). These images were convoluted with the assumption of a Gaussian-type contrast function determined from the CTF determination, which blurs the LIF intensity gradients in the images, especially close to the wall position. From the resulting LIF images, excitation spectra were obtained and fitted to derive the temperature (cf. section 4.1.2). The results in Fig. 67 show that, with a spatial resolution of 29 µm, the resulting temperature at the wall is measured as 785 K instead of the real 600 K.

The spatial resolution should be improved further in order to measure a continuous temperature profile at the wall surface. However, the insufficient spatial resolution

accounts for only ~200 K of the much larger (400 K) temperature difference observed in Fig. 66. This difference is subject of further investigations.

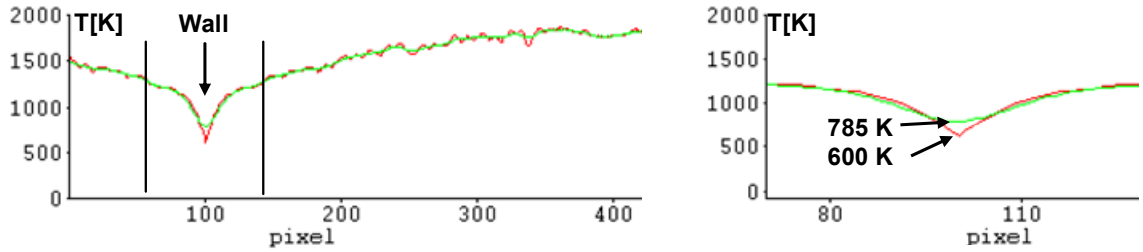

Fig. 67: Influence of the spatial resolution in LIF thermometry. The simulated wall temperature of 600 K (red line) is evaluated as 785 K (green line) due to a limited spatial resolution of 29 µm. The right part is a magnification of the left graph.

5.4.2 Concentration imaging in the quenched flame

In the surface boundary layer of a wall-quenched flame, the combustion process is interrupted and thus, intermediate flame species such as formaldehyde (H_2CO) and CO should be present. Also, the OH distribution is of interest, since it indicates the position of the flame front. All LIF-species measurements presented here were done by B. Lewerich and T. Fuyoto. The OH-LIF distribution was obtained with 248.46 nm excitation of the $A \leftarrow X(3,0)$ $P_2(8)$ transition and detection at 295 nm [241]. CH_2O-LIF was measured with 339.23 nm excitation in the $A^1A_2 \leftarrow X^1A_1$ band [242]. CO-LIF was detected by two-photon excitation at 230.117 nm in the $B^1\Sigma^+ \leftarrow\leftarrow X^1\Sigma^+$ band with detection at 482 nm in the $B^1\Sigma^+ \rightarrow A^1\Pi$ band. Results are shown for the high flow-rate case 2 in Fig. 68.

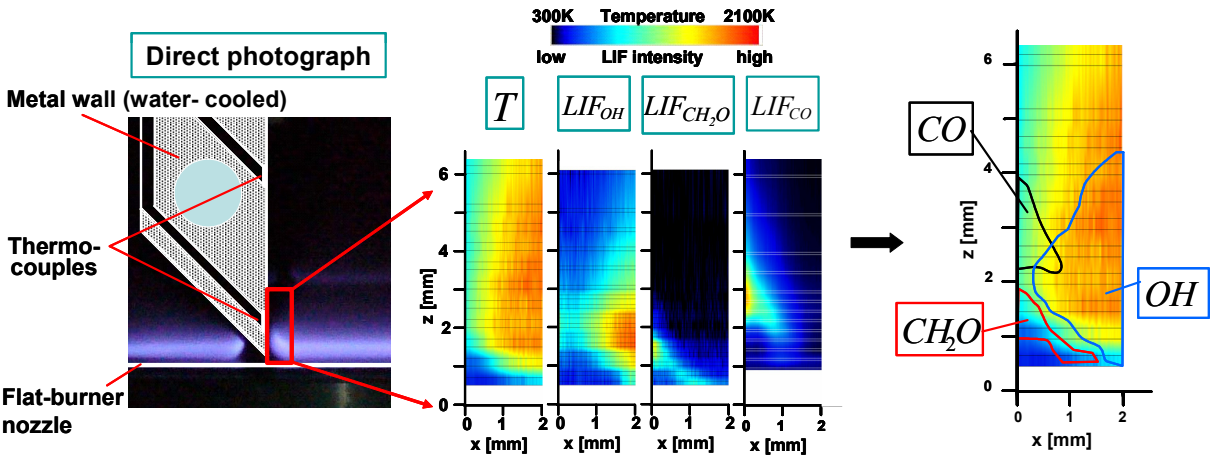

Fig. 68: LIF signal distributions of OH, CH_2O, and CO in the quenching boundary layer overlaid with the temperature field.

OH is found primarily in the hot regions of the free flame close to the flame front. CH_2O and CO are present in regions close to the wall. When overlaying the temperature field and the species distributions, the retarded chemical reaction path way is visible within the boundary layer (Fig. 69). Methane reacts to CH_2O at 1 – 2 mm above the burner. Further oxidation to CO occurs further downstream at 2 – 4 mm height. Complete oxidation to CO_2 is not achieved within the observed 6 mm height. Even higher CO concentrations are found in the low flow-rate case 1, since the temperature is lower.

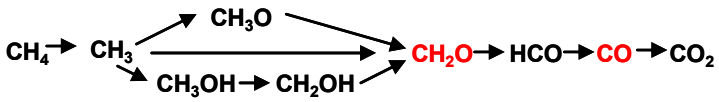

Fig. 69: Reaction path way for complete methane oxidation. The measured species are high-lighted.

In principle, the combination of temperature and LIF measurements enables quantitative concentration measurements, because the obtained LIF signals can be corrected for their temperature dependence. However, more research is necessary in order to obtain quantitative concentration data by interpretation of the raw e.g. OH-LIF intensity distribution. Minima of OH-LIF are not found on the wall, where they are supposed to be the lowest, but 0.4 mm away from the wall. The OH-LIF intensity on the wall is higher by ~10%. This is probably caused by the variation of the effective fluorescence lifetime in the near-wall region. Here, the density of combustion products such as H_2O, which are strong quenchers of fluorescence, decrease in the vicinity of the surface because of a variable gas composition in the quenched area. This leads to a variation in fluorescence quantum yield (cf. section 3.1.1). 2-D numerical simulations of the major combustion species are necessary to account for these effects.

5.5 Relevance of temperature during nano-particle synthesis

Low-pressure premixed flames are a promising route for the synthesis of nano-sized semi-conducting metal-oxide particles. Materials including SnO_2, TiO_2, and ZnO are widely used for gas-sensing devices, photo-catalysis and (opto)electronic devices. The temperature-time history of the nano-particle formation within the flame is an important factor that influences particle size, morphology and crystallinity. Therefore, detailed information concerning the gas-phase temperature distribution within the reaction chamber is of specific interest [243]. The flame temperature must be known in order to numerically simulate nano-particle formation based on kinetic modeling. It depends on the fuel/air ratio, the dilution by inert gases, the precursor (i.e. metal-organic species carrying the desired metal atoms), and the total pressure. It also varies with the thermal management of the reactor, e.g. a cooled sinter matrix at the gas inlet and cooling at the reactor walls. The results of this section were published in [146,168] and the data was taken to validate numerical simulation codes for nano-particle formation developed by A. Kowalik and Prof. P. Roth at the University of Duisburg-Essen [184,244].

5.5.1 Experimental setup

In this experiment, the scanning multi-line NO-LIF thermometry approach was applied for the first time to a low-pressure flame. 200 ppm NO were added to the fresh gases, since there is no natural NO production in a H_2/O_2/Ar flame. This small amount did not show any disturbance of the lean flame and ensures negligible laser attenuation by NO inside the reactor. The laser attenuation was below 0.2% over the 10 cm cross-section of the apparatus for the strongest absorption feature. The spectral range C (Table 6, 225.19 – 225.10 nm) was chosen for acquiring excitation spectra, shown in Fig. 70.

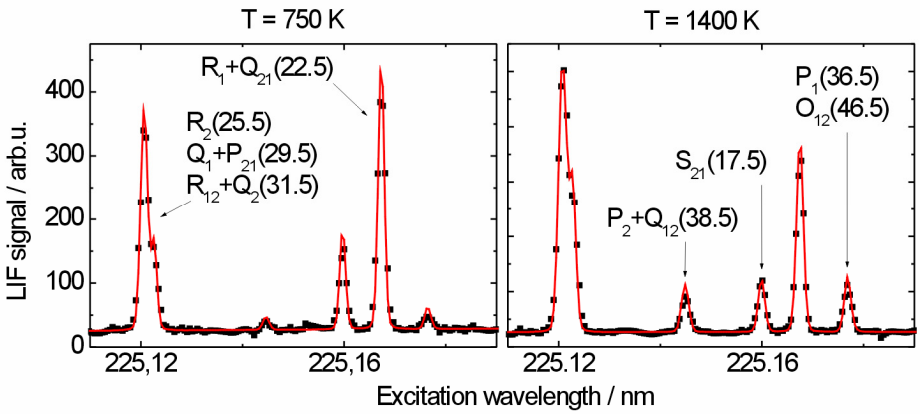

Fig. 70: Experimental (symbols) and the fitted simulated (lines) excitation spectra for two different temperatures. The labels show the respective rotational transition in the NO A-X(0,0) band.

For each scan, images at 191 wavelength positions, each averaged over 50 laser shots, were taken at equal spectral intervals of 0.1 cm^{-1}. The laser energy was monitored on a shot-by-shot basis, and the LIF signal intensity was corrected linearly. The full data set is acquired within a few minutes. The precision of the temperature measurements is better than ±1%. This was derived from the root mean square (RMS) deviation of the temperature values inside a homogeneous area of each temperature field. Multiple measurements were conducted to ensure reproducibility, which was found to be in the ±1% range, if care was taken in stabilizing the thermal management of the reactor.

The laser beam is formed to a relatively thick light sheet of 50×10 mm^2 in order to avoid saturation of the LIF signal (4.1.6). The LIF signal is focused with a Halle, $f = 200$ mm, achromatic UV lens onto an ICCD camera (Image Intense, LaVision, Table 8). Elastically-scattered light is suppressed by three long-pass filters (230 nm, LayerTec, Table 9). This ensures a high signal-to-noise ratio of the excitation spectra even with low NO concentrations of 200 ppm and a low laser fluence of 4 kW/cm^2. The general setup is described in section 4.1.2, an overview of the reactor is given in Fig. 71.

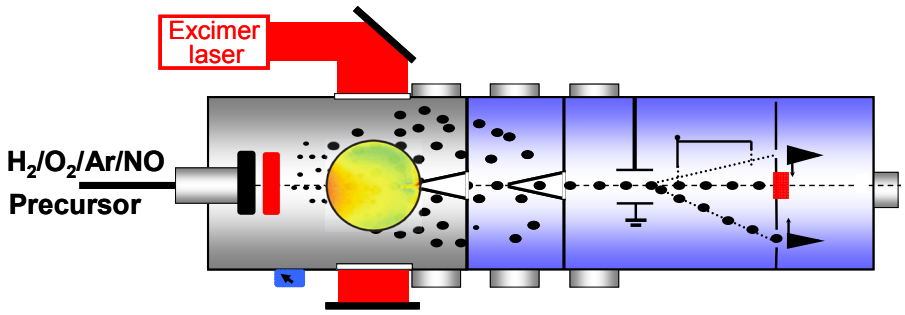

Fig. 71: Horizontal cut through the flat-flame reactor (left) and the particle mass spectrometer (right). Optical access is given through quartz glass windows.

The flat-flame reactor is described in detail elsewhere [245]. The 36 mm diameter sintered metal-plate burner head was centered in a 300 mm long, horizontally mounted, metal tube with a diameter of 100 mm. Optical access is possible through fused silica windows (50 mm diameter) from three sides. The burner head can be moved horizontally with respect to a reference position, where a skimmer nozzle extends into the reactor to enable online particle size measurements. Hydrogen is used as fuel, oxygen as oxidizer and the mixture is diluted with argon. Typical flow rates for e.g. TiO_2 nano-particle production are 600 sccm H_2, 800 sccm O_2, 500 sccm Ar, and 200 ppm of the precursor Titanium-Tetraisopropoxide (TTIP). The fuel/air ratio of this lean mixture is $\phi = 0.375$. The flow velocity inside the reactor reaches a few m/s.

A particle mass spectrometer is attached to the flame chamber in order to enable online characterization of the particles. The particles are separated by two skimmer nozzles in the center of the reactor. The flow is expanded into high vacuum to stop

particle growth. The supersonic particle-laden molecular beam is then analyzed by the mass spectrometer to obtain size distributions.

5.5.2 Results and discussion

Influence of nano-particle formation on the temperature distribution

The gas-phase temperature field was measured in the H_2/O_2/Ar/NO/TTIP flat flame of the reactor by moving the burner nozzle relative to the window position and with signal detection at the same position for five different burner distances. Fig. 72 a) shows the resulting temperature distribution in a 175×50 mm^2 horizontal area of the flame inside the reactor for typical operating conditions at a pressure of 3 kPa.

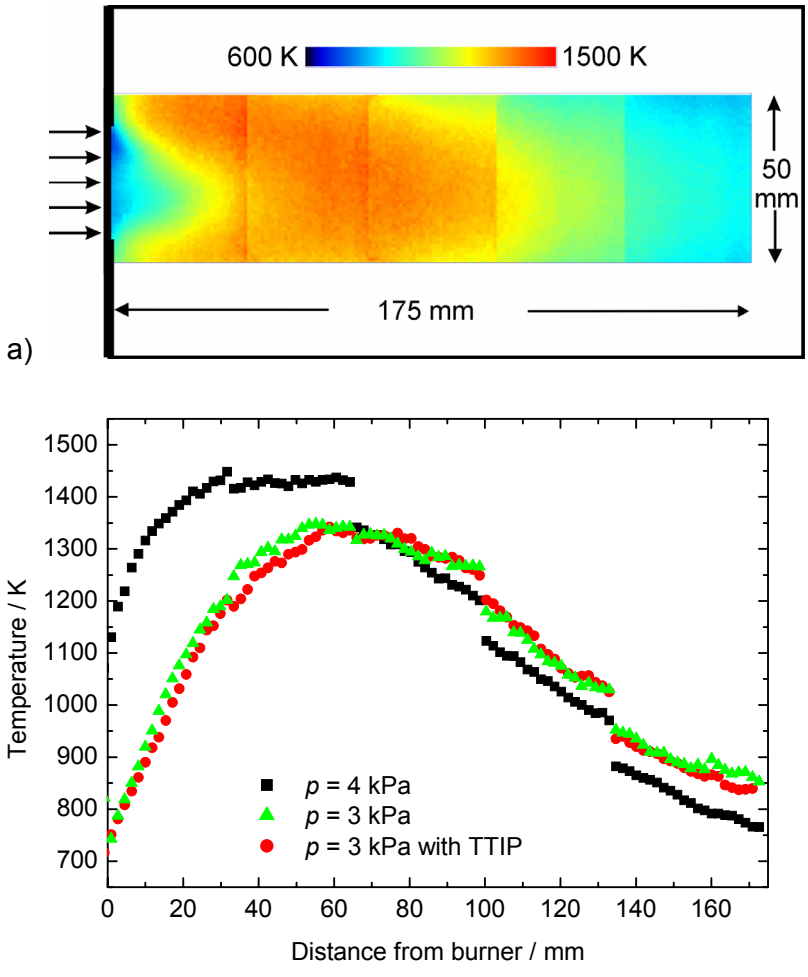

Fig. 72: a) Temperature distribution in a horizontal plane inside the reactor for p = 3 kPa; b) Temperature as a function of distance from the burner head for the centerline of the reactor. Steps in the profiles result from the measurement procedure and are not caused by noise.

The spatial resolution in the horizontal plane is 1×1 mm^2, with a light-sheet thickness of 10 mm. The burner head is situated on the left side, where the incoming cold

premixed fresh gas is located. Fig. 72 b) shows temperature profiles along the centerline of the reaction chamber for three different conditions. Because of the light sheet thickness of 10 mm, we integrate the signal within a 10 mm wide area around the centerline in Fig. 72 a). At a pressure of 4 kPa, the fresh gas is heated up by the flame reactions, until a maximum temperature of 1430 K is reached at about 40 mm distance from the burner surface. After that, the post-flame gas cools down to 750 K at 175 mm distance.

At 3 kPa, which is typically used for TiO_2 nano-particle production, the flame front extends about 60 mm into the reaction chamber and the maximum temperature is only 1340 K. After 80 mm distance from the burner head, the burnt gas temperature decreases with a similar rate for both pressures. At lower pressure, the gas temperature at the end of the observation zone is higher, since the residence time inside the chamber is shorter, and consequently the heat transfer to the walls is lower. The measurement procedure by moving the burner head and detecting at the same position can lead to steps in the temperature profile due to an increasing cooling surface between the burner head and the detection position.

Measurements were done with and without the addition of TTIP. It was found that the precursor decomposition, the oxidation of the side chains and the nano-particle generation process do not influence the temperature field within the measurement precision for the titanium system at our precursor concentration of 200 ppm. The NO-LIF signal strength is identical with and without TTIP addition, even for NO concentrations lower than the TTIP concentration, which proves that NO is chemically inert and does not react with TTIP in an e.g. ligand exchange reaction.

The effect of different NO concentrations on the temperature measurements was investigated and is shown in Fig. 73. The NO concentration was varied between 100 and 1000 ppm while all other parameters were kept constant. No effect on the temperature results could be detected within the observed concentration range. The standard deviation of the measurements increases with lower NO concentration because of the lower signal-to-noise ratio of the excitation spectra. This effect can be compensated by increasing the averaging of the LIF images over a larger number of laser pulses. Parameter studies further show that a richer flame with a fuel/air ratio $\phi = 0.667$ has a slightly higher maximum temperature than the $\phi = 0.375$ case.

In stabilized, premixed atmospheric-pressure flat flames, the flame front is situated close to the sinter matrix (cf. Fig. 64 or Fig. 78). In this low-pressure flame, the heating zone is stretched as far as 60 mm into the reaction chamber. This enables a homogeneous heating even of highly diluted precursor/gas mixtures, and supports the formation of small and only softly agglomerated nano particles. Particle formation starts instantaneously after the decomposition of the precursors by condensation, growth, coagulation, agglomeration, and sintering. Depending on the time the particles travel through the reaction zone, their size and morphology are different [246].

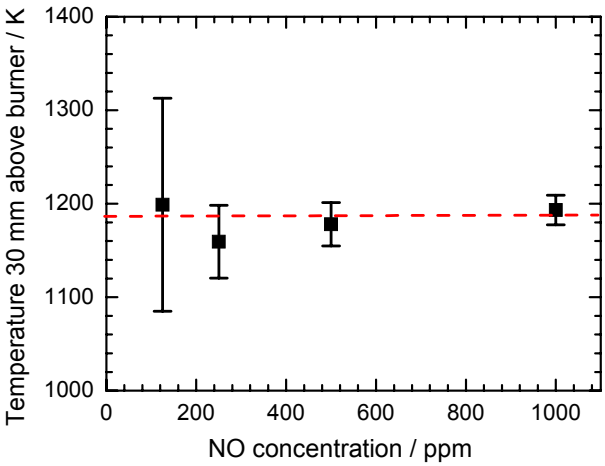

Fig. 73: A variation in NO concentration does not influence the measured temperature at 30 mm distance from the burner head.

It was proven that the multi-line NO-LIF technique is capable of providing accurate temperature data during nano-particle synthesis without influencing the nano-particle generation process. This permits a detailed investigation of the effect of nano-particle synthesis on the temperature inside the reactor for other precursors than TTIP in future work. $Fe(CO)_5$ is used to produce iron oxide particles. The production of metal oxides is a strongly exothermal process that releases heat. Nevertheless, the addition of several 100 ppm of precursor does not significantly influence the overall heat release of the flame. Hence, no major change in the temperature distribution is expected in the presence of precursors.

On the other hand, the precursors may affect the chemical reactions in the flame by influencing the rates of elementary reactions as known from effective flame quenchers like ferrocen and $Fe(CO)_5$, where gas-phase iron compounds like FeO and FeOH react in catalytic cycles with flame carrier radicals like H and OH. The super equilibrium concentrations of these radicals are reduced towards their equilibrium values, resulting in a reduction in flame speed [247]. This could indeed affect the overall chemical reactions, spatially shift the flame front and, hence, the temperature distribution.

Nano-particle flame-synthesis reactor design

Experiments were performed to actively control the temperature distribution inside the reactor in order to enable tuning of nano-particle specifications. A second reactor was set up in which the burner chamber was expanded from 100 to 150 mm diameter. Multi-line NO-LIF thermometry was used to measure the temperature distribution inside this reactor with identical equipment and conditions as described above. The temperature distributions in a horizontal plane in the center of both reactors are shown in Fig. 74 a) as well as a quantitative comparison of the central 10×10 mm^2 in Fig. 74 b).

With a new sinter matrix, the fresh gas zone at the left side is larger, colder, and symmetric. In the upper temperature field, the sinter matrix was partly congested in the center since it was used a long time for nano-particle generation. Larger cold zones were found at the edge of the matrix above and below the central line (not shown here). Maximum temperatures were ~1340 K at a distance of 60 – 70 mm from the burner head under both conditions shown in Fig. 74. The right part of the temperature profile represents the exhaust gas zone after complete combustion. The rate of cooling depends on heat transfer to the walls of the reactor and is significantly higher with a smaller chamber. The gases in the 100 mm diameter chamber cool down to 900 K at a distance of 150 mm, whereas the gases in the larger chamber stay above 1200 K at this distance.

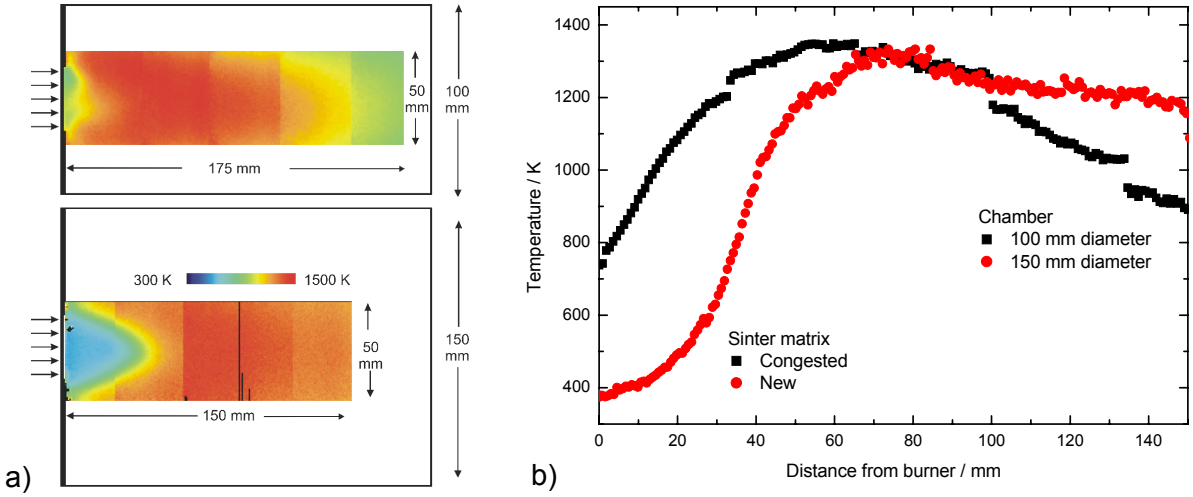

Fig. 74: a) Temperature distribution in a horizontal plane inside both reactors with 100 and 150 mm diameter indicated by the black frames; b) Temperature as a function of distance from the burner head for the centerline of both reactors.

5.5.3 Comparison of NO LIF and H_2O TDLAS

Multi-line NO-LIF thermometry (section 4.1) yields spatially-resolved temperature information in contrast to two-line H_2O TDLAS (section 4.2), that yields line-of-sight temperature information. For a quantitative comparison, both techniques were applied to measure the temperature in the low-pressure $H_2/O_2/Ar$ flame of the 150 mm diameter reactor described in the previous sections capable of nano-particle synthesis under identical conditions. The NO-LIF thermometry results were shown in Fig. 74.

The setup for TDLAS thermometry in the low-pressure flame is shown in Fig. 75 for a single-pass arrangement. The sensor described in section 4.2 was used. For the actual measurements, a double-pass configuration was realized with a mirror on one side of the reactor and laser collimation and detection on the other side to increase the signal-to-noise ratio of the absorption spectra. Also, wedged windows (2°) were installed in an

angle of 15° in order to avoid etalon effects while transmitting the laser beam. The path length in room air was kept small in order to avoid absorption by water in ambient air.

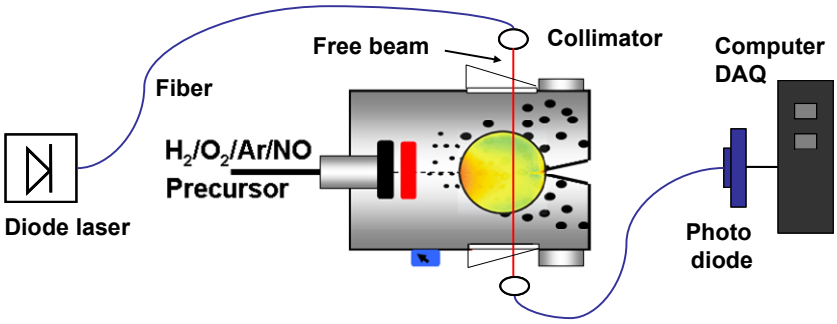

Fig. 75: Experimental setup of H_2O-TDLAS thermometry applied to a low-pressure flat-flame nano-particle synthesis reactor. The area accessible with NO-LIF is indicated.

Experimental spectra as well as the fit results are shown in Fig. 76 for measured temperatures of 700 K and 1100 K. The maximum absorbance is about 1% and 4% for the high and low *E"* transition peaks, respectively. For low temperatures the absorption is even smaller than 1%, which makes it difficult to clearly separate the small absorption peak from the overall transmission signal by fitting a baseline (cf. Fig. 46) to the raw data. However, compared to spectra at atmospheric pressure shown in Fig. 46, both peaks are well separated from interfering peaks at p = 3 kPa, and a precise evaluation is possible.

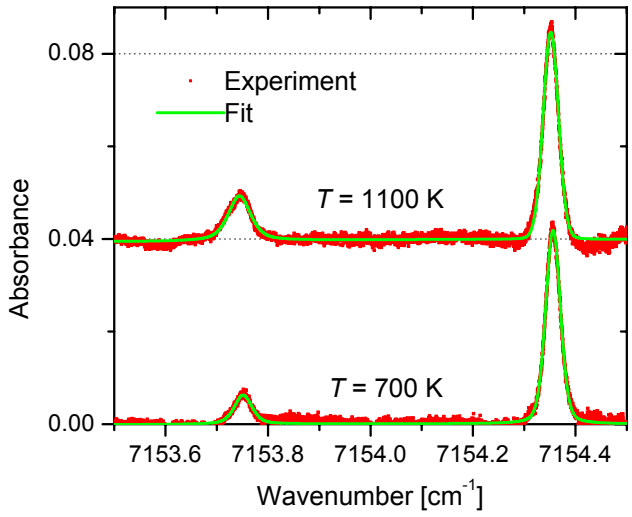

Fig. 76: Experimental (dots) and fitted (line) H_2O TDLAS absorption spectra measured in the low-pressure $H_2/O_2/Ar$ flame at 3 kPa.

The resulting temperature profiles obtained by both methods are shown in Fig. 77. Both methods show a strong increase in temperature within the first 50 – 70 mm and a

slight decrease later. The NO-LIF temperature profile represents the temperature of the central 10×10 mm² of the reactor. The H_2O-TDLAS temperature measurements represent the line-of-sight temperature along the absorption path between both windows. There is no coflow. Hence, water is present in the entire chamber. The RMS standard deviation of ten repeated measurements is about ±20 K and is plotted as error bars.

On the left side of the profile, the fresh gas temperature is measured by NO LIF to ~400 K. However, there is no water present before combustion. Therefore, the H_2O-TDLAS measurement of ~700 K represents an average of the flame zone at the edge of the burner outlet (cf. Fig. 74 a) and the colder regions close to the windows of the reactor that are not accessible with NO LIF. Later in the flame, NO-LIF temperatures are around 1200 K, whereas H_2O-TDLAS results show ~900 K. The lower value is explained by averaging the central flame zone and the much colder regions close to the windows.

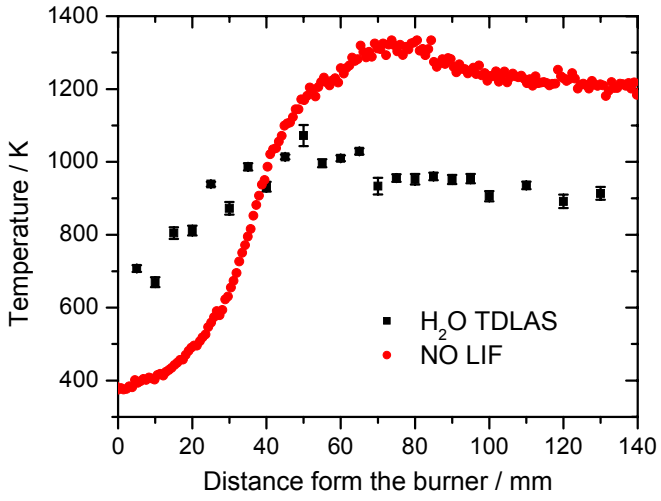

Fig. 77: Temperature against distance from the burner measured with NO LIF and H_2O TLDAS.

Due to the line-of-sight nature of this two-line TDLAS sensor, only averaged temperatures can be obtained in such inhomogeneous systems. Worse, the obtained average does not represent the average of the real temperature distribution but only the average of the absorbances at different temperatures, since the absorbances for the used transitions are strongly non-linear with temperature (cf. Fig. 43 a), especially within the observed temperature range (400 – 1300 K). The resulting uncertainty on the averaged temperature could be obtained similar to the procedure explained in section 4.1.5.

A probability density function of the spatial temperature distribution can in principle be obtained by using a TDLAS sensor accessing more than two transitions with different ground-state energies simultaneously. Such a sensor is currently setup and will be used in future work [117].

5.6 A flame as fuel reformer for a solid-oxide fuel cell

Fuel cells are a promising technology for a high-efficiency conversion of chemical energy carriers to electricity by electrochemical reactions, thus providing an excellent way to save fossil fuels in the future. For the utilization of hydrocarbon fuels, a reformer unit is usually required to generate CO/H_2 enriched gas mixtures. This, however, makes fuel cell systems more complex, more expensive and less efficient. In cooperation with Shinko Electric Industries, Japan, and with Prof. J. Warnatz as well as W. G. Bessler (Interdisciplinary center for scientific computing (IWR), Heidelberg University), a simple alternative to a reformer is investigated: A direct-flame fuel cell (DFFC) setup.

The operation principle of a DFFC is based on the combination of an open flame with a solid-oxide fuel cell (SOFC) in a simple, "no-chamber" setup [248] illustrated in Fig. 78. In this system, a fuel-rich flame is placed a few millimeters from the anode. It serves as partial oxidation reformer while at the same time providing the heat required for SOFC operation. The cathode is freely exposed to ambient air. Flame and fuel cell are geometrically and electrochemically coupled. The goal of this configuration is not to replace existing reformer technologies but to generate (additional) electricity in existing combustion systems in a combined heat and power setup. Results obtained so far were published in confidential reports to Shinko and in [185,249,250].

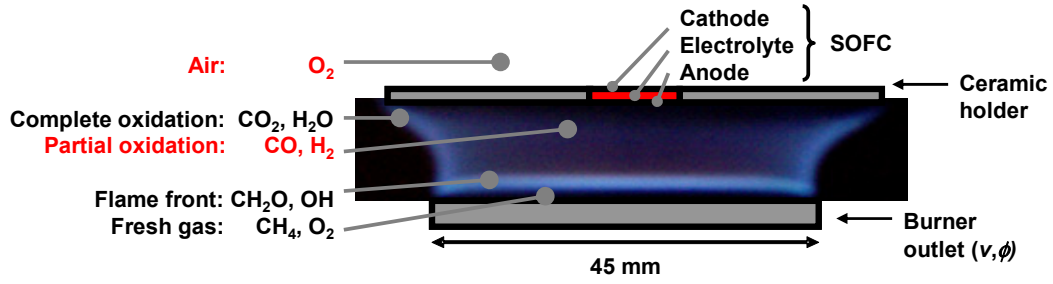

Fig. 78: Operation principle of a direct-flame fuel cell (DFFC). The species consumed by the SOFC for electricity generation are high-lighted.

In Fig. 78, the flame chemistry is sketched: The rich fuel/air mixture reacts within the primary flame front, which is only a fraction of a mm thick [18]. From detailed studies of flame structure and chemistry it is known that the exhaust gases of rich ($\phi > 1.0$) premixed hydrocarbon/air flames consist of a mixture of mainly N_2, CO_2, H_2O, CO, and H_2, while molecular oxygen present in the fresh gases is consumed nearly quantitatively within the flame front [18,251,252]. This is generally true for all kinds of hydrocarbons, including alcohols, liquid and solid fuels.

In order to assess the nature of fuel species available for the SOFC, calculations of the equilibrium gas composition and adiabatic flame temperature were performed for

CH_4/air flames of various equivalence ratios $\phi = 0.8 - 1.6$. The upper value corresponds to the inflammability limit [253]. The simulations were carried out with the CANTERA software package [254] using thermodynamic data from the NIST-JANAF thermodynamic tables [255]. The resulting major species and temperatures are shown in Fig. 79. The concentrations of H_2 and CO increase with higher equivalence ratio and together reach values of up to 20% for very rich flames ($\phi > 1.5$). Temperature peaks close to stoichiometric conditions ($\phi = 1.05$) and decreases towards both lean and rich flames. Given these observations, we believe that the chemical compounds that are available at the SOFC anode for conversion into electricity are both, H_2 and CO.

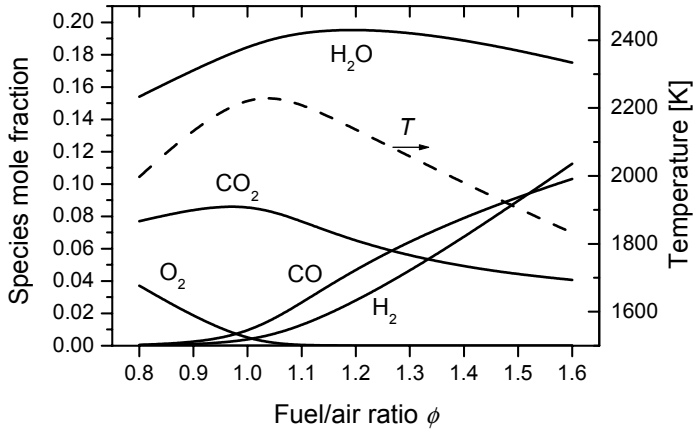

Fig. 79: Equilibrium calculations of major species concentrations and adiabatic temperature for CH_4/air flames of different equivalence ratios.

The exhaust gas of stoichiometric and lean flames ($\phi \leq 1.0$) consists only of fully-oxidized species (N_2, CO_2, H_2O; excess O_2 for $\phi < 1.0$). This explains the observation that the DFFC system does not yield any electrical power when operated with stoichiometric or lean flames: There is simply no fuel available for the fuel cell.

Near the hot flame front, radical species such as H, OH and CHO can be present in the gas phase in the per-cent range. However, closer to the anode surface, the radical concentrations will strongly decrease to the order of parts per million. Although radicals may be highly reactive towards electrochemical oxidation, their low abundance most likely makes their contribution negligible. These issues are discussed in more detail in [250], based on detailed combustion and electrochemistry simulations.

Complete oxidation of the CO and H_2 that is not consumed by the SOFC to H_2O and CO_2 occurs at the side of the setup upon mixture with ambient air in a secondary flame front visible in Fig. 78. The functional principle of an SOFC is explained as follows: O_2 from ambient air is consumed by the cathode. O^{2-} ions are generated and transported through the electrolyte, which is an ionic conductor but an electric isolator. At the anode, the O^{2-} ions react with surface-adsorbed CO or H atoms to generate water and electrons.

- Cathode: $\frac{1}{2}\ O_2 + 2e^- \rightarrow O^{2-}$
- Anode: $H_2 + O^{2-} \rightarrow H_2O + 2e^-$ and $CO + O^{2-} \rightarrow CO_2 + 2e^-$
- Overall reactions: $H_2 + \frac{1}{2}O_2 \rightarrow H_2O$ and $CO + \frac{1}{2}O_2 \rightarrow CO_2$

The overall reactions are identical to combustion of H_2 and CO. However, the electrochemical reactions within the SOFC have the advantage, that the ion transport inside the fuel cell is spatially separated from the electron transport in an electric circuit outside the cell. Therefore, electricity is directly obtained, and the efficiency of a fuel cell system is not restricted to the efficiency of the Carnot cycle, as is the case for common power-plant electricity generation including a combustion process and turbines.

There are a number of advantages to the DFFC approach. First, the system is very fuel-flexible. Because intermediate flame species are similar for all kinds of hydrocarbons, the DFFC can be operated on virtually any carbon- or hydrogen-containing fuels. Horiuchi et al. demonstrated electrochemical power generation using various gaseous (methane, ethane, propane, n-butane), liquid (ethanol, butanol, kerosine), and solid (paraffine wax, wood) fuels [248,256]. Second, the DFFC is operated in a very simple, no-chamber setup. The anode is simply held into the exhaust gases close to a fuel-rich combustion flame. The cathode breathes ambient air. The system is thermally self-sustained, and there are no high-temperature sealing issues. Third, the system is started up rapidly (within seconds). The flame heat release brings the fuel cell rapidly to its operation temperature, and there is no external heater required for start-up. These features make the DFFC an attractive system for energy conversion, in particular for combined heat and power applications.

There are also a number of drawbacks associated with the DFFC type setup. This includes the relatively low overall electrical efficiency. An inherent property of the DFFC is that part of the fuel's chemical energy is consumed in the flame and is therefore not available for electricity generation. Furthermore, material stress is a particular challenge. The operating environment close to a flame can induce significant thermal stress to the SOFC.

The DFFC concept is somewhat similar to the single-chamber solid-oxide fuel cell (SCFC) concept. In the latter, the same premixed fuel/air mixture is supplied to both anode and cathode, and electrochemical fuel oxidation and oxygen reduction is achieved through selective (electro-)catalysts [257-260]. Within the anode, an H_2/CO-rich atmosphere is formed via heterogeneous fuel partial oxidation reactions [261]. In the DFFC, although the setup is even simpler, the two electrodes see different gas atmospheres. The fuel is partially oxidized by homogeneous combustion chemistry several millimeters in front of the anode, while the cathode breathes ambient air. This setup relaxes the catalyst selectivity requirement needed for SCFCs and can therefore operate at higher temperature; it also allows higher concentrations of H_2/CO at the anode and O_2 at the

cathode. Thus, the DFFC system potentially yields increased performance and efficiency. Furthermore, it does not require an external heater for the start-up phase. Finally, because partial oxidation takes place in the gas phase instead of inside the porous electrodes, the coking problems associated with higher hydrocarbons are significantly reduced in the DFFC compared to the SCFC concept.

The idea of using rich flames for the production of synthesis gas via partial oxidation is not new. The approach has been demonstrated by several authors, in particular with the help of porous combustors [262-264]. Kendall et al. have presented a tubular SOFC system with integrated catalytic partial oxidation operated on methane and butane [265,266]. To the best of our knowledge, the use of a free flame to operate a solid oxide fuel cell was first published by Horiuchi et al. [248,256] who demonstrated the feasibility of power generation using a DFFC with a Bunsen-type burner.

5.6.1 Experimental setup

The SOFC is based on a samarium-doped ceria ($Ce_{0.8}Sm_{0.2}O_{2-\delta}$, SDC, approx. 0.2 mm) electrolyte, which is a comparably low-temperature oxygen-ion conductor. The exact composition and the fabrication procedure were published in [185].

A flat-flame burner was used because this kind of burner applies a gas outlet that yields homogeneous gas outflow velocities over the whole area of the burner. Here, this is realized using a water-cooled porous bronze sinter matrix. The resulting flame front is parallel to the burner outlet (Fig. 78). This geometry is well-suited for direct coupling to a planar fuel cell. Furthermore, because characteristic parameters such as species concentrations and temperature in the center region of the burner only show axial, but no radial variation, this setup can be numerically studied using a one-dimensional stagnation-point flow model [250,252]. This allows to calculate species concentrations in the gas phase at the DFFC anode surface [250].

The burner was mounted to a height-adjustable stage with a height resolution of 0.5 mm that allowed conducting experiments with variable distances d between the SOFC and the burner matrix. The burner flame (45 mm diameter) is larger than the SOFC (13 mm diameter) in order to provide homogeneous temperature and gas composition over the complete SOFC area. This setup thus allows electrochemical characterization under defined operating conditions.

The SOFC was centered in the middle of the flame with the anode facing the flame. A 100 mm diameter ceramic disc with a central hole of 13 mm diameter was used as holder for the SOFC. The SOFC was glued to the disc with the aid of a high-temperature stable ceramic glue (Kerathin K 1800). This setup is completely gas-tight. It was used to avoid convection or diffusion of flame gases from the large-diameter burner to the cathode side.

The temperature of the upper ceramic disc surface was measured by a surface thermocouple (NiCrNi) right next to the SOFC as shown in Fig. 80. The temperature at the disc surface was found to be only slightly higher (ca. 40 K) than the temperature measured directly at the cathode surface of the SOFC. Also, the H_2O-TDLAS sensor described in section 4.2 was applied to measure the gas-phase temperature within the partial oxidation zone of the flame close to the SOFC anode surface (Fig. 80). Results of the temperature measurements are discussed in section 5.6.3.

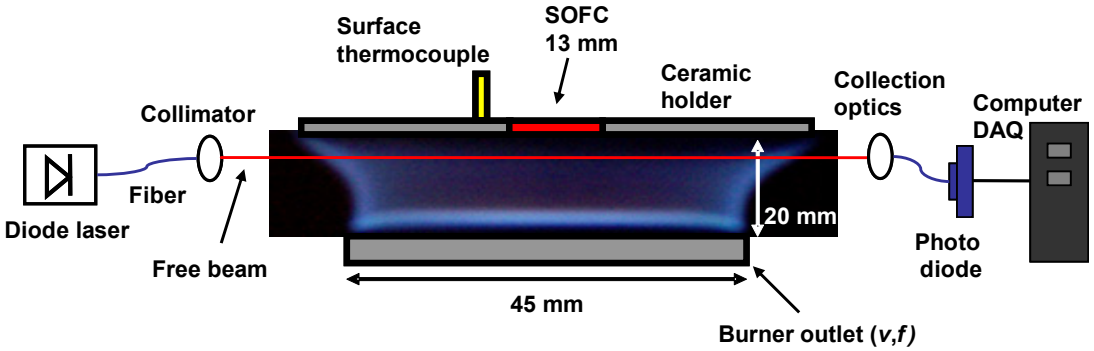

Fig. 80: Temperature measurements in the DFFC system with laser diagnostics and thermocouples.

5.6.2 Electrochemical characterization

An automated test facility (Basytec) was used to acquire polarization curves. A single polarization curve measurement was acquired during ~100 s. This slow acquisition was performed in order to give the dynamic processes at the SOFC electrodes time to adjust to steady-state while changing the working current. Flame operating conditions, such as equivalence ratio, fuel inflow velocity, and distance between burner and SOFC were varied in order to investigate the influence of these parameters on SOFC performance.

Premixed methane/air, propane/air and butane/air flames were investigated over a wide range of equivalence ratios ($\phi = 1.0 - 1.9$), gas inflow velocities ($v = 10 - 30$ cm/s) and distances between burner and SOFC ($d = 5 - 20$ mm). For each condition, a current-voltage curve and the cathode surface temperature were recorded. It was generally observed that for stoichiometric or lean flames ($\phi \leq 1.0$) the SOFC did not yield any power output (open circuit voltage = 0 V), since the fuel was completely burnt in the flame. Electrical power could be drawn only for rich flames ($\phi > 1.0$).

Typical current/voltage curves are shown in Fig. 81 for methane/air flames for varying ϕ and d at $v = 20$ cm/s. The open circuit voltage (OCV) is around 0.8 – 0.9 V, which is a typical value for the mixed ionic-electronic conducting electrolyte (SDC) used here, where the electronic current leads to a short-circuiting of the SOFC and reduces the cell voltage [261,267]. The current/voltage curve is almost linear, with a typical maximum

current density of ~400 mA/cm² and a maximum power density of 80 mW/cm² at a cell voltage of 400 mV. The full data set for all fuels is available in [185]. In the following, the experimental results are discussed in terms of the maximum power density that could be reached in each case. The maximum power density for all methane/air flames is plotted versus ϕ, v and d in Fig. 82.

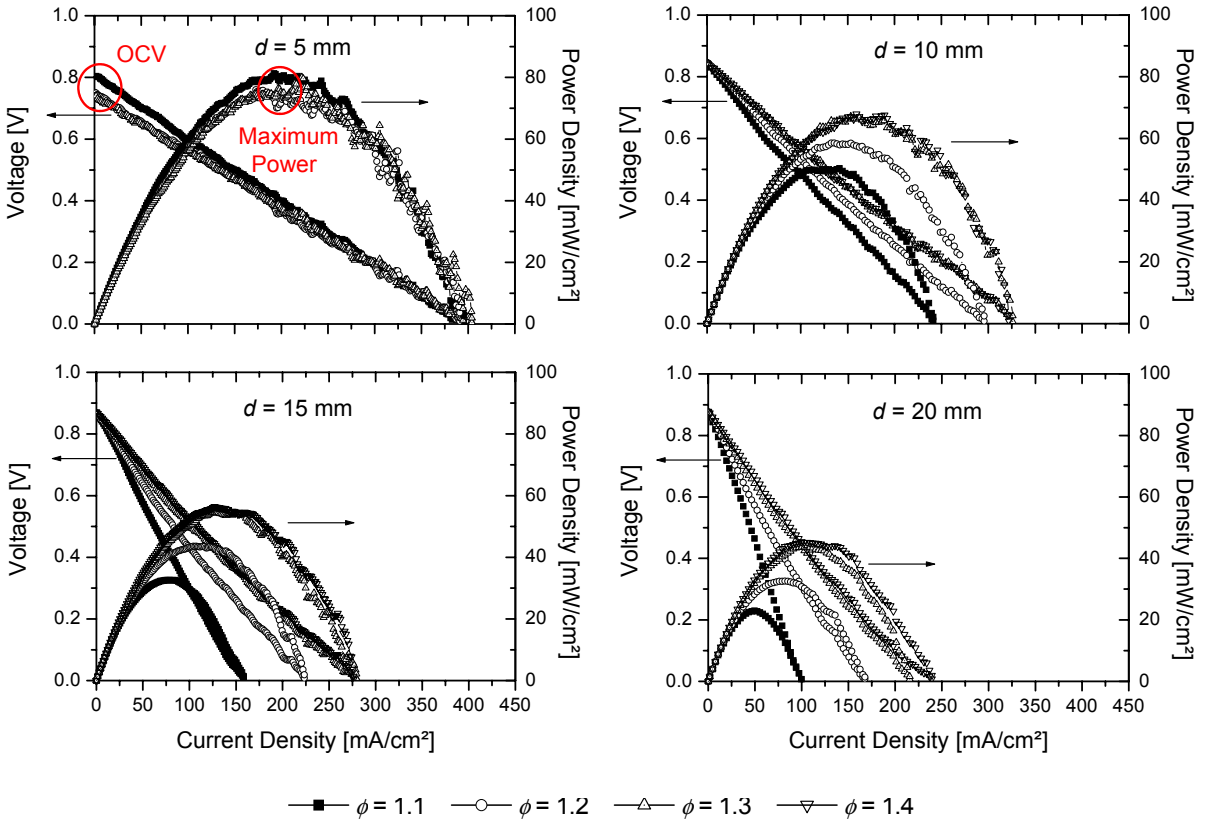

Fig. 81: Polarization curves of a DFFC system operated on methane for 20 cm/s gas inflow velocity for different distances from the burner (indicated in the figures) for equivalence ratios ϕ = 1.1 – 1.4. The OCV and the maximum power density are indicated in the first graph.

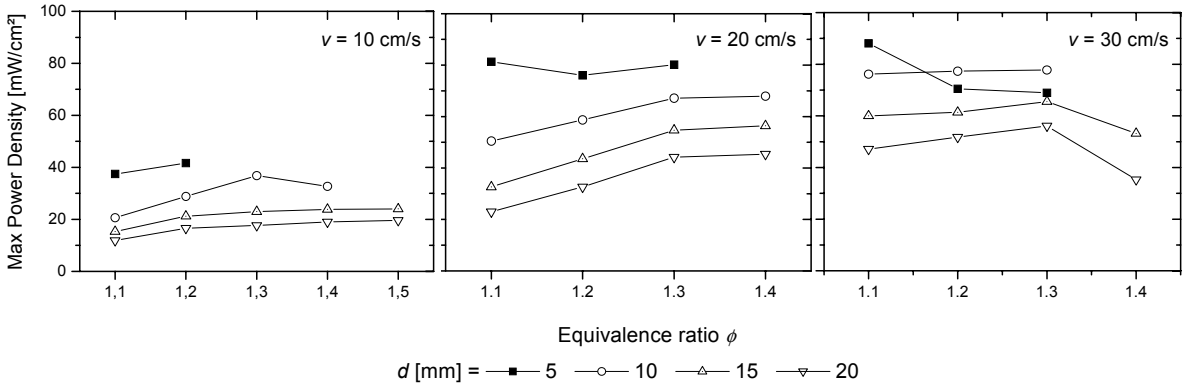

Fig. 82: Methane-operated DFFC: Maximum power density versus equivalence ratio ϕ, distance between burner and SOFC d, and gas inlet velocity v.

The general trend that is observed is an increase in power density with increasing ϕ, increasing v and decreasing d. However, there is some scatter, in particular at high ϕ, high v and low d, so that a simple maximization of ϕ and v and minimization of d does not lead to the highest performance. The apparently missing data points are conditions where the flame was either unstable or could not be lighted at all.

It should be noted that these experiments were not designed to reach maximum power output but to provide defined conditions at the SOFC. For higher gas inflow velocities, and thus increased fuel cell temperature, power densities of up to 200 mW/cm^2 were reached [249].

5.6.3 Temperature relevance in the DFFC system

The SOFC power output is extremely dependent on the cell temperature. At ambient temperature, no power output is observed because the ion conductivity of the SDC electrolyte is very low. The O^{2-} conductivity in this Perovskite-type ceramics is due to oxygen vacancies in the crystal lattice structure induced by dopants. It increases with higher temperature due to the rising structural instability of the lattice enabling oxygen ion (vacancy) transport. The surface reactions at the cathode and the anode exhibit strong temperature dependence as well. Therefore, it is important to quantify the temperature influence on the DFFC power output to understand and optimize the system.

H_2O-TDLAS temperature measurements

The H_2O-TDLAS two-line thermometry sensor described in section 4.2 was applied to measure the gas-phase temperature of methane/air flat flames with the setup shown in Fig. 80. A plate was fixed 20 mm above the burner outlet and the temperature was measured at 15 mm height above the burner. In order to raise the signal-to-noise ratio of the absorption spectra, the absorption path length was increased; a double-pass arrangement was realized with the laser collimation and collection at the same side of the burner and a mirror at the other side.

The free beam path length in room air was kept small so that absorption by water in ambient air could not be detected. Typical experimental absorption spectra obtained in the flame as well as the Voigt fit of the three peaks are presented in Fig. 83 for temperatures of 1100 and 1700 K. The areas A_i used for two-line thermometry are indicated. As expected, the area A_1 belonging to the high E'' transition is smaller than the area A_2 (cf. Fig. 43 and Table 11). Also, A_1 decreases strongly with lower temperature.

The temperatures measured in the flat flame of the DFFC system are presented in Fig. 84 and range from 900 to 1700 K. The RMS standard deviation of ten repeated

measurements is between about ±20 K and is plotted as error bars. The overall accuracy and the reproducibility of these measurements are ±50 K based on uncertainties in the spectroscopic parameters and experimental fluctuations.

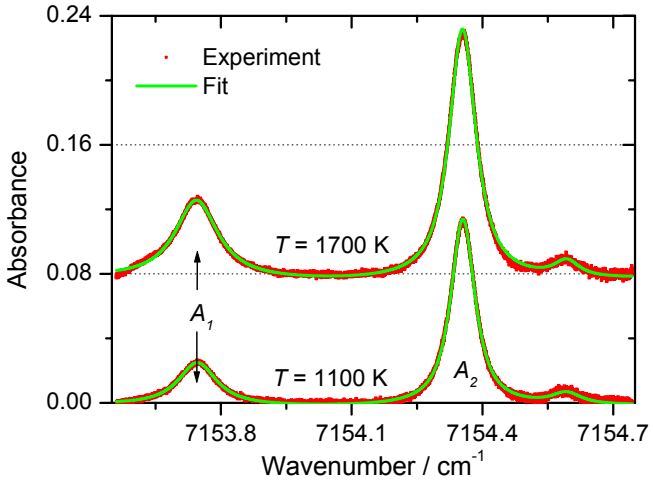

Fig. 83: Typical water absorption spectra in a methane/air flat flame at different temperatures indicated in the figure. The areas A_i are used for temperature evaluation.

The flame temperature generally increases for higher v because of larger heat release. Maximum temperatures are found at $\phi \sim 1.3$ and decrease to higher and lower ϕ. This result is in contrast to the expected maximum at $\phi \sim 1.05$ (Fig. 79). The shift to higher ϕ is due to the line-of-sight nature of the measurements. In rich flames, a second flame front is built at the edge of the burner upon mixture of the unburnt gas with air (Fig. 80). This region is even hotter than the center flame (cf. Fig. 62, lower row, left). As a result, the line-of-sight averaged temperature presented here peaks at $\phi \sim 1.3$.

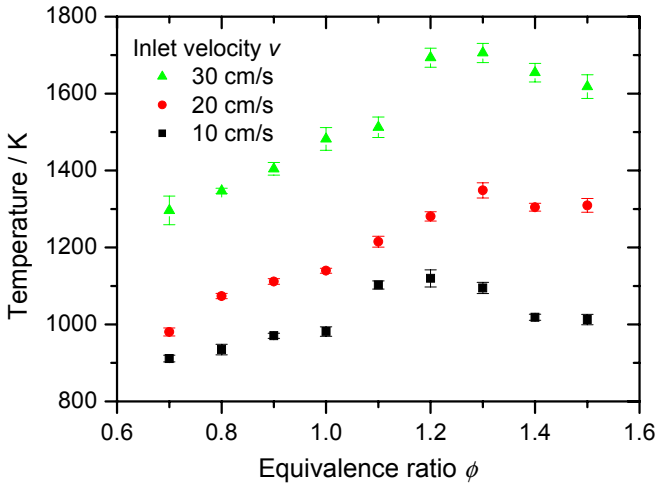

Fig. 84: Gas temperatures in the CH_4/air flat flame at a height of 15 mm above the burner surface for a variation in ϕ and v.

The DFFC power output can directly be correlated with the flame temperature. Fig. 85 shows the comparison for the $\phi = 1.3$ case. The electric power density and the flame temperature rise almost linearly with increasing v in this range.

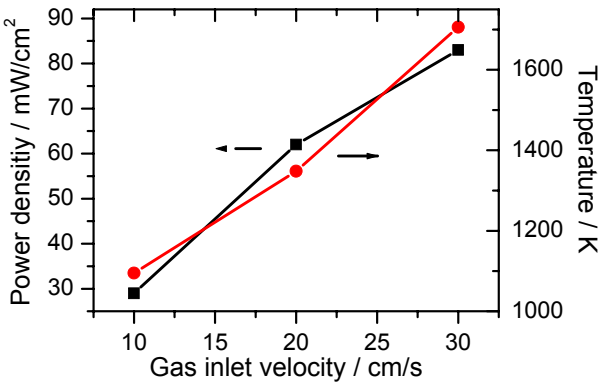

Fig. 85: Correlation of the flame temperature close to the anode and the DFFC power output for $\phi = 1.3$ methane/air flat flames.

Surface thermocouple temperature measurements

The temperature of the ceramic disc holder surface on the cathode side was measured using a thermocouple as indicated in Fig. 80. For the various flame and fuel conditions investigated, it varies between ~600 and 1000 K. The observed maximum power densities are plotted versus the measured temperatures in Fig. 86. Here, the left panel shows the collection of all data, while the right panel shows data at one single value of the equivalence ratio ($\phi = 1.3$). In the latter case, all flames have approximately the same H_2 and CO concentrations in the exhaust gas.

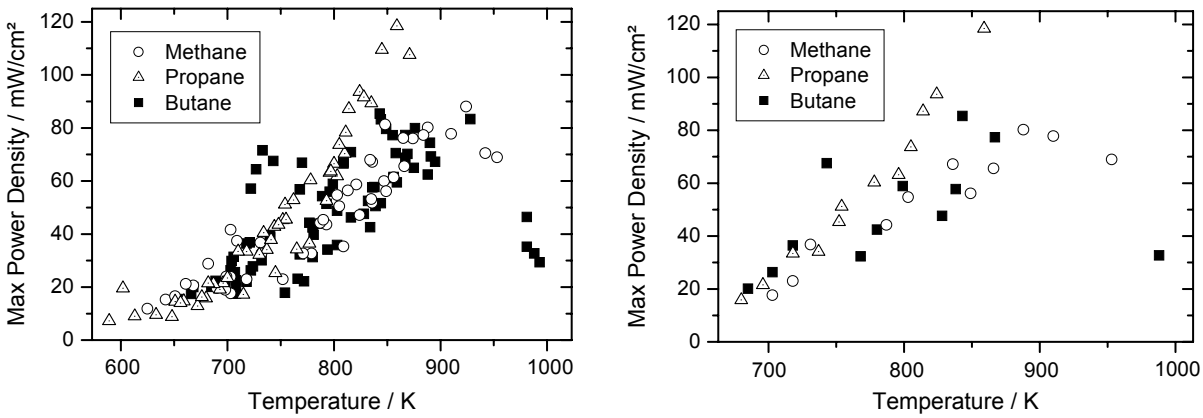

Fig. 86: Maximum power density versus measured cell temperature for all investigated conditions (left) and for all $\phi = 1.3$ flames (right) [185].

The data shown in Fig. 86 reveal a strong correlation between the cell's maximum power density and its temperature. Indeed, the temperature dominates the influence of the other flame parameters, as the scatter in the data for one fixed temperature is smaller than the temperature dependence of the whole data set. The data also confirm that there is no systematic difference between the various fuels investigated; only the propane flames seem to have a slightly higher power output at high cell temperature. The scatter of the data shown in Fig. 86 is an indication of the instability of the flames. It is lowest for propane and increases for methane and butane. When comparing the data at a constant equivalence ratio (Fig. 86, right), the propane flames show an almost linear relationship between power output and cell temperature.

There are several possible interpretations for the distinct temperature dependence of the cell performance, including the temperature-dependent conductivity of the electrolyte, or the electrochemical kinetics of either cathode or anode. A more detailed analysis is subject of ongoing investigations.

The origin of the strong variation in cell temperature (600 – 1000 K) lies in the different flame configurations. In general, the only heat source within the DFFC system is the exothermic combustion chemistry that takes place in the thin (sub-mm) flame front. It leads to a heating of the gas phase, and the SOFC is heated via conduction and convection from the gas phase. The DFFC system loses heat via three mechanisms: (1) Heat conduction and convection away from the cathode surface; (2) heat conduction from the gas phase to the cooled sinter plate of the burner, in particular at short distances between burner and SOFC; (3) radiation from both SOFC surfaces.

Consequently, we observe that cell temperature (and therefore cell performance) increases with increasing gas inflow velocity (more overall flame heating power), decreasing distance between burner and SOFC (increased conductive heat transport towards SOFC), and decreasing equivalence ratio (stoichiometric or slightly rich flames are hottest). However, the power output decreases above 900 K, probably due to the rising electronic conductivity of the SDC electrolyte that short-circuits the cell internally. The OCV drops with higher cell temperature (cf. Fig. 81, d = 5 mm).

6 Summary and conclusions

There is strong scientific evidence that the rising energy consumption of our modern, globally acting societies causes unpredictable changes in the world-wide climate because of emissions of green-house gases associated with the combustion of fossil fuels. Next to global effects, local environmental reactions are observed as well: Acid rain follows nitric oxide emissions; lung cancer can be caused by soot particles. Hence, there is a large need for improving the efficiency and cutting down emissions of power plants and engines. This, however, is only possible through detailed knowledge of the physical and chemical conditions of the combustion process. The measurement techniques that were improved within this thesis allow quantitative, non-intrusive probing of important quantities. These data are required to validate numerical models that finally allow developing efficient combustion processes with low emissions.

Temperature is very important in combustion processes, especially for chemical reaction rates and fluid dynamics. This thesis focuses on the development of laser-based techniques for quantitative gas-temperature measurements in practical combustion processes. The outline of this work is divided into four major sections: First, the physical and spectroscopic background is provided for laser-based thermometry. Then, the most frequently used laser-based thermometry methods are introduced and compared. The next chapter focuses on the advantages and the optimization of the two methods developed in this thesis. In the last section, a wide range of applications is presented to emphasize the accuracy and versatility of the improved techniques.

Thermocouples or other techniques requiring thermal contact are widely used for temperature measurements. Unfortunately, the investigated system is influenced by probe measurements and the time response is slow. In order to overcome these drawbacks, optical methods have been developed. The physical base of the measurement techniques optimized and applied in this thesis is the Boltzmann distribution. The unique properties of laser light allow the quantitative probing of single quantum states of specific molecules. As a result, temperature distributions can be measured with nanosecond time resolution and without influencing the system under study.

Multiple laser-based thermometry methods have been developed within the last decades. Rayleigh scattering, spontaneous Raman scattering, Coherent Anti-Stokes Raman

Scattering (CARS), laser-induced fluorescence (LIF), and laser absorption spectroscopy (LAS) are the most widely used techniques. Rayleigh scattering provides strong signals but requires careful signal interpretation. Spontaneous Raman scattering requires expensive high-power lasers since the signal intensity is low. CARS thermometry has a high accuracy but allows point-wise measurements only. LIF and LAS techniques were used in this thesis. LAS thermometry allows a compact setup and recently became inexpensive due to the availability of cheap diode lasers. However, absorption techniques necessarily integrate information along the line of sight. LIF methods provide strong signals and are frequently used for imaging thermometry. The LIF thermometry developed in this thesis is an accurate and robust technique that can be applied to all kinds of practical combustion systems including spray combustion, sooting flames, and regions close to solid walls.

In this thesis, special emphasis was set on a frequency-scanning multi-line temperature-imaging technique based on LIF excitation spectra of nitric oxide (NO). This calibration-free method was optimized within this work such that accurate (±1 K at ambient temperature, ±2% at flame temperatures) measurements are possible in practical environments. Throughout this work, laser excitation at 225 nm with red-shifted fluorescence detection was applied. The Raman-shifted KrF excimer-laser setup was optimized such that 3 mJ of 225 nm laser light were available for LIF measurements, twice as much as before. Numerical and experimental studies were conducted to identify temperature-sensitive spectral excitation strategies for the different applications. New detection filters were selected that enable efficient (85%) NO-LIF detection while blocking scattered laser light by a factor of 10^7. This ratio was improved by two orders of magnitude with regard to the previous setup. As a result, lower NO seeding (200 ppm) is required and, hence, the target object is less disturbed.

With the multi-line NO-LIF technique, it is necessary to time-average the NO-LIF signal prior to spectra evaluation. This, however, leads to a systematic error in turbulent systems that was quantified for all applications in this work. This effect contributes with ±3% to the measurement uncertainty in turbulent zones of flames. In contrast, the deviations were found to be negligible in all other applications investigated here.

In order to obtain LIF signals with a high signal-to-noise ratio, it is desirable to use high laser fluences. This leads to saturated NO-LIF signals that are usually quantified based on the assumption that quenched molecules cannot return to the laser-coupled ground state within the time of the laser pulse. In cooperation with Dr. T. B. Settersten (CRF, Sandia, USA), experimental evidence was found for the first time that, in contrast to mechanisms proposed in the literature, up to 60% of the quenched molecules do return to the ground state. Hence, population cycling can affect saturation and must be taken into account in saturated LIF spectroscopy.

In comparison to LIF spectroscopy, LAS thermometry allows an inexpensive and much more compact setup using fiber-coupled diode lasers. However, the accuracy of this technique is limited in inhomogeneous media due to the line-of-sight nature of LAS. In collaboration with Prof. R. K. Hanson and Dr. J. B. Jeffries (Stanford University, USA) a two-line thermometry sensor based on tunable diode-laser absorption spectroscopy (TDLAS) of water was built. Using transitions with high ground-state energies, flame temperature measurements were possible without interference from cold boundary layers.

The multi-line NO-LIF temperature-imaging method and two-line H_2O-TDLAS thermometry were applied to quantitatively measure the gas temperature over a wide range of pressures (3 – 500 kPa) and temperatures (270 – 2200 K) in various systems.

Several modern combustion devices are based on spray combustion. However, sprays represent difficult environments for optical diagnostics due to the intense scattering off droplets. With multi-line NO-LIF thermometry, gas-temperature fields could be measured in ethanol spray flames. The data was required to validate new numerical models for ethanol spray combustion developed by Prof. E. Gutheil (Heidelberg University).

Direct-injection spark-ignition internal-combustion (IC) engines show high fuel efficiency but, so far, unexplained misfires occur regularly. Accurate measurement techniques are needed to image the temperature during spray evaporation. In cooperation with the Robert Bosch GmbH, Germany, NO LIF was used to quantify the evaporative cooling caused by the pulsed ethanol spray. Depending on the injection pressure, a decrease of up to 10 K within a few milliseconds could be measured with an excellent reproducibility of ±1 K. This data is important to further develop efficient IC engines.

Laser-induced incandescence (LII) is a powerful soot diagnostics tool. However, for precise particle-size measurements, accurate gas-temperature data is required. It is typically determined by soot pyrometry, which is a line-of-sight technique. In this thesis, it was found that temperature data obtained by soot pyrometry can deviate several hundred Kelvin from spatially resolved NO-LIF thermometry. Hence, temperature data obtained by soot pyrometry must be treated with care.

NO-LIF thermometry has been applied to lean high-pressure flames before. Measurements in sooting flames are extremely difficult due to scattering and strong NO reburn that severely diminishes NO concentrations in rich flames. In this thesis, NO-LIF thermometry could be applied successfully to image the gas temperature in sooting high-pressure flames up to 0.5 MPa. This data is required for the correct interpretation of LII signals for soot diagnostics at elevated pressures.

In IC engines, many pollutants are formed close to the cylinder walls. However, this region has not been studied in very much detail so far. In collaboration with Toyota Central R&D Labs, Japan, temperature distributions in boundary layers of solid-wall

quenched flames could be measured. A high spatial resolution of 29 µm was reached to resolve the steep temperature gradient at the wall, but a step in the temperature profile is observed at the wall that is subject of ongoing discussion. This data enables quantitative LIF species measurements and the optimization of the IC engine thermal management.

Nano-particle properties are strongly size dependent. Their size in turn is influenced by the temperature during production. In this thesis, NO-LIF and H_2O-TDLAS thermometry were applied to measure the gas temperature in a nano-particle flame-synthesis reactor. Both methods complement each other since the data is gained from different positions in the reactor. The data were taken to validate numerical models for nano-particle formation developed at the University of Duisburg-Essen. These models permit to control nano-particle sizes during gas-phase synthesis.

Solid oxide fuel cells (SOFCs) permit an efficient energy conversion with low emissions that can contribute to a cleaner environment on the way to a regenerative energy future. In cooperation with Shinko Electric Industries, Japan, and with Prof. J. Warnatz as well as Dr. W. G. Bessler (IWR, University of Heidelberg), H_2O TDLAS was applied to understand and optimize a direct-flame fuel cell (DFFC) system, whose power output is extremely temperature dependent. In the DFFC setup, a SOFC is directly coupled to a flame and electrochemically converts the unburnt fuel into electricity. This technology can now be applied to combined heat and power systems.

The versatile laser-based measurement techniques developed and improved within this thesis enable quantitative and non-intrusive probing of the gas-phase temperature in practical combustion devices. Accurate knowledge of this important quantity allows developing efficient power plants and engines with low emissions of green-house gases and toxic pollutants.

7 Publications

7.1 Articles in peer-reviewed journals

- H. Kronemayer, K. Omerbegovic, C. Schulz: *Quantification of the evaporative cooling in an ethanol spray created by a gasoline direct-injection system measured by multi-line NO-LIF gas-temperature imaging*; Appl. Opt., accepted (2007).
- H. Kronemayer, P. Ifeacho, C. Hecht, T. Dreier, H. Wiggers, C. Schulz: *Gas-temperature imaging in a low-pressure flame reactor for nano-particle synthesis with multi-line NO-LIF thermometry*; Appl. Phys. B **88**, 373-377 (2007).
- I. Düwel, H.-W. Ge, H. Kronemayer, R. Dibble, E. Gutheil, C. Schulz, J. Wolfrum: *Experimental and numerical characterization of a turbulent spray flame*; Proc. Combust. Inst. **31**, 2247-2255 (2007).
- H. Kronemayer, D. Barzan, M. Horiuchi, S. Suganuma, Y. Tokutake, C. Schulz, J. Warnatz, W. G. Bessler: *A direct-flame solid oxide fuel cell (DFFC) operated on methane, propane and butane*; Journal of power sources **166**, 120-126 (2006).
- T. B. Settersten, B. D. Patterson, H. Kronemayer, V. Sick, C. Schulz, J. W. Daily: *Branching ratios for quenching of nitric oxide A ($^2\Sigma^+(v'=0)$) to X ($^2\Pi(v''=0)$)*; Phys. Chem. Chem. Phys. **8**, 1-11 (2006).
- T. Lee, W. G. Bessler, H. Kronemayer, C. Schulz, J. B. Jeffries, R. K. Hanson: *Quantitative temperature measurements in high-pressure flames with multi-line NO-LIF thermometry*; Applied Optics **44**, 6718-6728 (2005).
- H. Kronemayer, W. G. Bessler, C. Schulz: *Gas-phase temperature imaging in spray systems using multi-line NO-LIF thermometry*; Appl. Phys. B **81**, 1071-1074 (2005).

7.2 Non peer-reviewed articles and conference publications

- M. Vogler, D. Barzan, H. Kronemayer, C. Schulz, M. Horiuchi, S. Suganuma, Y. Tokutake, J. Warnatz, W. G. Bessler: *Direct-Flame Solid-Oxide Fuel Cell (DFFC): A Thermally Self-Sustained, Air Self-Breathing, Hydrocarbon-Operated SOFC System in a Simple, No-Chamber Setup* (10th International Symposium on Solid Oxide Fuel Cells (SOFC-X), Nara, Japan, 2007).
- H. Kronemayer, P. Ifeacho, J. Yin, C. Hecht, H. Wiggers, C. Schulz: *Tunable diode-laser absorption spectroscopy for gas-temperature measurements in a direct-flame fuel cell system and a flat-flame nano-particle synthesis reactor* (Gordon Conference on Laser Diagnostics in Combustion, Poster, Oxford, UK, 2007).
- T. Fuyoto, B. Lewerich, H. Kronemayer, T. Fujikawa, K. Akihama, T. Dreier, C. Schulz: *Temperature and species measurement in a quenching boundary layer on a flat flame burner* (Gordon Conference on Laser Diagnostics in Combustion, Poster, Oxford, UK, 2007).
- H. Kronemayer, C. Schulz: *Gas-phase temperature imaging in combustion systems in a wide temperature and pressure range using multi-line NO-LIF thermometry* (Gordon Conference on Laser Diagnostics in Combustion, Poster, Oxford, UK, 2007).
- C. Hecht, H. Kronemayer, P. Ifeacho, H. Wiggers, C. Schulz: *Atomic LIF spectroscopy for species-concentration measurements in a low-pressure flame-reactor for nano-particle synthesis* (Gordon Conference on Laser Diagnostics in Combustion, Poster, Oxford, UK, 2007).
- A. Kowalik, P. Ifeacho, H. Kronemayer, H. Wiggers, P. Roth, C. Schulz: *Comparison of numerical simulation and experimental investigations on TiO2-nanoparticle synthesis in premixed flames* (VDI Berichte, Berlin, Germany, 2007).
- H. Kronemayer, P. Ifeacho, C. Hecht, H. Wiggers, C. Schulz: *Gas-phase temperature imaging in a nano-particle synthesis low-pressure flame reactor with multi-line NO-LIF thermometry* (European Combustion Meeting (ECM), Chania, Greece, 2007).
- H. Kronemayer, W. G. Bessler, M. Vogler, M. Horiuchi, S. Suganuma, Y. Tokutake, C. Schulz, J. Warnatz: *A Flame as Fuel Reformer for Solid Oxide Fuel Cells* (7th European SOFC Forum, Luzern, Switzerland, 2006).
- M. Vogler, W. G. Bessler, H. Kronemayer: *A flame as fuel reformer for Solid Oxide Fuel Cells* (3rd Fuel Cell Research Symposium on Modelling and Experimental Validation, Duebendorf, Switzerland, 2006).
- H. Kronemayer, C. Schulz, M. Vogler, W. G. Bessler, J. Warnatz, M. Horiuchi, S. Suganuma, Y. Tokutake: *A flame as fuel reformer for solid oxide fuel cells* (International Symposium on Combustion, Poster, Heidelberg, Germany, 2006).

- H. Kronemayer, K. Omerbegovic, C. Schulz: *Quantification of the Evaporative Cooling in an Ethanol Spray Measured by Multi-Line NO-LIFGas-Temperature Imaging* (International Symposium on Combustion, Poster, Heidelberg, Germany, 2006).
- T. Fuyoto, B. Lewerich, H. Kronemayer, T. Fujikawa, K. Akihama, C. Schulz: *Temperature and species measurement in a quenching boundary layer on a flat-flame burner* (International Symposium on Combustion, Poster, Heidelberg, Germany, 2006).
- B. D. Patterson, T. B. Settersten, H. Kronemayer, V. Sick, W. G. Bessler, C. Schulz, J. W. Daily: *Measurements of direct quenching from NO A $^2\Sigma^+(v'=0)$ to X $^2\Pi(v''=0)$* (Laser Applications for Chemical, Security and Environmental Analysis (LACSEA), Lake Tahoe, Nevada, USA, 2006).
- M. Hofmann, H. Kronemayer, B. F. Kock, H. Jander, C. Schulz: *Soot diagnostics at elevated pressure: Laser-induced incadescence and multi-line NO-LIF thermometry* (4th Australien Conference on Laser Diagnostics in Fluid Mechanics and Combustion, University of Adelaide, South Australia, Australia, 2005).
- H. Kronemayer, M. Hofmann, H. Jander, K. Omerbegovic, B. F. Kock, and C. Schulz: *Gas-phase temperature imaging in sooting flames with multi-line NO-LIF thermometry* (1st International Bunsen Discussion Meeting and Workshop on Laser-induced incandescence, Poster, Duisburg, Germany, 2005).
- M. Hofmann, H. Kronemayer, B. F. Kock, H. Jander, C. Schulz: *Laser-induced incandescence and multi-line NO-LIF thermometry for soot diagnostics at high pressures* (European Combustion Meeting (ECM), Louvain-la-Neuve, Belgium, 2005).
- H. Kronemayer, I. Düwel, C. Schulz: *Temperature imaging in spray flames* (European Combustion Meeting (ECM), Louvain-la-Neuve, Belgium, 2005).
- K. Omerbegovic, B. F. Kock, H. Kronemayer, M. Hofmann, C. Schulz: *Vergleich von Ruß- und Gasphasentemperatur in Ethylen/Luft Flammen* (VDI Berichte, Braunschweig, Germany, 367, 2005).
- H. Kronemayer, I. Düwel, C. Schulz: *Gasphasen- und Flüssigkeits-Temperaturmessungen in Sprayflammen* (VDI Berichte, Braunschweig, Germany, 341, 2005).
- H.-W. Ge, M. Vogelgesang, E. Gutheil, I. Düwel, H. Kronemayer, C. Schulz: *Experimental and Numerical Investigation of Turbulent Spray Flows* (Int. Symp. on heat and mass transfer in spray systems, Antalya, Turkey, 2005).
- I. Düwel, H. Kronemayer, C. Schulz, H.-W. Ge, E. Gutheil: *Numerical simulation and experimental investigation of droplet size distribution in non-reactive turbulent spray flows* (Proccedings of the 20th ILASS-Europe Meeting, Orleans, France, 2005).

- H. Kronemayer, I. Düwel, C. Schulz: *Temperature Imaging in Spray Flames with Laser-Induced-Fluorescence Spectroscopy* (Gordon Conference on Laser Diagnostics in Combustion, Poster, Mount Holyoke, MA, USA, 2005).
- M. Hofmann, H. Kronemayer, H. Jander, B. F. Kock, C. Schulz: *Primary soot particle sizing with laser-induced incandescence at high pressures* (Gordon Conference on Laser Diagnostics in Combustion, Poster, Mount Holyoke, MA, USA, 2005).
- H. Kronemayer, B. Lewerich, W. Koban, T. Fuyoto, K. Akihama, J. Bruebach, A. Dreizler, C. Schulz: *Temperature Imaging in Surface Boundary Layers with Laser-Induced-Fluorescence Spectroscopy* (Gordon Conference on Laser Diagnostics in Combustion, Poster, Mount Holyoke, MA, USA, 2005).
- T. Fuyoto, H. Kronemayer, B. Lewerich, W. Koban, K. Akihama, C. Schulz: *Laser-based temperature imaging close to surfaces with toluene and NO-LIF* (International Conference on Optical and Laser Diagnostics (ICOLAD), London, UK, 2005).
- T. B. Settersten, B. D. Patterson, H. Kronemayer, V. Sick, W. G. Bessler, C. Schulz, J. W. Daily: *Population cycling in saturated laser-induced fluorescence detection of nitric oxide* (4^{th} Joint Meeting of the US Sections of the Combustion Institute, USA, 2005).
- T. Lee, W. G. Bessler, H. Kronemayer, C. Schulz, J. B. Jeffries, R. K. Hanson: *Quantitative temperature measurements in high-pressure flames with multi-line nitric oxide (NO)-LIF thermometry* (4^{th} Joint Meeting of the US Sections of the Combustion Institute, USA, 2005).
- H. Kronemayer, W. G. Bessler, C. Schulz: *Multi-line NO-LIF gas-temperature imaging in spray systems* (International Symposium on Combustion, Poster, Chicago, USA, 2004).
- W. G. Bessler, H. Kronemayer, C. Schulz, T. Lee, J. B. Jeffries, R. K. Hanson: *Quantitative multi-line NO-LIF temperature imaging in flames over a wide pressure range* (Laser Applications to Chemical and Environmental Analysis (LACEA), Annapolis, Maryland, USA, 2004).
- H. Kronemayer: *Spektroskopische Messung der Gastemperatur mittels NO-LIF in Spraysystemen* (Diploma thesis, University of Heidelberg, Germany, 2004).

8 References

1. www.ipcc.ch, *Climate change 2007 - the physical science basis*. 2007.
2. E. Altvater, *Das Ende des Kapitalismus wie wir ihn kennen* (Westfälisches Dampfboot, 2006).
3. www.IEA.org, *Key world energy statistics 2006*. 2007.
4. J. Ferin, G. Oberdörster, D. P. Penney, S. C. Soderholm, R. Gelein, and H. C. Piper, "Increased pulmonary toxicity of ultrafine particles? I. particle clearance, translocation, morphology," J. Aerosol Sci. **21**, 381-384 (1990).
5. G. Oberdörster, J. Ferin, G. Finkelstein, P. Wade, and N. Corson, "Increased pulmonary toxicity of ultrafine particles? II. Lung lavage studies," J. Aerosol Sci. **21**, 384-387 (1990).
6. J. G. Grabmaier, "Die Silicium-Solarzelle für terrestrische Anwendungen," Naturwissenschaften **70**, 127-132 (1983).
7. U. Bossel, "The hydrogen illusion - why electrons are a better energy carrier," Cogeneration and on-site power production, 55-59 (march-april 2004).
8. E. Ivers-Tiffée, *Brennstoffzellen und Batterien* (IWE Karlsruhe, 2004).
9. K. Ledjeff-Hey, F. Mahlendorf, and J. Roes, *Brennstoffzellen - Entwicklung, Technology, Anwendung* (C.F. Müller Verlag, Heidelberg, 2001).
10. A. Heinzel, F. Mahlendorf, and J. Roes, *Brennstoffzellen - ein Überblick* (C.F. Müller Verlag, Heidelberg, 2006).
11. P. McKendry, "Energy production from biomass (part 1): overview of biomass," Bioresource Technology **83**, 37-46 (2002).
12. P. McKendry, "Energy production from biomass (part 2): conversion technologies," Bioresource Technology **83**, 47-54 (2002).
13. P. McKendry, "Energy production from biomass (part 3): gasification technologies," Bioresource Technology **83**, 55-63 (2002).
14. J. Wolfrum, "Lasers in combustion: From basic theory to practical devices," Proc. Combust. Inst. **27**, 1-42 (1998).
15. K. Kohse-Höinghaus and J. B. Jeffries, *Applied Combustion Diagnostics* (Taylor and Francis, New York, 2002).
16. J. Wolfrum, T. Dreier, V. Ebert, and C. Schulz, "Laser-based combustion diagnostics," in *Encyclopedia of Analytical Chemistry*, R.A. Meyers, Editor (J. Wiley & Sons Ltd., Chichester, 2000), p. 2118-2148.
17. M. V. Heitor and A. L. N. Moreira, "Thermocouples and sample probes for combustion studies," Prog. Energy Combust. Sci. **19**, 259-278 (1993).

18. J. Warnatz, U. Maas, and R. W. Dibble, *Combustion*, 3. ed (Springer, Heidelberg, 2001).

19. C. Schulz, A. Dreizler, V. Ebert, and J. Wolfrum, *Combustion Diagnostics*. Springer Handbook of Experimental Fluid Dynamics, ed. C. Tropea, J. Foss, and A. Yarin (Springer, 2006, in press about 80 pages).

20. A. Eckbreth, *Laser Diagnostics for Combustion Temperature and Species*. Energy and Engineering Science (Taylor & Francis, 1998).

21. A. Dreizler, V. Ebert, and C. Schulz, *Temperature measurement via absorption, light scattering and laser-induced fluorescence*. Springer Handbook, ed. C. Tropea, J. Foss, and A. Yarin (Springer, 2006, in press about 80 pages).

22. W. P. Stricker, "Measurements of temperature in laboratory flames and practical devices," in *Applied Combustion Diagnostics*, K. Kohse-Höinghaus and J.B. Jeffries, Editors (Taylor and Francis, New York, 2002).

23. N. M. Laurendeau, "Temperature measurements by light-scattering methods," Prog. Energy Combust. Sci. **14**, 147-170 (1988).

24. W. G. Bessler and C. Schulz, "Quantitative multi-line NO-LIF temperature imaging," Appl. Phys. B **78**, 519-533 (2004).

25. M. G. Allen, "Diode laser absorption sensors for gas dynamic and combustion flows," Measurement Science and technology **9**, 545-562 (1998).

26. W. Yao, T. A. Knuuttila, K. K. Nummila, J. E. Martikainen, A. S. Oia, and O. V. Lounasmaa, "A versatile nuclear demagnetization cryostat for ultralow temperature research," Journal of low temperature physics **120**, 121-150 (2000).

27. W. Ketterle, E. A. Cornell, and C. E. Wieman, "for the achievement of Bose-Einstein condensation in dilute gases of alkali atoms, and for early fundamental studies of the properties of the condensates," The Nobel Prize in Physics (2001).

28. *Wikipedia enzyclopedia*. http://en.wikipedia.org/wiki/Temperature, may 2007.

29. *Wikipedia enzyclopedia*. http://en.wikipedia.org/wiki/Temperature_measurement, may 2007.

30. T. Lee, W. G. Bessler, H. Kronemayer, C. Schulz, J. B. Jeffries, and R. K. Hanson, "Quantitative temperature measurements in high-pressure flames with multi-line NO-LIF thermometry," Appl. Opt. **44**, 6718-6728 (2005).

31. F. K. Kneubühl and M. W. Sigrist, *Laser*, 4 ed (Teubner, Stuttgart, 1995).

32. W. Demtröder, *Laserspektroskopie. Grundlagen und Techniken*, 3 ed (Springer, Berlin-Heidelberg-New York, 1993).

33. C. K. Rhodes, ed. *Excimer Lasers*, 2 ed. Topics in Applied Physics (Springer, Berlin-Heidelberg-New York-Tokyo, 1984).

34. C. A. Brau and J. J. Ewing, "Emission spectra of XeBr, XeCl, XeF, and KrF*," J. Chem. Phys. **63**, 4640-4647 (1975).

35. T. Dreier, A. Dreizler, and J. Wolfrum, "The application of a raman-shifted tunable KrF excimer laser for laser-Induced fluorescence combustion diagnostics," Appl. Phys. B **55**, 381-387 (1992).

36. M. Bierry, R. Frey, and F. Pradère, "Multimegawatt tunable infrared source up to 7.7 μm," Rev. Sci. Instrum. **48**, 733-737 (1977).

37. L. D. Schoulepnikoff, V. Mitev, V. Simeonov, B. Calpini, and H. v.d. Bergh, "Experimental investigation of high-power single-pass Raman shifters in the ultraviolet with Nd:YAG and KrF lasers," Appl. Opt. **36**, 5026-5043 (1997).

38. M. J. T. Milton, G. Ancellet, A. Apituley, J. Bosenberg, W. Carnuth, F. Castagnoli, R. Trickl, H. Edner, L. Stefanutti, T. Schaberl, A. Sunesson, and C. Weitkamp, "Raman-shifted laser sources suitable for differential-absorption lidar measurements of ozone in the troposphere," Appl. Phys. B **66**, 105-113 (1998).

39. P. Lallemand and P. Simova, "Stimulated Raman Spectroscopy in Hydrogen Gas," J. Mol. Spectr. **26**, 262-276 (1968).

40. W. G. Bessler, F. Hildenbrand, and C. Schulz, "Two-line laser-induced fluorescence imaging of vibrational temperatures of seeded NO," Appl. Opt. **40**, 748-756 (2001).

41. R. Hall, G. E. Fenner, T. Kingsley, J. Soltys, and O. Carlson, "Coherent light emission from GaAs junctions," Phys. Rev. Letters **9**, 366-369 (1962).

42. *Wikipedia enzyclopedia*. http://en.wikipedia.org/wiki/Laser_diode, june 2007.

43. G. Herzberg, *Molecular spectra and molecular structure. I. Spectra of diatomic molecules*, 2 ed (Krieger, Malabar, Florida, 1950).

44. A. C. Eckbreth, *Laser diagnostics for combustion temperature and species*, 2 ed (Gordon and Breach, Amsterdam, The Netherlands, 1996).

45. D. M. Hirst, *Potential energy surfaces. Molecular structure and reaction dynamics* (Taylor and Francis, London-Philadelphia, 1985).

46. H. Haken and H. C. Wolf, *Molekülphysik und Quantenchemie. Einführung in die experimentellen und theoretischen Grundlagen*, 3 ed (Springer, Berlin-Heidelberg-New York, 1998).

47. G. Wedler, *Lehrbuch der Physikalischen Chemie*, 3 ed (VCH, Weinheim-New York, 1987).

48. J. Humlicek, "An efficient method for evaluation of the complex probability function: the Voigt function and its derivatives," J. Quant. Spectrosc. Radiat. Transfer **21**, 309-313 (1979).

49. A. Thorne, U. Litzén, and S. Johannson, *Spectrophysics* (Springer Verlag, Heidelberg, 1999).

50. I. I. Sobelman, L. A. Vainshtein, and E. A. Yukov, *Excitation of atoms and broadening of spectral lines*. Springer Series on Atoms and Plasmas (Springer Verlag, Berlin, 1995).

51. B. R. Lewis, S. T. Gibson, and P. M. Dooley, "Fine-structure dependence of predissociation linewidth in the Schumann-Runge bands of molecular oxygen," J. Chem. Phys. **100**, 7012-7035 (1994).

52. M. D. DiRosa and R. K. Hanson, "$_2$ and H_2O at high temperatures," J. Quant. Spectrosc. Radiat. Transfer **52**, 515-529 (1994).

53. M. D. DiRosa and R. K. Hanson, "$_2O$, O_2 and NO at 295K," J. Mol. Spectrosc. **164**, 97-117 (1994).

54. A. Y. Chang, M. D. DiRosa, and R. K. Hanson, "Temperature dependence of collision broadening and shift in the NO A-X(0,0) band in the presence of argon and nitrogen," J. Quant. Spectrosc. Radiat. Transfer **47**, 375-390 (1992).

55. A. O. Vyrodov, J. Heinze, and U. E. Meier, "$_2$, Ar, and He at elevated pressures measured by laser-induced fluorescence," J. Quant. Spectrosc. Radiat. Transfer **53**, 277-287 (1995).

56. J. Bruebach, J. Zetterberg, A. Omrane, Z. S. Lie, M. Alden, and A. Dreizler, "Determination of surface normal temperature gradients using thermographic phosphors and filtered Rayleigh scattering," Appl. Phys. B **84**, 537-541 (2006).

57. K. Kohse-Höinghaus and J. B. Jeffries, eds. *Applied Combustion Diagnostics* (Taylor&Francis, New York, 2002).

58. K. Kohse-Höinghaus, "Laser techniques for the quantitative detection of reactive intermediates in combustion systems," Prog. Energy Combust. Sci. **20**, 203-279 (1994).

59. J. W. Daily, "Laser induced fluorescence spectroscopy in flames," Prog. Energy Combust. Sci. **23**, 133-199 (1997).

60. E. W. Rothe, Y. Gu, A. Chryssostomou, P. Andresen, and F. Bormann, "Effect of laser intensity and of lower-state rotational energy transfer upon temperature measurements made with laser-induced predissociative fluorescence," Appl. Phys. B **66**, 251 (1998).

61. H. Zacharias, J. B. Halpern, and K. H. Welge, "Two-photon excitation of NO ($A^2\Sigma^+$, v´ = 0,1,2) and radiation lifetime and quenching measurements," Chem. Phys. Lett. **43**, 41-44 (1976).

62. G. F. Nutt, S. C. Haydon, and A. J. McIntosh, "Measurement of electronic quenching rates in nitric oxide using two-photon spectroscopy," Chem. Phys. Lett. **62**, 402-404 (1979).

63. I. S. McDermid and J. B. Laudenslager, "Radiative lifetimes and electronic quenching rate constants for single-photon-excited rotational levels of NO ($A^2\Sigma^+$, v´ = 0)," J. Quant. Spectrosc. Radiat. Transfer **27**, 483-492 (1982).

64. J. Luque and D. R. Crosley, *LIFBASE: Database and spectral simulation for diatomic molecules*. 1999, SRI International, MP-99-0099, (www.sri.com/cem/lifbase).

65. W. G. Bessler, C. Schulz, V. Sick, and J. W. Daily, "A versatile modeling tool for nitric oxide LIF spectra (http://www.lifsim.com)," in *3rd Joint meeting of the US sections of The Combustion Institute* (Chicago, 2003), PI1-6.

66. R. Kienle, M. P. Lee, and K. Kohse-Hoinghaus, "A scaling formalism for the representation of rotational energy transfer in OH A in combustion experiments," Appl. Phys. B **63**, 403-418 (1996).

67. P. H. Paul, J. A. Gray, J. L. D. Jr., and J. W. T. Jr., "A model for temperature-dependent collisional quenching of NO $A^2\Sigma^+$," Appl. Phys. B **57**, 249-259 (1993).

68. J. E. Dec and J. O. Keller, "High speed thermometry using two-line atomic fluorescence," Proc. Combust. Inst. **21**, 1737-1745 (1986).

69. J. Engström, J. Nygren, M. Aldén, and C. F. Kaminski, "Two-line atomic fluorescence as a temperature probe for highly sooting flames," Opt. Lett. **25**, 1469-1471 (2000).

70. C. F. Kaminski, J. Engström, and M. Aldén, "Quasi-instantaneous two-dimensional temperature measurements in a spark ignition engine using 2-line atomic fluorescence," Proc. Combust. Inst. **27**, 85-93 (1998).

71. R. Cattolica, "OH rotational temperature from two-line laser-excited fluorescence," Appl. Opt. **20**, 1156-1166 (1981).

72. P. Andresen, A. Bath, W. Groger, H. W. Lulf, G. Meijer, and J. J. ter Meulen, "Laser-induced fluorescence with tunable excimer lasers as a possible method for

instantaneous temperature field measurements at high pressures: checks with an atmospheric flame," Appl. Opt. **27**, 365-378 (1988).

73. A. Arnold, B. Lange, T. Bouché, Z. Heitzmann, G. Schiff, W. Ketterle, P. Monkhouse, and J. Wolfrum, "Absolute temperature fields in flames by 2D-LIF of OH using excimer lasers and CARS spectroscopy," Ber. Bunsenges. Phys. Chem. **96**, 1388-1392 (1992).

74. J. M. Seitzman and R. K. Hanson, "Two-line planar fluorescence for temporally resolved temperature imaging in a reacting supersonic flow over a body," Appl. Phys. B **57**, 385-391 (1993).

75. B. K. McMillin, J. M. Seitzman, and R. K. Hanson, "Comparison of NO and OH planar fluorescence temperature measurements in scramjet model flowfields," AIAA J. **32**, 1945-1952 (1994).

76. B. Atakan, J. Heinze, and U. E. Meier, "OH laser-induced fluorescence at high pressures: spectroscopic and two-dimensional measurements exciting the A-X (1,0) transition," Appl. Phys. B **64**, 585-591 (1997).

77. M. Tsujishita, A. Hirano, M. Yokoo, T. Sakuraya, and Y. Takeshita, "Accurate thermometry using NO and OH laser-induced fluorescence in an atmospheric pressure flame," JSME International Journal Series B **42**, 119-126 (1999).

78. A. T. Hartlieb, B. Atakan, and K. Kohse-Höinghaus, "Temperature measurement in fuel-rich non-sooting low-pressure hydrocarbon flames," Appl. Phys. B **70**, 435-445 (2000).

79. R. L. McKenzie and K. P. Gross, "Two-photon excitation of nitric oxide fluorescence as a temperature indicator in unsteady gasdynamic processes," Appl. Opt. **20**, 2153-2165 (1981).

80. K. P. Gross and R. L. McKenzie, "Singe-pulse gas thermometry at low temperatures using two-photon laser-induced fluorescence in NO-N_2 mixtures," Opt. Lett. **8**, 368-370 (1983).

81. J. M. Seitzman, G. Kychakoff, and R. K. Hanson, "Instantaneous temperature field measurements using planar laser-induced fluorescence," Opt. Lett. **10**, 439-441 (1985).

82. K. P. Gross and R. L. McKenzie, "Measurements of fluctuating temperatures in a supersonic turbulent flow using laser-induced fluorescence," AIAA J. **23**, 1932-1936 (1985).

83. K. P. Gross, R. L. McKenzie, and P. Logan, "Measurement of temperature, density, pressure, and their fluctuations in supersonic turbulence using laser-induced fluorescence," Exp. Fluids **5**, 372-380 (1987).

84. B. K. McMillin, J. L. Palmer, and R. K. Hanson, "Temporally resolved, two-line fluorescence imaging of NO temperature in a transverse jet in a supersonic cross flow," Appl. Opt. **32**, 7532-7545 (1993).

85. M. P. Lee, B. K. McMillin, and R. K. Hanson, "Temperature measurements in gases by use of planar laser-induced fluorescence imaging of NO," Appl. Opt. **32**, 5379-5396 (1993).

86. A. O. Vyrodov, J. Heinze, M. Dillmann, U. E. Meier, and a. W. Stricker, "Laser-induced fluorescence thermometry and concentration measurements on NO A-X (0,0) transitions in the exhaust gas of high pressure CH_4/air flames," Appl. Phys. B **61**, 409-414 (1995).

87. M. Yorozu, Y. Okada, and A. Endo, "Two dimensional rotational temperature measurement by multiline laser induced fluorescence of nitric oxide in combustion flame," Opt. Rev. **3**, 293-298 (1996).

88. E. A. Brinkman, G. A. Raiche, M. S. Brown, and J. B. Jeffries, "Optical diagnostics for temperature measurement in a dc arcjet reactor used for diamond deposition," Appl. Phys. B. **64**, 689-697 (1997).

89. M. Tamura, J. Luque, J. E. Harrington, P. A. Berg, G. P. Smith, J. B. Jeffries, and D. R. Crosley, "Laser-induced fluorescence of seeded nitric oxide as a flame thermometer," Appl. Phys. B **66**, 503-510 (1998).

90. P. C. Palma, T. J. McIntyre, and A. F. P. Houwing, "PLIF thermometry in shock tunnel flows using a Raman-shifted tunable excimer laser," Shock Waves **8**, 275-284 (1998).

91. W. M. Ruyten, M. S. Smith, L. L. Price, and W. D. Williams, "Three-line fluorescence thermometry of optically thick shock-tunnel flow," Appl. Opt. **37**, 2334-2339 (1998).

92. G. Dilecce, M. Simek, M. Vigliotti, and S. De Benedictis, "Fast LIF approach to NO rotational temperature and density measurement: application to a gas-dynamic expansion," Appl. Spectrosc. **54**, 824-831 (2000).

93. J. B. Bell, M. S. Day, J. F. Grcar, W. G. Bessler, C. Schulz, P. Glarborg, and A. D. Jensen, "Detailed modeling and laser-induced fluorescence imaging of nitric oxide in a NH_3-seeded non-premixed methane/air flame," Proc. Comb. Inst. **29**, in press (2002).

94. W. G. Bessler, C. Schulz, T. Lee, D. I. Shin, M. Hofmann, J. B. Jeffries, J. Wolfrum, and R. K. Hanson, "Quantitative NO-LIF imaging in high-pressure flames," in *Optical and Laser Diagnostics*, C. Arcoumanis and K.T.V. Grattan, Editors (Institute of Physics, Bristol, Philadelphia, 2003), p. 107-114.

95. H. Kronemayer, W. G. Bessler, and C. Schulz, "Gas-phase temperature imaging in spray systems using multi-line NO-LIF thermometry," Appl. Phys. B **81**, 1071-1074 (2005).

96. M. P. Lee, P. H. Paul, and R. K. Hanson, "Quantitative imaging of temperature fields in air using planar laser-induced fluorescence of O2," Opt. Lett. **12**, 75-77 (1987).

97. G. Laufer, R. L. McKenzie, and D. G. Fletcher, "Method for measuring temperatures and densities in hypersonic wind tunnel air flows using laser-induced O_2 fluorescence," Appl. Opt. **29**, 4873-4883 (1990).

98. M. S. Smith, L. L. Price, and W. D. Williams, "Laser-induced fluorescence diagnostics using a two-line excitation method," AIAA J. **31**, 478-482 (1993).

99. A. A. Roller, A., M. Decker, V. Sick, J. Wolfrum, W. Hentschel, and K.-P. Schindler, "Non-Intrusive temperature measurements during the compression phase of a DI Diesel engine," SAE Technical Paper Series No. 952461 (1995).

100. T. Ni-Imi, T. Fujimoto, and N. Shimizu, "Method for planar measurement of temperature in compressible flow using two-line laser-induced iodine fluorescence," Opt. Lett. **15**, 918-920 (1990).

101. A. Kido, S. Kubota, H. Ogawa, and N. Miyamoto, "Simultaneous measurements of concentration and temperature distributions in unsteady gas jets by an Iodine LIF method," SAE Technical Paper Series No. 980146 (1998).

102. F. Grossmann, P. B. Monkhouse, M. Ridder, V. Sick, and J. Wolfrum, "Temperature and pressure dependences of the laser-induced fluorescence of gas-phase acetone and 3-pentanone," Appl. Phys. B **62**, 249-253 (1996).

103. M. C. Thurber, F. Grisch, and R. K. Hanson, "Temperature imaging with single- and dual-wavelength acetone planar laser-induced fluorescence," Opt. Lett. **22**, 251-253 (1997).

104. S. Einecke, C. Schulz, V. Sick, A. Dreizler, R. Schießl, and U. Maas, "Two-dimensional temperature measurements in an SI engine using two-line tracer LIF," SAE Technical Paper Series No. 982468 (1998).

105. M. Luong, W. Koban, and C. Schulz, "Novel strategies for imaging temperature distribution using Toluene LIF," in *International Conference on Laser Diagnostics, ICOLAD2005* (London, 2005).

106. W. Koban, J. D. Koch, V. Sick, N. Wermuth, R. K. Hanson, and C. Schulz, "Predicting LIF signal strength for toluene and 3-pentanone under engine-related temperature and pressure conditions," Proc. Combust. Inst. **30**, 1545-1553 (2005).

107. W. Koban and C. Schulz, "Toluene as a tracer for fuel, temperature and oxygen concentrations," SAE technical paper series 2005-01-2091 (2005).

108. W. Koban, J. D. Koch, R. K. Hanson, and C. Schulz, "Toluene LIF at elevated temperatures: Implications for fuel/air ratio measurements," Appl. Phys. B **80**, 147-150 (2005).

109. E. W. Rothe, Y. Gu, A. Chryssostomou, P. Andresen, and F. Bormann, "Effect of laser intensity and of lower-state rotational energy transfer upon temperature measurements made with laser-induced predissociative fluorescence," Appl. Phys. B **66**, 251-258 (1998).

110. J. W. Daily and E. W. Rothe, "Effect of laser intensity and lower-state rotational energy transfer upon temperature measurements made with laser-induced fluorescence," Appl. Phys. B **68**, 131-140 (1999).

111. W. G. Bessler and C. Schulz, "Quantitative multi-line NO-LIF temperature imaging," Appl. Phys. B, in review (2004).

112. W. G. Bessler, C. Schulz, T. Lee, J. B. Jeffries, and R. K. Hanson, "Carbon dioxide UV laser-induced fluorescence in high-pressure flames," Chem. Phys. Lett. **375**, 344-349 (2003).

113. V. Ebert and J. Wolfrum, "Absorption spectroscopy," in *Optical Measurement Techniques and Applications*, F. Mayinger, Editor Berlin, 1994), p. 273-312.

114. D. S. Baer, R. K. Hanson, M. E. Newfield, and N. K. J. M. Gopaul, "Multiplexed Diode-Laser Sensor System for Simultaneous H2O, O2 and Temperature Measurements," Opt. Lett. **19**, 1900-1902 (1994).

115. E. R. Furlong, D. S. Baer, and R. K. Hanson, "Combustion control using a multiplexed diode-laser sensor system," in *Symposium (International) on Combustion* (1996), 2851-2858.

116. V. Nagali and R. K. Hanson, "Design of a diode-laser sensor to monitor water vapour in high pressure combustion gases," Appl. Opt. **36**, 9518-9527 (1997).

117. D. W. Mattison, J. T. C. Liu, J. B. Jeffries, and R. K. Hanson, "Tunable diode-laser temperature sensor for evaluation of a valveless pulse detonation engine," in *The 43rd AIAA Aerospace science meeting and exhibit* (Reno, NV, USA, 2005).

118. L. Ma, S. T. Sanders, J. B. Jeffries, and R. K. Hanson, "Monitoring and control of a pulse detonation engine using a diode-laser fuel concentration and temperature sensor," in *Proceedings of the Combustion Institute* (2002), 161-166.

119. H. Teichert, T. Fernholz, and V. Ebert, "Simultaneous in situ measurements of CO, H2O and gas temperatures in a full-sized coal-fired power plant by near-infrared diode lasers," Appl. Opt. **42**, 2043-2051 (2003).

120. G. B. Riecker, J. T. C. Liu, J. B. Jeffries, R. K. Hanson, T. Mathur, M. R. Gruber, and C. D. Carter, "Diode laser sensor for gas temperature and H2O concentration in a scramjet combustor using wavelength modulation spectroscopy," in *41st AIAA/ASME/SAE/ASEE Joint Propulsion Conference and Exhibit* (Tucson, Arizona, USA, 2005).

121. J. T. C. Liu, J. B. Jeffries, and R. K. Hanson, "Wavelength modulation absorption spectroscopy with 2f detection using multiplexed diode lasers for rapid temperature measurements in gaseous flows," Appl. Phys. B **78**, 503-511 (2004).

122. G. G. Stokes, Mathematical and Physical Papers (1880).

123. T. Landenfeld, A. Kremer, E. P. Hassel, J. Janicka, T. Schäfer, J. Kazenwadel, C. Schulz, and J. Wolfrum, "Laser-diagnostic and numerical study of strongly swirling natural gas air flames," Proc. Combust. Inst., **27**, 1023-1029 (1998).

124. R. W. Dibble and R. E. Hollenbach, "Laser Rayleigh thermometry in turbulent flames," Proc. Combust. Inst. **18**, 1489-1499 (1981).

125. C. Schulz, V. Sick, J. Wolfrum, V. Drewes, M. Zahn, and R. Maly, "Quantitative 2D single-shot imaging of NO concentrations and temperatures in a transparent SI engine," Proc. Combust. Inst. **26**, 2597-2604 (1996).

126. J. Warnatz, U. Maas, and R. W. Dibble, *Combustion* (Springer verlag, Berlin, 1999).

127. V. Bergmann, W. Meier, D. Wolff, and W. Stricker, "Application of spontaneous Raman and Rayleigh scattering and 2D LIF for the characterization of a turbulent $CH_4/H_2/N_2$ jet diffusion flame," Appl. Phys. B **66**, 489-502 (1998).

128. R. S. Barlow, C. D. Carter, and R. W. Pitz, "Multiscalar diagnostics in turbulent flames," in *Applied Combustion Diagnostics*, K. Kohse-Höinghaus and J.B. Jeffries, Editors (Taylor & Francis, New York, 2002), p. 384-407.

129. D. Geyer, A. Kempf, A. Dreizler, and J. Janicka, "Scalar dissipation rates in isothermal and reactive turbulent opposed-jets: 1D-Raman/Rayleigh experiments supported by LES," Proceedings of the Combustion Institute **30**, 681-689 (2004).

130. J. N. Forkey, N. D. Finkelstein, W. R. Lempert, and R. B. Miles, "Demonstration and characterization of filtered Rayleigh scattering for planar velocity measurements," AIAA Journal **34**, 442-448 (1996).

131. D. Hoffman, K.-U. Münch, and A. Leipertz, "Two-dimensional temperature determination in sooting flames by filtered Rayleigh scattering," Opt. Lett. **21**, 525-527 (1996).

132. R. B. Miles, J. N. Forkey, and W. R. Lempert, *AIAA paper 92-3894* (1992).

133. J. Zetterberg, Z. S. Li, M. Afzelius, and M. Aldén, "Two-dimensional temperature measurements in flames using filtered Rayleigh scattering at 254 nm," in *European Combustion Meeting* (2003).

134. R. S. Barlow, C. D. Carter, and R. W. Pitz, "Multi-scalar diagnostics in turbulent flames," in *Applied Combustion Diagnostics*, K. Kohse-Höinghaus and J.B. Jeffries, Editors (Taylor & Francis, London, 2003).

135. D. F. Marran, J. H. Frank, M. B. Long, and S. H. Stårner, "Intracavity technique for improved Raman / Rayleigh imaging in flames," Opt. Lett. **20**, 791-793 (1995).

136. W. Meier, R. S. Barlow, Y.-L. Chen, and J.-Y. Chen, "Raman/Rayleigh/LIF measurements in a turbulent CH4/H2/N2 jet diffusion flame: experimental techniques and turbulence–chemistry interaction," Combustion and Flame **123**, 326-343 (2000).

137. H. W. Schrötter, *Linear Raman Spectroscopy: A state of the art report*. Non-linear Raman spectroscopy and its chemical applications, ed. W. JKiefer and D.A. Long. Vol. 93 (Nato Advanced Study Institute Series, series C, Mathematical and Physical Sciences, Dordrecht NL, 1982).

138. D. Geyer, *1D-Raman/Rayleigh experiments in turbulent-opposed jet flows.*, in *EKT*. 2004, Technische Universität Darmstadt: Darmstadt.

139. A. C. Eckbreth, "CARS Thermometry in Practical Combustors," Combust. Flame **39**, 133-147 (1980).

140. R. J. Hall, "Intensity Convolutions of CARS Spectra," opt. Communn. **52**, 360-366 (1985).

141. R. E. Teets, "Accurate Convolutions of Coherent anti-Stokes Raman Spectra," Opt. Lett. **9**, 226-228 (1984).

142. M. Péalat, M. Lefebvre, J.-P. E. Taran, and P. L. Kelley, "Sensitivity of Quantitative Vibrational Coherent anti-Stokes Raman Spectroscopy to Saturation and Stark Shifts," Phys. Rev. **38**, 1948-1965 (1988).

143. M. L. Koszykowski, R. L. Farrow, and R. E. Palmer, "Calculation of Collisionally Narrowed Coherent anti-Stokes Raman Spectroscopy Spectra," Opt. Lett. **10**, 478-480 (1985).

144. S. Kröll, M. Aldén, T. Berglind, and R. J. Hall, "Noise Characteristics of Single Shot Broadband Raman-resonant CARS with single- and multimode Lasers," Appl. Opt. **26**, 1068-1073 (1987).

145. A. O. Vyrodow, J. Heinze, M. Dillmann, U. E. Meier, and W. Stricker, "Laser-induced fluorescence thermometry and concentration measurements on NO A-X (0,0) transitions in the exhaust gas of high pressure CH_4/air flames," Appl. Phys. B. **61**, 409-414 (1995).

146. H. Kronemayer, P. Ifeacho, C. Hecht, H. Wiggers, and C. Schulz, "Gas-temperature imaging in a low-pressure flame reactor for nano-particle synthesis with multi-line NO-LIF thermometry," Appl. Phys. B **DOI: 10.1007/s00340-007-2721-8** (2007).

147. W. G. Bessler, C. Schulz, T. Lee, D. I. Shin, M. Hofmann, J. B. Jeffries, J. Wolfrum, and R. K. Hanson, "Quantitative NO-LIF imaging in high-pressure flames," Appl. Phys. B **75**, 97-102 (2002).

148. M. Hofmann, H. Kronemayer, B. F. Kock, H. Jander, and C. Schulz, "Laser-induced incandescence and multi-line NO-LIF thermometry for soot diagnostics at high pressures," in *European Combustion Meeting (ECM)* (Louvain-la-Neuve, Belgium, 2005).

149. M. Hofmann, H. Kronemayer, B. F. Kock, H. Jander, and C. Schulz, "Soot diagnostics at elevated pressure: Laser-induced incadescence and multi-line NO-LIF thermometry," in *4th Australien Conference on Laser Diagnostics in Fluid Mechanics and Combustion* (University of Adelaide, South Australia, Australia, 2005).

150. K. Omerbegovic, B. F. Kock, H. Kronemayer, M. Hofmann, and C. Schulz, "Vergleich von Ruß- und Gasphasentemperatur in Ethylen/Luft Flammen," in *VDI Berichte* (Braunschweig, Germany, 2005), 367-373.

151. H. Kronemayer, I. Düwel, and C. Schulz, "Gasphasen- und Flüssigkeits-Temperaturmessungen in Sprayflammen," VDI-Berichte **1888**, 341-346 (2005).

152. I. Düwel, H.-W. Ge, H. Kronemayer, R. Dibble, E. Gutheil, C. Schulz, and J. Wolfrum, "Experimental and numerical characterization of a turbulent spray flame," Proc. Combust. Inst. **31**, 2247-2255 (2007).

153. W. G. Bessler, *Quantitative nitric oxide concentration and temperature imaging in flames over a wide pressure range with laser-induced fluorescence*, in *Naturwissenschaftlich-Mathematische Gesamtfakultät*. 2003, Ruprecht-Karls Universität Heidelberg: Heidelberg, Germany.

154. C. Amiot, R. Bacis, and G. Guelachvili, "$^2\Pi$ v=0,1,2 levels of $^{14}N^{16}O$. Preliminary results on the v=0,1 levels of $^{14}N^{17}O$, $^{14}N^{18}O$, and $^{15}N^{16}O$.," Can. J. Phys. **56**, 251-265 (1978).

155. F. R. Gilmore, "$_2$, NO, O_2 and corresponding ions," J. Quant. Spectrosc. Radiat. Transfer **5**, 369-390 (1965).

156. P. H. Paul, "γ-bands of nitric oxide," J. Quant. Spectrosc. Radiat. Tranfer **57**, 581-589 (1997).

157. L. G. Piper and L. M. Cowles, "$^2\Sigma^+$-$X^2\Pi$) transition," J. Chem. Phys. **85**, 2419-2422 (1986).

158. J. R. Reisel, C. D. Carter, and N. M. Laurendeau, "Einstein coefficients for rotational lines of the (0,0) Band of the NO $A^2\Sigma^+$ - $X^2\Pi$ system," J. Quant. Spectrosc. Radiat. Transfer **47**, 43-54 (1992).

159. A. Y. Chang, M. D. DiRosa, and R. K. Hanson, "Temperature dependence of collision broadening and shift in the NO A-X(0,0) band in the presence of argon and nitrogen," J. Quant. Spectrosc. Radiat. Transfer **47**, 375-390 (1992).

160. M. D. DiRosa and R. K. Hanson, "Collision broadening and shift of NO (0,0) absorption lines by O_2 and H_2O at high temperatures," J. Quant. Spectrosc. Radiat. Transfer **52**, 515-529 (1994).

161. P. H. Paul, J. A. Gray, J. L. Durant Jr., and J. W. Thoman Jr., "A model for temperature-dependent collisional quenching of NO $A^2\Sigma^+$," Appl. Phys. B **57**, 249-259 (1993).

162. T. B. Settersten, B. D. Patterson, and J. A. Gray, "Temperature- and species dependent quenching of NO A 2Sigma+(v'=0) probed by two-photon laser-induced fluorescence using a picosecond laser," J. Chem. Phys. **124**, 234308 (2006).

163. P. Andresen, G. Meijer, H. Schluter, H. Voges, A. Koch, W. Hentschel, W. Oppermann, and E. Rothe, "Fluorescence imaging inside an internal combustion engine using tunable excimer lasers," Appl. Opt. **29**, 2392-2404 (1990).

164. W. P. J. Partridge and N. M. Laurendeau, "Formulation of a dimensionless overlap fraction to account for spectrally distributed interactions in fluorescence studies," Appl. Opt. **34**, 2645 (1995).

165. W. H. Press, W. T. Vettering, S. A. Teukolsky, and B. P. Flannery, *Numerical Recipes in C: The art of Scientific Computing*, 2 ed (Cambridge University Press, New York, 1992).

166. J. W. Daily, T. B. Settersten, W. G. Bessler, C. Schulz, and V. Sick, "A computer code to simulate laser excitation and collision dynamics in nitric oxide," in *4th*

Joint Meeting of the U.S. Sections of the Combustion Institute (Drexel University in Philadelphia, PA on March 20-23, 2005, 2005).

167. J. W. Daily, W. G. Bessler, C. Schulz, V. Sick, and T. B. Settersten, "Nonstationary collisional dynamics in determining nitric oxide laser-induced fluorescence spectra," AIAA **43** (2005).

168. H. Kronemayer, P. Ifeacho, C. Hecht, H. Wiggers, and C. Schulz, "Gas-phase temperature imaging in a nano-particle synthesis low-pressure flame reactor with multi-line NO-LIF thermometry," in *European Combustion Meeting (ECM)* (Chania, Greece, 2007).

169. T. B. Settersten, B. D. Patterson, H. Kronemayer, V. Sick, C. Schulz, and J. W. Daily, "Branching ratios for quenching of nitric oxide A (2Sigma+(v'=0)) to X (2Pi(v"=0))," Phys. Chem. Chem. Phys. **8**, 1-11 (2006).

170. P. H. Paul, J. A. Gray, J. L. D. Jr., and J. W. T. Jr., "Collisional quenching corrections for laser-induced fluorescence measurements of NO $A^2\Sigma^+$," AIAA Journal **32**, 1670-1675 (1994).

171. H. Zacharias, F. de Rougemont, T. F. Heinz, and M. M. T. Loy, "Ionization probabilities of $A\ ^2\Sigma^+$ (v'=0,1,2) and $B\ ^2\Pi$(v'=0,2) states of NO," J. Chem. Phys. **105**, 111 (1996).

172. K. G. McKendrick, J. Chem. Soc., Faraday Trans. **94**, 1921-1932 (1998).

173. X. Zhou, X. Liu, J. B. Jeffries, and R. K. Hanson, "Development of a sensor for temperature and water concentration in combustion gases using a single tunable diode laser," Meas. Sci. Technol. **14**, 1459-1468 (2003).

174. X. Zhou, J. B. Jeffries, and R. K. Hanson, "Development of a fast temperature sensor for combustion gases using a single tunable diode laser," Appl. Phys. B **81**, 711-722 (2005).

175. X. Liu, J. B. Jeffries, R. K. Hanson, K. M. Hinckley, and M. A. Woodmansee, "Development of a tunable diode laser sensor for measurements of gas turbine exhaust temperature," Appl. Phys. B **82**, 469-478 (2006).

176. D. W. Mattison, J. B. Jeffries, R. K. Hanson, R. R. Steeper, S. De Zilwa, J. E. Dec, M. Sjoberg, and W. Hwang, "In-cylinder gas temperature and water concentration measurements in HCCI engines using a multiplexed-wavelength diode-laser system: Sensor development and initial demonstration," Proc. Combust. Inst., 791-798 (2007).

177. J. T. C. Liu, G. B. Rieker, J. B. Jeffries, R. K. Hanson, M. R. Gruber, C. D. Carter, and T. Mathur, "Near infrared diode laser absorption diagnostic for temperature and water vapor in a scramjet combustor," Appl. Opt. **44**, 6701-6711 (2005).

178. K. M. Hinckley, J. B. Jeffries, and R. K. Hanson, "A wavelength-multiplexed diode laser sensor for temperature measurements in pulse detonation engines," in *42nd AIAA Aerospace Science Meeting and Exhibit* (Reno, NV, USA, 2004).

179. S. T. Sanders, J. A. Baldwin, T. P. Jenkins, D. S. Baer, and R. K. Hanson, "Diode-laser sensor for monitoring multiple combustion parameters in pulse detonation engines," Proc. Combust. Inst. **28**, 587-594 (2000).

180. D. W. Mattison, C. M. Brophy, S. t. Sanders, L. Ma, K. M. Hinckley, J. B. Jeffries, and R. K. Hanson, "Pulse detonation engine characterization and control using tunable diode-laser sensors," Journal of propulsion and power **19**, 568-572 (2003).

181. C. N. Banwell and E. M. Mccash, *Fundamentals of molecular spectroscopy*, 4th edition ed (McGraw-Hill International (UK) Limited, 1994).

182. L. S. Rothman, D. Jacquemart, A. Barbe, D. C. Benner, M. Birk, L. R. Brown, K. Carleer, C. Chackerian Jr., Chance, L. H. Coudert, V. Dana, V. M. Devi, J.-M. Flaut, R. R. Gamache, A. Goldmann, J.-M. Hartmann, K. W. Jucks, A. G. Maki, S. T. Mandin, S. T. Massie, J. Orphal, A. Perrin, C. P. Rinsland, M. A. H. Smith, J. Tennyson, R. N. Tolchenov, R. A. Toth, J. Vander Auwera, P. Varanasi, and G. Wagner, "The HITRAN 2004 molecular spectroscopic database," J. Quant. Spectrosc. & Radiat. Transf. **96**, 139-204 (2004).

183. T. Fuyoto, H. Kronemayer, B. Lewerich, W. Koban, K. Akihama, and C. Schulz, "Laser-based temperature imaging close to surfaces with toluene and NO-LIF," in *ICOLAD* (London, UK, 2005).

184. A. Kowalik, P. Ifeacho, H. Wiggers, C. Schulz, and P. Roth, "TiO2 nanoparticle formation in a premixed flame and a plasma reactor: comparison between experiment and numerical simulation," in *European Combustion Meeting (ECM)* (Chania, Greece, 2007).

185. H. Kronemayer, D. Barzan, M. Horiuchi, S. Suganuma, Y. Tokutake, C. Schulz, J. Warnatz, and W. G. Bessler, "A direct-flame solid oxide fuel cell (DFFC) operated on methane, propane and butane," Journal of power sources **166**, 120-126 (2007).

186. A. N. Karpetis and A. Gomez, "An experimental study of well-defined turbulent non-premixed spray flames," Combust. Flame **121**, 1-23 (2000).

187. M. S. Raju, "On the Importance of Chemistry/Turbulence Interactions in Spray Computations," Numerical Heat Transfer 2 **41**, 409-432 (2002).

188. R. Cabra, T. Myhrvold, J.-Y. Chen, R. W. Dibble, A. N. Karpetis, and R. S. Barlow, "Simultaneous laser-Raman-Rayleigh-LIF measurements and numerical modeling results of a lifted turbulent H_2/N_2 jet flame in a vitiated flow," Proc. Combust. Inst. **29**, 1881-1888 (2002).

189. H. Kronemayer, I. Düwel, and C. Schulz, "Gasphasen- und Flüssigkeits-Temperaturmessungen in Sprayflammen," in *VDI Berichte* (Braunschweig, Germany, 2005), 341-346.

190. H. Kronemayer, I. Düwel, and C. Schulz, "Temperature imaging in spray flames," in *European Combustion Meeting (ECM)* (Louvain-la-Neuve, Belgium, 2005).

191. I. Düwel, *Spray combustion diagnostics with tracer-based laserinduced fluorescence imaging*, in *Naturwissenschaftlich-Mathematische Gesamtfakultät*. 2007, Ruprecht-Karls Universität Heidelberg: Heidelberg, Germany, http://www.ub.uni-heidelberg.de/archiv/7349/.

192. I. Düwel, H. Kronemayer, C. Schulz, H.-W. Ge, and E. Gutheil, "Numerical simulation and experimental investigation of droplet size distribution in non-reactive turbulent spray flows," in *Proccedings of the 20th ILASS-Europe Meeting* (Orleans, France, 2005).

193. H.-W. Ge, M. Vogelgesang, E. Gutheil, I. Düwel, H. Kronemayer, and C. Schulz, "Experimental and Numerical Investigation of Turbulent Spray Flows," in *Int. Symp. on heat and mass transfer in spray systems* (Antalya, Turkey, 2005).

194. H.-W. Ge, *Probability Density Function Modeling of Turbulent Non-reactive and Reactive Spray Flows*, in *Naturwissenschaftlich-Mathematische Gesamtfakultät*. 2006, Ruprecht-Karls Universität Heidelberg: Heidelberg, Germany, http://www.ub.uni-heidelberg.de/archiv/6478/.

195. S. K. Aggarwal and S. Chitre, "On the structure of unconfined turbulent spray flames," Combustion Science and Technology **81**, 97-113 (1992).

196. D. A. Greenhalgh and M. C. Jermy, "Laser diagnostics for droplet measurements for the study of fuel injection and mixing in gas turbines and IC engines," in *Applied combustion diagnostics*, K. Kohse-Höinghaus and J.B. Jeffries, Editors (Taylor & Francis, London, 2002).

197. C.-N. Yeh, Kosaka, H., and Kamimoto, T., " A fluorescence / scattering imaging technique for instantaneous 2-D measurement of particle size distribution in a transient spray," Proc. 3rd Congr. on Opt. Part. Sizing, Yokohama-Japan, (1993).

198. I. Düwel, T. Kunzelmann, J. Schorr, C. Schulz, and J. Wolfrum, "Application of fuel tracers with different volatilities for planar LIF/Mie drop sizing in evaporating systems," in *Proc. of the 9th ICLASS 2003* (Sorrento, Italy, 2003).

199. P. Lavieille, F. Lemoine, G. Lavergne, and M. Lebouché, "Evaporating and combusting droplet temperature measurements using two-color laser-induced fluorescence," Exp. Fluids **31**, 45-55 (2001).

200. I. Düwel, J. Schorr, J. Wolfrum, and C. Schulz, "Laser-induced fluorescence of tracers dissolved in evaporating droplets," Appl. Phys. B **78**, 127-131 (2004).

201. C. Hollmann and E. Gutheil, "Flamelet-Modeling of Turbulent Spray Diffusion Flames Based on a Laminar Spray Flame Library," Combust. Sci. and Tech. **135**, 175 - 192 (1998).

202. S. B. Pope, *Turbulent flow* (Cambridge University Press, Camebridge, 2000).

203. R. O. Fox, *Computational models for turbulent reacting flows* (Camebridge University Press, Camebridge, 2003).

204. C. Taut, C. Correa, O. Deutschmann, J. Warnatz, S. Einecke, C. Schulz, and J. Wolfrum, "3D-modeling with Monte-Carlo-PDF methods and laser diagnostics of the combustion in a two-stroke engine," Proc. Combust. Inst. **28**, 1153-1159 (2000).

205. M. S. Raju, "On the importance of chemistry/turbulence interactions in spray computations," Num. Heat transfer Part B **41**, 409-432 (2002).

206. T. Kunzelmann, *Charakterisierung von Sprayflammen mittels abbildender Laserspektroskopie*, in *Naturwissenschaftlich-Mathematische Gesamtfakultät*. 2002, Ruprecht-Karls Universität Heidelberg: Heidelberg, Germany, http://www.ub.uni-heidelberg.de/archiv/3046/.

207. T. D. Fansler and M. C. Drake, "Designer diagnostics for developing direct-injection gasoline engines," Journal of Physics: Conference Series **45**, 1-17 (2006).

208. J. Fischer, A. Velji, U. Spicher, F. Zimmermann, and C. Schulz, "Measurement of the equivalence ratio in the spark gap region of a gasoline direct injection engine with spark emission spectroscopy and tracer-LIF," SAE Technical Paper **2001-01-1295** (2004).

209. A. M. Lippert, T. D. Fansler, M. C. Drake, and A. S. Solomon, "High-speed imaging and CFD modeling of sprays and combustion in a spray- guided spark-ignition direct injection engine," in *6. AVL Internationales Symposium für Verbrennungsdiagnostik* (Baden-Baden, 2004).

210. S. Einecke, C. Schulz, and V. Sick, "Measurement of temperature, fuel concentration and equivalence ratio fields using tracer LIF in IC engine combustion," Appl. Phys. B **71**, 717-723 (2000).

211. F. Beyrau, A. Bräuer, T. Seeger, and A. Leipertz, "Gas-phase temperature measurement in the vaporizing spray of a gasoline direct-injection injector by use

of pure rotational coherent anti-Stokes Raman scattering," Optics Letters **29**, 247-249 (2003).

212. H. Kronemayer, K. Omerbegovic, and C. Schulz, "Quantification of the evaporative cooling in an ethanol spray created by a gasoline direct-injection system measured by multi-line NO-LIF gas-temperature imaging," Appl. Opt. **submitted** (2007).

213. M. Versluis, N. Georgiev, L. Martinsson, M. Aldén, and S. Kröll, "2D absolute OH concentration profiles in atmospheric flames using planar LIF in a bi-directional laser beam configuration," Appl. Phys. B **65**, 411-417 (1997).

214. A. G. Bailey, *Electrostatic spraying of liquids*. Electrostatics and elecotrostatic application series, ed. J.F. Hughes (John Wiley & Sons, Inc., New York, 1988).

215. R. B. Cole, *Electrospray ionization mass spectrometry*, ed. R.B. Cole (John Wiley & Sons, Inc., New York, 1997).

216. J. B. Fenn, M. Mann, C. K. Meng, S. F. Wong, and C. M. Whitehouse, "Electrospray ionization for mass spectrometry of large biomolecules," Science **246**, 64-71 (1989).

217. R. E. Hetrick, H. S. Hilbert, M. H. Parsons, and W. F. Stockhausen, *Fuel injection systems and strategy*. 1997, Ford Global Technologies, Inc.: United States Patent 5,671,716.

218. R. E. Hetrick and M. H. Parsons, *Electrospray fuel injection*. 1998, Ford Global Technologies, Inc.: United States Patent 5,725,151.

219. H. Kronemayer and I. Düwel, *Electrospray project*. 2006, Internal report, 5 pages, Prof. J. Wolfrum, Physical Chemistry Institute, Heidelberg University.

220. A. D'Alessio, *Particulate carbon: Formation during combustion*, ed. D.C. Siegla and G.W. Smith (Plenum Press, New York, 1983, 207).

221. "Health effects of transport-related air pollution," M. Krzyzanowski, B. Kuna-Dibbert, and J. Schneider, Editors (World Health Organisation, 2005), p. 30.

222. B. F. Kock, T. Eckhardt, and P. Roth, "In-cylinder sizing of Diesel particles by time-resolved laser-induced incandescence (TR-LII)," Proc. Combust. Inst. **29**, 2775-2781 (2002).

223. B. Quay, T.-W. Lee, T. Ni, and R. J. Santoro, "Spatially resolved measurements of soot volume fraction using laser-induced incandescence," Combust. Flame **97**, 384-392 (1994).

224. L. A. Melton, "Soot diagnostics based on laser heating," Appl. Opt. **23**, 2201-2208 (1984).

225. D. R. Snelling, F. Liu, G. J. Smallwood, and Ö. L. Gülder, "Evaluation of the nanoscale heat and mass transfer model of LII: Prediction of the excitation intensity," in *34th National Heat Transfer Conference* (Pittsburgh, 2000).

226. S. Will, S. Schraml, K. Bader, and A. Leipertz, "Performance characteristics of soot primary particle size measurements by time-resolved laser-induced incandescence," Appl. Opt. **37**, 5647-5658 (1998).

227. B. F. Kock and P. Roth, "Two-color TR-LII applied to in-cylinder Diesel particle sizing," in *Proc. of the European Combustion Meeting* (Orléans, 2003).

228. D. L. Hofeldt, "Real-time soot concentration measurement technique for engine exhaust streams," SAE Technical Paper Series No. 930079 (1993).

229. H. Bladh and P.-E. Bengtsson, "Characteristics of laser-induced incandescence from soot in studies of a time-dependent heat and mass-transfer model," Appl. Phys. B **78**, 241-248 (2004).

230. M. Hofmann, B. Kock, and C. Schulz, "A web-based interface for modeling laser-induced incandescence (www.LIISim.com)," in *European Combustion Meeting (ECM)* (Chania, Greece, 2007).

231. M. Hofmann, W. G. Bessler, C. Schulz, and H. Jander, "Laser-induced incandescence (LII) for soot diagnostics at high pressure," Appl. Opt. **42**, 2052-2062 (2003).

232. M. Hofmann, *Laser-induced incandescence for soot diagnostics at high pressure*, in *Naturwissenschaftlich-Mathematische Gesamtfakultät*. 2006, Ruprecht-Karls Universität Heidelberg: Heidelberg, Germany.

233. H. Zhao and N. Ladommatos, "Optical diagnostics for soot and temperature measurements in Diesel engines," Prog. Energy Combust. Sci. **24**, 221-255 (1998).

234. P. A. Berg, G. P. Smith, J. B. Jeffries, and D. R. Crosley, "Nitric oxide formation and reburn in low-pressure methane flames," Proc. Combust. Inst. **27**, 1377-1384 (1998).

235. S. Prucker, W. Meier, and W. Stricker, "A flat flame burner as calibration source for combustion research: Temperatures and species concentrations of premixed H2/air flames," Rev. Sci. Instrum **65**, 2908-2911 (1994).

236. M. Kerker, *The Scattering of Light and Other Electromagnetic Radiation* (Academic Press, New York, 1969).

237. K. C. Smyth and C. R. Shaddix, "The elusive History of m = 1.57 - 0.56i for the Refractive Index of Soot," Combust. Flame **107**, 314-320 (1996).

238. E. W. Rothe and P. Anresen, "Application of tunable excimer lasers to combustion diagnostics: a review," Appl. Optics **36**, 3971-4033 (1997).

239. K. Wakai, et al, "Correction method of radiation loss of thermocouples for high temperature gas measurements," Journal of gas turbine society (Japan) **7**, 33-38 (1979 [http://www.gifu-u.ac.jp/~wakailab/index_e.html]).

240. M. Saffman, "Parametric Studies of a solid wall quenching layer," Combustion and flame **55**, 141-159 (1984).

241. R. Schießl, U. Maas, A. Hoffmann, J. Wolfrum, and C. Schulz, "Method for absolute OH-concentration measurements in premixed flames by LIF and numerical simulations," Appl. Phys. B **78**, 519-533 (2004).

242. D. I. Shin, T. Dreier, and J. Wolfrum, "Spatially resolved absolute concentration and fluorescence-lifetime determination of H2CO in atmospheric-pressure CH4/air flames," Appl. Phys. B **72**, 257 (2001).

243. V. Simanzhenkov, P. Ifeacho, H. Wiggers, J. Knipping, and P. Roth, "Synthesis of germanium oxide nanoparticles in low-pressure premixed flames," Journal of Nanoscience and Nanotechnology **4**, 157-161 (2004).

244. A. Kowalik, P. Ifeacho, H. Kronemayer, H. Wiggers, P. Roth, and C. Schulz, "Comparison of numerical simulation and experimental investigations on TiO2-nanoparticle synthesis in premixed flames," in *VDI Berichte* (Berlin, Germany, 2007).

245. D. Lindackers, M. G. D. Strecker, P. Roth, C. Janzen, and S. E. Pratsinsis, Combust. Sci. Tech. **123**, 287 (1997).

246. C. Janzen and P. Roth, Combust. Flame **125**, 1150 (2001).

247. G. T. Linteris, V. R. Katta, and F. Takahashi, "Experimental and numerical evaluation of metallic compounds for supressing cup-burner flames," Comb. Flame **138**, 78-96 (2004).

248. M. Horiuchi, S. Suganuma, and M. Watanabe, "Electrochemical power generation directly from combustion flame of gases, liquids, and solids," J. Electrochem. Soc. **151**, A1402-A1405 (2004).

249. M. Vogler, D. Barzan, H. K. Kronemayer, C. Schulz, M. Horiuchi, S. Suganuma, Y. Tokutake, J. Warnatz, and W. G. Bessler, "Direct-Flame Solid-Oxide Fuel Cell (DFFC): A Thermally Self-Sustained, Air Self-Breathing, Hydrocarbon-Operated SOFC System in a Simple, No-Chamber Setup," in *10th International Symposium on Solid Oxide Fuel Cells (SOFC-X)* (Nara, Japan, 2007).

250. H. Kronemayer, W. G. Bessler, M. Vogler, M. Horiuchi, S. Suganuma, Y. Tokutake, C. Schulz, and J. Warnatz, "A flame as fuel reformer for solid oxide fuel cells," in *7th European Solid Oxide Fuel Cell Forum* (Lucerne, Switzerland, 2006).

251. I. Glassman, *Combustion*, 3 ed (Academic Press, San Diego-London-Boston-New York-Sydney-Tokyo-Toronto, 1996).

252. R. J. Kee, M. E. Coltrin, and P. Glarborg, *Chemically reacting flow. Theory and practice* (John Wiley & Sons, 2003).

253. R. C. Weast and M. J. Astle, eds. *CRC Handbook of chemistry and physics*, 63 ed (CRC press, Boca Raton, Florida, 1982).

254. D. G. Goodwin, *Cantera* (http://www.cantera.org, 2001-2005).

255. M. W. Chase, C. A. Davies, J. R. Downey, D. J. Frurip, R. A. McDonald, and A. N. Syverud, "JANAF Thermochemical Tables," J. Phys. Chem. Ref. Data **14**, Supplement 1 (1985).

256. M. Horiuchi, S. Suganuma, M. Watanabe, and Y. Tokutake, "Direct flame fuel cells - SOFC operation with combustion flames," in *6th European Solid Oxide Fuel Cell Forum* (Lucerne, Switzerland, 2004), 154-162.

257. T. Hibino, H. Atsuko, I. Takao, T. Jun-ichi, Y. Shin-ichiro, and S. Mitsuro, "A low-operating-temperature solid oxide fuel cell in hydrocarbon-air mixtures," Science **288**, 2031-2033 (2000).

258. Z. Shao, S. M. Haile, J. Ahn, P. D. Ronney, Z. Zhan, and S. A. Barnett, "A thermally self-sustained micro solid-oxide fuel-cell stack with high power density," Nature **435**, 795-798 (2005).

259. T. W. Napporn, X. Jacques-Bédard, F. Morin, and M. Meunier, "Operating conditions of a single-chamber SOFC," J. Electrochem. Soc. **151**, A2088-A2094 (2004).

260. P. Jansinki, T. Suzuki, F. Dogan, and H. U. Anderson, "Impedance spectroscopy of single chamber SOFC," Solid State Ionics **175**, 35-38 (2004).

261. Y. Hao, Z. Shao, J. Mederos, W. Lai, D. G. Goodwin, and S. M. Haile, "Recent advances in single-chamber fuel cells: Experiment and modeling," Solid State Ionics, in press (2006).

262. J. P. Bingue, A. V. Saveliev, A. A. Fridman, and L. A. Kennedy, "Hydrogen production in ultra-rich filtration combustion of methane and hydrogen sulfide," Int. J. Hydrogen Energy **27**, 643-649 (2002).

263. H. Pedersen-Mjaanes, L. Chan, and E. Mastorakos, "Hydrogen production from rich combustion in porous media," Int. J. Hydrogen Energy **30**, 579-592 (2005).

264. R. S. Dhamrat and J. L. Ellzey, "Numerical and experimental study of the conversion of methane to hydrogen in a porous media reactor," Combust. Flame **144**, 698-709 (2006).

265. K. Kendall, C. M. Finnerty, J. C. Austin, and T. Alston, "Ceramic fuel cells to replace metal burners," J. Mat. Sci. **36**, 1119-1124 (2001).

266. C. M. Finnerty, G. A. Tompsett, K. Kendall, and R. M. Ormerod, "SOFC system with integrated catalytic fuel processing," J. Power Sources **6**, 459-463 (2000).

267. M. Gödickemeier and L. J. Gauckler, "Engineering of solid oxide fuel cells with ceria-based electrolytes," J. Electrochem. Soc. **145**, 414-421 (1998).

9 Acknowledgements – Danksagung

Sehr herzlich möchte ich mich bei Prof. Dr. Jürgen Wolfrum für die Aufnahme in seinen außerordentlich durchdacht und effizient organisierten Arbeitskreis danken. Herr Wolfrum, Sie strahlen mit Ihrer freundlichen und ermutigenden Art eine besondere Begeisterung für Forschung und Wissenschaft aus. Nur durch Ihren ständigen Einsatz war die Arbeit an diesem hochinteressanten Thema möglich.

Ganz besonders danke ich Prof. Dr. Christof Schulz für die hervorragende Betreuung. Christof, vielen Dank für die ständige Unterstützung, die vielen Ratschläge und die Hilfe bei all meinen Fragen. Dank Deiner stets offenen und interessierten Einstellung ist exzellente Forschung auf diesem interdisziplinären Gebiet erst möglich. Vielen Dank für die einzigartigen Möglichkeiten, die Du mir in den letzten Jahren geboten hast.

Ausdrücklich möchte ich mich auch bei Dr. Wolfgang Bessler bedanken. Wolfgang, ohne Deine detaillierten Vorarbeiten wäre diese Dissertation nicht möglich gewesen. Vielen Dank auch für die enge Zusammenarbeit auf dem zukunftsweisenden Gebiet der Brennstoffzellentechnologie.

Ich danke allen Kollegen in Heidelberg und besonders denen, die mich in der zweiten Hälfte der 3 Jahre dauernden Arbeit nach Duisburg begleitet haben. Max und Burkhard, danke für eure Freundschaft und die kurzweilige Zeit im Büro und im Labor sowie für schöne Abende in Heidelberg und Duisburg, Skifahren und vieles mehr. Burkhard, durch deinen großen Einsatz als erster Laserdiagnostik-Experte in Duisburg hast du mir den Start in Duisburg erheblich erleichtert. Axel, danke für deine tatkräftige Unterstützung bei Laser-Reparaturen. Daniel, Frank, Isabell, Kemal, My Yen und Wieland: Vielen Dank für die gute Zeit mit Euch, für alle Unterstützung, Hilfe und nette Diskussionen.

Ein großer Dank geht an die Duisburger Kollegen, die nicht nur im Rahmen des Umzugs unermüdliches Engagement gezeigt haben: Ralf, Barbara, Christian, Dieter, Hartmut, Huinan, Ludger, Michaela, Mustapha, Natascha, Pascal, und Yin sowie die gesamte Laserdiagnostik-, Motoren-, Nanopartikel- und Stoßrohrgruppe; danke für die Unterstützung und das nette kollegiale Klima. Thomas, vielen Dank für das Korrekturlesen dieser Arbeit.

Einen nicht zu unterschätzenden Beitrag zum Gelingen dieser Arbeit tragen die Werkstätten des PCI in Heidelberg (Uwe, Gerhard, und Herr Weiß) und des IVG in Duisburg (Jörg Albrecht, Herr Jermann, Herr Kietzmann, Herr Visser). Vielen Dank für die zügige Bearbeitung zahlreicher Aufträge.

Für die großzügige Bereitstellung eines Einspritzsystems danke ich Herrn Grzeszik und der Robert Bosch GmbH. Bei Frau Dr. H. Jander von der Universität Göttingen bedanke ich mich für die Leihgabe eines Flachflammenbrenners.

I would like to thank Prof. R. K. Hanson for the great opportunity to visit his group at Stanford University even twice. Especially, I want to thank Dr. Jay Jeffries for his hospitality and scientific guidance and Tonghun, John, Heije, and Greg for an introduction to the American way of life. I am also grateful to Tom Settersten at the CRF at Sandia National Laboratories, Livermore, for his hospitality and the chance to work in his lab as well as for scientific discussions.

I also want to thank Mr. Horiuchi from Shinko Electric Industries, Japan, and Takayuki Fuyoto from Toyota Central R&D Labs for fruitful collaborations as well as for insights in the Japanese country and culture.

Further, I want to thank Prof. E. Gutheil and Hai-Wen Ge for helping me to understand numerical simulations.

Für die Finanzierung, insbesondere der zahlreichen Auslandsreisen, möchte ich der DFG und dem DAAD danken. Auslandsaufenthalte sind von unschätzbarem Wert und ermöglichen in der Tat eine persönliche als auch wissenschaftliche Horizonterweiterung. Auch für die Unterstützung im Rahmen des SFB 359 und des SFB 445 sowie des IGK 710 und des GRK 1114 bin ich dankbar.

Ich danke allen, die mich während des Studiums begleiteten und diese Zeit unvergesslich gemacht haben.

Ein ganz besonderer Dank gebührt meiner Familie. Meinen Eltern und Großeltern danke ich herzlich für die ständigen Ermutigungen und großzügige Unterstützung. Mein Bruder Ralf ist immer für ein, selbst wissenschaftliches, Gespräch zu haben. Simone, ich bin dir unendlich dankbar für Deine Geduld und Liebe und nicht zuletzt für die Tatsache, dass Du Dich mit mir auf das Abenteuer Ruhrgebiet eingelassen hast.

Erklärung:

Hiermit erkläre ich an Eides statt, dass ich die hier vorliegende Arbeit selbstständig verfasst und keine anderen als die angegebenen Quellen und Hilfsmittel benutzt habe.

Heidelberg, den . . . .

(Helmut Kronemayer)